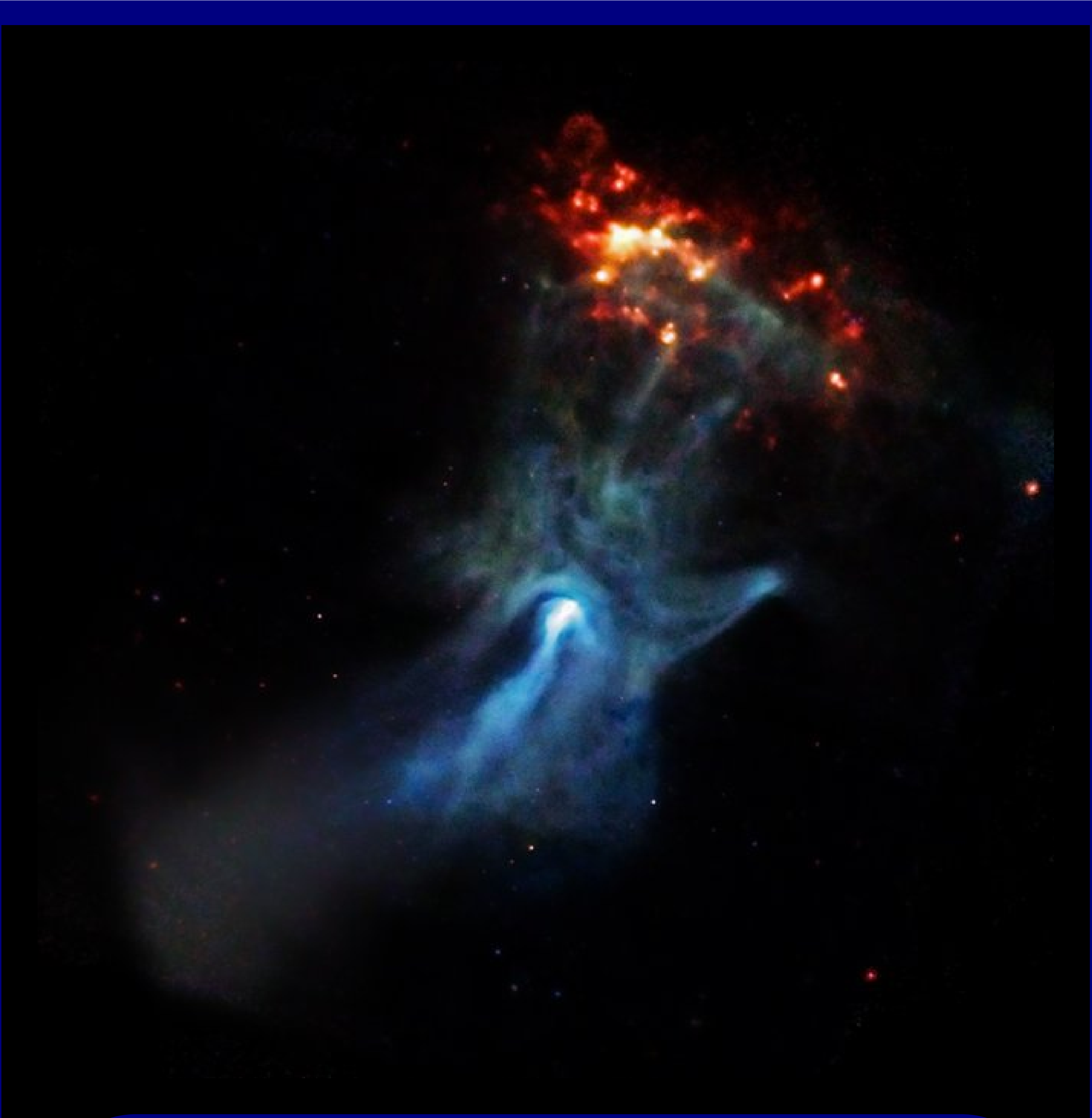

Observations of Compact Objects

Diplomarbeit von Eugenia Litzinger

Friedrich-Alexander-Universität Erlangen-Nürnberg
Dr. Karl Remeis-Sternwarte Bamberg & ECAP

Observations of Compact Objects

Diplomarbeit
im Studiengang Diplom Physik
an der Friedrich-Alexander-Universität Erlangen-Nürnberg

vorgelegt von

Eugenia Litzinger

Dr. Karl Remeis-Sternwarte Bamberg & ECAP

Betreuer:

Prof. Dr. Jörn Wilms
Prof. Dr. Matthias Kadler

16. Dezember 2011

The image on the title page shows the young pulsar PSR B1509−58 observed by *Chandra* from 2004 to 2005. The image is 19.6 arcmin across. The colors depend on the energy range: red (0.5–1.7 keV), green (1.7–3.0 keV), blue (3.0–8.0 keV) (Credit: NASA/CXC/SAO/P.Slane, et al.).

Zusammenfassung

In dieser Diplomarbeit wurden Beobachtungen kompakter Objekte, wie Neutronensterne und aktive Galaxien, mittels Röntgensatelliten und optischer Monitore ausgewertet. Dabei kann man die Arbeit in zwei Teile gliedern.

Im ersten Teil wurden die Röntgendaten des Rossi X-ray Timing Explorers (*RXTE*) des Pulsars PSR B1509−58 über einen Zeitraum von 14 Jahren analysiert. Dabei wurden sowohl Phasen-gemittelte als auch Phasen-aufgelöste Spektren für die drei bedeutendsten Kalibrationsepochen des Satelliten erzeugt. Die Spektren konnten mit einem absorbierten Potenzgesetz gut beschrieben werden. Die Pulsperiode von B1509−58 nahm kontinuierlich zu und keine Sprünge, sogenannte Glitches, waren zu sehen. Bei den phasenaufgelösten Spektren konnte das Spektrum des Pulsars von dem umgebenden Pulsarwindnebel selektiert werden. Dabei konnte die unterschiedliche Physik der beiden Teile untersucht werden. Durch regelmäßige Beobachtungen und konstante Parameter der Spektren eignet sich diese Quelle sehr gut als Kalibrationsquelle für den instrumentellen Hintergrund von *RXTE* und damit auch für andere Missionen.

Im zweiten Teil wurden ausgesuchte aktive Galaxien des TANAMI-Samples untersucht. Dabei wurden die Röntgen- und optischen Beobachtungen des X-ray Multi-Mirror Mission (*XMM-Newton*) von vier Quellen (PKS 2004−447, PKS 2005−489, Pictor A und PKS 2155−304) analysiert. Zusätzlich wurden noch Röntgendaten des *Swift*-Satelliten der Quelle PKS 0208−512 dazugenommen. Die Spektren konnten sehr gut mit einem absorbierten Potenzgesetz, bzw. einem geknickten Potenzgesetz, beschrieben werden. Unterschiede in der Aktivität einiger Quellen konnten gesehen werden, was auf nicht konstante Akkretion schließen lässt. Zusammen mit den optischen Daten von *XMM-Newton* konnte zu vier Objekten eine spektrale Energieverteilung ermittelt werden. Da es nicht genug Datenpunkte für eine komplette Verteilung gab, konnte das Spektrum, dass normalerweise aus zwei Höckern besteht, die zu unterschiedlichen Strahlungsmechanismen gehören, nur angedeutet werden.

Abstract

In this diploma thesis compact objects like neutronstars and active galactic nuclei were analyzed using X-ray satellites and optical monitors. One can divide the work in two parts.

In the first part the X-ray data of the Rossi X-ray Timing Explorer (*RXTE*) over 14 years for the pulsar PSR B1509−58 were analyzed. This includes both, phase-averaged and phase-resolved spectra generated for the three major calibartion epochs of the satellite. The spectra could be well described by an absorbed power law. The pulse period of B1509−58 increased continuously and no jumps, called glitches, were seen. In the phase-resolved spectra the spectrum of the pulsar could be selected from the surrounding pulsar wind nebula. These demonstrated the different physics of the two parts. Through regular observations and constant parameters of the spectra, these source is very well suited as a calibration source for the instrumental background of *RXTE* and also for other missions.

In the second part selected active galaxies of the TANAMI-sample were examined. Here, the X-ray and optical observations of the X-ray Multi-Mirror Mission (*XMM-Newton*) of four sources (PKS 2004−447, PKS 2005−489, Pictor A and PKS 2155−304) were analyzed. In addition, X-ray data of the *Swift*-satellite for the source PKS 0208−512 were taken. The spectra could be well described by an absorbed power law and broken power law, respectively. Differences in the activity of some sources could be seen, suggesting non-constant accretion. Together with the optical data of *XMM-Newton* for four objects a spectral energy distribution were determined. Since there were not enough data points for a complete distribution, the spectrum, that usually consists of two humps which belong to different radiation mechanisms, was only hinted at.

Contents

The small image on the title page shows the western dome of the Dr. Karl Remeis-Observatory in Bamberg, Germany.

And God said, “Let there be light,” and there was light. God saw that the light was good, and he separated the light from the darkness.

(Genesis, 1.3-1.5)

1 X-ray on the sky

From the Greek to Galilei

When God made light he did it in one day and thereto work for astronomers for years. The sparkly points on the sky always fascinated humankind. The first explanations for their origin are as different and numerous as the nations on the Earth. The Greek and Romans saw Gods and mythological creatures like dragons and unicorns in them. The name of the bright, white streak on the sky has one of its origin in a Greek myth: ‘The baby Heracles, son of the first God Zeus and the mortal women Alcmene, was loved above all by his father. He wanted his son to own godlike qualities and to get immortal. Therefore, he decided to let him drink the milk from his wife Hera. But as the child was not her own, Zeus did it secretly and sent out his herald Hermes. As Hera was asleep he laid Heracles aside her and let him suck her milk. When Hera woke up and saw the unknown child she pushed him away and her squirted milk became the Γαλαξ΄ιας (Galaxias, Milky Way) (after Eratosthenes, see Ridpath, 1989).‘ It is seen that people soon began to search for the answer of the question: *Why is the world and its paraphernalia like it is?* One of my favorite conversations about the origin of the stars is from the animation *The Lion King* (Walt Disney, 1994). The meerkat Timon, the warthog Pumbaa and the lion Simba lie on a hill after a large dinner. They have a look on the sky:

Pumbaa: "Timon, ever wonder what those sparkly dots are up out there?"
Timon: "Pumbaa, I don’t wonder I know."
Pumbaa: "Uh, what are they?"
Simon: "They’re fireflies. Fireflies that got tacked up on that big bluish-black thing."
Pumbaa: "Uh, sure? I always thought they were balls of gas, burning billion of miles away."
Simon: "Pumbaa, for you every thing is gas."
Pumbaa: "Simba, what do you think?"
...
Simba: "Somebody once told me that the great kings of the past are up there. Watching over us."
Pumbaa: "Really?"
Timon: "You mean a bunch of royal dead guys are watching us? Pff, ha ha ha!"
Simba (embarrassed): "Yeah, pretty dumb, eh?".

In the beginning of the exploration of the nature of the "dots up out there" people laughed at the visionaries. It was clear, that the motion of the planets, the Moon and the stars

Figure 1.1: Painting of the Greek myth about "The origin of the Milky Way" (1575–1580) by Jacopo Tintoretto (1518–1594), National Gallery, London (Source: `http://en.wikipedia.org/wiki/File:Jacopo_Tintoretto_011.jpg`)

was regular, but why should it not if God was the creator? Everything in the universe was adjusted at the Earth. This geocentric model was teached to the end of the Middle Ages. The apparent backward motion of the planets was explained by Claudius Ptolemy (AD 90 – AD 168) in his *Mathematices syntaxeos biblia XIII* (Mathematical Treatise, about AD 150, also known as *Almagest*). Thereby the planets move on epicycles, the movement on small circles on a big circle, around the earth (see Fig. 1.2). These views were shaken in 1610 when Galileo Galilei (February 15, 1564 — January 8, 1642) turned his telescope, which has only been invented recently, on the Jupiter and saw moons orbiting the big planet. This was the first time that celestial bodies were discovered which clearly do not revolve around Earth. Galilei set the Sun as the middle of the Universe and the Earth was orbiting it like the other planets. Thus, he confirmed the hypothesis of Nicolaus Copernicus (February 19, 1473 — May 24, 1543), which he published in 1543 in his work *De revolutionibus orbium coelestium* (On the Revolutions of the Celestial Spheres). The church did not agree with his thesis and forced Galilei 1633 to revoke if he not wanted to be burnt at the stake. He revoked but he is said to have muttered „Eppur si muove“ (and it [the Earth] does move) when leaving the courtroom. But the progress was not stopped. Johannes Kepler's (December 27, 1571 — November 15, 1630) description of the planetary orbits as ellipses in his work *Harmonices Mundi* (The Harmony of the World, 1619), forced the heliocentric world view which, however, was enforced in the 18th century.

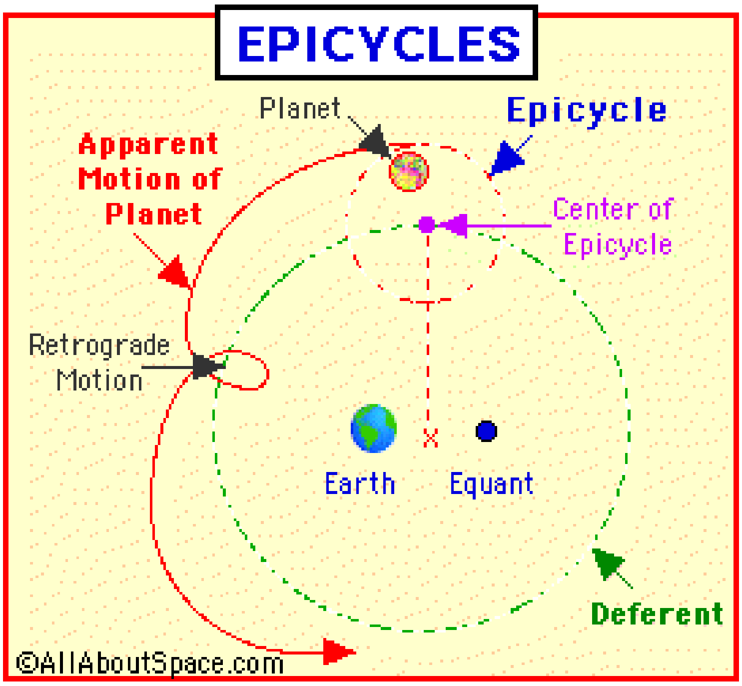

Figure 1.2: Explanation of the retrograde movement of the inner planets with epicycles by Ptolemy (Source: `http://www.enchantedlearning.com/subjects/astronomy/glossary/indexe.shtml`).

The discovery of the electromagnetic spectrum

One century later, in the 19th century, it was discovered that the electromagnetic spectrum consists of more than only visible light. James Clerk Maxwell (June 13, 1831 – November 5, 1879) was the founder of the electromagnetism. He combined electricity and magnetism with his famous equations (Maxwell equations). In addition, he predicted waves of oscillating electric an magnetic fields that move through empty space. He calculated the velocity of this waves to 310,740,000 m/s. In his work Maxwell wrote in 1864 (Maxwell, 1865): *„This velocity is so nearly that of light, that it seems we have strong reason to conclude that light itself (including radiant heat, and other radiations if any) is an electromagnetic disturbance in the form of waves propagated through the electromagnetic field according to electromagnetic laws.“* This hypothesis was confirmed by Heinrich Hertz (February 22, 1857 – January 1, 1894) in 1886 (Hertz, 1887). Konrad Wilhelm Röntgen (March 27, 1845 – February 10, 1923) discovered "a new type of rays" on November 8, 1895 (Röntgen, 1895). He called them X-rays to distinguish them from other rays. Their properties were that they go through materials where visible light is shielded. Only thick metal shielding, such as lead, could not be penetrated by the rays. For this discovery Röntgen was awarded the first Nobel Prize for physics in 1901.

This discoveries opened up completely new possibilities, also for astronomy. However, the first none optical electromagnetic waves from an celestial object were measured in 1933. Karl Jansky (October 22, 1905 — February 14, 1950) detected a radio signal from an object outside our Solar System (Jansky, 1933), the center of the Milky Way. For other wavelengths it is difficult to receive a signal on Earth's surface because Earth's atmosphere

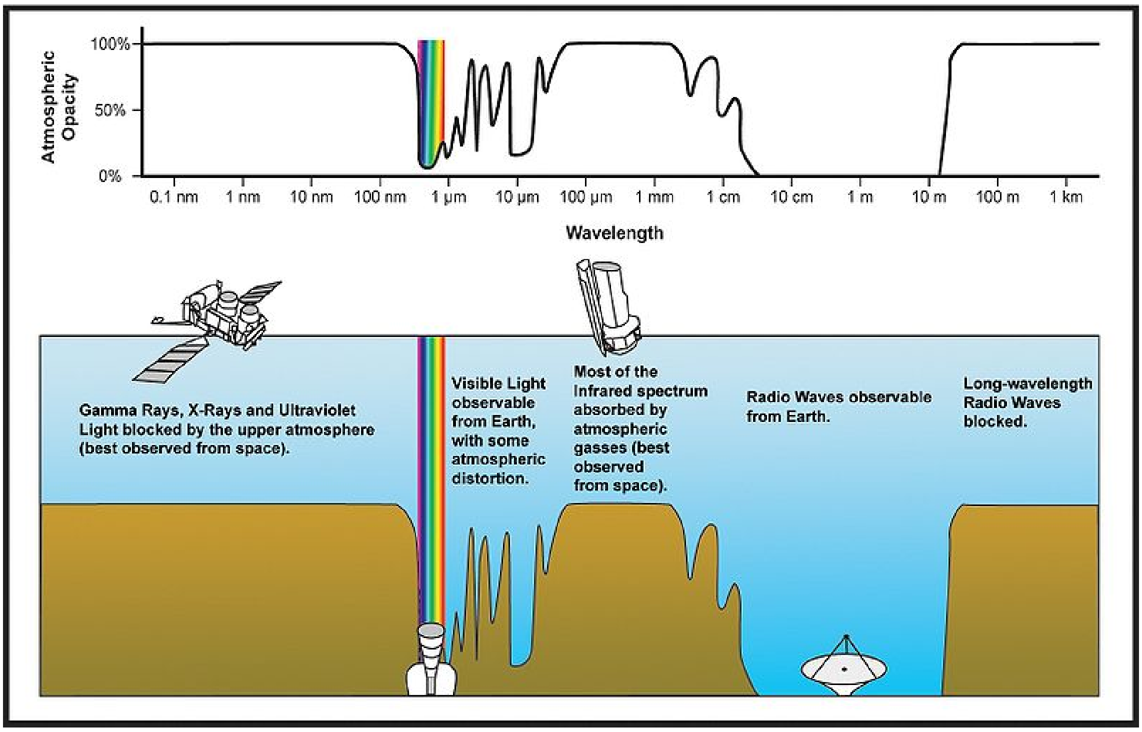

Figure 1.3: Plot of the opacity of the Earth's atmosphere for different wavelengths of the electromagnetic spectrum and types of observations of celestial sources. (Source: NASA public domain, acquired from Wikimedia Commons)

is not permeable for all electromagnetic waves (see Fig.1.3). Infrared, ultraviolet, X-ray and gamma-ray astronomy must be done by balloons, rockets or satellites. The first measurements of X-rays from the Sun were taken with a V-2 rocket on January 28, 1949. Although this observations the first detection of a cosmic X-ray source in 1962 was a surprise. Scorpius X-1 (Sco X-1) has a X-ray emission 10,000 times higher than its optical emission and 100,000 times greater than the emission of the Sun in all wavelengths. A new field of astronomy was born, but it was still limited due to the low height of the balloons and rockets.

Modern X-ray astronomy

As the human started to conquer the universe a new time of X-ray astronomy dawned. The first men made object in Earth's orbit was the artificial satellite *Sputnik 1*. It was launched by the Soviet Union on October 4, 1957. After this day things changed. In the USA the *National Aeronautics and Space Administration* (NASA) was founded on October 1, 1958 (see `http://history.nasa.gov/sputnik/`). Now the way was open to explore the universe and of course also Earth from the space. The *UHURU*[1] satellite (lifetime: December 12, 1970 – March 1973, energy range: 2–20 keV) was the first earth-orbiting X-ray satellite. It scanned the sky and detected 339 X-ray sources. The first X-ray observatory was the *Astronomical Netherlands Satellite* (ANS) in 1974 (NASA, News Release

---

[1] `http://heasarc.nasa.gov/docs/uhuru/uhuru.html`

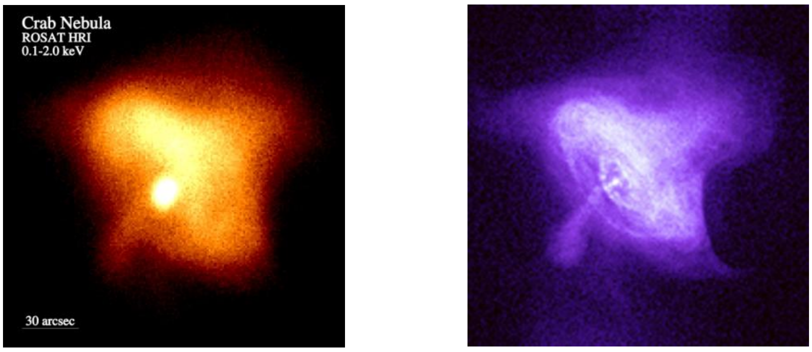

(a) (b)

Figure 1.4: X-ray image of the Crab Nebula taken with (*a*) *ROSAT* in the 0.1–2.0 keV range (Credit: S. L. Snowden USRA, NASA/GSFC) and (*b*) *Chandra* in the 0.5–8.5 keV range (Credit: NASA/CXC/SAO). The better angular resolution of *Chandra* is clear visible.

70–91, lifetime: August 30, 1974 – June 14, 1977, energy range: 0.1–30 keV and UV: 150–330 nm). The *High Energy Astronomy Observatory 2* (*HEAO-2*) or *Einstein Observatory* (lifetime: November 12, 1978 – April 1981, energy range: 0.2–20 keV) detected thousands of new celestial sources and yielded the first X-ray images of them. An all-sky survey of X-rays was done by *ROSAT*[2] (**RO**entgen**SAT**ellit, lifetime: June 1, 1990 – February 12, 1999, energy range: 0.1–2.5 keV (X-ray), 62-206 eV (EUV); *ROSAT* entered the Earth's atmosphere on October 23, 2011). Thereby 60,000 new sources were found. One of the longest time in space and work had the *Rossy X-ray Timing Explorer* (*RXTE*, lifetime: December 30 1995 – present, energy range: 2–60 keV (PCA), 2–10 keV (ASM), 15–250 keV (HEXTE); see Sec. 3.1, *RXTE* will re-enter the Earth's atmosphere at the end of the year 2011). It can detect emissions as brief as 10–100 μs. *BeppoSAX* (lifetime: April 30, 1996 – April 30, 2002, energy range: 0.1–300 keV) detected short gamma-ray bursts for which the redshift could be calculated more accurately. The *Chandra X-ray Observatory*[3] (*Chandra*, lifetime: July 23, 1999 – present, energy range: 0.1–10 keV) belongs together with the *Hubble Space Telescope*[4] (optical, lifetime: April 25, 1990 – present), the *Compton Gamma Ray Observatory*[5] (lifetime: April 5, 1991 – June 4, 2000, energy range: 30 keV – 300 GeV), and the *Spitzer Space Telescope* (infrared, lifetime: August 25, 2003 – present) to the *Great Observatory Program.* Pictures taken by *Chandra* have an angular resolution of 0.5 arcseconds, almost ten times better than *ROSAT* with 4 arcseconds (see Fig. 1.4). With the *X-ray Multi-mirror Mission Newton* (*XMM-Newton*, working time: 1999 – present, energy range:0.1–15 keV (*EPIC-pn* and *MOS*) and optical: 180–600 nm (*OM*); see Sec. 5.1) the *European Space Agency* send out *"the biggest scientific satellite ever built in Europe. Its telescope mirrors are amongst the most powerful ever developed in the world, and with its sensitive cameras it can see much more than any previous X-ray satellite."*[6] The *Swift Gamma-Ray Burst Mission* (*Swift*, lifetime: November 20, 2004 –today, energy range: 0.3–3 keV (XRT), 15–150 keV (BAT) and optical: 170–650 nm (UVOT); see Sec. 5.3) was one of the last but not *the last* X-ray satellites launched. It serves, like *BeppoSAX*, to investigate

---

[2] `http://heasarc.gsfc.nasa.gov/docs/rosat/`

[3] `http://www.nasa.gov/mission_pages/chandra/main/index.html`

[4] `http://hubble.nasa.gov/`

[5] `http://heasarc.gsfc.nasa.gov/docs/cgro/index.html`

[6] `http://sci.esa.int/science-e/www/area/index.cfm?fareaid=23`

gamma-ray bursts and to learn more about the early universe.

In this thesis two different topics will be discussed. In the first part I will introduce the forming and structure of neutron stars and pulsars and their radiation mechanism (Chap. 2). Following this I will analyze 14 years of data of the pulsar PSR B1509−58 (Chap. 3) taken with the *Rossy X-ray Timing Explorer* (Sec. 3.1). Phase averaged as well as phase resolved spectra of the three major calibration epochs of *RXTE* are analyzed (Sec. 3.3.2, Sec. 3.3.3). At the end of the first part I will summarize the results for B1509−58 (Sec. 3.4).

In the second part four active galactic nuclei (AGN, Chap. 4) of the TANAMI (Chap. 5) sample were analyzed in the X-ray and the optical with the *X-ray Multi-Mirror Mission Newton* (*XMM-Newton*, Sec. 5.1, Sec. 5.2) satellite and one only in the X-ray with the *Swift*-satellite (Sec. 5.3, Sec. 5.4). For the first four sources spectral energy distributions (SED, see the Sections 5.2) were made to show the behavior of AGN's over the frequency range. In the end I will give an overview about all the results in Chapter 6.

> The most beautiful thing we can experience is the mysterious. It is the source of all true art and all science.
>
> *(Albert Einstein)*

2 Neutron stars and Pulsars

Stars are like human: they were born, they develop and at the end they die. And like human there are different groups of stars:

- the silent ones - small stars which have not enough mass to start hydrogen-burning and end their life as a brown dwarf
- the normal ones - stars like our sun which burn hydrogen and end up as a red giant
- and the big ones - massive stars which live their life like a rock star: excessive short life with an explosive end

The latter ones, or their final stages, play a major role in the first part of this thesis. I will give a rough overview about the evolution of a star which has enough mass to end up as a neutron star and the mechanism how this star produces this kind of stellar object (see Fig. 2.1; for more details about the evolution of a star, I recommend Kippenhahn & Weigert (1990), Prialnik (2000) and Padmanabhan (2001)). After this I will describe the physics of a pulsar and the origin of the radiation of an isolated neutron star (for more details to this part see Lyne & Graham-Smith, 1998; Haensel et al., 2007).

2.1 Evolution

Stars are born in cold (20–30 K) molecular clouds which consist of neutral hydrogen ($\rho = 10^6\,\mathrm{cm}^{-3}$). This clouds are located along the spiral arms of galaxies (i.e., elliptical galaxies do not produce stars anymore). In our Milky Way one of the closest and most beautiful star forming regions is the Orion Nebula (see Fig. 2.2). The clouds are stable as long as the gravitation and the gas pressure are in equilibrium. Due to shock waves of exploding stars or stellar winds this equilibrium can be broken. Once the gravitation exceeds the gas pressure the cloud will collapse. The Jean's Mass, M_J, gives the lower limit for the mass where a molecular cloud is still stable (see Eq. 2.1, Jean's Criterion):

$$M > M_J = \left(\frac{5k_\mathrm{B}T}{G\mu m_\mathrm{u}}\right)^{\frac{3}{2}}\left(\frac{3}{4\pi\rho_0}\right) \tag{2.1}$$

where k_B is the Boltzmann Constant, T the temperature of the cloud, G the Gravitation Constant, μ_u the atomic mass of the molecular of which the cloud consists and ρ_0 the

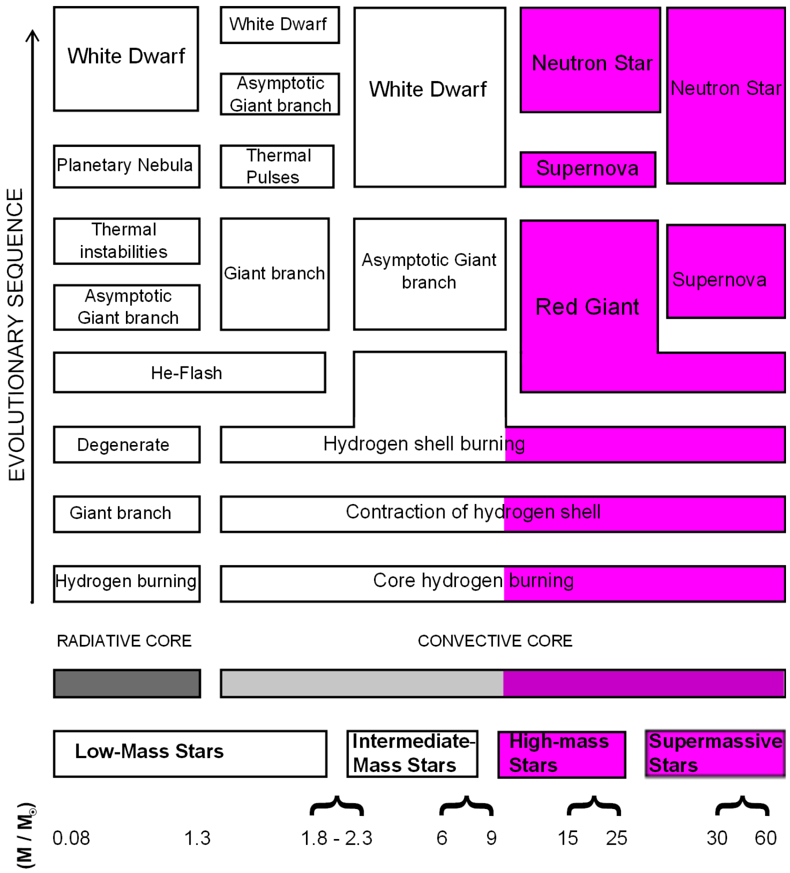

Figure 2.1: Overview of the stellar evolution of stars with different masses after Padmanabhan (2001, Fig. 1.2). The magenta path shows the evolution of massive stars which end up as a neutron star.

density. If the mass of a protostar reaches $0.08\,M_\odot$ core fusion starts. Protostars with a mass higher than $8\,M_\odot$ are called massive stars and the nuclear evolution of this type of stars from the beginning to their end is described in the following.

2.1.1 Nuclear evolution

Due to its origin in a molecular cloud a star exists of neutral hydrogen. This hydrogen can fuse to helium at temperatures of some 10^6 K according to the schematic:

$$4p \rightarrow {}^4\mathrm{He} + 2e^- + 2\nu_e + \gamma + E \tag{2.2}$$

For this hydrogen burning two cycles are possible which depends on the mass and therefore of the temperature in the core on the star. Stars with a mass smaller than $1.5\,M_\odot$ gain energy by the *proton-proton chain* (pp chain). There, two protons react to form a deuterium nucleus ^{2}H by β^+ decay (this is very unusual and has a small cross-section), which than reacts with another proton to ^{3}He. The final steps to get a ^{4}He nucleus can be processed on three different ways (see Fig. 2.3), which depends again on the temperature: ppI for $T \leq 2 \times 10^7$ K, ppII for $T = 1.4 - 2.3\ \times 10^7$ K and ppIII for $T \geq 2.3\ \times\ 10^7$ K.

Figure 2.2: The Orion Nebula (Image Credit & Copyright: Jesús Vargas (Astrogades) & Maritxu Poyal (Maritxu)).

More massive stars gain energy by the CNO cycle, which dominates above 2×10^7 K. During this process the carbon, nitrogen and oxygen nuclei work as catalysts and are destroyed and reformed. The number of CNO (and F) nuclei stays constant in time.

The energy generation for the two processes are very different. While for the pp chain it is $\propto T^5$, it is $\propto T^{17}$ for the CNO cycle and therefor more effective.

When 10–20 % of the hydrogen are exhausted in the core, it will contract. The density and the temperature increase to a value where helium-burning starts. The process for this reaction is called triple-α reaction due to three ^{4}He nuclei (α particles), which take place. The more massive stars can reach densities and temperatures in their cores, which are needed for higher nuclear burning and thus higher elements were produced. Burning mechanism take not place in the core only, but also in shells around it, where the temperature is high enough for fusion of lighter elements. This is called *shell burning* (see Fig. 2.5). The nuclear reactions take place as long as there is a net energy generation. The highest element which can be produced is ^{56}Fe. All higher elements can only be generated by an input of energy.

A star like our Sun would also burn helium, but when the supply decreases, the density and temperature is not high enough for starting higher nuclear reactions. The radius of the Sun would increase due to the shell burning and the surface temperature would decrease. Such a star is than called a *red giant*.

All the phases of burning last a typically time. The nuclear timescale for the different states can be calculated by

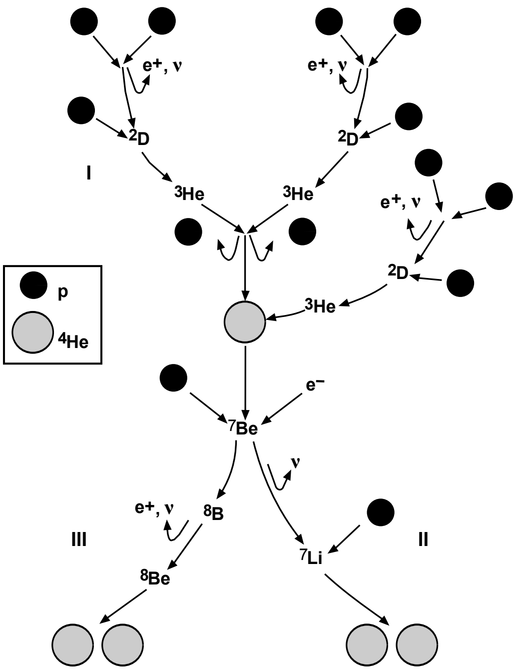

Figure 2.3: Nuclear reactions of the pp I, II and III chain (Prialnik, 2000, Fig. 4.3).

Table 2.1: Timescales of the burning stages of a $20\,M_\odot$ star (Thielemann et al., 2011).

Fuel	ρ_c $(\mathrm{g\,cm^{-3}})$	T_c $(10^9\,\mathrm{K})$	τ (yr)	L_{phot} $(10^{38}\,\mathrm{erg\,s^{-1}})$
Hydrogen	5.6	0.04	1.0×10^7	2.7
Helium	9.4×10^2	0.19	9.5×10^5	5.3
Carbon	2.7×10^5	0.81	3.0×10^2	4.3
Neon	4.0×10^6	1.70	3.8×10^{-1}	4.4
Oxygen	6.0×10^6	2.10	5.0×10^{-1}	4.4
Silicon	4.9×10^7	3.70	2 days	4.4

$$\tau_{\mathrm{nuc}} = \frac{E_{\mathrm{nuc}}}{L} = \varepsilon X \frac{M}{L} \tag{2.3}$$

where E_{nuc} is the net energy for the process, L the luminosity of the star, ε the rate of the fuel per gram and X the percentage of the fuel that can be used. For a $25\,M_\odot$ star the timescales are shown in Table 2.1.1.

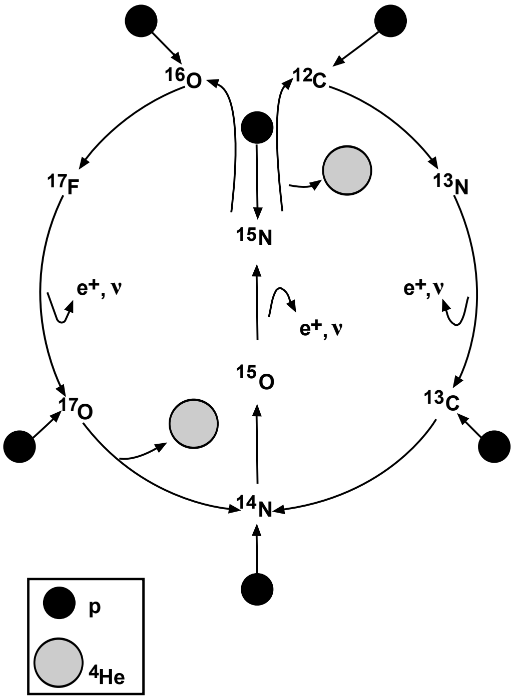

Figure 2.4: Nuclear reactions of the CNO bi-cycle (Prialnik, 2000, Fig. 4.4).

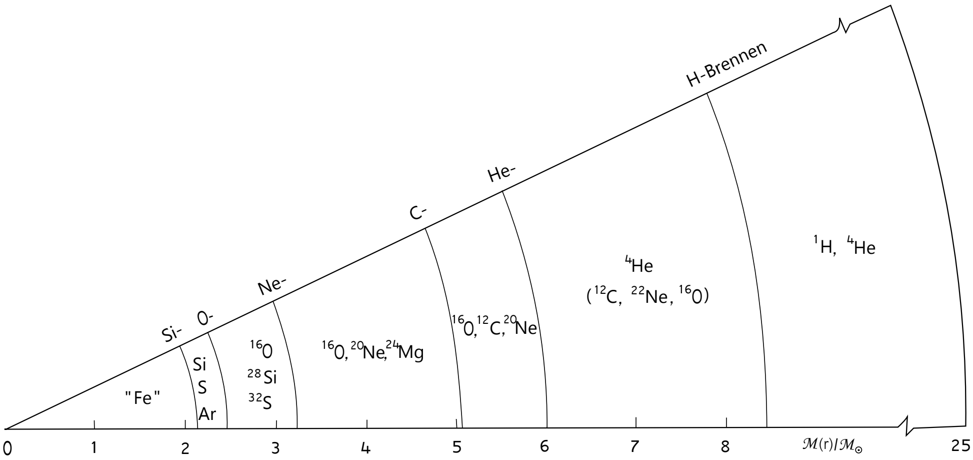

Figure 2.5: "Onion-shell structure" of a $25\,M_\odot$ star after Si-burning (Unsöld & Baschek, 1988, Fig. 5.4.9).

2.2 Core collapse supernovae

The fuel of a star is not infinite. Once it is "empty", the core fusion stops and the pressure from it, e.g., the radiation pressure P_r (see Eq. 2.8) or the electron pressure $P_\mathrm{e} = n_\mathrm{e} k_\mathrm{B} T$, is lost. Therefore the gravity pressure becomes stronger. In the center of the star an iron-core with degenerated electrons, i.e., their energy is much higher than in a thermal gas, up to the Chandrasekhar limit is produced (Chandrasekhar, 1931). It starts to shrink and the temperature increases. ^{56}Fe starts photodisintegration, which means that the photons have enough energy to destroy atomic nucleus of higher elements

Figure 2.6: Pictures of the spiral galaxy M51 (Whirlpool-galaxy, distance (7.1 ± 2.1) Mpc, Takáts & Vinkó 2006): *(left)* taken on May 2, 2009 with the 40 cm MAEDE telescope of the Remeis Observatory, Bamberg, by H. Hirsch and M. Hanke; *(right)* taken on June 27, 2011 by M. Wille. The supernova SN 2011dh from May is marked with an small arrow.

$$^{56}\mathrm{Fe} + \gamma \rightarrow 13\,^{4}\mathrm{He} + 4n \tag{2.4}$$

$$^{4}\mathrm{He} + \gamma \rightarrow 2p^{+} + 2n \tag{2.5}$$

Free electrons are captured by heavy nuclei and protons if the core temperature increases to $T_\mathrm{c} \sim 8 \times 10^{9}\,\mathrm{K}$ and the density to $\rho_\mathrm{c} \sim 10^{10}\,\mathrm{g\,cm^{-3}}$ (neutronization):

$$p^{+} + e^{-} \rightarrow n + \nu_e \tag{2.6}$$

The resulting neutrinos ν_e results into an energy loss of the dying star because they are not interacting with the material of the star. For a $20\,M_\odot$ star the energy loss for photons amounts to $L_\gamma = 4.4 \times 10^{38}\,\mathrm{erg\,s^{-1}}$, while for the neutrinos it is with $L_\nu = 3.1 \times 10^{45}\,\mathrm{erg\,s^{-1}}$ almost 7 mio. times more energy lost (see Wilms, 2007). Due to their capture the degeneracy pressure of the electrons falls off. The core collapses in free fall ($\sim$ 40 ms). The speeds reaches supersonic so that the outer parts of the star do not realize what happens inside. The pressure increases further by neutronization and the density goes up to $\rho_\mathrm{c} \sim 8 \times 10^{14}\,\mathrm{g\,cm^{-3}}$, i.e., the density of an atomic nuclei, and becomes therefore incompressible. A neutron star with a solid surface is formed. The infalling material is stopped by the compact object and is bounced back. At the shock front the temperature and velocity increases and shock waves form. Due to the high density some neutrinos interact with the material and heat it up. The shock wave needs 20 ms to run through the outer shells, which still do not realize the incident, and breaks through the surface. The star explodes ("prompt hydrodynamic explosion"). Such an explosion is called *Supernova Type II*, or *Ib/Ic* if the progenitor was a so called *Wolf-Rayet star*, a star who pushed off his outer H- and He-shells during its former evolution.

The result of such a type II supernova is a compact object with typical masses $M \sim 1.4$–$3\,M_\odot$ and radii $R \sim 10\,\mathrm{km}$, consisting of a large fraction of neutrons: a **Neutron Star**.

2.3 Neutron Stars

The existence of neutron stars was predicted early by Baade & Zwickey (1934). But the measurement techniques and physical understanding was not good enough to detect and describe them. Oppenheimer & Volkoff calculated the first models for neutron stars in 1939 (Oppenheimer & Volkoff, 1939). In the next years particle physicists tried to understand the problem of matter at extreme densities.

The structure of a neutron star is still theoretical because one cannot look inside it. The *equation of state* shows the relationship between the gravitational pressure $P = P_g$ and the density ρ inside a neutron star:

$$P = \frac{nRT}{V} = \frac{Nk_{\mathrm{B}}T}{V} = \rho\frac{k_{\mathrm{B}}T}{\mu m_u} = P_g, \tag{2.7}$$

where n is the number of moles of a substance, R the ideal gas constant, T the absolute temperature of the gas, V its volume, N the number of molecules, k_{B} the Boltzmann constant, $\mu = \mathrm{A}/(\mathrm{Z}+1)$ the mean molecular weight, A and Z being the atomic weight and atomic number of the predominant nuclei, and m_u the atomic mass constant.

For massive stars this formula has to be expand to:

$$P = P_g + P_r; \quad P_r = \frac{1}{3}aT^4, \tag{2.8}$$

where P_r is the radiation pressure and a the radiation constant.

2.3.1 Structure

Fig. 2.7 shows a schematic supposed structure of a neutron star. The description of the structure is taken from Lyne & Graham-Smith (1998). There are two main components: a crystalline solid crust and a neutron liquid interior. This parts can be divided at a density near $\rho_0 = 2.8\times10^{14}$ g cm^{-3}, i.e., the density of nuclear matter. From the surface ($\rho \sim 10^6$ g cm^{-3}) to the center ($\rho \sim 10^{15}$ g cm^{-3}) the density covers a range of about nine orders of magnitude. The outer crust is a solid envelope consisting mainly of ^{56}Fe. At densities smaller than 4×10^{11} g cm^{-3} no free neutrons outside the nuclei exist. Above this density the neutrons drip out of the neutron-enriched ions and form a free neutron liquid. This neutron liquid is the main part of the central core and a superfluid. Only about 5% are protons and electrons. An essential component of the neutron superfluid can interpenetrate the inner part of the crust and lead to irregularities in the rotating of the neutron star. So called "glitches" can than be seen in the pulse period, i.e., a jump in the period development. The crust and the neutron liquid interior are coupled through the magnetic field of the star. Densities up to 10^{15} g cm^{-3} are supposed to be in the center of a neutron star. These densities could squeeze the neutrons to form mesons and kaons, which might form a solid core. This solid core could also be a reason for glitches.

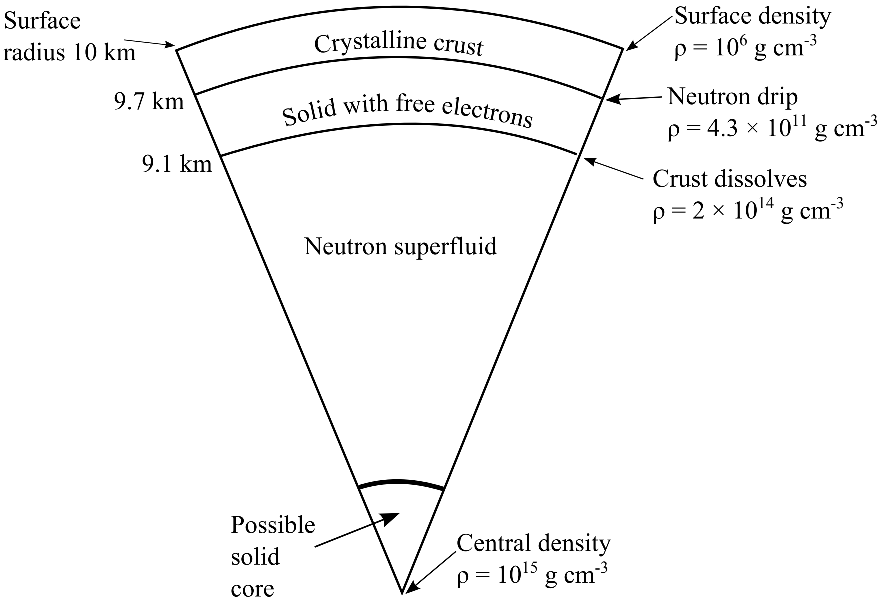

Figure 2.7: Typical cross-section of a neutron star (after Lyne & Graham-Smith, 1998).

2.4 Pulsars

Pulsars are a group of neutron stars, which send out electromagnetic radiation which can be measured. The first pulsar was detected in 1967 by Jocelyn Bell and Anthony Hewish. Due to the conservation of the angular momentum after the supernova, a pulsar has a very high rotational period. The total angular momentum J of a homogeneous sphere with angular velocity ω before the supernova is

$$J = I\omega \quad \text{where} \quad I = \frac{2}{5}MR^2. \tag{2.9}$$

After the explosion it is conserved ($J_{\text{before}} = J_{\text{NS}}$):

$$\frac{2}{5}M_{\text{before}}R^2_{\text{before}}\omega_{\text{before}} = \frac{2}{5}M_{\text{NS}}R^2_{\text{NS}}\omega_{\text{NS}}. \tag{2.10}$$

Therefore the angular velocity and the rotation period P, respectively, for the neutron star can be calculated as

$$\omega_{\text{NS}} = \left(\frac{M_{\text{before}}}{M_{\text{NS}}}\right)\left(\frac{R_{\text{before}}}{R_{\text{NS}}}\right)^2 \omega_{\text{before}} \quad \text{or} \quad P_{\text{NS}} \sim \left(\frac{R_{\text{before}}}{R_{\text{NS}}}\right)^2 P_{\text{before}}. \tag{2.11}$$

Due to the fact that the radius and mass of the progenitor's core are much bigger than for the neutron star, the angular velocity and therefore the rotation period are very high.

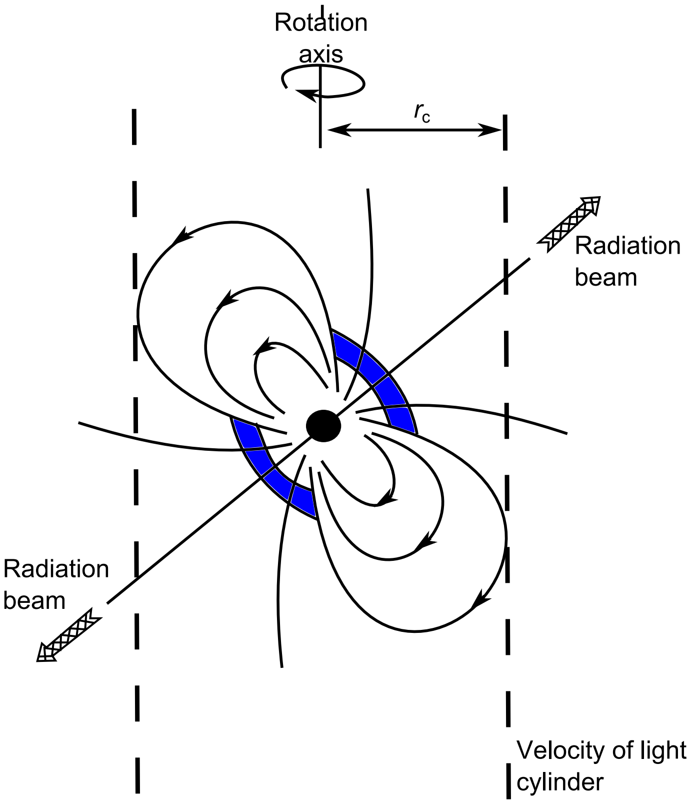

Figure 2.8: Structure of a pulsar magnetosphere. Within a radial distance $r_c = c/\Omega$ of the rotation axis there is a charge-separated, co-rotating magnetosphere. The edge of the polar caps is defined by the magnetic lines which touch the velocity-of-light cylinder. Radio emission from the polar caps is colored blue (after Lyne & Graham-Smith, 1998, Fig. 2.3).

Another conserved observable is the magnetic flux $\Phi = BR^2$, where B is the magnetic field. The conservation scheme is the same as for the angular momentum and one gets for the magnetic field of a neutron star:

$$B_{\mathrm{NS}} = \left(\frac{R_{\mathrm{before}}}{R_{\mathrm{NS}}}\right)^2 B_{\mathrm{before}}. \tag{2.12}$$

That means that radio pulsars (isolated neutron stars) have strong magnetic fields up to $10^6 \ldots 10^8$ T. The magnetic dipole of a pulsar is misaligned to its rotation axis (see Fig. 2.8). Therefore the electromagnetic waves are radiated at the rotation frequency. The radiation is the main reason of rotational energy loss and leads to a slowdown in the pulse period. For young pulsars, e.g., B1509−58 or the Crab pulsar, this outward energy flow is sufficient to provide high-energy particles in a surrounding nebula: the *pulsar wind nebula*. The rotational energy of a young pulsar is the source of energy for synchrotron radiation (see Sec. 2.4.1).

The rotating magnetic field induces a local electric field, which influences a region around the pulsar to a radial distance $r_c = c/\omega$, i.e., the distance where a co-rotating extension of the pulsar would have a speed equal to the velocity of light c. This radial distance describes the "velocity-of-light cylinder". Inside this cylinder there is an ionized "magnetosphere" of

Figure 2.9: The "lighthouse" model for pulsars and the resulting pulse profile. (Pictures taken from an animation by Michael Kramer. To watch the movie see the online version of (Lorimer, 2008, Fig. 2) at `http://relativity.livingreviews.org/Articles/lrr-2008-8/`)

high-energy plasma within the beam of radiation originates.

This beam of radiation forms the radio pulses of a pulsar. The pulse profile can be described by a "lighthouse" model where once the light is directed to the observer's line of sight and the other time directed away (see Fig. 2.9). High-energy particles move along the open field lines over a magnetic pole. The beam is therefore rigidly attached to the solid surface of the neutron star. The other high-energy radiation, like the X-ray radiation, originates in a separated region closer to the velocity-of-light cylinder. There, the particles are high-charged up to 10^{15}eV.

The rotation period of a pulsar gets slower with time. For rotation-powered pulsars, i.e., pulsars which have no companion and have a very high rotational energy, this time can be calculated. From the actual rotation period of a pulsar one can estimate its age by comparing its energy E_{rot} to its rotational energy release $\dot{E}_{\mathrm{rot}}$ (Eq. 2.13).

$$E_{\mathrm{rot}} = \frac{1}{2} I\omega^2 \propto \frac{I}{2} P^{-2}, \quad \text{where} \quad P = \frac{2\pi}{\omega} \tag{2.13}$$

$$\dot{E}_{\mathrm{rot}} = \frac{\mathrm{d}E_{\mathrm{rot}}}{\mathrm{d}t} = -IP^{-2}\dot{P} = I\omega\dot{\omega} \tag{2.14}$$

$$\rightarrow \tau_c \sim -\frac{E_{\mathrm{rot}}}{\dot{E}_{\mathrm{rot}}} \sim \frac{IP^{-2}/2}{IP^{-3}\dot{P}} = \frac{P}{2\dot{P}} \tag{2.15}$$

This age is called the *characteristic pulsar age.*

By plotting the pulse period versus the spin-down in a P–$\dot{P}$ diagram one can study the evolution of pulsars (Lorimer, 2008). Differences in P and $\dot{P}$ imply fundamental different magnetic field strengths and ages of the pulsars. In Fig. 2.10 one can see the current sample of radio pulsars. Lines of constant B, $\dot{E}$ and τ_c are drawn. Millisecond pulsars have typically values of 10^8 G and 10^9 yr, while normal pulsars have values of 10^{12} G and 10^7 yr. The most energetic pulsars are the very young normal pulsars and the rapidly spinning millisecond pulsars.

2.4.1 Synchrotron radiation

Synchrotron radiation or *Magnetobremsstrahlung* is the main radiation mechanism for pulsars. The radiation is emitted by relativistic[1] charged particles in a magnetic field (see

---

[1] For non-relativistic particles, this radiation is called *cyclotron radiation.*

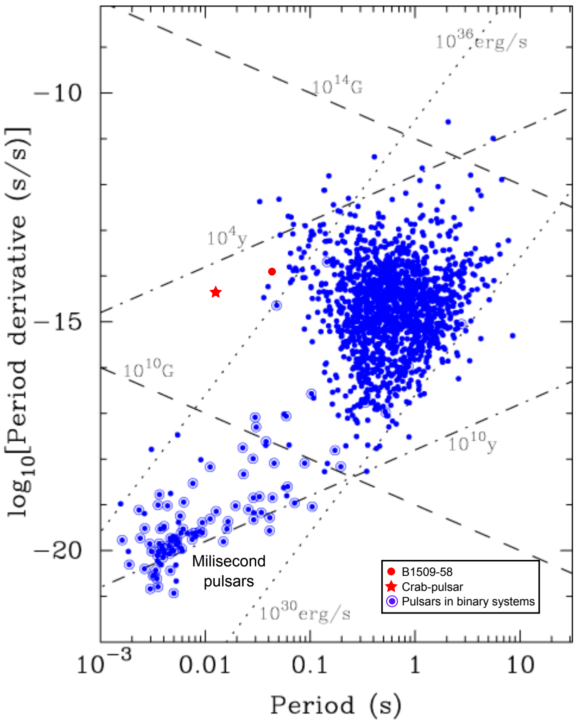

Figure 2.10: The $P-\dot{P}$ diagram showing the current sample of radio pulsars. The position of the Crab-pulsar (red star) and PSR B1509−58 (red circle) are marked in the plot. Lines of constant magnetic field (dashed), characteristic age (dash-dotted) and spin-down energy loss rate (dotted) are also shown (after Lorimer, 2008, Fig. 3).

Wilms, 2008; Rybicki & Lightman, 2004). The motion of a particle with mass m, charge q, velocity v and energy E in a magnetic field $\mathbf{B}$ can be described by the *Lorentz-force* (Eq. 2.18) which results from the following two relativistic equations:

$$\frac{\mathrm{d}}{\mathrm{d}t}(\gamma m\mathbf{v}) = \frac{q}{c}\mathbf{v}\times\mathbf{B} \tag{2.16}$$

$$\frac{\mathrm{d}}{\mathrm{d}t}(\gamma mc^2) = q\mathbf{v}\cdot\mathbf{E} = 0, \tag{2.17}$$

where $\gamma = \frac{1}{\sqrt{1-\left(\frac{v}{c}\right)^2}} = \frac{E}{mc^2}$ and c is the speed of light. From the last equation follows, that $\gamma =$ constant or that $|\mathbf{v}| =$ constant. Therefore, only one formula remains:

$$\frac{\mathrm{d}\mathbf{p}}{\mathrm{d}t} = m\gamma\dot{\mathbf{v}} = \frac{q}{c}\mathbf{v}\times\mathbf{B}. \tag{2.18}$$

The velocity of the particle can be separated into a component along the magnetic field $\mathbf{v}_{||}$ and in a plane normal to the field $\mathbf{v}_{\perp}$. Than one have

$$\dot{\mathbf{v}}_{||} = 0, \quad \dot{\mathbf{v}}_{\perp} = \frac{q}{\gamma mc}\mathbf{v}_{||}\times\mathbf{B}. \tag{2.19}$$

Therefore no acceleration parallel to the **B**-field exists and $\mathbf{v}_{||}$ is constant. Due to the fact, that $|\mathbf{v}| =$ constant, $|\mathbf{v}_\perp|$ is constant, too. The solution for Eq. 2.19 is, projected on the normal plane, a circular motion. In combination with the uniform motion along the magnetic field lines the motion is *helical.* The frequency of the rotation of the particle, also called gyration, is

$$\omega_B = \frac{qB}{\gamma mc} = \frac{\omega_\mathrm{L}}{\gamma}, \tag{2.20}$$

where $\omega_\mathrm{L} = 2\pi\nu_\mathrm{L}$ is the *Larmor-frequency.* The acceleration is orthogonal to the velocity, so that the total emitted radiation is

$$P = \frac{2q^2}{3c^3}\gamma^4 \frac{q^2B^2}{\gamma^2 m^2 c^2} v_\perp^2. \tag{2.21}$$

This formula has to be averaged over all angles for an isotropic distribution of velocities. Finally, one gets the total radiative power of a single particle in a magnetic field

$$P = \frac{4}{3}\sigma_T c \beta^2 \gamma^2 U_B, \tag{2.22}$$

where $\sigma_T = 8\pi r_0^2/3$ is the Thomson cross section and $U_B = B^2/8\pi$ the magnetic energy density. The geometry of the synchrotron emission is shown in Fig. 2.11. The emitted radiation of a single particle has dipole characteristic. For the relativistic case, the Lorentz-transformation into the laboratory system depends on the Doppler beaming effect, which results in a cone with an opening angle of $\Delta\theta \approx \gamma^{-1}$. The beam passes the observer, when it is pointing toward him (see Fig. 2.9). The characteristic frequency for the pulses can be expressed as

$$\omega_\mathrm{c} = \gamma^2\omega_\mathrm{L} = \frac{eB}{mc}\left(\frac{E}{mc^2}\right)^2. \tag{2.23}$$

In the case, that the particles follow a power law distribution

$$n(\gamma)\mathrm{d}\gamma = n_0\gamma^{-p}\mathrm{d}\gamma, \tag{2.24}$$

the process is called *nonthermal synchrotron radiation.* The spectral energy distribution (SED) $P_\nu$for a particle with energy $E = \gamma mc^2$ can than be written as

$$P_\nu(\gamma) \propto \nu^{-\frac{p-1}{2}} \tag{2.25}$$

with the *spectral index* α being

$$\alpha = \frac{1-p}{2}. \tag{2.26}$$

Therefore the emitted spectrum of a particle assemble following a power law distribution is again a power law, because it is the superposition of all single power law (see Fig. 2.12).

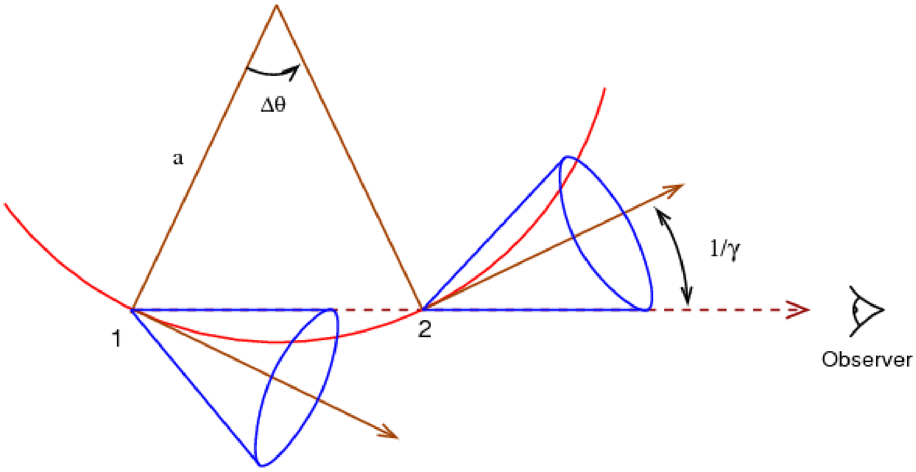

Figure 2.11: Synchrotron emission cones of an accelerated particle moving along the magnetic field lines (Rybicki & Lightman, 2004, Fig. 6.2).

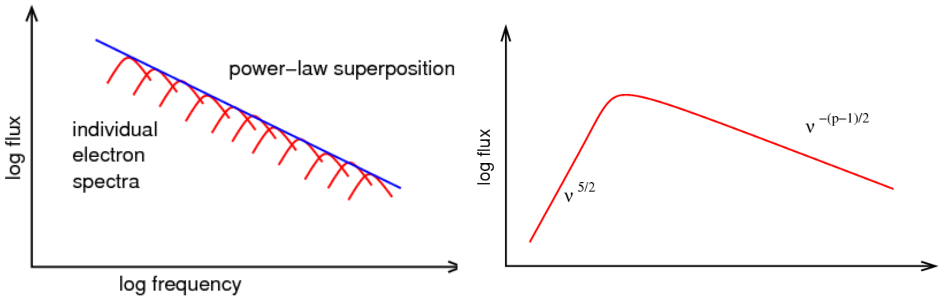

Figure 2.12: Synchrotron radiation of a particle distribution *(left)* resulting in a power law spectrum ($P_\nu \sim \nu^\alpha$) with a cutoff at lower energies due to synchrotron self-absorption *(right)* (after Shu, 1991, Fig. 18.6).

Below a certain energy, the cutoff energy, the particles are optically thick for synchrotron radiation. This phenomena is called the *synchrotron self-absorption*.

If I can't picture it, I can't understand it.

(Albert Einstein)

3 Monitoring PSR B1509$-$58

In the first part of this Diploma Thesis I analyzed 14 years of X-ray data taken with the *Rossy X-ray Timing Explorer* (*RXTE*, see Sec. 3.1) of the pulsar PSR B1508$-$58. In the following sections I will first give an overview over the satellite and its instruments. Afterwards the pulsar and its properties will be described. The last part of this chapter will deal with the observations and their analysis method and the resulting outcomes. The sections 3.2–3.4 of this diploma thesis are based on the associated paper Litzinger et al. (prep).

3.1 The Rossi X-ray Timing Explorer

The *Rossi X-ray Timing Explorer* (*RXTE*) was launched on December 30, 1995 into an *Low Earth Orbit (LEO)* of about 580 km. Its orbital period is $\sim 90\,\mathrm{min}$ and it has an inclination of 23°. On board of the satellite there are three instruments which allow to take data in an energy range of 2–200 keV: the *All-Sky Monitor* (ASM), the *Proportional Counter Array* (PCA) and the *High Energy X-ray Timing Experiment* (HEXTE) (Fig. 3.1). Data from the last two were analyzed in this thesis. In the next sections (Sec. 3.1.1–3.1.3) I will give an overview about the instruments.

3.1.1 The All-Sky Monitor (ASM)

The *All Sky Monitor* (ASM) is, as the name says, an instrument to observe the whole sky. With it astronomers try to find out where and what happens on the sky and how the X-ray emission changes on long timescales (hours to years). It monitors independently from PCA and HEXTE the $\sim$ 100 brightest 2–12 keV sources in the sky (Swank et al., 1995a). No data from this instrument was used for this thesis. For more details see therefore Levine et al. (1996) and Swank et al. (1995b).

3.1.2 The Proportional Counter Array (PCA)

The *Proportional Counter Array* (PCA, Jahoda et al., 2006) consists of five large-area ($\sim 1600\,\mathrm{cm}^2$) *proportional counter units* (PCU). Observations are performed with high timing and modest spectral resolution. The PCA has a 1° collimator (FWHM) and its

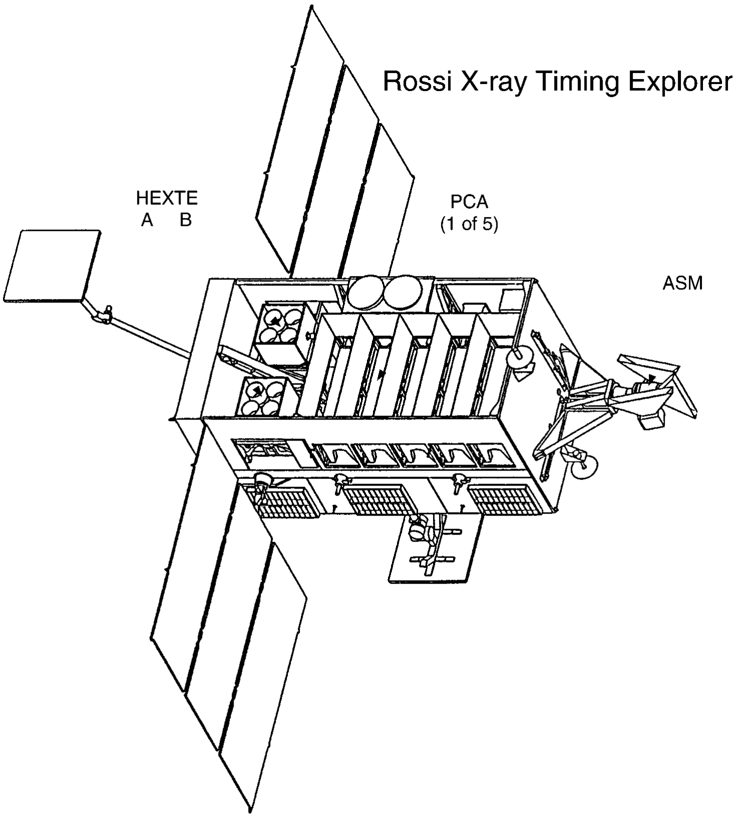

Figure 3.1: View of the *RXTE* spacecraft from above. The PCA and HEXTE instruments are inside the satellite housing. The ASM is on the end with clearance to view the sky.

background is very well modeled, so it is just confusion and not systematic limited to fluxes of $\approx 4 \times 10^{-12}\,\mathrm{erg\,s^{-1}\,cm^{-2}} \approx 0.3\,\mathrm{counts\,s^{-1}\,PCU^{-1}}$ in the 2–10 keV band, up to $20000\,\mathrm{counts\,s^{-1}\,PCU^{-1}}$ for bright sources.

The structure of the PCUs is identical for all five units (see Fig. 3.2). On the top of the detector there is a mechanical collimator (FWHM $\sim 1^\circ$) followed by an aluminized Mylar window, a propane-filled "veto" volume, a second Mylar window and a xenon-filled main counter. The bodies of the detector are constructed of aluminum and surrounded by a graded shield, which consists of a layer of tin followed by a layer of tantalum. As a calibration source ^{241}Am is used. From this source six calibration lines with energies between 13 and 60 keV are provided (Zhang et al., 1993, see Fig. 3.3 after). The lines around 30 keV become stronger with the time. For the analysis of the epoch averaged spectra of the calibration epoch 5 it was necessary to add additional Gaussian lines to improve the spectra fits at this energies (see Sec. 3.3.2).

Due to diffusion from the xenon layer into the propane layer calibration near the xenon L edge at 4.78 keV is necessary, too. For this the Crab pulsar and B1509−58 (Sec. 3.3.2) were monitored. The energies for the lines were found at 4.78, 5.10 and 5.45 keV for the Crab. For B1509−58 it was not possible to model all three Gaussian and therefore only one additional Gaussian at an energy of 4.58 keV was added.

For the analysis PCU2 only top layer data was used because it is the only PCU which

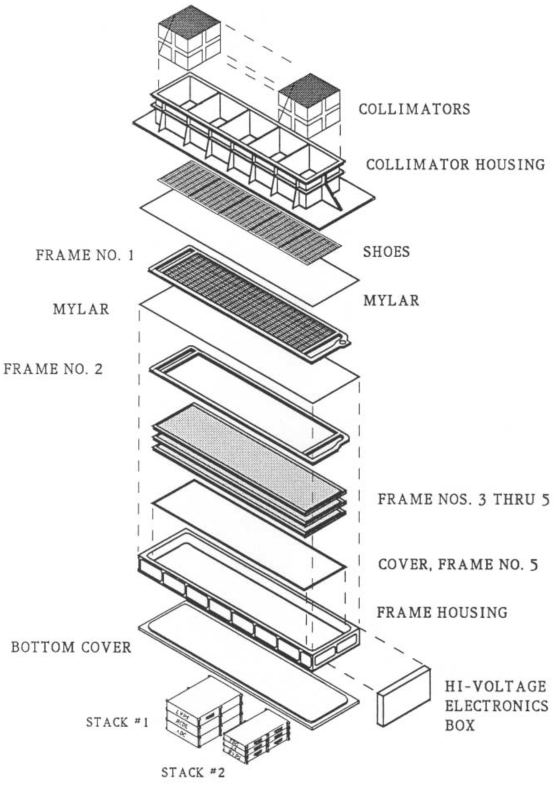

XTE/PCU EXPLODED VIEW

Figure 3.2: Structure of one PCA detector. The "frames" hold the anodes that define the various detector layers. In frame 1 are the propane anodes; frame 2 defines the first xenon signal layer; the second and third xenon layers and the xenon veto layer are defined by frames 3–5. On the back of frame 5 the calibration source, not visible, is covered (Jahoda et al., 2006, Fig. 2).

were switched on during the whole monitoring and is the best calibrated one. PCU0 lost its propane layer suddenly on May 12, 2000. The same happened to PCU1 on December 25, 2006 due to a micrometeorite impact.

3.1.3 The High Energy X-ray Timing Experiment (HEXTE)

The *High Energy X-ray Timing Experiment* (HEXTE) is co-aligned to the PCA to provide observations of individual sources in the 2–250 keV energy range. It is sensitive to X-ray fluxes on timescales from milliseconds to days. The limitation is only due to telemetry and the source intensity. The HEXTE consists of two independent clusters A and B. Each cluster comprise four NaI(Tl)/CsI(Na) phoswich scintillation counters collimated by a lead honeycomb. The scintillation crystals have a diameter of 18.3 cm and a thickness of 0.3 cm. The collimators are co-aligned so that each cluster have a 1° FWHM, similar to the PCA. The net open area of the eight detectors is $\sim$ 1600 cm^2. To determine a near real-time estimation of the instrument background, the HEXTE clusters are "rocking". That means that they move their viewing directions between an off-, on-, off-source position. The angular offset is 1.5°, which can be increased to 3.0°. The rocking can be set to only one

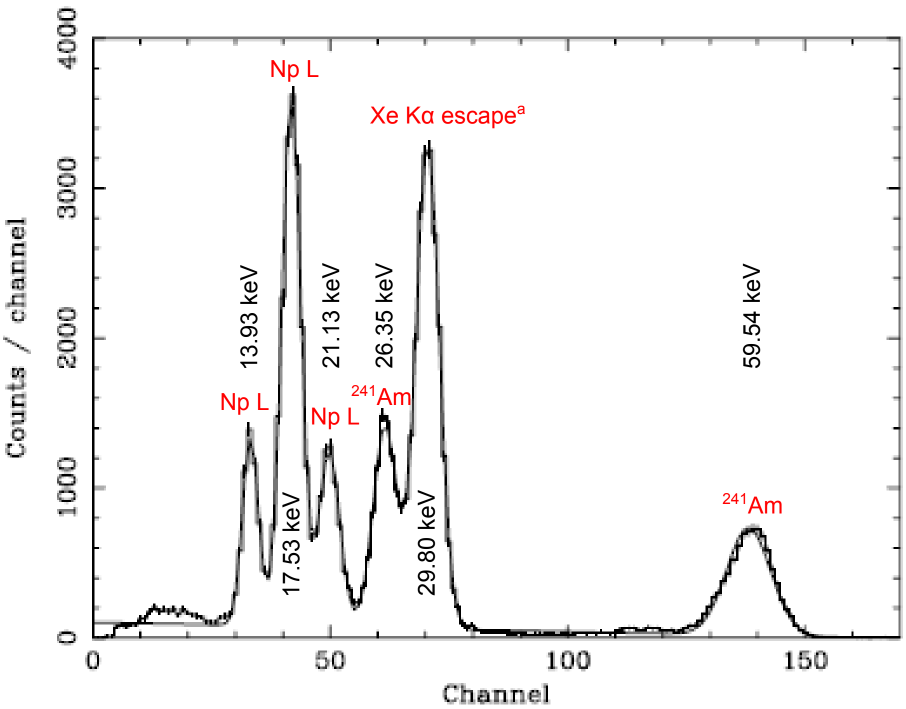

Figure 3.3: Data and Gaussian fits to the PCA ^{241}Am calibration lines. The data was collected in PCU2 during sky-background pointings in September, 2000. The energy of the lines and their source are shown in the figure (^{a} blend of escape peak and escape photon; (after Jahoda et al., 2006, Fig. 7)).

side to avoid confusion with a source in the background field. The rocking axis of cluster A and B are orthogonal to each other and therefore four background-regions are sampled around a given source. The rocking function of cluster A showed anomalies from December 2004 onward. The movement between on- and off-source did not work smoothly. Therefore it was parked on an on-source position on October 20, 2006 to avoid the case that it freezes in an other position and, if cluster B fails, no on-source data will be available. Similar problems were seen for cluster B some years later in December 2009. Because of that cluster B was parked in an off-source position on March 29, 2010. A software is available which allows to use the cluster B background for cluster A. In my thesis I used only data were the clusters rocked.

As for the PCA a ^{241}Am calibration source is used (see Fig.3.4). In contrast to the PCA calibration source, the HEXTE source shows no impact on the spectra.

An overview about the properties of the three instruments on board *RXTE* are shown in Table 3.1.

After 16 years of good work *RXTE* will be crashed on the Earth's atmosphere at the end of the year 2011.

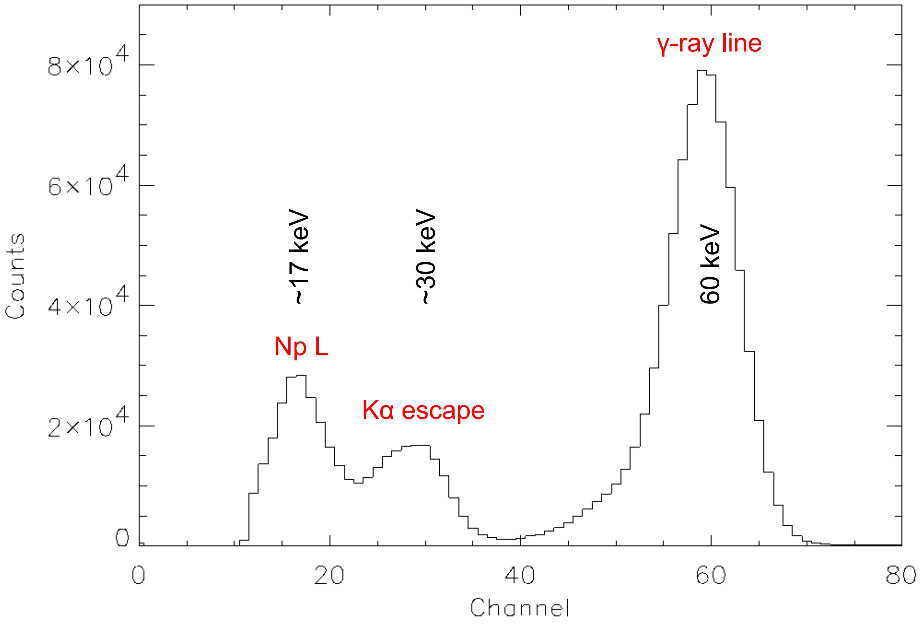

Figure 3.4: Calibration histogram of the HEXTE ^{241}Am gain control source. The data was taken on January 10, 1997. The gamma-ray line at 60 keV, the Np L lines around 17 keV and the K-escape lines around 30 keV are evident (after Rothschild et al., 1998, Fig. 3).

Table 3.1: Properties of the instruments on board *RXTE*.

Instrument	FoV [arcmin]	Energy range [keV]	Energy resolution [$\Delta E/E$]	Time resolution
PCA	60	2–60	5.5	1 μs
HEXTE	60	15–250	6.7	10 μs
ASM	360 × 5400	1.5–12	∼ 2.5	90 s

3.2 PSR B1509−58

The pulsar PSR B1509−58 (RA:15h13m55.52s, DEC:-59h08m08.8s, J2000.0) was discovered in *Einstein X-Ray Observatory* data from 1979 and 1980 by Seward & Harnden (1982). The radio counterpart was shortly thereafter found by Manchester et al. (1982). A possible optical counterpart was proposed by Caraveo et al. (1994). It lies in the constellation Circinus and is associated to the supernova remnant G320.4−1.2 (MSH 15−52). PSR B1509−58 was established by Seward et al. (1984) as one of a few known Crab-like sources. That means a young pulsar powering a synchrotron nebula by its spin-down and not by an accretion disc. The nebula is considerably larger and its surface brightness is lower than that of the Crab, though. The pulse period amount of P ∼151 ms is slower than that of the Crab (∼90 ms). Its very high spin-down rate of $\dot{P} \sim 1.5 \times 10^{-12}\,\mathrm{s\,s^{-1}}$ leads to a characteristic age of $P/2\dot{P} \sim 1.6 \times 10^{3}\,\mathrm{yr}$ (e.g., Zhang & Cheng, 2000), i.e., comparable to that of the Crab ($\sim 1.3 \times 10^{3}\,\mathrm{yr}$).

The morphology of SNR G320.4−1.2 has been well studied from radio to X-ray wave-

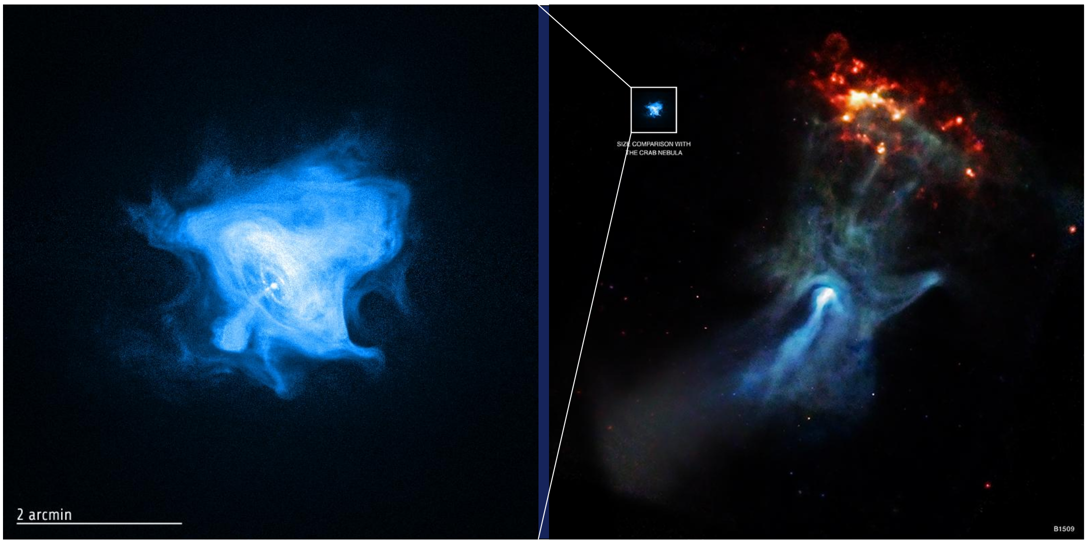

Figure 3.5: Size comparison between PSR B1509−58 (right) and the Crab Nebula (left). Shown is the X-ray emission of the pulsars powering the synchrotron nebulae. The similar structure around the pulsars is seen (Credit: B1509−58 (NASA/CXC/SAO/P.Slane et al.); Crab (NASA/CXC/SAO/F.Seward et al.))

lengths (e.g., Caswell et al., 1981; Seward et al., 1983; Trussoni et al., 1996; Gaensler et al., 1999; Mineo et al., 2001). From *ROSAT* and, more recently, *Chandra* images it is known that the structure of the emission region around the pulsar resembles the one around the Crab, i.e., consisting of an elongated pulsar wind nebula (PWN), toroidal arc structures, and a bright collimated jet along the axis of the PWN (Brazier & Becker, 1997; Gaensler et al., 2002; DeLaney et al., 2006). An additional prominent feature of the SNR at radio to X-ray wavelengths is the H II region RCW89, which lies $\sim 10'$ north of the pulsar, in the direction of the counter-jet (Rodgers et al., 1960; Tamura et al., 1996; Gaensler et al., 2002; Yatsu et al., 2005)[1]. Several bright X-ray emission regions are observed within RCW89, coinciding with radio synchrotron knots (Gaensler et al., 1999). The analysis of their X-ray spectra supports the picture that the H II region is powered by a precessing jet from B1509−58 (Tamura et al., 1996; Brazier & Becker, 1997; Yatsu et al., 2005). Basic features of the morphology, i.e., the elongation and spectral changes along the axis connecting the pulsar and the H II region, have also been confirmed at higher X-ray energies, e.g., by ASCA from 0.4–10 keV (Tamura et al., 1996), by *BeppoSAX* from 1.6-10 keV (Mineo et al., 2001), and by *INTEGRAL* from 17–100 keV (Forot et al., 2006). Recently, the asymmetric pulsar wind nebula has even been observed at energies up 40 TeV with *HESS* (Aharonian et al., 2005), which has been interpreted as emission due to inverse Compton scattering of relativistic electrons in the PWN with soft photons (including cosmic microwave background radiation).

The Rossi X-ray Timing Explorer (*RXTE*) has been performing the most extensive X-ray observations of B1509−58 to date, with roughly monthly 3–5 ks long monitoring observations since early 1996, i.e., since launch. Recently, 7.6 yr of timing data from this

---

[1] Tamura et al. (1996) report the detection of non-thermal emission between B1509−58 and RCW89 with *ASCA*. Gaensler et al. (2002), however, do not detect a counter-jet with *Chandra*, while Yatsu et al. (2005) interpret a weak, elongated structure in the *Chandra* image as part of the counter-jet.

campaign have been used, together with 21.3 yr of radio timing data (from *MOST* and *Parkes*), to perform a detailed pulse arrival time analysis (Livingstone et al., 2005, 2007). This analysis was expanded to 14.7 yr of X-ray data to improve the results (Livingstone & Kaspi, 2011). No glitches have been observed during this time. An ephemeris including pulse frequency derivatives up to $\dddot{\nu}$ was derived and the braking index was measured to be n =2.839±0.001 (where n =3 corresponds to a magnetic dipole). Spectral analysis of early monitoring data from 1996 as well as in-orbit-checkout observations have been presented by Marsden et al. (1997) and Rots et al. (1998).

In this thesis I extend the spectral analysis of the *RXTE* monitoring data up to and including the observations of April 2010 (Litzinger et al., prep). In Sec. 3.3.1 the campaign is introduced in greater detail and the data reduction is described. I then present the pulse phase averaged analysis of the data set (Sec. 3.3.2): the spectra of each monitoring observation are modeled, as well as spectra averaged over the three major calibration epochs of the Proportional Counter Array, PCA. The phase averaged parameters are especially interesting for current and future calibration work involving a comparatively weak source: the monitoring observations allow us to look for possible changes of the spectral parameters over time and thus asses calibration effects as well as intrinsic source stability, while the calibration epoch averaged spectra are well suited to derive spectral parameters with high significance, which can be compared to, e.g., results from future missions or to those for the Crab. The following section (Sec. 3.3.3) is dedicated to the pulse phase resolved analysis. Again results, namely the calculation of pulse period ephemeris, time averaged pulse profiles and the high quality phase resolved spectroscopy is presented. The high phase resolution that can be obtained with the PCA opens an almost completely unexplored window for studying the physics of B1509−58, as does the time sampling of the monitoring campaign. The results are summarized and discussed in Sec. 3.4.

3.3 Data analysis

3.3.1 Observations and data extraction

Approximately monthly monitoring observations of B1509−58 have been performed with the Proportional Counter Array (PCA, Sec. 3.1.2, nominal energy range 2–60 keV, Jahoda et al., 1996, 2006) and the High-Energy X-ray Timing Experiment (HEXTE, Sec. 3.1.3, nominal energy range 17–250 keV Rothschild et al., 1998). The raw data are available from NASA's online data archive `HEASARC`[2] (proposal IDs: P10208, P20802, P30704, P40704, P50705, P60703, P70701, P80803, P90803, P91803, P92803, P93803, P94803, P95803). The observatory internal extraction software `PCAEXTRACT` version 1.11 was used to obtain the phase averaged PCA spectra, backgrounds, and responses. The South Atlantic Anomaly (SAA, see Fürst, 2008) exclusion criterion was relaxed to 10 min, which is now known to be sufficient for monitoring analysis. A few of the monitoring observations could not be included in the following analysis, namely the first six of AO3 (1998), during which there was a 1° pointing offset from the source position, and 90803-01-09-02 (enhanced PCA background). In addition sub-ObsIDs 10208-01-09-00, 80803-01-07-01 (no PCA `GoodXenon` data), 40704-01-09-00 (PCA exposure lower than 500 s), 70701-01-09-00,

---

[2] NASA's Archive of Data on Energetic Phenomena, `http://heasarc.gsfc.nasa.gov/`.

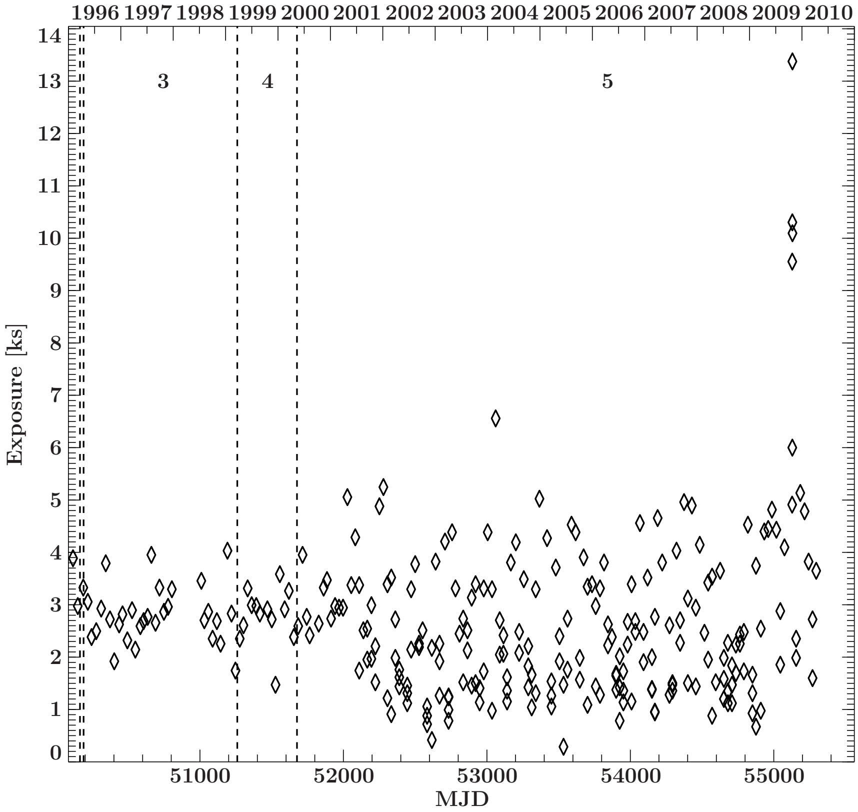

Figure 3.6: Exposure times of the *RXTE* monitoring observations of B1509−58. The values shown were derived from PCA's PCU2, which has never been switched off during an observation. Vertical lines and associated numbers denote the PCA calibration epochs with the first two epochs lasting a few weeks, only.

80803-01-10-01, 91803-01-04-02 (electronratio for PCU2 > 0.1 cps) and 93803-01-12-00 (no PCA `Standard2f` data) were omitted from the phase resolved analysis. Some monitoring observations and sub-ObsIDs did not result in valid HEXTE spectra since cluster A was not performing the nominal on-source/off-source rocking cycle (AO1, AO3, 90803-01-11-00, 91803-01-11-00, 91803-01-13-00, 91803-01-13-01, AO11, AO12, AO13, AO14) and B respectively (AO1, AO3, AO14). Only data from PCA's top layer were analyzed, as recommended for a weak source. The newest available version, "eMv20051128", of the background model "Faint" was used. Fig. 3.6 shows the exposure times for all monitoring observations, derived from the phase averaged PCA spectra described in Sec. 3.3.2. The average exposure increased from 2.7 ks to 4.1 ks in 2001. Note, however, that since the beginning of 1999 not always all of the five PCA proportional counter units (PCUs) were on during the observations, with only PCU0 and PCU2 never being "rested". After confirming in Sec. 3.3.2 that PCU2 spectra suffer less from calibration effects than spectra accumulating data from all available PCUs, all following analysis are based entirely on PCU2 data.

Phase averaged PCA spectra for each monitoring observation were extracted using data from the `Standard2f` data mode. They were modeled over the energy range from 3 to 20 keV (Sec. 3.3.2). Throughout this thesis version 1.6.1-26 of `ISIS` (*Interactive Spectral*

Interpretation System[3]) was used for spectral modeling. The source is not bright enough to allow constraining spectral parameters with the HEXTE in a single monitoring observation, therefore no HEXTE data are included in the analysis of individual pointings (Sec. 3.3.2). For a more sensitive spectral analysis, the `Standard2f` mode PCA spectra were accumulated over each of the three major PCA calibration epochs 3–5, and the corresponding background spectra and response matrices were created. The same was done for HEXTE standard event data mode spectra of epoch 4 and 5. During epoch 3 HEXTE was only rocking, i.e., measuring background, in AO2 (1997). Only these data were included in the accumulated epoch 3 HEXTE spectrum, leading to a total exposure comparable to that of the much shorter epoch 4. Simultaneous PCA and HEXTE broad band fits were performed, up to 150 keV for epoch 3, 4 and 5 (Sec. 3.3.2).

The pulse phase resolved analysis for the PCA is based on high time resolution `GoodXenon` event mode data, filtered for PCU2 top layer events. For HEXTE standard event mode data were used again. Barycentered pulse phase- and energy resolved source count rates (`pha2` files) were created for both instruments using a modified version of the `FTOOL`[4] *ikfasebin*, which is also taking the HEXTE deadtime into account (Kreykenbohm et al., 2002). Backgrounds and response matrices were obtained applying standard `FTOOLS`. For each `GoodXenon`-ligthcurve a period was calculated with the `ISIS` command *epfold*[5] (see Sec. 3.3.3). From the change of the period over time an ephemeris was determined (see Table 3.5 for the values calculated from this analysis). For each monitoring observation PCA pulse profiles for the energy range of 3–40 keV were extracted from the `pha2` files. The maximum of all profiles was shifted to phase 1.0. Peak and off-peak were then defined to the phases $\Phi = 0.88$–1.25 and $\Phi = 0.44$–0.75, respectively. For the pulsed emission a new background had to be defined so that really just the spectrum of the pulsar is seen and nothing from the PWN around. Therefore, the phase of $\Phi = 0.5$–0.7 was used as a new background, where the count rate stays nearby constant. This background is subtracted from the pulsed emission in the analysis and remains a spectrum that can be assigned to the pulsar. Calibration epoch averaged PCA pulse profiles for the energy ranges of 3–20 keV and 20–40 keV were created by averaging individual pulse profiles (Sec. 3.3.3).Pulse phase resolved PCA spectra with a resolution of $\Delta\Phi = 0.03$ were accumulated for each of the three epochs. Both the pulsed (256 phase bins, using a modified back-phase spectrum as background) and the unpulsed (256 phase bins, using the regular background) spectra were fitted over the energy range from 3–50 keV for epoch 3 and 4, and from 3–30 keV for epoch 5, respectively. In addition HEXTE spectra of the pulsed and unpulsed emission were created using all available data for which HEXTE was rocking, and were modeled up to 200 keV for the pulsed emission and up to 150 keV for the unpulsed emission (Sec. 3.3.3).

3.3.2 Phase averaged spectra

Monitoring observation spectra

Phase averaged PCA spectra for each monitoring observation have been studied for PCU2. In addition to the standard absorbed power law spectral shape, clear indications of a narrow

---

[3] `http://space.mit.edu/cxc/isis/`

[4] `http://heasarc.nasa.gov/ftools/ftools_menu.html`

[5] A detailed description of the method of epoch folding can be found in the Master-thesis by Matthias Kühnel (Kühnel, 2011).

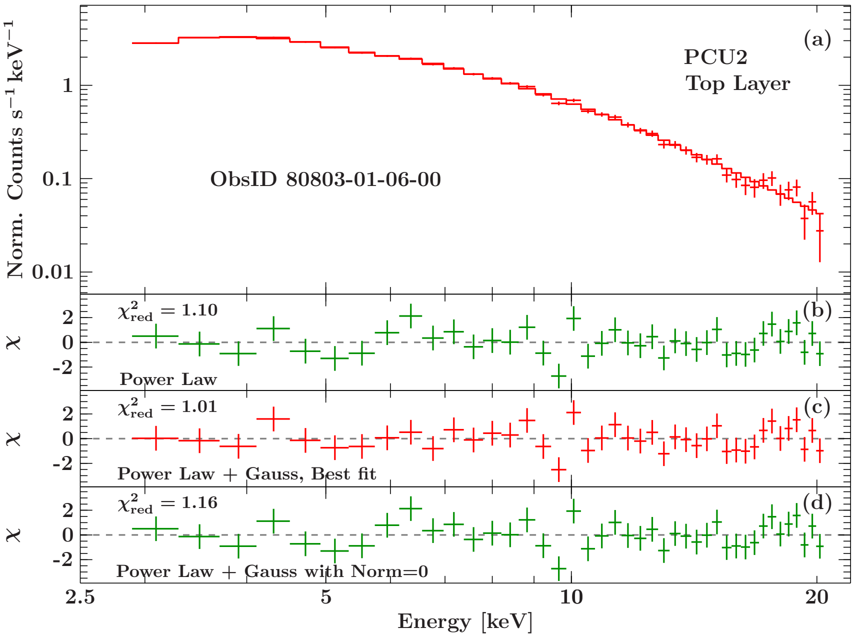

Figure 3.7: (*a*) Counts spectrum and best fit model for the phase averaged PCA PCU2 top layer spectrum of ObsID 80803-01-06-00, a representative monitoring observation. See Table 3.2 for the best fit parameters. (*b*) Residuals for fitting an absorbed power law. (*c*) As (*b*) but including the Gaussian iron line component at ∼6.4 keV. Best fit residuals. (*d*) As (*c*) but setting the normalization of the iron line to 0.

iron Kα line was found, even in the short monitoring exposures. The line is modeled by a Gaussian component added to the power law. Its energy E_{Fe} and width σ_{Fe} cannot be well constrained, therefore the former was set to 6.4 keV and the latter to 0.1 keV in the fits. It could be confirmed that this does not significantly influence the results for the continuum parameters. A marginal detection of the iron line in the unpulsed spectrum was also reported by (Marsden et al., 1997). Another parameter that is difficult to constrain with these short PCA observations is the column density of neutral hydrogen N_{H}. I used the absorption model `phabs` and adopted the abundance table `angr` of Anders & Grevesse (1989) in order to be able to compare our results with previous N_{H} measurements from X-ray spectra. See Sec. 3.3.2 for values obtained with the updated abundance table `wilm` of Wilms et al. (2000). Two different strategies for N_{H} were applied: (i) including it in the model as a free parameter, and (ii) freezing it to $0.6\times10^{22}\,\mathrm{cm}^{-2}$. The latter value is roughly consistent with the results obtained from fitting the phase averaged spectra (Table 3.4). It is also consistent with the value of $(0.59\pm0.06)\times10^{22}\,\mathrm{cm}^{-2}$ found for nearby RCW89 by Tamura et al. (1996) with *ASCA*. Generally the N_{H} values reported from modeling the unpulsed spectra are in the range from 0.6 to $0.9\times10^{22}\,\mathrm{cm}^{-2}$ (Trussoni et al., 1990; Kawai et al., 1993; Cusumano et al., 2001). The situation for the pulsed component is more complex, possibly because of a curved spectral shape (Cusumano et al., 2001, see also Sec. 3.3.3). The radio dispersion measure of B1509−58, finally, allows one to estimate N_{H} to $\sim0.8\times10^{22}\,\mathrm{cm}^{-2}$ (Marsden et al., 1997, and references therein).

Before the parameters obtained for the two spectral modeling options (two N_{H} strategies) are presented for all monitoring observations, I first describe the spectrum and best fit model for one representative exposure, ObsID 80803-01-06-00. Fig. 3.7*a* shows the cor-

Table 3.2: Best fit parameters for the phase averaged PCU2 spectrum of ObsID 80803-01-06-00 (Fig. 3.7).

Parameters	Value
Γ	2.052 ± 0.005
A_Γ [$10^{-2}\,\mathrm{keV}^{-1}\,\mathrm{cm}^2\,\mathrm{s}^{-1}$ @ 1 keV]	7.65 ± 0.07
N_H [$10^{22}\,\mathrm{cm}^{-2}$]	0.96 ± 0.14
E_Fe [keV]	6.4 ± 0.3
σ_Fe [keV]	$0.004^{+0.866}_{-0.004}$
A_Fe [$10^{-4}\,\mathrm{cm}^{-2}\,\mathrm{s}^{-1}$]	1.0 ± 0.5
EW [eV]	62
A_Bkgcorr [%]	+1.8
Exposure [ks]	3.4
Energy Range [keV]	3 − 20
χ^2_red/dof	0.87/41
$F_{4-10\,\mathrm{keV}}$ [$10^{-11}\,\mathrm{erg\,cm}^{-2}\,\mathrm{s}^{-1}$]	9.86 ± 0.09
$F_{10-20\,\mathrm{keV}}$ [$10^{-11}\,\mathrm{erg\,cm}^{-2}\,\mathrm{s}^{-1}$]	7.14 ± 0.06

The model in `ISIS` notation is `phabs`×`(powerlaw+egauss)`. All uncertainties are 90% confidence levels for one interesting parameter.

responding 3.4 ks PCU2 counts spectrum as well as the best fit model. In this case N_H was a free parameter in the fit, as well as the iron line parameters, in order to illustrate their typical behavior. The best fit parameters and their uncertainties are listed in Table 3.2. Note that in the phase averaged analysis the background normalization is optimized (i.e., the background is used as a correction file in `ISIS`), where A_bkgcorr gives the amount of the correction in %. The model provides a good fit with a power law index of 2.052 ± 0.005, closer to the values previously found for the unpulsed than the pulsed spectrum (Sec. 3.3.4). The value obtained for N_H is as expected. The Gaussian line parameters are canonical for a moderately strong iron neutral Kα line at 6.4 keV. The equivalent width of $EW = 62\,\mathrm{eV}$ represents a rather weak example, since the average value is found to be around 74 eV (Table 3.4). Indicating a narrow line, the width σ_Fe is consistent with 0, which led us to freeze σ_Fe to 0.1 keV in the monitoring fits. The best fit residuals are shown in Fig. 3.7*c*. The influence of the iron line is apparent in the other two residual panels, where Fig. 3.7*b* is based on a fit without the Gaussian component and Fig. 3.7*d* was obtained by setting the line strength A_Fe to 0 in the best fit.

Looking at the whole monitoring campaign again, one can examine the total background subtracted count rates for each spectrum. Fig. 3.8 shows the PCU2 top layer rates. The declining trend is understood as being due to the diffusion of xenon gas of the main counters into the propane veto layer. The effect is modeled in the response matrix and amounts to ~1% per year (Jahoda et al., 2006), consistent with the ~14.8% reduction that can be seen over 14 years for B1509−58.

Results of modeling the phase averaged spectra are displayed in Fig. 3.9, for PCU2 only. N_H was a free parameter in these fits. The fits are generally very good with χ^2_red between 0.5 and 1 (Fig. 3.9*f*). No systematic uncertainties were taken into account. The fact that the χ^2_red values are not centered around 1 might indicate that the uncertainty assumed for the background model is slightly overestimated (K. Jahoda, priv. comm.). The epoch 4/5

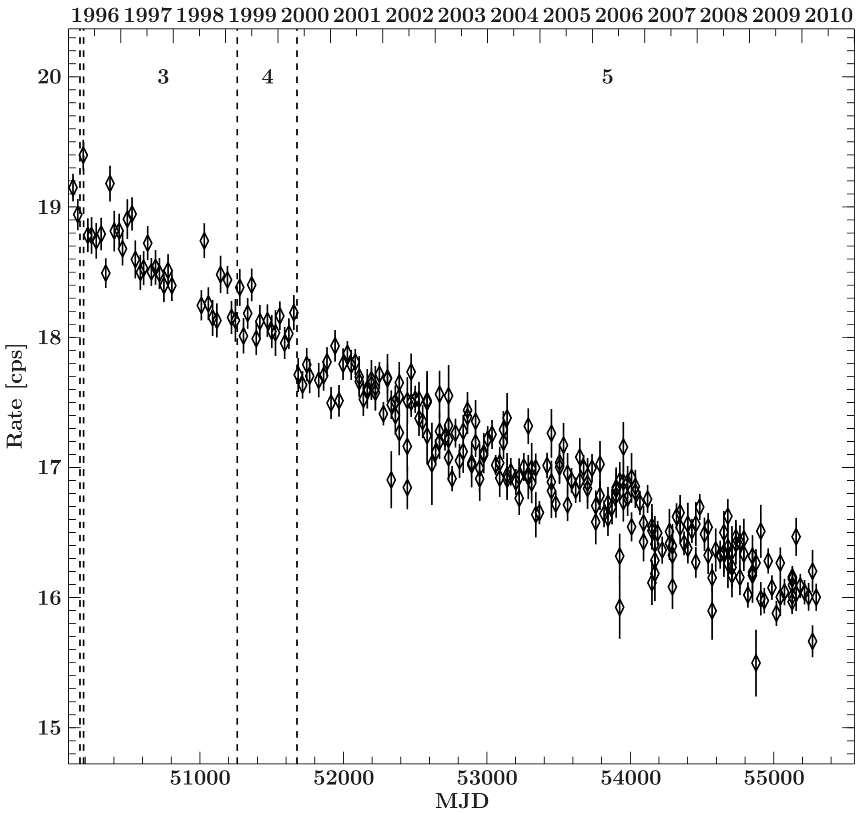

Figure 3.8: Evolution of the background subtracted PCU2 top layer rates for B1509−58 over the monitoring campaign. The whole PCA energy range of ~2–100 keV is included. The observed decline is an instrumental effect (see text).

boundary in 2000 is due to the loss of the propane layer of PCU0. A gradual decline of ~7% during epoch 5 is seen in the 4–10 keV flux (Fig. 3.9*a*). Keeping the declining rates in mind (Fig. 3.8) it is very likely that this remaining flux decline is also a calibration effect. I concentrate on the PCU2 only spectra in the following sections. The best fit values for this case are given in Table 3.3.

For the PCU2 spectra the mean value and standard deviation for the correction parameter for the normalization of the background are 1.17±0.21% prior to epoch 5 and 1.29±0.17% during epoch 5. Therefore it is verified that the observed gradual flux decline is not due to that much higher correction values during epoch 5.

From Fig. 3.9 it can be concluded that the power law parameters obtained from modeling the epoch averaged spectrum for epoch 5 (next section) might be affected on a $\lesssim$3% level by calibration uncertainties and that setting N_{H} to a value similar to those previously found does not improve the results. The option that the described trends are not calibration related but, e.g., due to a weakening of the pulsed spectral component is not supported by the phase resolved analysis (Sec. 3.3.3).

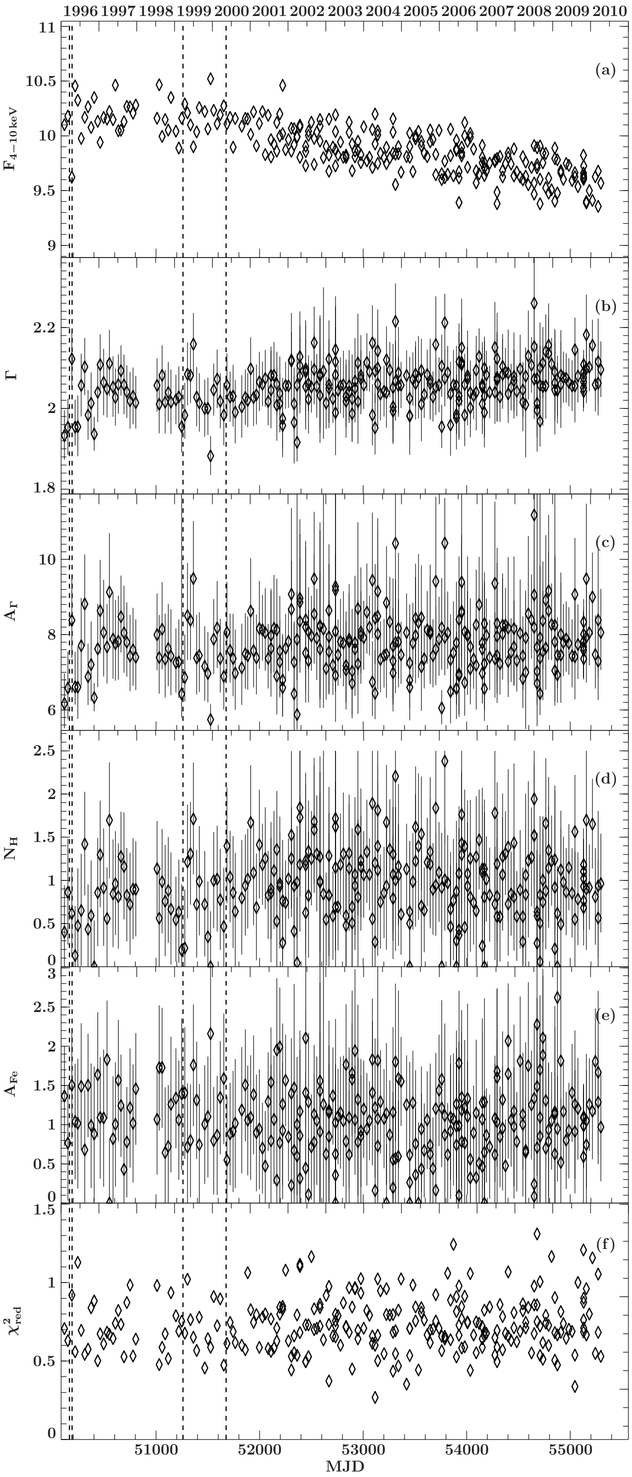

Figure 3.9: Spectral parameters for fitting the PCU2 top layer spectra for each monitoring observation with an absorbed power law and iron line. The model is quoted in Table 3.2. Here the iron line energy and width have been fixed to E_{Fe}=6.4 keV and σ_{Fe}=0.1 keV. The following parameters are shown: *(a)* Absorbed 4–10 keV flux $F_{4-10\,\mathrm{keV}}$, *(b)* photon index Γ, *(c)* power law normalization A_Γ at 1 keV, *(d)* hydrogen column density N_{H}, *(e)* iron line flux A_{Fe},*(f)* goodness of the fit χ^2_{red}. All units and parameter values of these fits are listed in Table 3.3.

Table 3.3: Best fit parameters for the phase averaged PCU2 spectra of all monitoring observations (Fig. 3.9), abbreviated table.

ObsID	Start Time [MJD]	Exposure [s]	$F_{4-10\,\mathrm{keV}}$ $\left[10^{-11}\,\mathrm{erg\,cm^{-2}\,s^{-1}}\right]$	Γ	A_Γ $\left[10^{-2}\,\mathrm{keV^{-1}\,cm^{-2}\,s^{-1}}\right]$	N_H $\left[10^{22}\,\mathrm{cm^{-2}}\right]$	A_Fe $\left[10^{-4}\,\mathrm{cm^{-2}\,s^{-1}}\right]$	A_Bkgcorr [%]	χ^2_red
90803-01-05-00	53202.135	4192	0.980±0.008	$2.04^{+0.07}_{-0.07}$	$7.4^{+1.0}_{-0.9}$	0.9±0.6	1.1±0.7	1.02±0.06	0.55
90803-01-06-00	53225.184	2080	0.989±0.012	$2.04^{+0.09}_{-0.09}$	$7.5^{+1.5}_{-1.2}$	0.9±0.8	$1.1^{+0.9}_{-1.0}$	1.00±0.08	0.80
90803-01-06-01	53225.250	2480	0.975±0.010	$2.12^{+0.09}_{-0.08}$	$8.8^{+1.6}_{-1.3}$	1.7±0.7	≤ 0.8	1.02±0.08	0.96
90803-01-07-00	53257.694	3488	0.980±0.009	$2.10^{+0.07}_{-0.07}$	$8.3^{+1.2}_{-1.0}$	1.4±0.6	0.9±0.7	1.04±0.07	0.79
90803-01-08-00	53288.825	1424	0.984±0.014	$2.05^{+0.10}_{-0.10}$	$7.7^{+1.8}_{-1.5}$	$1.3^{+1.0}_{-0.9}$	1.2±1.0	1.02±0.10	0.68
90803-01-08-01	53288.891	1824	1.015±0.012	$2.00^{+0.10}_{-0.09}$	$7.3^{+1.5}_{-1.2}$	1.1±0.8	$0.20^{+0.96}_{-0.20}$	0.93±0.09	0.44
90803-01-08-02	53288.956	2208	1.003±0.010	$1.99^{+0.09}_{-0.09}$	$7.0^{+1.3}_{-1.0}$	0.8±0.8	$0.6^{+0.9}_{-0.6}$	0.99±0.09	0.80
90803-01-09-00	53312.528	1040	0.956±0.016	$2.21^{+0.10}_{-0.13}$	$10.4^{+1.8}_{-2.3}$	$2.20^{+0.30}_{-1.08}$	$0.6^{+1.3}_{-0.6}$	1.13±0.12	0.55
90803-01-09-01	53312.584	1664	0.983±0.013	$2.07^{+0.10}_{-0.10}$	$7.8^{+1.7}_{-1.4}$	1.0±0.9	1.8±1.0	1.03±0.10	0.69
90803-01-10-00	53340.844	3296	0.990±0.009	$2.06^{+0.07}_{-0.07}$	$7.8^{+1.2}_{-1.0}$	1.1±0.6	$0.6^{+0.8}_{-0.6}$	1.02±0.07	0.47
90803-01-10-01	53340.934	1312	0.984±0.014	$2.09^{+0.12}_{-0.10}$	$8.2^{+2.0}_{-1.6}$	1.2±1.0	1.6±1.2	0.97±0.10	0.82
90803-01-11-00	53366.671	5024	0.967±0.008	$2.06^{+0.06}_{-0.06}$	$7.5^{+0.9}_{-0.8}$	0.6±0.5	1.6±0.6	1.02±0.06	1.02
90803-01-13-00	53419.812	4272	0.981±0.008	$2.08^{+0.07}_{-0.07}$	$8.1^{+1.0}_{-1.0}$	1.1±0.6	1.3±0.7	1.04±0.06	0.35
91803-01-01-02	53449.982	1536	0.980±0.013	$2.02^{+0.10}_{-0.10}$	$7.2^{+1.6}_{-1.2}$	$0.6^{+0.9}_{-0.6}$	≤ 0.9	1.00±0.10	0.71
91803-01-01-00	53450.050	1264	1.002±0.015	$1.98^{+0.12}_{-0.10}$	$6.8^{+1.7}_{-1.0}$	$0.5^{+1.0}_{-0.5}$	$0.26^{+1.15}_{-0.26}$	0.99±0.10	0.54
91803-01-01-01	53450.118	1056	0.990±0.016	$1.98^{+0.07}_{-0.06}$	$6.6^{+0.6}_{-0.6}$	≤ 1.1	$0.6^{+1.2}_{-0.6}$	0.97±0.10	0.71
91803-01-02-00	53480.651	3712	0.967±0.009	$2.07^{+0.07}_{-0.07}$	$7.8^{+1.0}_{-1.0}$	1.0±0.6	1.3±0.7	1.04±0.07	0.98
91803-01-03-00	53506.612	2400	0.997±0.010	$2.08^{+0.09}_{-0.08}$	$8.4^{+1.5}_{-1.3}$	$1.6^{+0.8}_{-0.7}$	$0.4^{+0.9}_{-0.4}$	1.00±0.08	0.84
91803-01-03-01	53506.749	1920	1.000±0.012	$2.06^{+0.10}_{-0.09}$	$8.0^{+1.6}_{-1.3}$	1.2±0.8	$0.8^{+1.0}_{-0.8}$	1.00±0.09	0.76

The full table for all 259 monitoring observations is available in the appendix of this thesis (Sec. A.1, Table A.1 and A.2). In addition to the columns shown above it also contains the end time of each observation in MJD, the start and end times in yyyy-mm-ddThh:mm:ss format, the 10–20 keV flux $F_{10-20\,\mathrm{keV}}$ in 10^{-11} erg cm^{-2} s^{-1}, and the number of degrees of freedom for each fit. All uncertainties indicate the 90% confidence interval.

Epoch averaged spectra

Time averaged PCA and HEXTE spectra were created by averaging individual monitoring spectra between MJD 50188 and 51259 (epoch 3), MJD 51259 and 51677 (epoch 4), and from MJD 51677 onward (epoch 5). For the HEXTE data from both clusters were added. For the PCA PCU2 top layer data were selected. Fig. 3.10, Fig. 3.11, and Fig. 3.12 show the epoch averaged counts spectra together with the best simultaneous PCA and HEXTE models, and the associated best fit residuals. The spectral parameters and their uncertainties as well as additional information about the three fits are given in Table 3.4. No systematic uncertainties have been added to the spectra before modeling them and calculating the χ^2_{red} values quoted in the table. Overall the parameters found for all three epochs agree well. The iron line equivalent width is found to lie between 67 and 87 eV. As can be expected these values are somewhat smaller than those for the unpulsed spectrum determined in Sec. 3.3.4 (84–126 eV) and by Marsden et al. (1997, 129 eV). The three spectra are further consistent in requiring a $\gtrsim$20% smaller absolute flux normalization for the HEXTE than for the PCA. All fluxes in Table 3.4 are quoted with respect to the PCA ($c_{\mathrm{PCA}} = 1$). The background correction parameters for both instruments are consistently small, on the order of -0.3% (epoch 3 and 4) and $+0.2\%$ (epoch 5) for the PCA and of $+0.5\%$ for the HEXTE. The reduced flux effect in epoch 5 is still visible and amounts to 4–5% in the 4–10 keV and 10–20 keV bands, depending on the exact model for epoch 5 (see below). In the lower energy band the absorbed and unabsorbed fluxes differ by $\sim$2%.

For N_{H} values from $(0.4–0.6)\times 10^{22}\,\mathrm{cm}^{-2}$ can be obtained. While epoch 3 and 4 are also consistent with values in the $(0.7–0.8)\times 10^{22}\,\mathrm{cm}^{-2}$ range, i.e., with previous measurements, the calibration related trend in epoch 5 amounts to a $\sim$40% reduction in this regard. In addition to N_{H} values obtained with the standard Anders & Grevesse (1989) abundances also N_{H} values based on the Wilms et al. (2000) abundances are quoted in the table and they are slightly larger, consistent with values around $1.2\times 10^{22}\,\mathrm{cm}^{-2}$ for epoch 3 an 4, i.e., a little bit larger than the radiodispersion measure (Sec. 3.3.2).

In the remaining two paragraphs of this section I describe the modeling of the three epoch averaged PCA and HEXTE spectra in greater detail. The treatment of the epoch 3 and epoch 4 spectra is very similar, although the PCA exposure for epoch 3 is almost twice as high, leading to stronger systematic features in the residuals, reflected in $\chi^2_{\mathrm{red}} = 1.13$ for epoch 3 and $\chi^2_{\mathrm{red}} = 0.92$ for epoch 4. Due to the availability of HEXTE background measurements for AO2, only, during epoch 3, the HEXTE exposures of epoch 3 and epoch 4 are comparable. The same simple spectral model as for the PCA monitoring spectra has been used, i.e., an absorbed power law plus Gaussian iron line, where all spectral parameters are tied for the PCA and HEXTE data sets, with exception of the overall flux normalization. For both epochs the spectra were rebinned in the same way: all PCA bins above `Standard2f` channel[6] 55 were grouped by a factor of 2[7] and for the HEXTE bins a grouping by a factor of 2 was applied up to channel[8] 50, increasing to a factor of 4 above. The accessible energy ranges also turned out to be the same for both epochs. The lower boundaries of 3 and 21 keV for the PCA and HEXTE spectra, respectively, are

---

[6] The energy-channel conversion table for the PCA can be found at `http://heasarc.nasa.gov/docs/xte/e-c_table.html`.

[7] That means that the counts of two adjacent channels are summarized.

[8] The energy-channel conversion table for HEXTE can be found at `http://heasarc.nasa.gov/FTP/xte/calib_data/hexte_files/DEFAULT/`

Table 3.4: Best fit parameters for the phase averaged PCU2 spectra of calibration epoch 3–5. For epoch 5 two different models were used (Fig. 3.10–3.12).

Parameter	Epoch 3	Epoch 4	Epoch 5	Epoch 5[a]
Γ	$2.025^{+0.011}_{-0.010}$	$2.027^{+0.016}_{-0.016}$	$2.002^{+0.016}_{-0.015}$	$2.023^{+0.009}_{-0.009}$
A_Γ [$10^{-2}\,\mathrm{keV}^{-1}\,\mathrm{cm}^2\,\mathrm{s}^{-1}$]	$7.51^{+0.16}_{-0.17}$	$7.5^{+0.3}_{-0.3}$	$6.8^{+0.3}_{-0.3}$	$7.15^{+0.14}_{-0.15}$
Γ_2				$1.74^{+0.6}_{-0.5}$
$A_{\Gamma 2}$ [$10^{-2}\,\mathrm{keV}^{-1}\,\mathrm{cm}^2\,\mathrm{s}^{-1}$]				$2.4^{+0.5}_{-0.4}$
N_H^b [$10^{22}\,\mathrm{cm}^{-2}$]	$0.766^{+0.099}_{-0.098}$	$0.83^{+0.16}_{-0.16}$	$0.40^{+0.17}_{-0.17}$	$0.62^{+0.09}_{-0.09}$
N_H^c [$10^{22}\,\mathrm{cm}^{-2}$]	$1.18^{+0.16}_{-0.15}$	$1.28^{+0.25}_{-0.24}$	$0.60^{+0.25}_{-0.25}$	$0.95^{+0.14}_{-0.14}$
E_Fe [keV]	$6.58^{+0.08}_{-0.09}$	$6.64^{+0.02}_{-0.24}$	$6.50^{+0.04}_{-0.03}$	$6.49^{+0.09}_{-0.02}$
σ_Fe [keV]	$0.00^{+0.22}_{-0.0}$	$0.0^{+0.3}_{-0.0}$	$0.15^{+0.10}_{-0.15}$	$0.007^{+0.128}_{-0.007}$
A_Fe [$10^{-4}\,\mathrm{cm}^{-2}\,\mathrm{s}^{-1}$]	$1.10^{+0.14}_{-0.14}$	$1.09^{+0.20}_{-0.20}$	$1.38^{+0.19}_{-0.17}$	$0.45^{+0.12}_{-0.12}$
EW [eV]	68	67	87	72
c_HEXTE	$0.65^{+0.06}_{-0.06}$	$0.78^{+0.06}_{-0.07}$	$0.80^{+0.03}_{-0.02}$	-
$A_\mathrm{Bkgcorr,PCA}$ [%]	-0.3	-0.2	$+0.2$	$+0.5$
$A_\mathrm{Bkgcorr,HEXTE}$ [%]	$+0.7$	$+0.5$	$+0.4$	$+0.01$
Exposure PCA [ks]	84.1	36.3	565.9	565.9
Exposure HEXTE [ks]	27.1	22.6	268.7	268.7
Energy Range PCA [keV]	3 – 49	3 – 49	3.5 – 35	3.5 – 35
Energy Range HEXTE [keV]	21 – 150	21 – 150	21 – 200	21 – 200
χ^2_red/dof	1.13/96	0.92/89	2.19/86	1.48/85
$F_{4-10\,\mathrm{keV}}$ [$10^{-11}\,\mathrm{erg\,cm}^{-2}\,\mathrm{s}^{-1}$]	$10.364^{+0.018}_{-0.018}$	$10.356^{+0.03}_{-0.04}$	$9.967^{+0.008}_{-0.007}$ [d]	$9.939^{+0.008}_{-0.008}$
$F^\mathrm{unabs}_{4-10\,\mathrm{keV}}$ [$10^{-11}\,\mathrm{erg\,cm}^{-2}\,\mathrm{s}^{-1}$]	$10.599^{+0.018}_{-0.019}$	$10.60^{+0.03}_{-0.03}$	$10.090^{+0.007}_{-0.008}$	$10.117^{+0.008}_{-0.008}$
$F_{10-20\,\mathrm{keV}}$ [$10^{-11}\,\mathrm{erg\,cm}^{-2}\,\mathrm{s}^{-1}$]	$7.739^{+0.014}_{-0.014}$	$7.714^{+0.021}_{-0.021}$	$7.441^{+0.006}_{-0.006}$ [e]	$7.382^{+0.006}_{-0.006}$
$F_{20-200\,\mathrm{keV}}$ [$10^{-11}\,\mathrm{erg\,cm}^{-2}\,\mathrm{s}^{-1}$]	$24.87^{+0.05}_{-0.04}$	$24.75^{+0.07}_{-0.07}$	$22.534^{+0.017}_{-0.016}$	$21.535^{+0.016}_{-0,016}$

[a] Model with two power laws. [b] Using the abundance table of Anders & Grevesse (1989). [c] Using the abundance table of Wilms et al. (2000). [d] $9.975^{+0.008}_{-0.008}$ and $9.967^{+0.008}_{-0.007}$ without modeling a negative residual at 9.3 keV and for setting the normalization of the 9.3 keV component to 0 in the best fit, respectively (see text for details). [e] $7.428^{+0.006}_{-0.006}$ and $7.441^{+0.006}_{-0.006}$ for the same cases as in [d]. All uncertainties indicate the 90% confidence interval.

determined by increasing systematic features at lower energies. The upper boundaries of 49 and 150 keV include additional instrumental features, especially around the PCA xenon K edge at 33 keV. While the effect is not producing strong residuals in epoch 3 and 4, it is clearly visible in epoch 5 and a way to take these instrumental features into account is described below.

Differences in the treatment of epoch 5 are due to its much longer total exposures compared to the other epochs (Table 3.4). In this case the PCA spectrum was rebinned by a factor of 2 only from `Standard2f` channel 71 upwards and the HEXTE grouping factors were 3, 5, 10, and 26 for the detector channel ranges 50–76, 77–101, 102–151, and 152 upwards. Due to strong systematic trends the lower boundary of the modeled PCA spec-

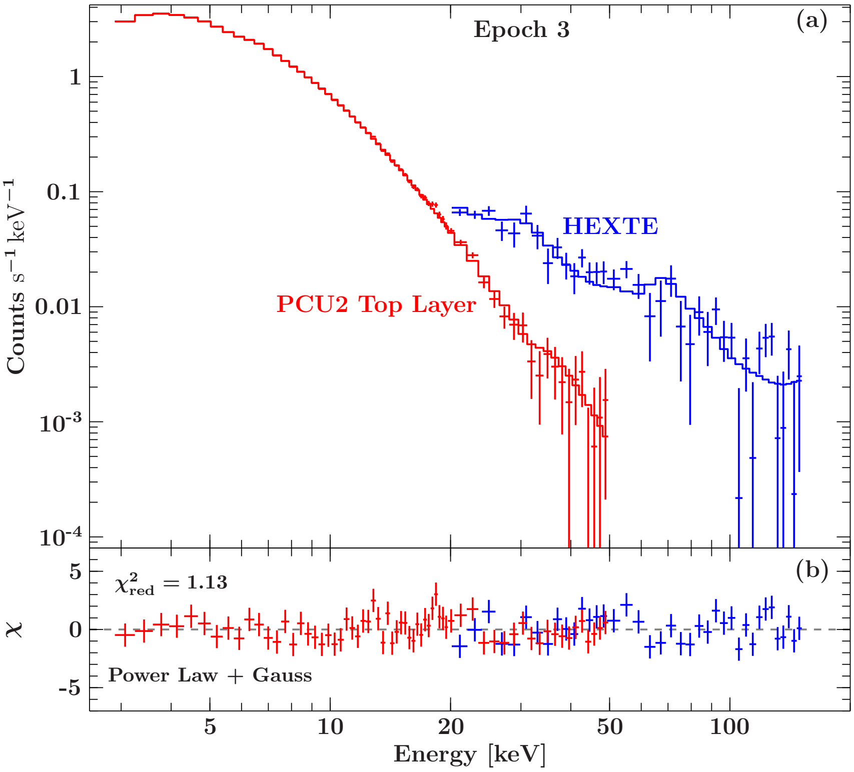

Figure 3.10: (*a*) PCU2 (top layer) and HEXTE counts spectra obtained by accumulating all suitable monitoring spectra of epoch 3 and best simultaneous fit model. See Table 3.4 for the best fit parameters. (*b*) Best fit residuals. The PCU2 data are shown in red and the HEXTE ones in blue. The residuals for the power law are shown in the same colors.

trum had to be increased to 3.5 keV and to 21 keV for the HEXTE. The upper boundaries were decreased to 35 keV for the PCA and increased to 200 keV for the HEXTE. The long exposure times lead to residuals that are clearly dominated by systematic uncertainties. For the PCA some of these features are known to be calibration related residuals (Jahoda et al., 2006; Rothschild et al., 2006) and if possible I took them into account in the spectral model for epoch 5: *(i)* The xenon L1 (4.78 keV), L2 (5.10 keV), and L3 (5.45 keV) edges produce strong discontinuities in the effective area, which can lead to residuals around 5 keV. While you can see two comparatively poorly described spectral bins between 4 and 5 keV in epoch 5, this feature was modeled by a single Gaussian absorption line component and improves the fit in this range. *(ii)* A broad negative residual is present around 9.3 keV. I model it with an additional negative Gaussian line at this energy with a width of 0.7 keV and a flux of $-2 \times 10^{-5}\,\mathrm{cm}^{-2}\,\mathrm{s}^{-1}$. It can be speculated that this residual might be related to imperfect modeling of the copper Kα emission line at 8.04 keV, which is due to fluorescence from the Be/Cu collimator. Rothschild et al. (2006) found the statistical need to include such a line of approximately the same (positive) flux in their fit of PCU2 spectra of CentaurusA. The best fit parameters quoted in Table 3.4, as well as Fig. 3.12, are based on including the additional components, constraining its parameters to the values given above. The 4–10 keV and 10–20 keV fluxes for both cases are quoted in Table 3.4 and indicate that it is not the absorption feature (alone) that causes the lower PCA flux in epoch 5. *(iii)* The presence of residuals near the 33 keV xenon K-edge has already

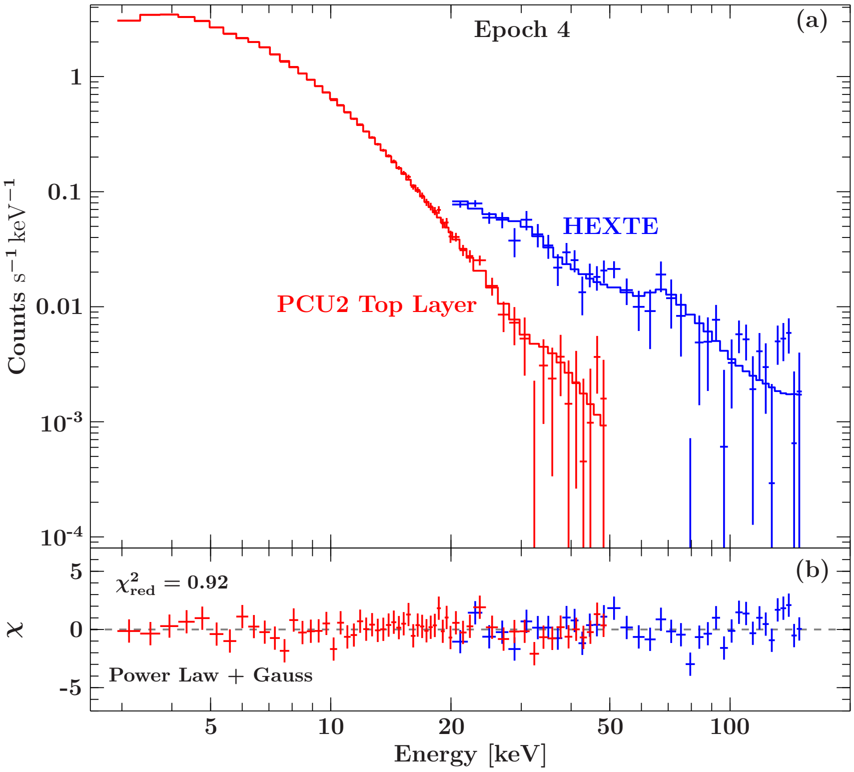

Figure 3.11: The same as Fig. 3.10 but for epoch 4.

been mentioned. Rothschild et al. (2006) explain that they are related to narrow residuals near 60 keV due to unflagged events from the americium calibration source and show that modeling the latter also improves the model at 30 keV since K-escape lines are produced around this energy. The shape of the residuals can be described as a set of two narrow Gaussian lines, one positive and one negative, indicating a slightly different gain between the background model and the observation. In the present case the line parameters are difficult to constrain, since above 35 keV the spectrum is consistent with 0. However, we modeled the 30 keV feature with two additional Gaussian components at 26 keV and 33 keV. Although this procedure does not significantly improve the $\chi^2_{\rm red}$ value of the fit in this case, I decided to include the additional three lines (the parameters were let free to check the values given above) in our best fit in order to illustrate the correction method. This has no significant influence on the other fit parameters. *(iv)* For epoch 5 it is seen that at higher energies the model does not describe the HEXTE data adequately. Therefore I used two different power laws for the PCA and HEXTE. The fit improves clearly from $\chi_{\rm red} = 2.19$ to $\chi_{\rm red} = 1.48$. The best fit model for epoch 5 in `ISIS` notation is thus of the form `phabs`×`(powerlaw(Isis_Active_Dataset) + egauss[Fe] + egauss[Cu?] + egauss[Am+] + egauss[Am-])`, where the normalizations of the three PCA instrument lines are set to 0 for the HEXTE data set. Even with this extended model systematic residuals remain ($\chi^2_{\rm red} = 1.48$).

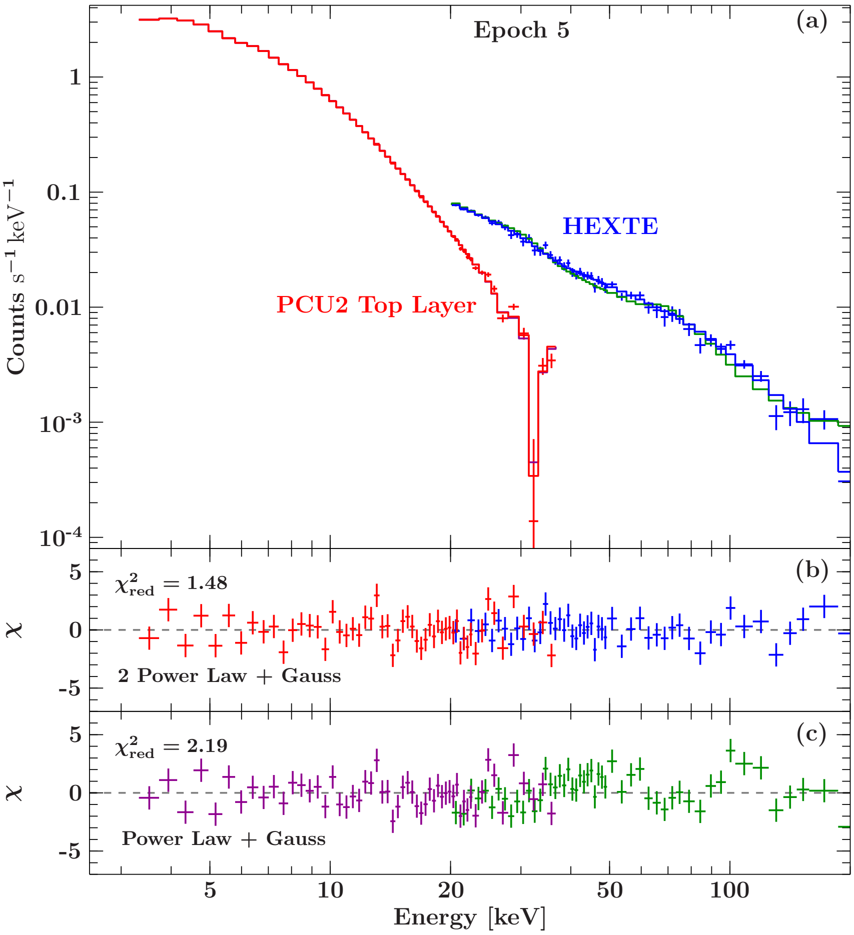

Figure 3.12: The same as Fig. 3.10 but for epoch 5. (*b*) Best fit residuals for two power laws. (*c*) Best fit residuals for a normal power law. The PCU2 residuals and model for case *(b)* are shown in red and in magenta for case *(c)*. The HEXTE residuals and model are shown in blue for case *(b)* and in green for case *(c)*.

3.3.3 Phase resolved spectra

In this section the phase resolved spectra were analyzed. I describe the calculation of the pulse period ephemeris, the aspects of the pulse profiles, the extraction of the pulsed and unpulsed emission and the spectral fits for the three major calibration epochs 3-5.

The X-ray properties of the pulsar itself, i.e., the pulse profile, the spectrum of the pulsed emission, and the evolution of the pulse period, have also been studied with many different instruments (e.g., Trussoni et al., 1990; Laurent et al., 1994; Gunji et al., 1994; Ulmer, 1994; Saito et al., 1997; Marsden et al., 1997), see recent summaries by Kuiper et al. (1999) and Cusumano et al. (2001). Pulsations have significantly been detected with *CGRO*-COMPTEL up to at least 10 MeV (Kuiper et al., 1999). Up to 300 keV the pulse profile shows a broad and asymmetric single peak, rising more steeply than decaying, that can roughly be described by the superposition of two Gaussian components (Cusumano et al., 2001). For the 2–16 keV *RXTE*-PCA profile their widths were found to be 0.056±0.008 and 0.386±0.012 in phase, while the 0.75–10 MeV *CGRO*-COMPTEL data suggest that the shape in this energy range is consistent with one broad Gaussian, and while there might be indications for a double-peaked pulse profile above 10 MeV (Kuiper et al., 1999). Different offsets in phase of the overall X-ray peak from the peak at radio wavelengths have been reported. While not all measurements are consistent for a given energy range or with an increasing delay with energy (Ulmer et al., 1993; Rots et al., 1998), they range from 0.25±0.02 in the 2–11 keV *Ginga*-LAC profile (Kawai et al., 1991) to 0.38±0.03 in the 0.75–30 keV *CGRO*-COMPTEL one (Kuiper et al., 1999). Interestingly, the latter coincides with the peak of the broad Gaussian at lower energies. The spectrum of the pulsed component is generally described by an absorbed power law and is very hard. It softens from the soft X-ray to γ-ray regime, with observed power law indices of 1.1±0.1 for *EXOSAT* (1.6–11 keV, Trussoni et al., 1990) and *ASCA* (0.7–10 keV, Saito et al., 1997), 1.30±0.05 for *Ginga* (2–60 keV, Kawai et al., 1993), 1.36±0.01 for *RXTE* (2–250 keV, Marsden et al., 1997), and 1.68±0.09 for *CGRO*-OSSE (0.05–5 MeV, Matz et al., 1994, consistent with BATSE and COMPTEL up to 10 MeV). Between 10 and 30 MeV a spectral break is observed (Kuiper et al., 1999). Cusumano et al. (2001) model the 0.1–300 keV spectrum with a curved function, however, up to ~200 keV no break has been found with *RXTE* (Sec. 3.3.4 and Marsden et al., 1997). The softer spectrum of the unpulsed component, i.e., of the PWN, can also be described by an absorbed power law (Trussoni et al., 1990; Kawai et al., 1993; Mineo et al., 2001; Forot et al., 2006; Aharonian et al., 2005), e.g., *RXTE* found 2.215±0.005 (2–250 keV, Marsden et al., 1997) and *INTEGRAL* found 2.12±0.05 (17–200 keV, Forot et al., 2006) for the power law index.

Pulse period ephemeris

To get the phase resolved spectra the data have to be extracted with the correct ephemeris. For this I first calculated the pulse period of each observation by folding the `GoodXenon`-lightcurve with the `ISIS` command `epfold`. This command cuts the lightcurve in different identical parts and folded them to the best period (see Fig. 3.13). For that the barytime, the countrate and the interval between the period should lie have to be refereed to the program. The former two information are from the lightcurve and the latter one was set between 150.7 and 152.0 ms, i.e., around the value of previous measurements of the period. The error for the pulse period could be calculated from Monte-Carlo simulations (`ISIS` command `epferror` (see Sec. A.2)). The number of Monte-Carlo loops was set to 500.

From all periods the frequency was calculated and then plotted versus the time. It shows that there is a clear declining trend in the frequency (Fig. 3.14) and therefore an increase in the period. The decline can be interpreted as almost linear and was modeled with a polynomial of the form

$$y(t) = \left(\left(\frac{1}{6}\dddot{\nu}(t-t_0) + \frac{1}{2}\ddot{\nu}\right)(t-t_0) + \dot{\nu}\right)(t-t_0) + \nu, \tag{3.1}$$

where $t_0 = 52921.0$ is the reference epoch, i.e., the mean time of the observations. The equation is built after the Horner-sheme to easily calculate the derivations up to the third grade. The values from this fit are listed in Table 3.5.

The values for ν and $\dot{\nu}$ are consistent with the values found at the Australian Pulsar Timing Data Archive (ATNF) available at `http://www.atnf.csiro.au/research/`

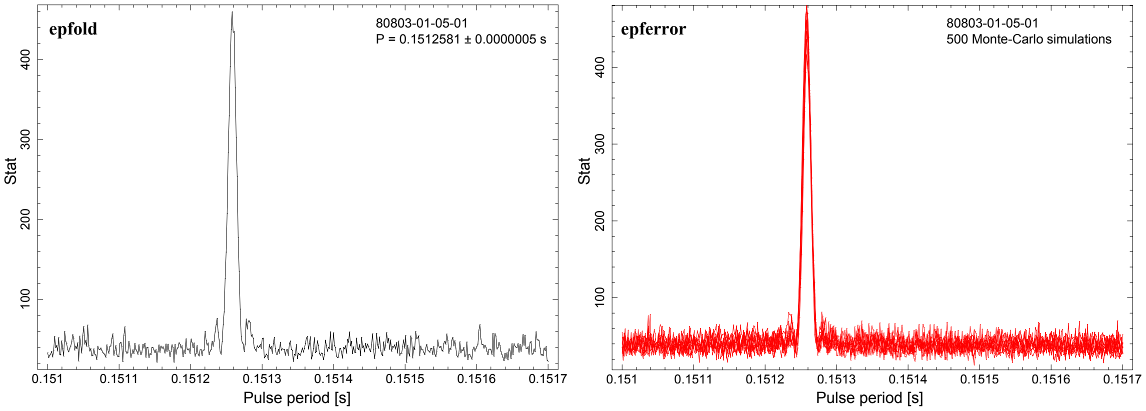

Figure 3.13: Folded lightcurve of ObsID 80806-01-05-01 and associated Monte-Carlo simulations. *(a)* The pulse period determined from `epfold` is defined as the peak-maximum. *(b)* The error is calculated from 500 Monte-Carlo simulations with `epferror`.

Table 3.5: Calculated timing ephemeris and comparison to other values.

Parameter	Value (this thesis)	ATNF	Livingstone 2005	Livingstone 2011
Dates (MJD)	50114.77503−55297.03509		45114−52925	50148.096−55521.082
Epoch (MJD)	52921.0	48355.0	49034.5	52834.589
ν(Hz)	6.60132±0.00001	6.6375697328	6.633598804(3)	6.611515243850(3)
$\dot{\nu}(10^{-11}\mathrm{s}^{-2})$	-6.697±0.002	-6.76935374	-6.75801754(4)	-6.694371307(6)
$\ddot{\nu}(10^{-21}\mathrm{s}^{-3})$	1.18±0.24	1.9587	1.95671(2)	1.9185594(5)
$\dddot{\nu}(10^{-30}\mathrm{s}^{-4})$	1.77±0.36	-1.02	-1.28(21)	-0.9139(2)

`pulsar/archive/` (Table 3.5), where the results of the pulsar timing observations of the *Parkes Observatory* are published. Though $\ddot{\nu}$ and $\dddot{\nu}$ are different to the values they lead to similar residuals (see Fig. 3.14). Livingstone et al. (2005) analyzed 21.3 yr of radio- and 7.6 yr of X-ray data. Including the X-ray resulted in large residuals over this time range. Comparing this ephemeris with the frequencies calculated with `epfold` showed the same effect. In 2011 they used only X-ray data and got values consistent with the ATNF (Livingstone & Kaspi, 2011). Calculating the frequencies from this ephemeris leads to much better residuals than before and they are consistent with the residuals for the ATNF and the ephemeris calculated in this work. Therefore I used this values to extract the phase resolved spectra.

Epoch averaged pulse profiles

The pulse profile of every observation was created from the `pha2`-files. The pulse profile shows one asymmetric single peak with a steep increase and a low decrease. To create the averaged pulse profiles for the three major calibration epochs a mean profile had to be found. This mean profile was not taken only from one observation but I made for every year an averaged pulse profile and then took the profile from 2003 as comparative profile because it lies between 1996 and 2010. The peak maximum of the 2003 profile was set to 1.0. After that for every observation the difference to the mean profile was calculated by a cross correlation, i.e., the mean profile was compared to the observation profile and shifted until they fit together. With the shifts the pulse profile of each observation was

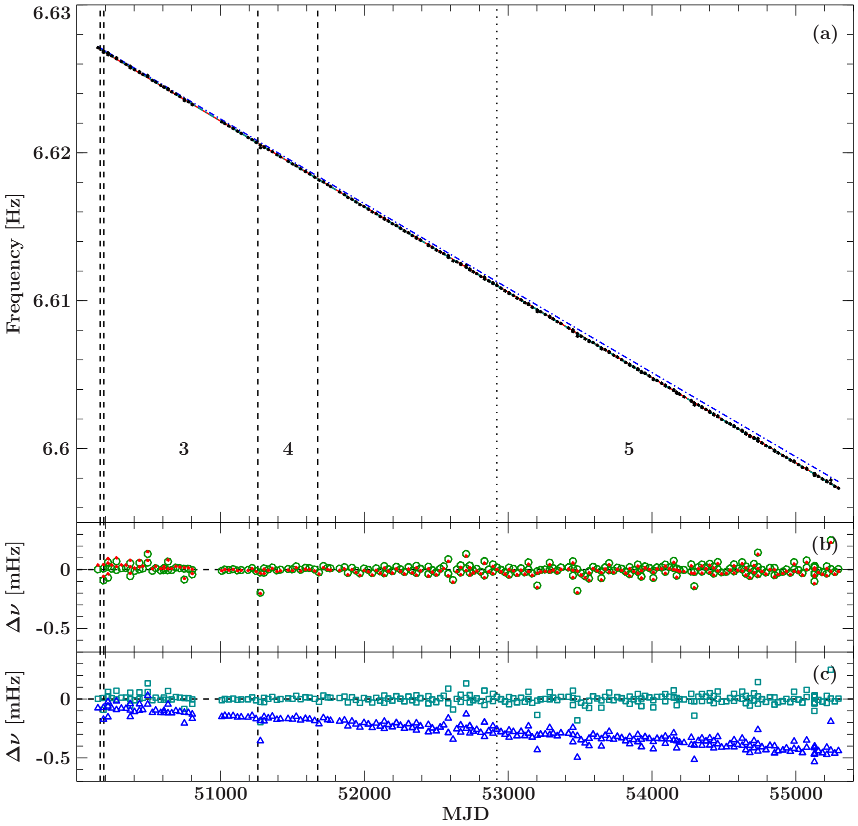

Figure 3.14: Pulse frequency ephemeris of B1509−58. *(a)* Frequencies of all monitoring observations of B1509−58 and best fit models. *(b)* Residuals for the ephemeris calculated after equation 3.1 (red points) and from the ATNF-ephemeris (green circles). *(c)* Residuals for the ephemeris from Livingstone et al. (2005) (blue triangles) and Livingstone & Kaspi (2011) (cyan squares).

shifted to phase 1.0 (see Fig. 3.15) and then added up to get the averaged pulse profile for the calibration epochs 3–5 (see Fig. 3.16). As for the single profiles no changes in the form of the profile are seen. Only the rate is going down due to the decrease in the PCU2 top layer. The different errorbars for the epochs are dependent of the number of observations. For epoch 3 there are 30, for epoch 4 13 and for epoch 5 213 observations. The errorbars for epoch 4 are therefore much bigger than for epoch 3 and epoch 5, respectively. This dependence is better seen by comparing the soft energy pulse profiles (3–20 keV, Fig.3.17*a*) with the hard energy pulse profiles (20–40 keV, Fig. 3.17*b*).

3.3.4 Epoch averaged phase resolved spectra

The pulse profile of B1509−58 is very good separated in a peak- and off-peak region. For both regions the `pha2`-files of the observations were extracted with the `FTOOL` `phaIIbin` in the corresponding phases (peak: $\Phi = 0.77$–1.25, off-peak: $\Phi = 0.44$–0.75). The resulting spectra were again added up to averaged phase resolved spectra for each epoch and for the pulsed and unpulsed emission there.

For the pulsed emission it is better to change the normal background to a background gen-

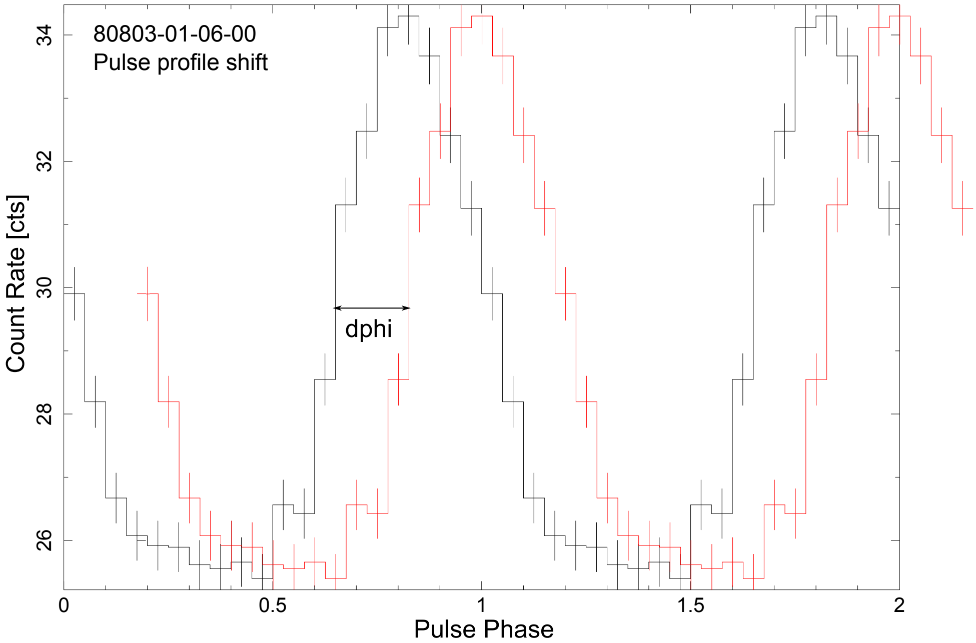

Figure 3.15: Pulse profile for the observation 80803-01-06-00 with 20 phasebins. The maximum of the profile was shifted by *dphi* to phase 1.0 to be aligned to the other observation pulse profiles.

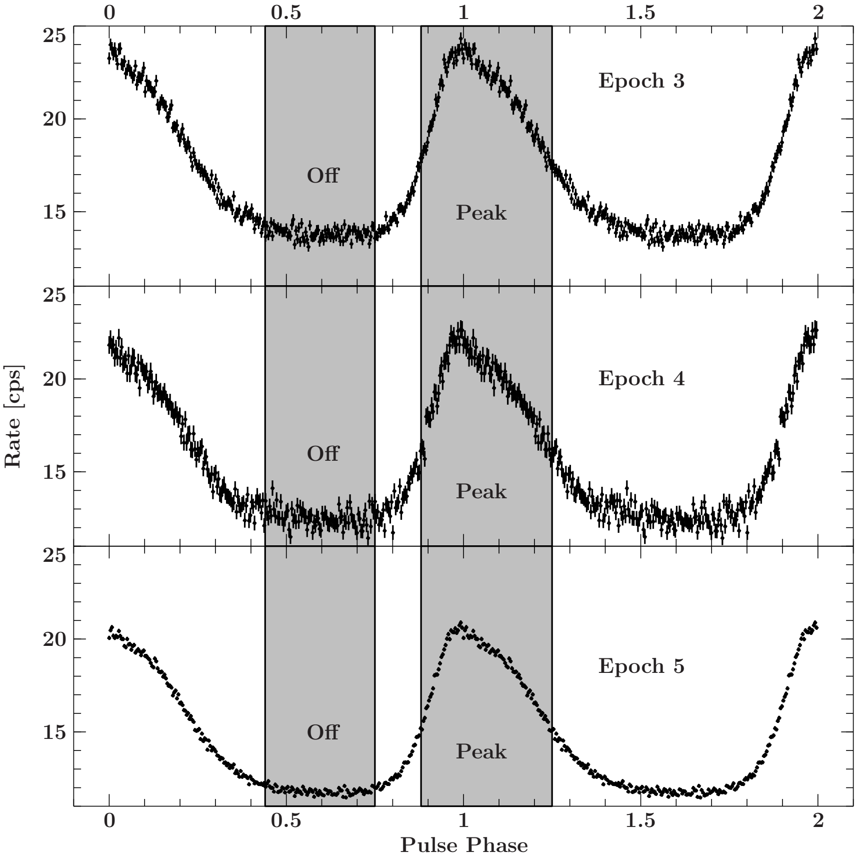

Figure 3.16: Epoch averaged pulse profiles for the PCA PCU2 top layer (energy range 3–43 keV).

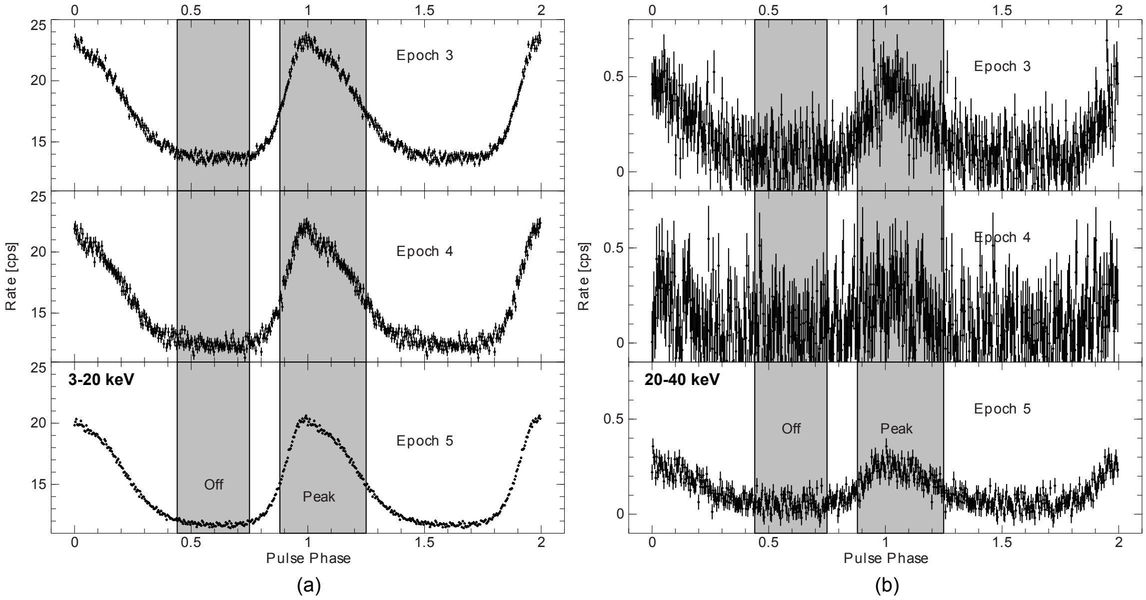

(a) (b)

Figure 3.17: Epoch averaged pulse profiles for two different energy bands. *(a)* Soft energy band from 3 to 20 keV and *(b)* hard energy band from 20 to 40 keV. The softness of the source is clearly seen.

erating by extracting the phase $\Phi = 0.5$–0.7 separately and then changing the background-key by hand. Otherwise one would see in the pulsed emission a mixture of the pulsar and the surrounding PWN. The spectra of the pulsed emission were then modeled by an absorbed power law (Fig. 3.18*a*), as the epoch averaged spectra before. The rebinning for the PCA PCU2 top layer was the same as in Sec. 3.3.2, while the HEXTE spectra were rebinned by factors of 2 and 4 for the detector channel ranges 20–40 and 41 upwards. There are no indications for an iron line in the pulsed emission. As for the epoch averaged spectra epoch 5 showed indications of a different behavior for the PCA and the HEXTE. Therefore I used again two power law to describe the different slopes of the spectra. The calculated values for epoch 3-5 are listed in Table 3.6. The values for the N_H and the photon index are consistent with previous measurements by (Marsden et al., 1997, $N_\mathrm{H} = 1.27 \times 10^{22}$ cm^{-2}, $\Gamma_\mathrm{pulsed} = 1.358 \pm 0.014$) and (Rots et al., 1998, $\Gamma = 1.345 \pm 0.010$).

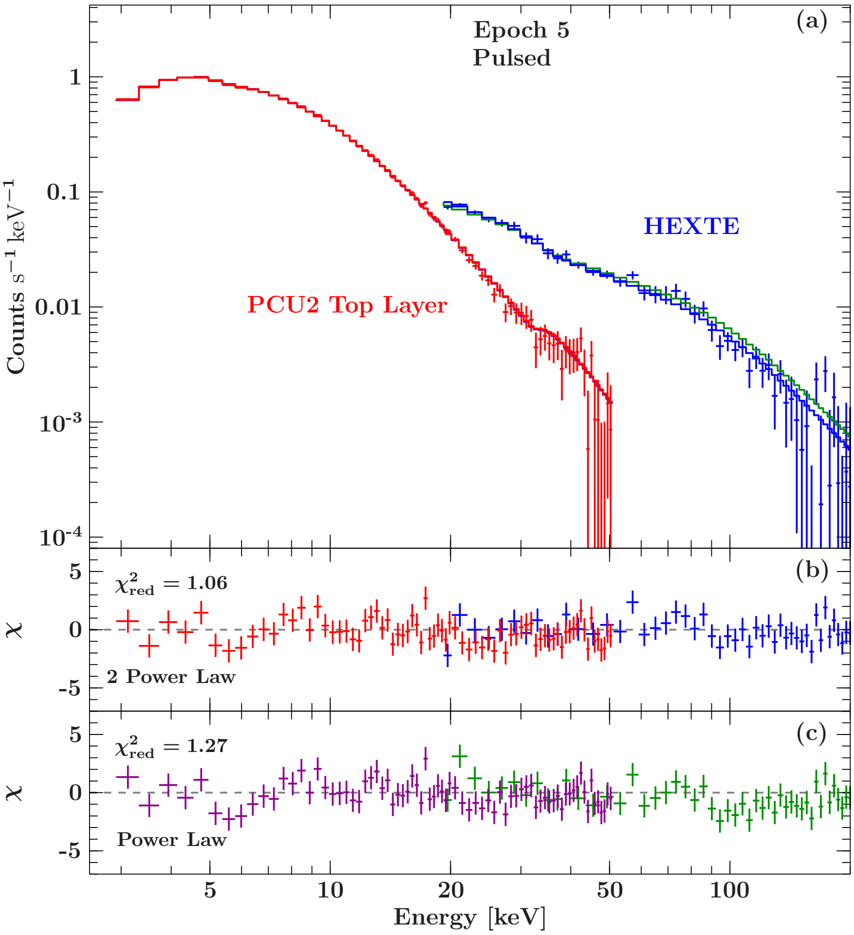

Figure 3.18: *(a)* PCU2 (top layer) and HEXTE counts spectra of the pulsed emission obtained by accumulating all suitable monitoring spectra of epoch 5 and with the best fit model of an absorbed power law and an additional power law for the HEXTE data. *(b)* Residuals for the best fit model. *(c)* Residuals for an absorbed power law. The models and corresponding residuals for the PCA PCU2 top layer are plotted in red for case *(b)* and in magenta for *(c)*. The colors for the same cases for the HEXTE are shown in blue and green.

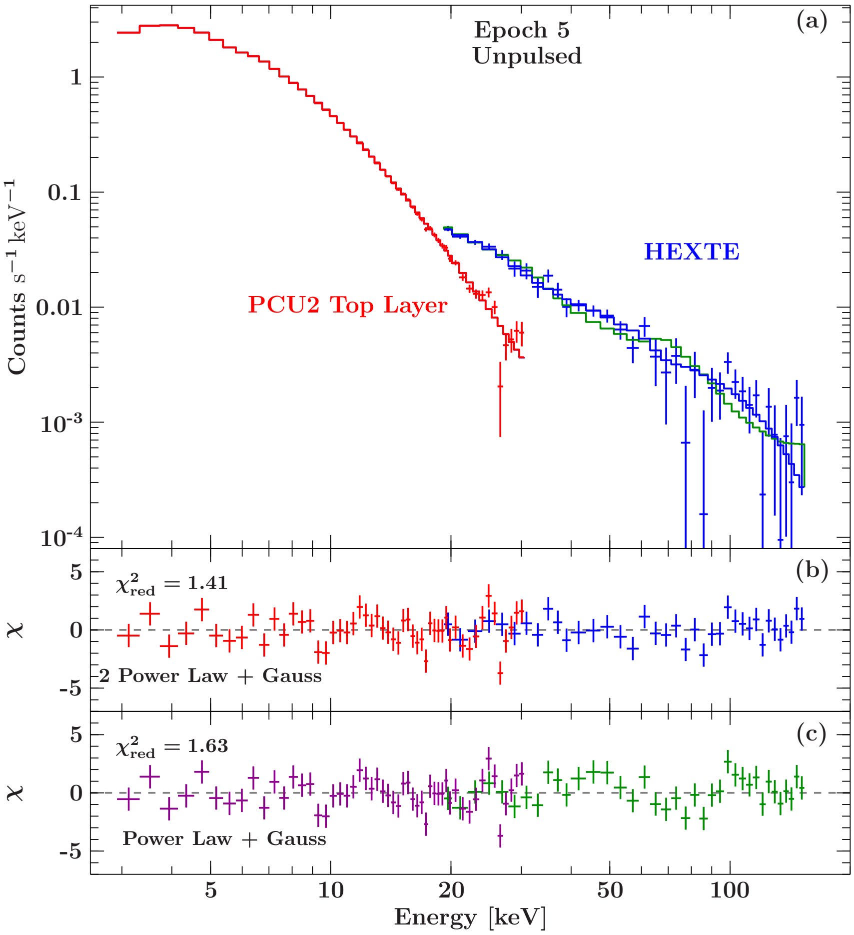

Figure 3.19: *(a)* The same as Fig. 3.18 but for the unpulsed emission.

The unpulsed emission was analyzed the same way as the pulsed emission (Fig. 3.19). Thereby a clear indication of an iron line at 6.4 keV could be found. The iron remained from the supernova explosion and is an indication of the supernova remnant, i.e., of interactions and reflections of the stellar material with the interstellar medium. It was modeled with an additional Gaussian component. The photon index of the unpulsed emission is higher as the one of the pulsed emission and therefore the spectrum is steeper. For epoch 5, similar to the phase averaged spectra, different models were fitted. None of them showed a clear improvement of the reduced χ^2. The values lie between 1.41 (two power law) and 1.68 (cutoff power law). Therefore a single absorbed power law was taken to be the best fit ($\chi^2_{\rm red} = 1.63$, Fig. 3.19*c*). The value for the photon index is consistent with the value obtained by (Marsden et al., 1997, $\Gamma = 2.215 \pm 0.005$).

Table 3.6: Best fit parameters for the phase averaged pulsed and unpulsed PCU2 spectra of calibration epoch 3-5.

Parameter	E3 pulsed	E4 pulsed	E5 pulsed	E5 pulsed	E3 unpulsed	E4 unpulsed	E5 unpulsed	E5 unpulsed
Γ	$1.35^{+0.04}_{-0.05}$	$1.40^{+0.06}_{-0.07}$	$1.392^{+0.016}_{-0.015}$	$1.375^{+0.017}_{-0.016}$	$2.23^{+0.03}_{-0.03}$	$2.23^{+0.04}_{-0.03}$	$2.264^{+0.009}_{-0.009}$	$2.265^{+0.010}_{-0.009}$
A_Γ [$10^{-2}\,\mathrm{keV}^{-1}\,\mathrm{cm}^2\,\mathrm{s}^{-1}$]	$0.95^{+0.09}_{-0.09}$	$1.09^{+0.17}_{-0.15}$	$1.03^{+0.04}_{-0.04}$	$0.99^{+0.04}_{-0.05}$	$8.8^{+0.6}_{-0.4}$	$9.0^{+0.6}_{-0.6}$	$9.2^{+0.3}_{-0.2}$	$9.25^{+0.18}_{-0.17}$
Γ_2				$1.53^{+0.06}_{-0.05}$				$1.78^{+0.16}_{-0.13}$
$A_\Gamma 2$ [$10^{-2}\,\mathrm{keV}^{-1}\,\mathrm{cm}^2\,\mathrm{s}^{-1}$]				$1.3^{+0.3}_{-0.3}$				$1.5^{+0.9}_{-0.5}$
N_H^a [$10^{22}\,\mathrm{cm}^{-2}$]	$2.1^{+0.7}_{-0.6}$	$3.08^{+1.02}_{-0.98}$	$2.7^{+0.3}_{-0.3}$	$2.5^{+0.3}_{-0.3}$	$1.1^{+0.3}_{-0.3}$	$1.1^{+0.4}_{-0.3}$	$1.33^{+0.08}_{-0.09}$	$1.33^{+0.09}_{-0.08}$
N_H^b [$10^{22}\,\mathrm{cm}^{-2}$]	$3.3^{+1.0}_{-1.0}$	$4.7^{+1.6}_{-1.5}$	$4.2^{+0.5}_{-0.4}$	$3.9^{+0.4}_{-0.5}$	$1.6^{+0.5}_{-0.3}$	$1.7^{+0.5}_{-0.5}$	$2.05^{+0.13}_{-0.12}$	$2.06^{+0.13}_{-0.11}$
E_Fe [keV]					$6.58^{+0.18}_{-0.06}$	$6.69^{+0.14}_{-0.22}$	$6.57^{+0.04}_{-0.08}$	$6.57^{+0.03}_{-0.08}$
σ_Fe [keV]					$0.35^{+0.19}_{-0.25}$	$0.0^{+0.6}_{-0.0}$	$0.014^{+0.19}_{-0.014}$	$0.013^{+0.190}_{-0.013}$
A_Fe [$10^{-4}\,\mathrm{cm}^{-2}\,\mathrm{s}^{-1}$]					$1.6^{+0.4}_{-0.4}$	$1.1^{+0.3}_{-0.3}$	$1.08^{+0.11}_{-0.08}$	$1.08^{+0.11}_{-0.08}$
EW [eV]					126	86	84	84
c_HEXTE	$0.66^{+0.07}_{-0.07}$	$0.77^{+0.09}_{-0.09}$	$0.76^{+0.03}_{-0.03}$		$0.44^{+0.13}_{-0.12}$	$0.60^{+0.12}_{-0.12}$	$0.72^{+0.04}_{-0.04}$	
$A_\mathrm{Bkgcorr,PCA}$ [%]					-1.5	-0.8	-0.02	± 0.0
$A_\mathrm{Bkgcorr,HEXTE}$ [%]					$+0.8$	$+0.4$	$+0.3$	-0.3
Exposure PCA [ks]	31.2	13.6	209.2	209.2	26.0	11.4	17.4	17.4
Exposure HEXTE [ks]	10.3	8.5	99.6	99.6	8.6	7.1	83.0	83.0
Energy Range PCA [keV]	$3-50$	$3-50$	$3-50$	$3-50$	$3-50$	$3-50$	$3-30$	$3-30$
Energy Range HEXTE [keV]	$20-200$	$20-200$	$20-200$	$20-200$	$20-150$	$20-150$	$20-150$	$20-150$
χ^2_red/dof	1.06/132	1.12/121	1.26/121	1.05/120	1.10/116	0.98/105	1.63/82	1.41/81
$F_{4-10\,\mathrm{keV}}$ [$10^{-11}\,\mathrm{erg}\,\mathrm{cm}^{-2}\,\mathrm{s}^{-1}$]	$4.41^{+0.05}_{-0.05}$	$4.48^{+0.08}_{-0.07}$	$4.294^{+0.018}_{-0.017}$	$4.326^{+0.018}_{-0.017}$	$8.39^{+0.03}_{-0.03}$	$8.38^{+0.05}_{-0.05}$	$8.106^{+0.012}_{-0.011}$	$8.067^{+0.011}_{-0.011}$
$F^\mathrm{unabs}_{4-10\,\mathrm{keV}}$ [$10^{-11}\,\mathrm{erg}\,\mathrm{cm}^{-2}\,\mathrm{s}^{-1}$]	$4.71^{+0.05}_{-0.05}$	$4.92^{+0.07}_{-0.08}$	$4.667^{+0.019}_{-0.019}$	$4.636^{+0.018}_{-0.019}$	$8.66^{+0.03}_{-0.03}$	$8.66^{+0.04}_{-0.04}$	$8.433^{+0.012}_{-0.011}$	$8.388^{+0.011}_{-0.012}$
$F_{10-20\,\mathrm{keV}}$ [$10^{-11}\,\mathrm{erg}\,\mathrm{cm}^{-2}\,\mathrm{s}^{-1}$]	$5.82^{+0.07}_{-0.06}$	$5.77^{+0.09}_{-0.09}$	$5.50^{+0.03}_{-0.03}$	$5.58^{+0.03}_{-0.03}$	$5.314^{+0.018}_{-0.018}$	$5.32^{+0.03}_{-0.03}$	$5.043^{+0.007}_{-0.007}$	$5.030^{+0.007}_{-0.007}$
$F_{20-200\,\mathrm{keV}}$ [$10^{-11}\,\mathrm{erg}\,\mathrm{cm}^{-2}\,\mathrm{s}^{-1}$]	$57.3^{+0.6}_{-0.6}$	$52.5^{+0.8}_{-0.9}$	$50.34^{+0.20}_{-0.21}$	$51.516^{+0.204}_{-0.205}$	$12.75^{+0.05}_{-0.04}$	$12.68^{+0.07}_{-0.07}$	$10.768^{+0.005}_{-0.004}$	$10.759^{+0.014}_{-0.015}$

[a] Using the abundance table of Anders & Grevesse (1989). [b] Using the abundance table of Wilms et al. (2000). The model in `ISIS` notation is `phabs`×`(powerlaw+egauss)` for the unpulsed and `phabs`×`powerlaw` for the pulsed spectrum. In addition to this model two power law were used for epoch 5 (`phabs`×`(powerlaw(Isis_Active_Dataset)+egauss)` for the unpulsed and `phabs`×`powerlaw(Isis_Active_Dataset)` for the pulsed emission). All uncertainties indicate the 90% confidence interval.

3.4 Conclusion

The pulsar B1509−58 was regular monitored by *RXTE* since 1996. It showed that the spectral parameters are nearly constant over the monitoring program. The seen decline in the flux or photon index is an indication for an instrumental effect in the PCU2 top layer. Calibration effects for the detector were clear visible in longer exposures as it was for the Crab (Jahoda et al., 2006). The L edges for the xenon layer could not be well constrained and therefore residuals remained. The pulse period of the source showed no glitches. Thus it was possible to calculate pulse period ephemeris which are in ν and $\dot{\nu}$ consistent with previous measurements. The pulsed and unpulsed spectra derived from the ephemeris are also constant over time. The origin of the iron line in the phase averaged spectra could be assigned to the unpulsed spectra and therefore as an indication for the supernova remnant around B1509−58.

Thunder is good, thunder is impressive;
but it is lightning that does the work.

(Mark Twain)

4 Active Galactic Nuclei

ACTIVE Galactic Nuclei (AGN) are very spectacular objects in the universe[1]. On pictures they are almost indistinguishable from stars (see Fig. 4.1). Only their spectra show the different behavior. They are galaxies with centers as bright as a hole galaxy ($L_{\mathrm{AGN}} \sim 10^{10}\,\mathrm{L}_\odot$). Their emission extends over a broad wavelength while the emission from "normal" galaxies is due to the stars in there and therefore thermal emission in the range between IR and UV[2]. Due to their brightness AGN can be observed to very great distances. The radiative energy of this objects is most likely produced by accretion onto a supermassive black hole (SMBH) in the center with $M \sim 10^{6\ldots8}\,M_\odot$ and an accretion rate of about $1\ldots2\,M_\odot/\mathrm{yr}$.

The study of AGN started at the beginning of the 20th century by Fath (1909). He observed the spectra of the nuclei of the brightest "spiral nebulae". Most of this nebulae showed absorption-line spectra. But in one of them, NGC 1068, he found six emission lines (Hβ, [O `II`], [Ne `III`] and three lines of [O `III`]). Edwin Hubble noted in 1926 the planetary-nebula-type emission-line spectra of three, now known, AGNs. Carl K. Seyfert (February 11, 1911 – June 13, 1960) found a class of spiral galaxies with a bright, pointlike central nucleus and broad optical emission lines (Seyfert, 1943). With the classification of the galaxies after their emission lines and behavior in the electromagnetic spectra (see Sec. 4.1), the class of AGNs was embedded into modern astrophysics.

4.1 Types of active galaxies

Seyfert galaxies

Seyfert galaxies are named after Carl K. Seyfert. This galaxies are highly redshifted. There are two types of this galaxies: **Seyfert 1** galaxies have a spectrum where the allowed lines, e.g. H `I` Balmer lines, are broader than the forbidden lines. Their widths correspond to velocities up to $10^4\,\mathrm{km\,s^{-1}}$ and therefore they come from a medium of high density ($n_\mathrm{e} \gtrsim 10^9\,\mathrm{cm^{-3}}$). The continuum of the spectrum is weak. **Seyfert 2** galaxies have a spectrum where the forbidden lines (e.g., [O `III` 5007]) are thin. They have a width of a few $10^2\,\mathrm{km\,s^{-1}}$. They come therefore from a thin medium with densities about

---

[1] I will concentrate on basic information from Osterbrock (1989) and Krolik (1998).

[2] The spectrum is a superposition of Planck-spectra according to the stellar temperature distribution.

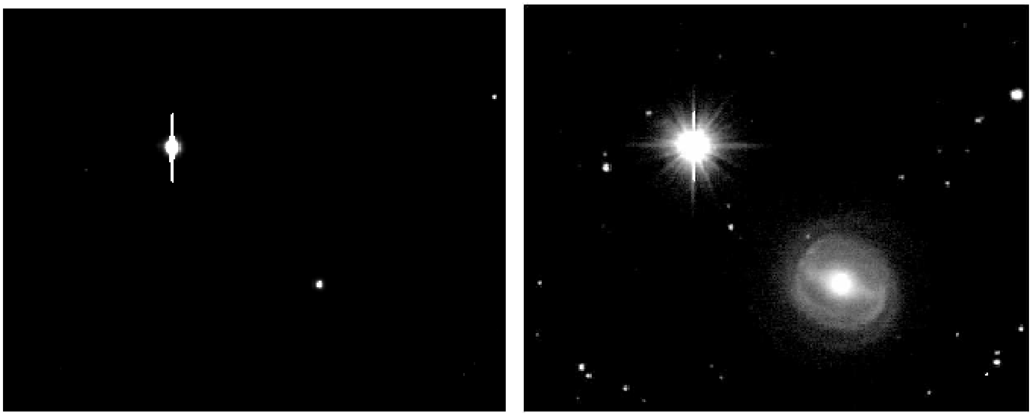

Figure 4.1: Optical image of the galaxy NGC 3783 with linear (left) and logarithmic (right) intensity scale. The origin of the pointlike object is seen on the latter. The emission of the core outshines the host galaxy. A foreground star of the Milky Way is also seen on the pictures.

$n_\mathrm{e} \sim 10^3 \ldots 10^6\,\mathrm{cm}^{-3}$. For this types there are also underclasses: **Narrow-line Seyfert 1** galaxies have the same properties as normal Seyfert 1 galaxies but with unusually narrow H I lines (see Osterbrock & Pogge, 1985). There are only five galaxies from this type known.

LINERS

LINERS (Low-Ionization Nuclear Emission Region) show a similar optical spectrum to Seyfert 2 galaxies but with a weaker continuum. The spectrum is therefore dominated by emission from low-ionization states. Together with Seyfert galaxies this type is found in early type spirals (Sa, Sb; Wilms & Kadler, 2010).

Quasars

With bolometric magnitudes up to $M_\mathrm{B} < -21.5\,\mathrm{mag}$, **Quasars** (Quasi-Stellar Radio Sources) are the most luminous AGN (Wilms & Kadler, 2010). An underclass of quasars are the QSOs (Quasi-Stellar Objects). All quasars show at least some radio emission. Due to the radio-to-optical flux ratio $R_\mathrm{r-o} = F(6\,\mathrm{GHz})/F(4400\,\mathrm{Å})$ (Kellermann et al., 1989) you can divide them into **radio-loud** ($R_\mathrm{r-o}$= 10–100) or **radio-quiet** ($0.1 < R_\mathrm{r-o} < 1$). The latter ones are $\sim 10\times$ more than the former ones. The optical spectra of QSOs are similar to them of Seyfert galaxies but with weaker absorption features from the galaxy and weaker narrow lines. An other class of quasars are **Flat-spectrum radio quasars** (FSRQs).

Radio galaxies

Radio Galaxies are typically elliptical galaxies which are fainter than QSOs. Their optical spectra are similar to those of Seyfert galaxies. There are **Narrow Line Radio Galaxies** (NLRG) and **Broad Line Radio Galaxies** (BLRG) which can be considered as radio-loud Seyfert-type galaxies. Such radio-loud object often show jets. There is a classification due the jet structure (Fanaroff & Riley, 1974): **Fanaroff-Riley class I** (FR I) are galaxies with a dominating nucleus and two asymmetric jets. They are less luminous but bright. The jets end in plumes. **Fanaroff-Riley class II** (FR II) galaxies have a powerful double-lobe with hotspots and a steep radio spectrum.

BL Lac

This type of radio-loud AGNs is named after the prototype BL Lacertae. It was first classified as a variable star with $m_\mathrm{B} = 14$–$16\,\mathrm{mag}$ (Hoffmeister, 1929). BL Lac objects have a flat spectrum without significant emission lines. The continuum shows high variability over the whole energy range and the spectrum is highly polarized. This indicates synchrotron radiation.

OVV quasars

For **Optically Violent Variables** (OVVs) optical features are seen due to weaker radio emission. This features show variability of $m_\mathrm{B} \gtrsim 0.1$ mag on the scale of days. Together with BL Lac objects and radio-loud quasars, OVVs form the group of **blazars** – radio-loud objects with a strong variability.

4.2 Unified model

Due to their similar spectra and behavior the different types of AGNs seem to have the same origin. The unified model tries to combine basic components of AGN with their orientation to the line of sight (Urry & Padovani, 1995). In the center of a "model" AGN there is a SMBH of a mass $M \sim 10^8\,M_\odot$. Around it the accretion disk ($r \sim 10^{-3}$ pc) can be found which is surrounded by the broad line region (BLR, $r \sim 0.01$–$0.1\,\mathrm{pc}$), that means a dense and fast rotating medium. After this a cold dust torus ($r \sim 1$–$10\,\mathrm{pc}$) and a narrow line region (NLR, $r \sim 100$–$1000\,\mathrm{pc}$) complete the model.

Radio-loud AGN have collimated jets of relativistic material outflowing orthogonal to the accretion disk. The jet emission process is due to synchrotron radiation from relativistic electrons in a magnetic field. In Figure 4.2 the different types of AGN can be seen. They depend on the inclination angle (see Table 4.1) and the spherical symmetry. So from different viewing positions (e.g., from an other solar system) the classification of a galaxy can vary.

Table 4.1: Simplified AGN unification (Peterson, 1997).

Radio	Orientation	
Properties	Face-on	Edge-on
Radio Quiet	Seyfert 1	Seyfert 2
	QSO	Far IR Galaxy?
Radio Loud	BL Lac	FR I
	BLRG	NLRG
	Quasar/OVV	FR II

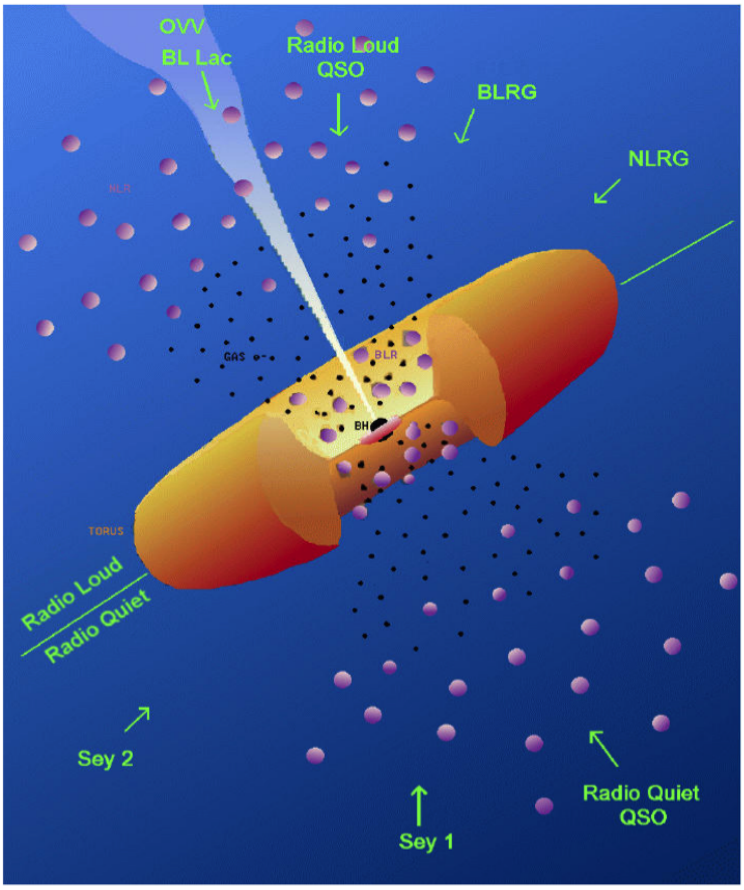

Figure 4.2: Unified model for radio-loud (upper half) and radio-quiet (lower half) AGN. They are all due to the same physics but different due to the viewing angle (arrows) (Credit: Urry & Padovani, 1995).

4.3 Radiation mechanism

AGN have a power law continuum. The physically mechanism of AGN which lead to the radiation in the X-ray is described in this section. The main mechanism is comptonization.

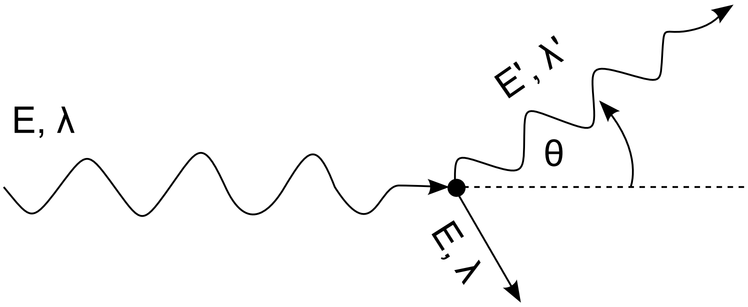

Figure 4.3: Geometry for Compton scattering of a photon by an electron initially at rest (after Rybicki & Lightman, 2004, Fig. 7.1).

4.3.1 Comptonization

Ejected particles collided sometime with other particles. After this collision they are scattered. For Thomson scattering the initial and the final wavelength are identical. In reality the light consists of high-energy photons which change their momentum and energy after scattering. For this reason a quantum picture has to be used: the **Compton scattering**. For an incoming photon with energy E and wavelength λ the energy/wavelength change can be expressed as:

$$E' = \frac{E}{1 + \frac{E}{m_\mathrm{e}c^2}(1-\cos\theta)} \quad \text{or} \tag{4.1}$$

$$\lambda' - \lambda = \frac{h}{m_\mathrm{e}c^2}(1-\cos\theta) = \lambda_\mathrm{c}(1-\cos\theta), \tag{4.2}$$

where λ_c is the *Compton wavelength.* For long wavelength $\lambda \gg \lambda_\mathrm{c}$ the scattering is closely elastic.

Averaging over θ, for $E \ll m_\mathrm{e}c^2$:

$$\frac{\Delta E}{E} \approx -\frac{E}{m_\mathrm{e}c^2}. \tag{4.3}$$

For thermal photons an energy transfer onto the electron is possible:

$$\frac{\Delta E}{E} = \frac{4kT - E}{m_\mathrm{e}c^2}. \tag{4.4}$$

Comptonization of soft X-ray from the accretion disk in the hot corona ($T \sim 10^8$ K) lead to a power law continuum in the AGN X-ray spectrum. In the disk power law photons are scattered after Thomson and lead to a *Compton Reflection Hump.* When these photons are absorbed in the disk, a fluorescent iron Kα line can be seen at 6.4 keV.

Another mechanism for X-ray radiation is the synchrotron radiation that was described in Sec. 2.4.1.

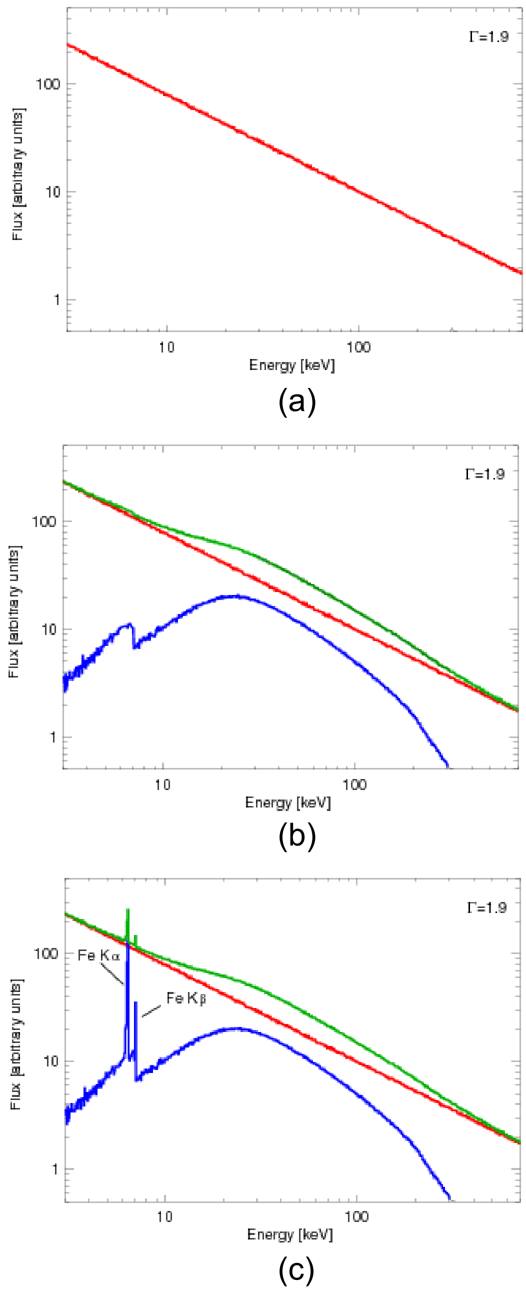

(a)

(b)

(c)

Figure 4.4: Composition of the AGN X-ray spectrum: *(a)* Power law continuum from comptonization. *(b)* Additional Compton reflection hump from Thomson scattering. *(c)* Iron Kα line through photoabsorption of power law photons in the disk (Wilms & Kadler, 2009).

> The most exciting phrase to hear in science, the one that heralds new discoveries, is not "Eureka!" ("I found it!") but rather "hmm....that's funny..."
>
> *(Isaac Asimov)*

5 TANAMI

TANAMI (Tracking Active Galactic Nuclei with Austral Milliarcsecond Interferometry)[1] is a project to image and monitor relativistic jet structures of AGN's on parsec-scales in the southern hemisphere with the *Australian/South-African Long Baseline Array* (LBA+). It started in November 2007 and every two months new monitoring were performed. TANAMI is tracking sources south of −30° declination (for the northern hemisphere, e.g. the *MOJAVE* program[2] is doing the same). At frequencies of 8.4 GHz and 22 GHz the images have milliarcsecond resolutions. Together with *Fermi* contemporaneously observations of Blazars were taken to understand the origin of gamma-ray emission.

Multifrequency studies of the spectral energy distribution of the sources play an important role of the program. The TANAMI-sample contains 76 sources of AGN in the southern hemisphere (as of September 20). The sources were, in addition to the LBA, observed with different satellites and telescopes in the range from gamma-ray, X-ray, UV, optical up to radio. An overview about the observations taken with the actually main X-ray satellites is seen in Table 5.1. This information were taken from NASA's online data archive HEASARC. The source type was searched on the NASA/IPAC Extragalactic Database[3] (NED) and from SIMBAD[4]. All sources were observed with *INTEGRAL*[5] and the main part with *Swift* (see Sec. 5.3), too. But only three samples were observed with all six X-ray satellites, namely Centaurus A, IC 4296 and PKS 2155-304. The main instruments used for this analysis were *XMM-Newton* (sec. 5.1) and *Swift*.

In the following section I analyzed four TANAMI sources with *XMM-Newton*. Namely PKS 2004−447, PKS 2005−489, Pictor A and PKS 2155−304. For the analysis I used data from the optical monitor (OM) and the EPIC cameras (pn and MOS1/2). For the source PKS 0208−512 the data of *Swift*-XRT were taken.

---

[1] `http://pulsar.sternwarte.uni-erlangen.de/tanami/`

[2] `https://www.physics.purdue.edu/astro/mojave/`

[3] `http://ned.ipac.caltech.edu`

[4] `http://simbad.u-strasbg.fr/simbad/`

[5] `http://www.esa.int/esaMI/Integral/index.html`

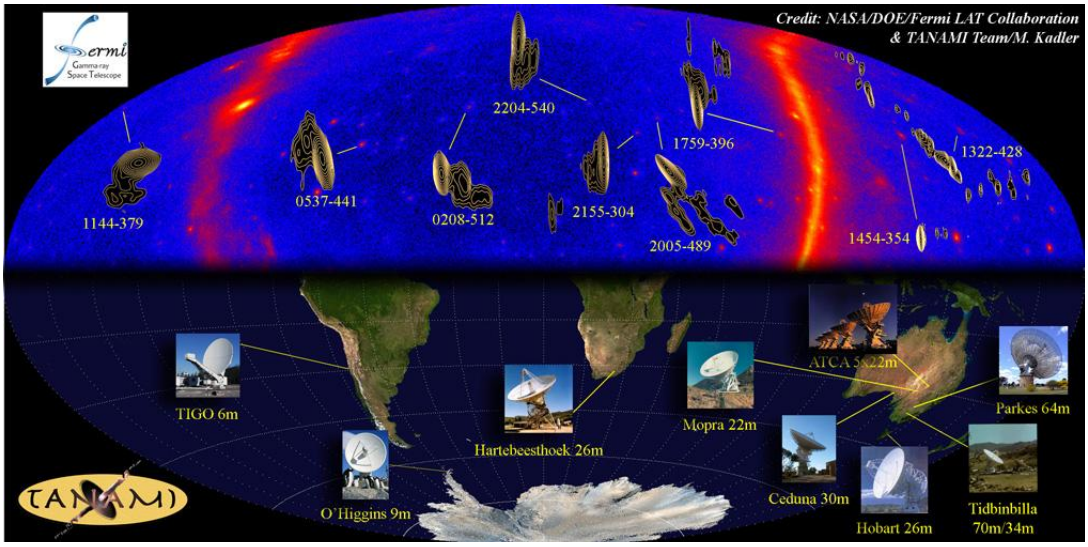

Figure 5.1: The *Fermi*/LAT γ-ray sky (top half, with south being up) and the positions of the radio telescopes on Earth's surface (bottom half, south being down) of the TANAMI-program. On the *Fermi* sky image TANAMI radio images of the brightest extragalactic γ-ray sources are overlaid. (Credit: NASA/Fermi-Collaboration, TANAMI-Team/M. Kadler)

Table 5.1: Observations of the TANAMI sources with X-ray satellites. The information are taken from HEASARC. Catalogs for the satellites were: Suzaku Master Catalog, INTEGRAL Public Pointed Science Window Data/INTEGRAL Science Window Data, XTE Master Catalog, XMM-Newton Master Log & Public Archive, Chandra Observations Log and the Swift Master Catalog. For the classification of the source SIMBAD- and NED-types were taken.

Object	Suzaku	Integral	XMM	RXTE	Swift	Chandra	SIMBAD type	NED type
PKS 0047−579	–	61/134	–	–	2	–	Quasar	QSO
PKS 0055−328	–	103/240	–	–	3	–	Radio Src.	QSO
PKS 0208−512	1	208/434	1	–	73	2	BL Lac	QSO
PKS 0227−369	–	81/180	–	–	3	–	Quasar	QSO
PKS 0244−470	–	200/419	–	–	1	–	Radio Galaxy	QSO
PKS 0302−623	–	50/133	–	–	2	–	Quasar	QSO
PKS 0308−611	–	48/129	–	–	3	–	Quasar	QSO
PMN J0334−3725	–	62/140	–	–	11	–	X-Ray Src.	VisS
PKS 0332−403	–	61/138	–	4	6	–	BL Lac	QSO
PKS 0402−362	–	36/106	–	–	10	1	Quasar	QSO
PKS 0405−385	–	35/87	–	1	3	–	Quasar	QSO
PMN J0413−5332	–	27/122	–	–	1	–	Radio Src.	Radio Src.
PKS 0426−380	–	75/166	–	–	12	–	BL Lac	QSO
PKS 0438−436	–	109/288	1	–	8	–	Quasar	QSO
PKS 0447−439	–	115/303	–	11	13	–	BL Lac	G
PKS 0454−463	–	109/298	–	–	4	1	Quasar	QSO
PKS 0506−612	–	538/2331	–	–	3	–	Quasar	QSO
PKS 0516−621	–	727/2889	–	–	9	–	Quasar	QSO
PICTOR A	–	109/283	3	5	2	11	Seyfert 1	G
ESO 362-G 021	–	285/620	2	–	18	3	BL Lac	G
PKS 0524−485	–	81/229	–	–	2	–	poss. Quasar	VisS
PMN J0529−3555	–	304/664	–	–	8	–	Radio Src.	VisS
PKS 0537−441	–	103/285	3	4	42	–	BL Lac	QSO
PKS 0625−35	1	103/236	3	–	2	1	Radio Galaxy	G
PKS 0637−752	–	777/2803	–	–	6	29	Seyfert 1	QSO
PKS 0700−661	–	667/2485	–	–	3	–	Quasar	QSO

continued on the next page

Observations of the TANAMI sources – continued

Object	Suzaku	Integral	XMM	RXTE	Swift	Chandra	SIMBAD	NED
PMN J0718−4319	–	186/472	–	–	6	–	X-ray Src.	Radio Src.
PKS 0736−770	–	294/1014	–	–	6	–	Quasar	QSO
PKS 0745−330	–	241/531	–	–	3	–	Radio Src.	Radio Src.
PMN J0810−7530	–	147/634	–	–	9	–	X-ray Src.	Radio Src.
PKS 1057−79	–	25/103	–	–	5	–	BL Lac	QSO
PKS 1101−536	–	1556/3319	–	–	4	1	Quasar	QSO
PKS 1104−445	–	143/295	–	–	4	–	Quasar	QSO
PKS 1144−379	–	59/157	–	6	5	–	BL Lac	QSO
PKS 1257−326	–	442/810	–	–	3	–	Quasar	QSO
ESO 443-G 024	–	406/777	–	–	1	1	Blazar	G
PKS 1313−333	–	667/1315	–	1 ssc	3	–	Quasar	QSO
Centaurus A	4	1143/2365	3	417	17	29	Seyfert 2	G
PMN J1326−5256	–	1434/3055	–	–	4	–	Radio Src.	Radio Src.
PMN J1329−5608	–	1830/3842	–	–	4	–	Radio Src.	Radio Src.
IC 4296	1	781/1555	1	1733	5	24	Radio Galaxy	G
PMN J1347−3750	–	1050/2092	–	–	4	–	Radio Src.	Radio Src.
PKS 1424−418	–	1411/2930	–	–	14	1	Quasar	QSO
PKS 1440−389	–	1292/2639	–	1	2	–	Radio Src.	G
PKS 1454−354	–	1108/2268	–	–	2	–	Quasar	QSO
PMN J1505−3432	–	1055/2172	–	2	2	–	AGN	Radio Src.
PMN J1508−4953	–	2028/4196	–	–	2	–	Radio Src.	VisS
PKS 1549−79	1	615/1469	2	–	2	–	Seyfert 2	G
PMN J1604−4441	–	3236/6695	–	–	2	–	Radio Src.	G
PMN J1603−4904	–	3637/7480	–	–	3	–	Radio Src.	VisS
PMN J1610−6649	–	871/2009	–	–	4	–	X-ray Src.	Radio Src.
PKS 1610−771	–	651/1530	–	–	7	–	Quasar	QSO
PMN J1617−5848	–	2169/4544	–	–	–	–	Quasar	QSO
PMN J1650−5044	–	3662/7621	–	257	–	–	AGN	VisS
PMN J1717−3342	–	7189/15088	–	2	–	–	BL Lac	QSO
PKS 1716−771	–	631/1346	–	–	5	–	Radio Src.	Radio Src.
NGC 6328	–	290/639	–	–	14	1	LINER-type AGN	G
PKS 1733−56	–	998/2055	–	–	–	1	Seyfert 1	G
PMN J1802−3940	–	3309/6848	–	–	2	–	Radio Src.	QSO
PMN J1808−5011	–	598/1254	–	–	9	–	Quasar	QSO
PKS 1814−63	–	318/702	2	–	–	1	Seyfert 2	G
PKS 1933−400	–	769/1663	–	–	1	–	Quasar	QSO
PKS 1934−63	–	175/410	–	–	–	1	Seyfert 2	G
PKS 1954−388	–	682/1436	–	–	4	–	Quasar	QSO
PKS 2004−447	–	448/968	1	–	8	–	Seyfert 1	QSO
PKS 2005−489	–	250/541	3	166	14	5	BL Lac	QSO
ESO 462-G 027	–	169/411	–	–	2	–	Galaxy	G
PKS 2052−474	–	50/158	–	–	9	1	Quasar	QSO
PKS 2106−413	–	88/241	–	–	–	–	Quasar	QSO
PMN J2139−4235	–	144/340	2	–	3	1	Radio Src.	G
PKS 2149−306	–	395/807	1	–	13	2	Quasar	QSO
ESO 075-G 041	–	60/143	1	–	3	3	Seyfert 1	G
PKS 2155−304	7	394/806	22	509	84	77	BL Lac	QSO
PKS 2204−540	–	40/80	–	–	6	–	Quasar	QSO
PKS 2326−477	–	43/94	–	–	4	1	Quasar	QSO
PKS 2355−534	–	2/9	–	–	5	–	Quasar	QSO

5.1 The X-ray Multi-Mirror Mission Newton

The *X-ray Multi-Mirror Mission Newton* (*XMM-Newton*) was launched by the *European Space Agency* (ESA) on December 10, 1999 in a 48 hours orbit. The 4 tonne and 10 m long satellite consists of four main elements[6] (Fig. 5.2):

- The *Focal Plane Assembly* (FPA), on which the two *Reflection Grating Spectrometer* (RGS, den Herder et al., 2001) readout cameras, an *European Photon Imaging Camera* (EPIC) PN (Strüder et al., 2001) and two EPIC MOS imaging detectors (Turner et al., 2001) are located.
- The 6.80 m long carbon fibre Telescope Tube.
- The spacecraft *Service Module* (SVM), contains the spacecraft sub-systems, the two solar-array wings, the *Telescope Sun Shield* (TSS) and the two S-band antennas mounted on their booms.
- The *Mirror Support Platform* (MSP), carrying the three mirrors assemblies, the *Optical Monitor* (OM, Mason et al., 2001) and the two star-trackers.

Its main goal is to do high quality X-ray spectroscopy on faint sources. Together with the X-ray telescopes an optical view of the sources is possible[7]. The instruments can work simultaneously with a good angular and spectral resolution.

5.1.1 The X-ray telescopes

The three X-ray telescopes on board *XMM-Newton* consist of 58 Wolter I mirrors in coaxial and confocal configuration (Aschenbach et al., 1987). The focal length is 7.5 m and the largest mirrors have a diameter of 70 cm. The angle of incidence range between 17 and 42 arcmin. One telescope has a direct light path through the mirrors while the other two have grating assemblies (see Sec. 5.1.2) in their light paths (Fig. 5.3). At the end of the light paths CCDs are located which count the incoming and reflected photons.

5.1.2 The Reflection Grating Spectrometer (RGS)

The two identical RGSs lie behind two of the three mirror assemblies. They consist of an array of reflection gratings (*Reflection Grating Array* (RGA)) which lie in the converging beam of the *XMM-Newton* telescope. The RGA contains 182 identical gratings with a size of 10 by 20 cm. They are very flat in the long direction, due to dispersion. No data from them where used for this work. For more details about the RGS see den Herder et al. (2001).

---

[6] See `http://xmm.esac.esa.int/external/xmm_user_support/documentation/technical/Spacecraft/index.shtml`. For more details about the observatory and its construction see the *XMM-Newton* website `http://sci.esa.int/science-e/www/area/index.cfm?fareaid=23`, the XMM-Newton Users Handbook `http://xmm.esac.esa.int/external/xmm_user_support/documentation/uhb/index.html` and Jansen et al. (2001).

[7] *XMM-Newton*, *Swift* and *INTEGRAL* are the only X-ray satellites at the moment who have this possibility.

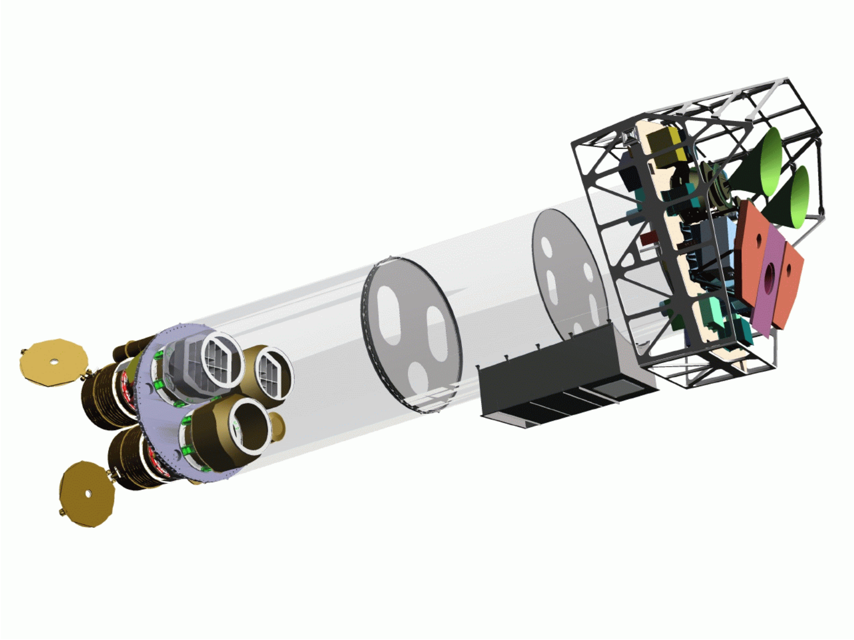

Figure 5.2: View of the *XMM-Newton* observatory. To the left the three mirror modules can be seen. To the right the instrument platform with all the radiators is visible (Jansen et al., 2001, Fig. 1).

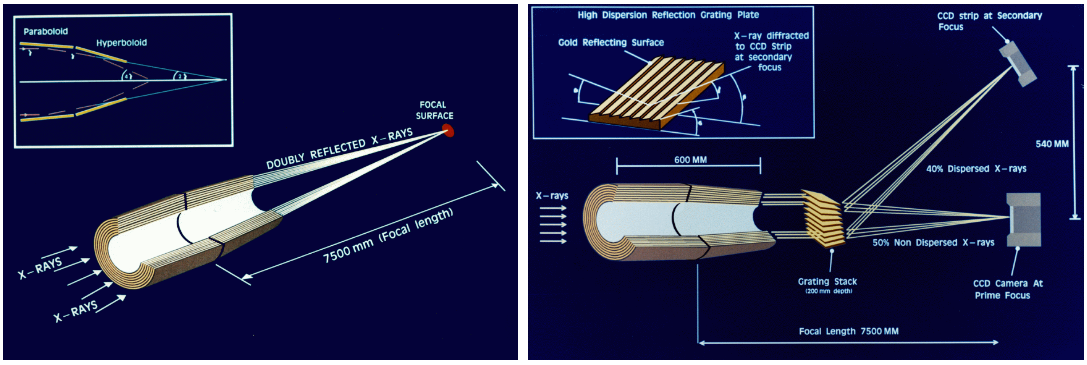

(a) (b)

Figure 5.3: Light path through the *XMM-Newton*'s X-ray telescopes. *(a)* With the pn camera in focus (not to scale). *(b)* With the grating assemblies (not to scale). 44% of the non-intercepted light passes to the primary MOS focus, while 40% of the incident light is intercepted by grating plates (ESA: XMM-Newton SOC, 2011, Fig. 2 and 3).

5.1.3 The European Photon Imaging Camera (EPIC)

At the end of each X-ray telescope one *European Photon Imaging Camera* (EPIC) is located. At the two telescopes with the grating assemblies there are EPIC MOS (Metal Oxide Semiconductor) CCD arrays and at the other an array called EPIC pn. They work in an energy range of 0.15–12 keV with a field of view of $30'$. The spectral ($E/\Delta E \sim 20$–50) and angular resolution ($\sim 6'' \, FWHM$; $\sim 15'' \, HEW$) are moderate. High time resolution can be performed with the EPIC pn camera down to 0.03 ms (timing mode) and 0.007 ms (burst mode).

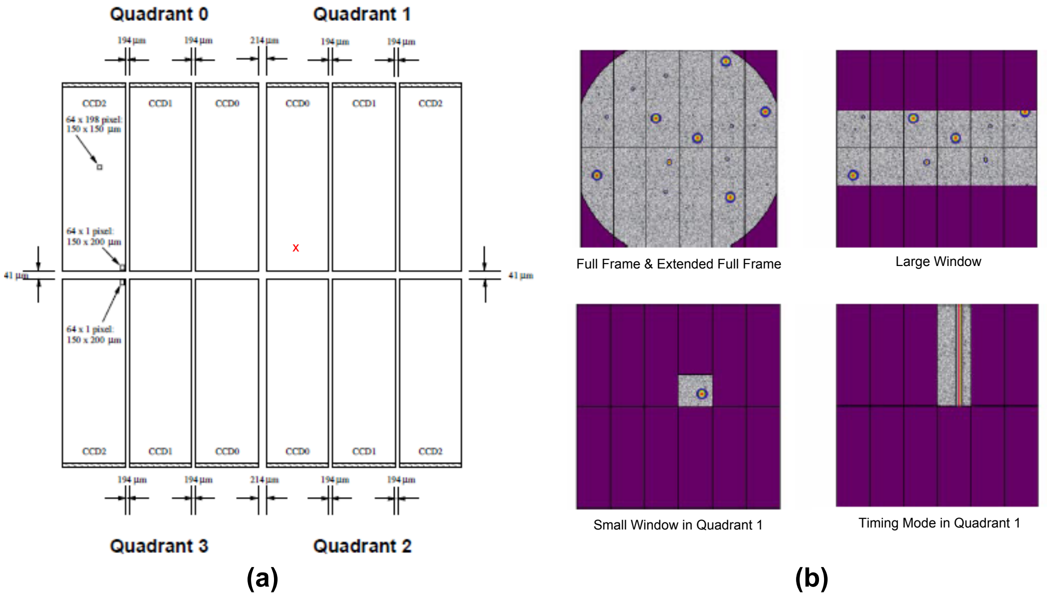

Figure 5.4: *(a)* Overview of the CCDs of the EPIC pn. The focal point of the X-ray telescope lies in CCD0 in quadrant 1 (marked with X). *(b)* Operating modes (Strüder et al., 2001, Fig. 2 and 3).

EPIC pn

The EPIC pn camera (Strüder et al., 2001) exist of 12 CCDs with a size of 13.6×4.4 arcmin. It is slightly offset with respect to the optical axis of the X-ray telescope so that an on-axis observation of a source does not fall in the center thus $\geq 90\%$ of the energy is counted on one CCD chip. CCDs are designed for photon intensity imaging, not for single photon counting. Therefore they must be operated such as only one X-ray photon hits the detector before it is read out. Are more than one photon hitting the detector before readout the energy of them is summarized and the number of photons and their energy is wrong. This phenomena is called *pile-up* (see Table 5.2 for the max. count rates to avoid this effect). For the pn there are six readout modes available (see Fig. 5.4):

- Full frame and extended full frame: all pixels of all CCDs are read out; the full FOV is covered
- Large window: the inner half of the area of the 12 CCDs is used for read out
- Small window: only a part of CCD0 in quadrant 1 is read out
- Timing and burst: CCD0 in quadrant 1 is operating in fast mode; imaging is made only along the column (RAWX) axis

EPIC MOS

The X-ray telescopes with the grating assemblies contain EPIC cameras with MOS CCDs (Short et al., 1998). There are seven individual identical, front-illuminated (the pn CCDs are back-illuminated) CCDs in the focal plane of each MOS camera. The two MOS cameras

Table 5.2: Parameters of the standard modes for the EPIC pn and MOS (after ESA: XMM-Newton SOC, 2011, Table 3).

MOS mode (pixels) [**1 pixel** = 1.1″]	**Time res.**	**Life time** [%]	**Max. count rate**^{1} **(flux)** **point source** [**cts** s^{-1}] [**mCrab**]^2
full frame (600 × 600)	2.6 ms	100.0	0.70 (0.24)
large window (198 × 384)	0.9 ms	99.5	1.8 (0.6)
small window (63 × 64)	0.3 ms	97.5	5 (1.7)
timing uncompressed (64 × 200)	1.75 ms	100.0	100 (35)

pn mode (pixels) [**1 pixel** = 4.1″]	**Time res.**	**Life time** [%]	**Max. count rate**^{1} **(flux)** **point source** [**cts** s^{-1}] [**mCrab**]^2
full frame (376 × 384)	73.4 ms	99.9	6 (0.7)
extended full frame (376 × 384)	199.1 ms	100.0	1 (0.12)
large window (198 × 384)	47.7 ms	94.9	6 (0.7)
small window (63 × 64)	5.7 ms	71.0	50 (6.5)
timing (64 × 200)	0.03 ms	99.5	800 (85)
burst (64 × 180)	0.007	3.0	60000 (6300)

1) "Maximum" count rate to avoid pile-up, including background.

2) 1 mCrab = 2.4 $\times 10^{-11}$ erg s^{-1} cm^{-2} (in the 2–10 keV energy range).

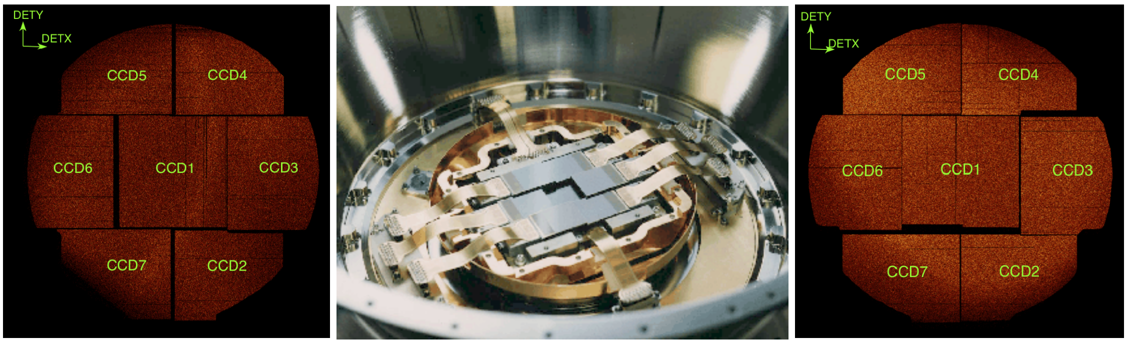

Figure 5.5: Alignment of the MOS CCDs. *(middle)* Picture of one MOS camera. It is seen that the inner chip lies behind the outer ring (Turner et al., 2001, Fig. 4). *(left)* MOS1. *(right)* MOS2 (ESA: XMM-Newton SOC, 2011, Fig. 20 and 21).

are rotated by 90deg with respect to each other. The alignment of the CCDs can be seen in Fig. 5.5. The central CCD lies in the focal point of the telescope and is located behind the outer chips. Physically the outer chips overlap with the inner one. Therefore there are dead spaces between the chips which are unusable areas due to detector edges. On March 9, 2005 (XMM revolution 0961) at about 01:30 hrs an event in the focal plane of MOS1 was registered. It might be attributed to a micrometeorite impact scattering debris into the focal plane. After that CCD6 was damaged and switched off.

For the MOS there are four readout modes comparing to the pn modes:

- Full frame: all pixels of all CCDs are read out; the full FOV is covered
- Large and small window: from the inner CCD only a part is read out; the outer CCDs are in full operation
- Timing uncompressed: 100 rows in a central window 100 pixel wide are operating in fast mode

For both, the pn and the MOS cameras, three filters are available:

- Thick filter: for bright sources which could degrade the energy scale and resolution of EPIC; suppressing the contamination for all point sources up to $m_V = 1$–4 (MOS) or $m_V = -2$–1 (pn)
- Medium filter: optical blocking is 10^3 less efficient than for the thick filter; for point sources as bright as $m_V = 6$–9
- Thin filter: optical blocking is 10^5 less efficient than for the thick filter; for point sources with an optical magnitude 12 magnitudes fainter than the limits for the thick filter

Data extraction

The extraction of the XMM data is dependent of the instrument and the mode in which the observation was taken. This can be easily find out on the XMM-webpage[8]. Putting the observation ID in the assigned field gets out all instruments and modes which were used.

The data extraction for the EPIC pn and MOS is very similar. First the data had to be prepared before they can be extracted and analyzed. The used software for the preparation and extraction was the *Science Analysis Software* (SAS, see `http://xmm.esac.esa.int/sas`, Version 10.0.0 (for OM) and Version 11.0.0 (for pn, MOS1 and MOS2)). The tool `xmmprepare` creates a directory containing links to the raw data of the observation. Thereby it had to be specified if the observation was taken in timing mode or in image mode. The next step is to extract the full chip to see where the source is located, how extended it is and if there are other sources around. From this a selection of the source- and background-region for the final extraction is possible so that the correct spectra of the source is analyzed and no counts of nearby sources are contaminating it.

For image mode I had a look at the image of the full chip first. To locate the source correctly on the chip the tool `simbad2ds9`, written by J. Wilms, was used. This tool produces a file of the region around a given source by searching SIMBAD. The region-file is than loaded into the image-file and the image coordinates of the source can be located. The source-region was then choosed as a circle around the source with the radius concentrating on the expansion of the source. Thereby the background-region was taken with the same radius but located in a region of the chip where no source-counts are seen (see Fig. 5.6). This is a problem for observations taken in small window mode for MOS because bright sources fill out the whole window. Therefore the background-region had to be selected on an outer chip (Fig. 5.7).

---

[8] `http://xmm2.esac.esa.int/external/xmm_obs_info/obs_view_frame.shtml`

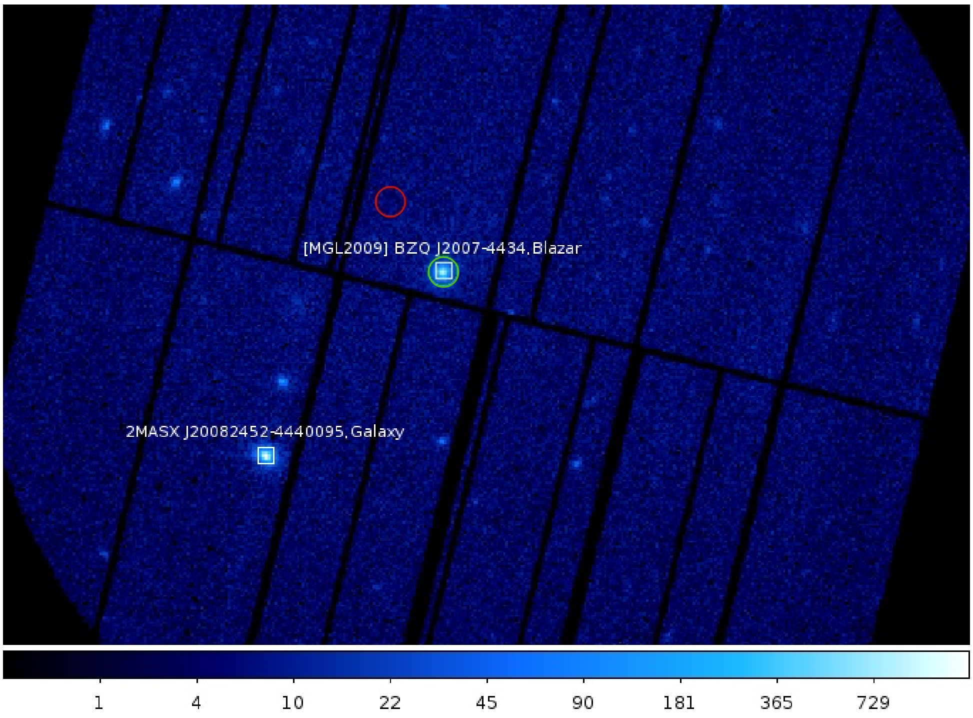

Figure 5.6: Source- (green circle) and background-region (red circle) for PKS 2004−447, ObsID 0200360201. Apart from the actual source a nearby galaxy is seen.

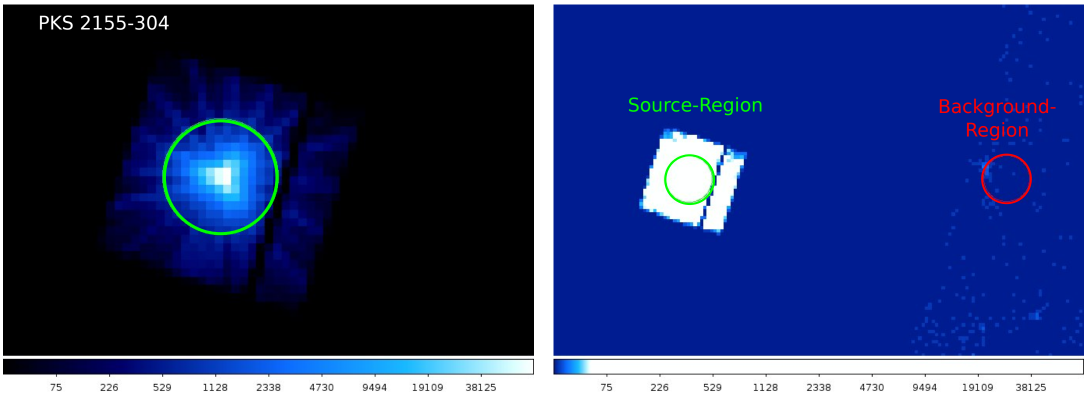

Figure 5.7: Source- (green circle) and background-region (red circle) for PKS 2155−304, ObsID 0080940101. The image was taken in small window mode for MOS2.

For timing mode a totally different way was done. In timing mode the chip is read out raw by raw very fast. In a histogram the counts per raw in x-coordinates are shown. The source is clearly shown as a peak (Fig. 5.8). For the pn the RAWX goes from 0 to 63 and from 0 to 630 for the MOS. The source-region is here selected around the peak and the background at the beginning and at the end of the raw but not at the first or last pixels to avoid chip-errors.

After this steps the correct spectrum can be extracted with `xmmextract` by defining the coordinates of the source and the background and their radii. The results had to be checked whether the spectrum looks like it should and if there is no pile-up. This can easily

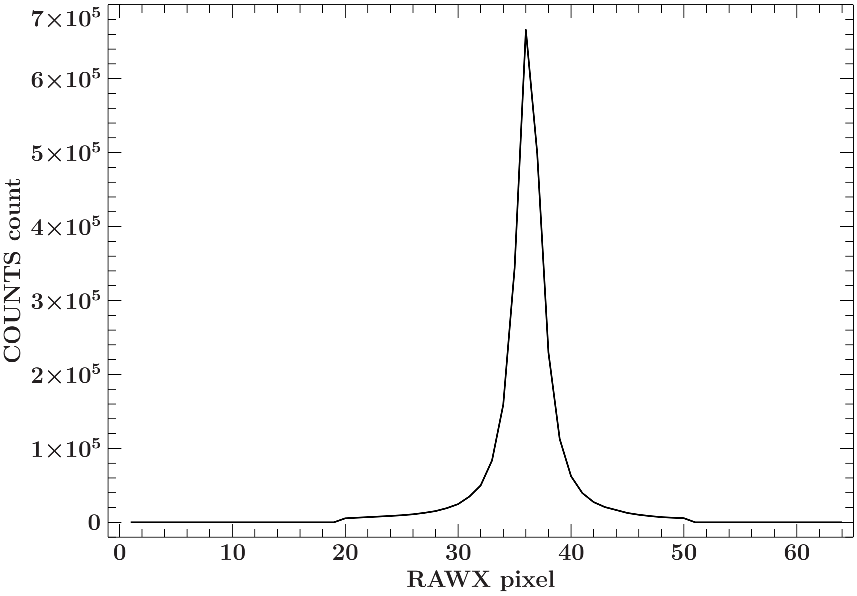

Figure 5.8: Timing mode histogram for PKS 2155−304, ObsID 0124930601. The source was extracted from rows 20–50 and the background from rows 2–10 and 60–63.

be found out by looking at the event-plot which is produced from the event-list of the CCD with the SAS-command `epatplot`. Here the single and double (defaultpattern for the pn) and normally single, double, triple and quadruple events (defaultpattern for the MOS) are plotted, respectively. The model how it should look like is seen, too. If the counted photons and the model did not fit there is pile-up (Fig. 5.9). To exclude this photons you have to cut out an inner circle from the source. The radius depends on the strength of the pile-up. To check whether the pile-up is gone the observed-to-model fractions for the single and double events should lie around 1. During my work I had the problem that `epatplot` did not work for the MOS data. So they could not be checked for pile-up. This is a problem because MOS is more sensitive for this feature than pn (see Table 5.2, last column). If there is pile-up seen in the pn data there is surely pile-up in the MOS data but for me it is not clear how to correlate the inner radii for the two cameras. Therefore I did not correct the MOS data for pile-up and used just the uncorrected spectra.

If the data were now extracted correctly and all artifacts that could lead to wrong spectra are eliminated the data can be analyzed. For AGNs a simple power law with galactic absorption was used (see Sec. 5.2).

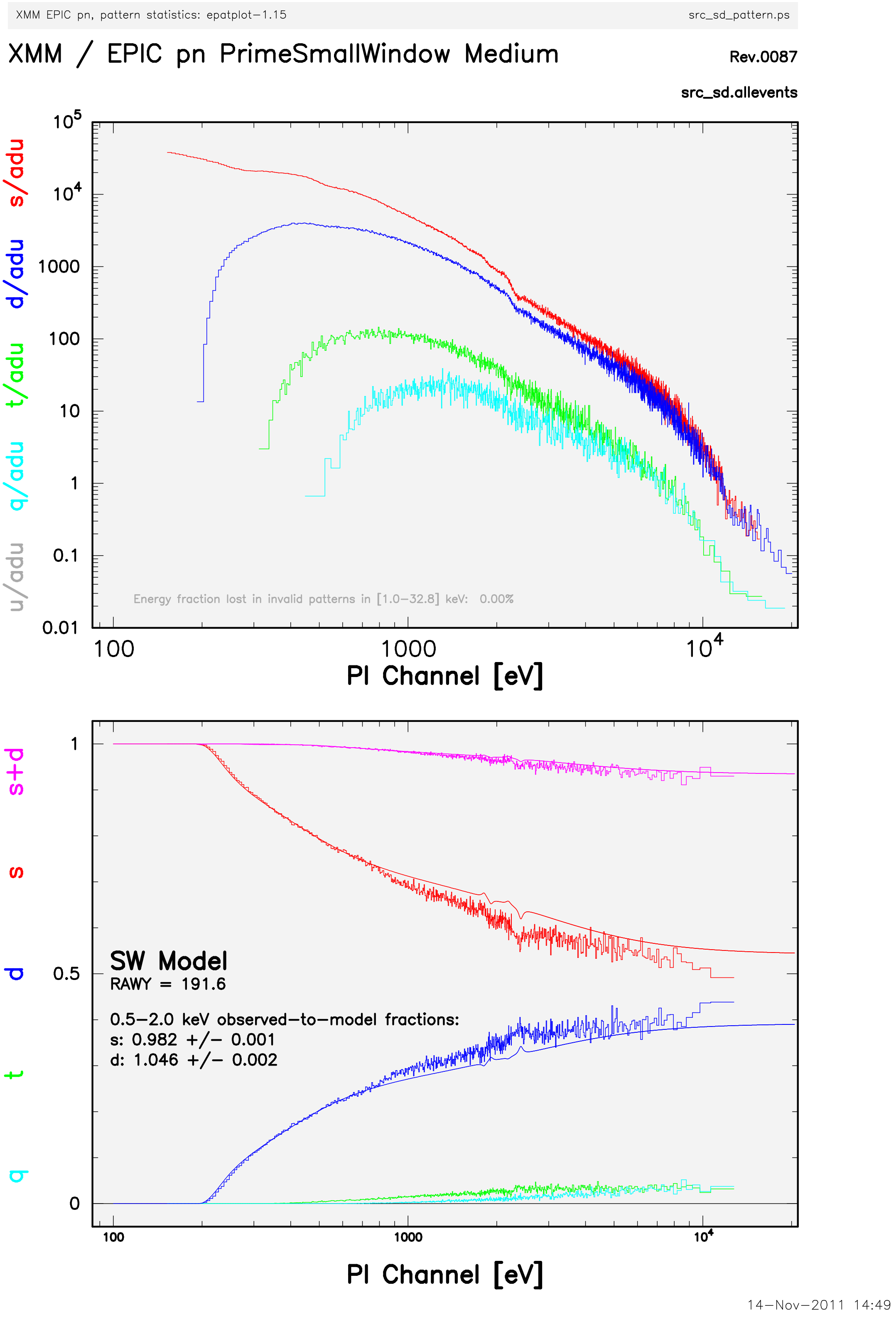

Figure 5.9: Event-plot for PKS 2155−304, ObsID 0124930201, with pile-up.

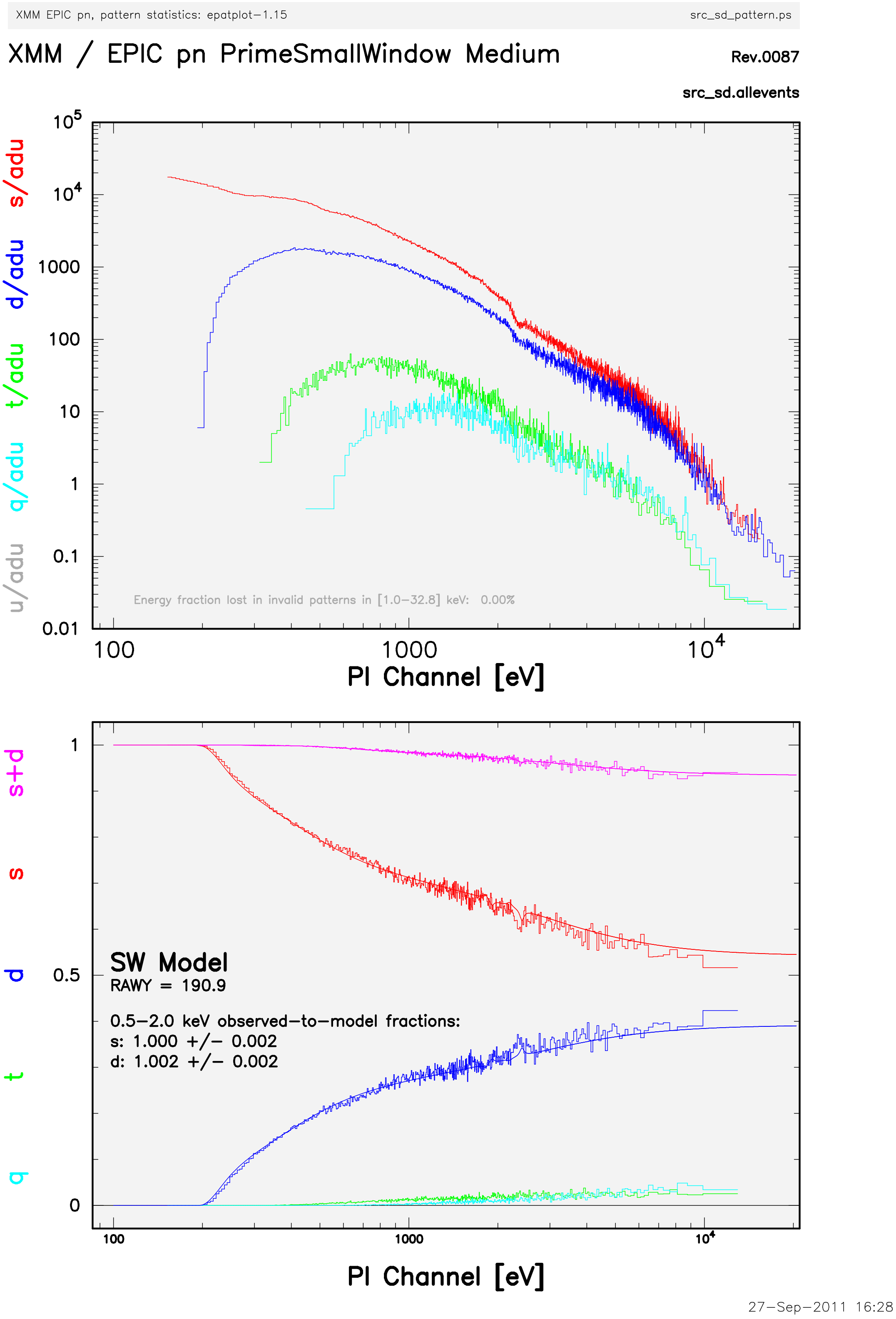

Figure 5.10: Event-plot for PKS 2155−304, ObsID 0124930201, with corrected pile-up.

Table 5.3: Filter names and positions in the filter wheel, their wavelength band and limited magnitudes (see (Mason et al., 2001, Table 2), (ESA: XMM-Newton SOC, 2011, Table 19-20)).

Filter wheel position number	Filter name	Wavelength band [nm]	Zeropoints [mag]
0	Blocked		
1	V	510–580	17.9633
2	Magnifier	380–650	
3	U	300–390	18.2593
4	B	390–490	19.2661
5	White (clear)	150–500	
6	Grism 2 (vis)	290–500	
7	UVW1	245–320	17.2038
8	UVM2	205–245	15.7724
9	UVW2	180–225	14.8667
10	Grism 1 (UV)	200–350	

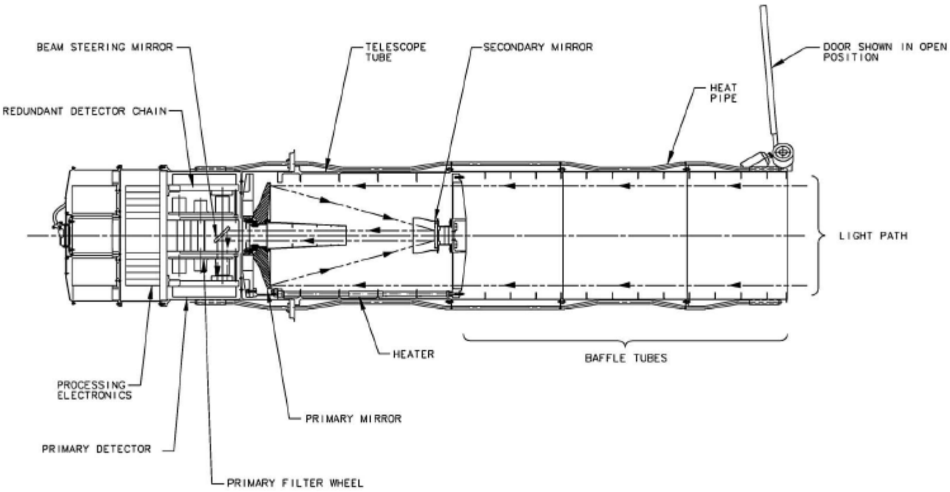

Figure 5.11: Mechanical drawing of the XMM-OM telescope module showing the light path through to the detectors (Mason et al., 2001, Fig. 1).

5.1.4 The Optical Monitor (OM)

Together with observations in the X-ray *XMM-Newton* is able to take data in the ultraviolet/optical band for multiwavelength observations. The OM is type of a Ritchey-Chretien telescope with a diameter of 30 cm and can cover light in the wavelength from 180 nm to 600 nm of the central 17 arcmin square region of the X-ray FOV (Fig. 5.11). The images can be taken with six different broad band filters and two grisms for low-resolution spectroscopy. In addition to them a "blocked" filter, which closes the way to the detector to avoid damage of it by looking at a bright source, and a "white" filter are on the wheel (see Table 5.3).

There are different modes in which images can be taken with the OM. In **Imaging Mode** more spatial coverage is attained but less time resolution. They can be taken at the full

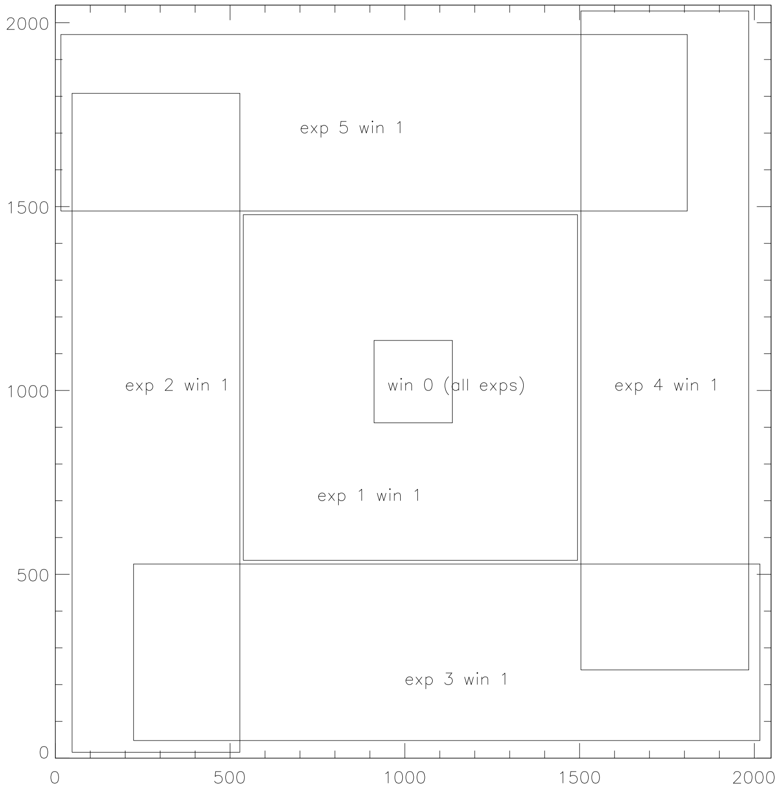

Figure 5.12: Imaging default mode windows (Mason et al., 2001, Fig. 2).

sampling of the instrument or binned by a factor of two. The maximum integration time for an exposure is 5 ks. In **Fast Mode** time resolution is attained but less spatial coverage. No binning is possible. For each observation default window configurations are available (Fig. 5.12).

Data extraction

For every of the six filters of the OM there are three modes possible: image mode, fast mode and grism mode.

The data extraction for the OM can be done in different ways. There is a step-by-step instruction[9] on the webpage for the different modes or they can be done by three different SAS tasks: `omichain`[10] (image mode), `omfchain`[11] (fast mode) and `omgchain`[12] (grism mode). These tasks do the step-by-step automatically and produce all the files which were needed: images, fits-tables with fluxes, tracking-plots.

---

[9] `http://xmm.esac.esa.int/sas/current/documentation/threads/`

[10] `http://xmm.esac.esa.int/sas/current/doc/omichain/omichain.html`

[11] `http://xmm.esac.esa.int/sas/current/doc/omfchain/index.html`

[12] `http://xmm.esac.esa.int/sas/current/doc/omgchain/omgchain.html`

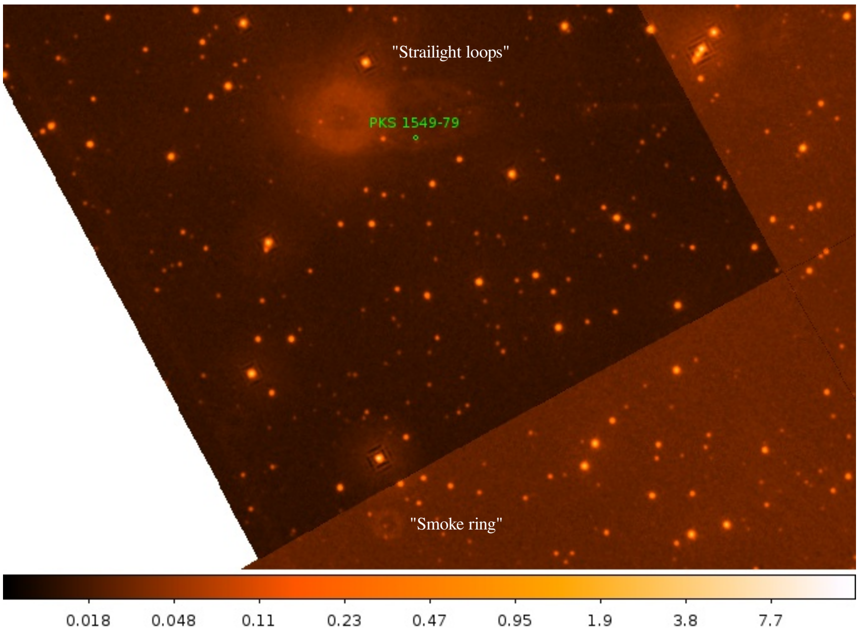

Figure 5.13: Straylight artifacts seen in one observation for PKS 1549−79, ObsID 0550970101. In the upper part of the picture straylight loops caused by reflection of a star outside the FOV are seen. The background is also enhanced and causes a "ring". In the lower part an out-of-focus ghost image of a bright star is seen. The position of the source PKS 1549−79 is marked in green.

Artifacts

Bright sources in the FOV or near the border of it can cause some artifacts on the images of the OM data (Fig. 5.13):

- Internal reflection of light within the detector window causes a faint, out-of-focus ghost image ("smoke ring").
- Reflection of the off-axis starlight and background light from apart of the detector housing form extended loops of emission ("straight loops").
- Diffuse background light falling on the ring causes an enhanced "ring" of emission near the center of the detector.

Count rates to flux calculation and reddening

The satellite measures counts per second that come from the source. These counts were calculated automatically by `omichain` into fluxes for every filter. To understand the conversion-factor from count rate to flux which is used for the OM (see SAS User Guide and CAL-TN-0019), J. Wilms and me did some estimations and calculations. We estimated the count rate R to be the integral over the effective area of the filter $A(E)$ times the energy-flux f_E and calculated it for the different wavelengths:

$$R = \int_0^\infty A(E)\frac{f_E}{E}\mathrm{d}E, \tag{5.1}$$

$$[f_E] = \mathrm{erg\ cm^{-2}\,s^{-1}\,keV^{-1}}.$$

Conversion $f_E \to f_\lambda$.

By definition the flux can be calculated as

$$F = \int_{E_1}^{E_2} f_E \mathrm{d}E \overset{!}{=} \int_{\lambda_1}^{\lambda_2} f_\lambda \mathrm{d}\lambda. \tag{5.2}$$

For $E = h\nu = \frac{hc}{\lambda}$ follows $\frac{\mathrm{d}E}{\mathrm{d}\lambda} = -\frac{hc}{\lambda^2}$

$\Rightarrow \mathrm{d}E = -\frac{hc}{\lambda^2}\mathrm{d}\lambda = -\frac{hc}{(hc)^2}E^2\mathrm{d}\lambda = -\frac{E^2}{hc}\mathrm{d}\lambda$

$$\int_{E_1}^{E_2} f_E \mathrm{d}E = -\int_{\lambda_2}^{\lambda_1} f_E \frac{hc}{\lambda^2}\mathrm{d}\lambda \tag{5.3}$$

We define $\lambda_2 = \frac{hc}{E_1}$ and $\lambda_1 = \frac{hc}{E_2}$ (this is correct, since we are switching limits).

Therefore we get $f_\lambda = f_E \frac{hc}{\lambda^2} \Rightarrow f_E = \frac{\lambda^2}{hc} f_\lambda$, and for the count rate follows

$$\begin{aligned} R = \int_0^\infty A(E)\frac{f_E}{E}\mathrm{d}E &= \int_0^\infty A(\lambda)\frac{\lambda^2}{hc}f_\lambda \frac{\lambda}{hc}\frac{hc}{\lambda^2}\mathrm{d}\lambda \\ &= \int_0^\infty A(\lambda)\frac{\lambda}{hc}f_\lambda \mathrm{d}\lambda \end{aligned} \tag{5.4}$$

We assume that $f_\lambda = \text{const.} = \tilde{f}_\lambda$ and rewrite Eq. 5.4 to

$$R = \tilde{f}_\lambda \int_0^\infty A(\lambda)\frac{\lambda}{hc}\mathrm{d}\lambda. \tag{5.5}$$

From this the conversion between the wavelength-dependent flux and the count rate follows to

$$\tilde{f}_\lambda = R \cdot \underbrace{\left[\int_0^\infty A(\lambda)\frac{\lambda}{hc}\mathrm{d}\lambda\right]^{-1}}_{\text{conversion factor}}. \tag{5.6}$$

Table 5.4: Count rate to flux conversion from different systems. The conversion in AB system and from standard stars is taken from Talavera & OMCal Team (2011), Table 17 and 18. In addition to the conversion factor after Wilms & Litzinger, the dereddened conversion factor and the fraction between the dereddened and reddened factor are shown.

AB system (wavelength)

Filter	UVW2	UVM2	UVW1	U	B	V
λ (Å)	2120.	2310.	2910.	3440.	4500.	5430.
f (erg/cm^2/count/Å)	5.67e-15	2.20e-15	4.77e-16	1.99e-16	1.24e-16	2.51e-16

From standard stars

Filter	UVW2	UVM2	UVW1	U	B	V
λ (Å)	2120.	2310.	2910.	3440.	4500.	5430.
f (erg/cm^2/count/Å)	5.71e-15	2.20e-15	4.76e-16	1.94e-16	1.29e-16	2.49e-16
error	0.054	0.0401	0.068	0.042	0.068	0.013

After Wilms & Litzinger

Filter	UVW2	UVM2	UVW1	U	B	V
λ (Å)	2148.	2334.	2947.	3486.	4347.	5429.
f (erg/cm^2/count/Å)	5.58e-15	2.17e-15	4.70e-16	1.95e-16	1.34e-16	2.52e-16
f_{red} (erg/cm^2/count/Å)	3.84e-14	1.38e-14	1.75e-15	6.02e-16	3.42e-16	5.13e-16
$f/f_{\text{red}}(E(B-V)=0.5)$	6.87	6.37	3.72	3.09	2.56	2.04

With this considerations we get values for the count rate to flux conversion which are very similar to the official ones from the Calibration Handbook of XMM[13] (Talavera & OMCal Team, 2011) (Table 5.4).

Due to the interstellar medium the optical fluxes are reddened, i.e., the measured flux is lower than the real flux. Therefore they had to be corrected. After Fitzpatrick (1999) the reddened flux can be expressed as

$$f_{red} = f \cdot 10^{-0.4 E_{B-V} \cdot curve}, \tag{5.7}$$

where f is the unreddened flux, *curve* the R-dependent (see Eq. 5.9) Galactic extinction curve from the paper and E_{B-V} the color excess, i.e., the difference of the measured $B-V$-colorindex to the real one

$$E(B-V) = (B-V) - (B-V)_0. \tag{5.8}$$

The extinction, i.e., the darkening of stellar and galactic objects due to the interstellar medium, is defined as

$$E(\lambda - V) = curve - R_V \Rightarrow curve = E(\lambda - V) + R_V, \tag{5.9}$$

where

---

[13] `http://xmm.vilspa.esa.es/docs/documents/CAL-TN-0019.pdf`

$$R_V = \frac{A_V}{E(B-V)}, \tag{5.10}$$

A_V is the visual extinction, specifies the ratio of the total to the selective extinction at V. R_V is set to the averaged Galactic value of 3.1 (Cardelli et al., 1989). The variable *curve* can now be replaced in the exponent of Eq. 5.7. It follows for the flux

$$f_{red} = f \cdot 10^{-0.4 E_{B-V} \cdot E(\lambda - V)} \cdot 10^{-0.4 E_{B-V} \cdot R_V}. \tag{5.11}$$

After Eq. 5.4 one can calculate the reddened count rate to

$$\begin{aligned} R_{red} &= \int_0^\infty A(\lambda) \frac{\lambda}{hc} f_{red}(\lambda) \mathrm{d}\lambda \\ &= \int_0^\infty A(\lambda) \frac{\lambda}{hc} f \cdot 10^{-0.4 E_{B-V} \cdot (E(\lambda - V) + R_V)} \mathrm{d}\lambda. \end{aligned} \tag{5.12}$$

With the same assessment as for Eq. 5.5 this equation can be written as

$$R_{red} = \tilde{f} \cdot \int_0^\infty A(\lambda) \frac{\lambda}{hc} \cdot 10^{-0.4 E_{B-V} \cdot (E(\lambda - V) + R_V)} \mathrm{d}\lambda. \tag{5.13}$$

We assumed $E(\lambda - V) \sim$ const. over the filter and got

$$R_{red} = \tilde{f} \cdot 10^{-0.4 E_{B-V} \cdot (E(\lambda - V) + R_V)} \int_0^\infty A(\lambda) \frac{\lambda}{hc} \mathrm{d}\lambda. \tag{5.14}$$

If $E(\lambda - V) \sim$ const., then the unreddened flux can be calculated from

$$f = f_{red} \cdot 10^{-0.4 E_{B-V} \cdot (E(\lambda - V) + R_V)}. \tag{5.15}$$

To check whether this assumption is correct, we calculated the ratio of the conversion factors

$$\frac{f}{f_{\mathrm{red}}} = \frac{\int_0^\infty A(\lambda) \frac{\lambda}{hc} \mathrm{d}\lambda}{\int_0^\infty A(\lambda) \frac{\lambda}{hc} \cdot 10^{-0.4 E_{B-V} \cdot (E(\lambda - V) + R_V)} \mathrm{d}\lambda}, \tag{5.16}$$

as a function of $E(\lambda - V)$ (see Table 5.4). One can see, that the dereddened flux must be higher than the reddened flux. Because of the difference between the literature wavelengths of the OM filters and the calculated mean averaged filter wavelength by Wilms & Litzinger,

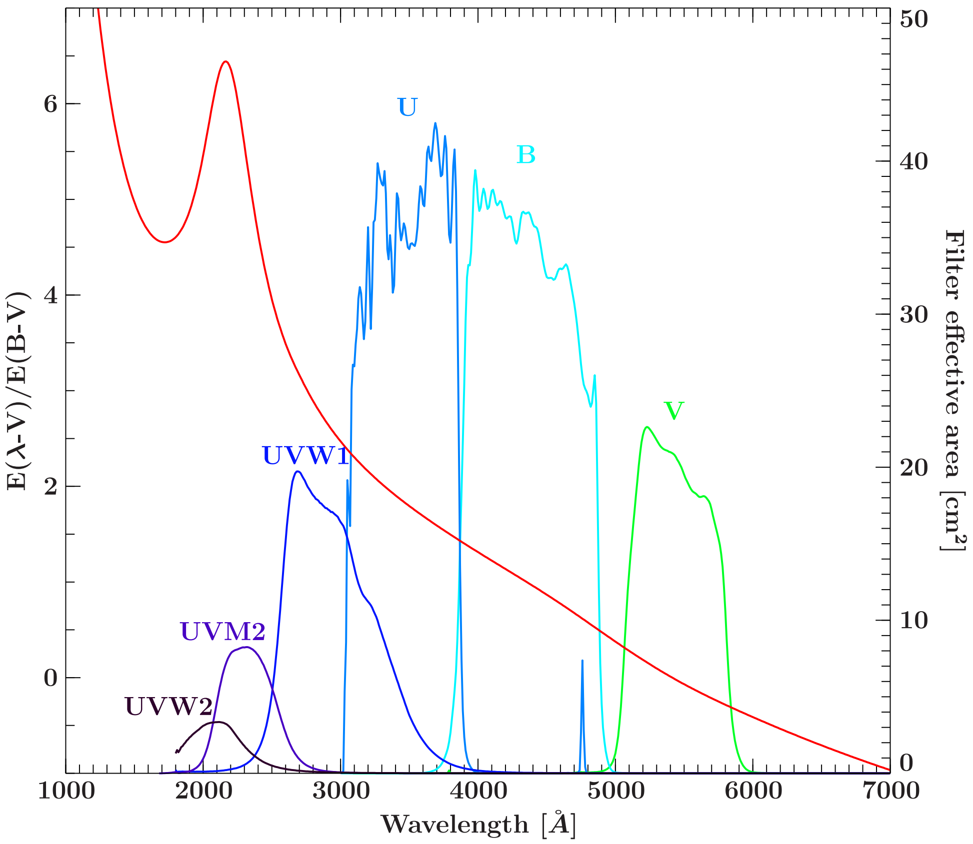

Figure 5.14: Effective area of the OM filters and extinction curve for $R_V = 3.1$ and $E(B-V) = 0.5$.

one cannot assume a constant dereddened factor for every filter. Therefore the dereddened fluxes were calculated after Fitzpatrick (1999) with the correct wavelengths for the filters. In Fig. 5.14 one can see the effective areas for the filters and overlaid the extinction curve for $E(B-V) = 0.5$. The UV-bump is clearly seen.

For the sources for which the value of $E(B-V)$ is not known one can calculate it from the hydrogen absorption column density $N_{\rm H}$ after Predehl & Schmitt (1995).

$$\begin{aligned} \frac{N_{\rm H}}{A_V} &= 1.79 \times 10^{21} \\ \overset{Eq.\ 5.10}{\Rightarrow} \quad E_{B-V} &= \frac{N_{\rm H}}{1.79 \times 10^{21} R_V}. \end{aligned} \tag{5.17}$$

5.2 Data analysis

The spectrum of an AGN can normally be well described by an absorbed power law. Therefore the `ISIS` model `tbnew`×`powerlaw` was used for the following analysis. For the hydrogen absorption column there were three strategies: *(i)* to let the value for the N_H as a free parameter, *(ii)* set it to the value of the Leiden/Argentine/Bonn (LAB) Galactic `HI` Survey[14] and *(iii)* add an additional absorption to case *ii* to check, if intrinsic absorption is seen. The abundance table was set to `wilm`.

5.2.1 PKS 2004-447

PKS 2004−447 is classified as a compact steep-spectrum (CSS) source and possible radio-loud narrow-line Seyfert 1 galaxy (NLS1) but with weak `F II` lines (Gallo et al. 2006; position (equinox 2000.0): $20^\mathrm{h}07^\mathrm{m}55^\mathrm{s}.2$, -44°34′44″). Its redshift was calculated to $z = 0.24$ (Drinkwater et al., 1997). The value for the galactic hydrogen absorption column was taken from the LAB to $3.17 \times 10^{20}\,\mathrm{cm}^{-2}$.

The source was observed with *XMM-Newton* between April 11 and 12, 2004 (revolution 0795, ObsID 0200360201) for 43 ks. The EPIC pn and MOS (MOS1 and MOS2) data were taken in full-frame mode with the medium filter. The OM was in full-low mode for the U, B, UVW1, UVM2 and UVW2 filters. The RGS collected data during the observation, too.

The EPIC spectra of 2004−447 were binned to a single-to-noise of 10 and by a factor of 4 for energies up to 10 keV. For the analysis the energy ranges of 0.4–10 keV for the pn and 0.55–10 keV were used. The spectra were than fitted with the models and strategies described in the preface of this section (Sec. 5.2) and in addition to them with a single power law to check whether the absorption is needed or not.

Previous measurements by Gallo et al. (2006) showed a soft excess below ∼0.6 keV for this data. They replaced the single power law with a broken power law and get significant improvement of $\Delta\chi^2 = 35$, with a break energy at $E_\mathrm{break} = 613^{+79}_{-59}$ eV. This excess is also seen in my analysis. The improvement for a broken power law is $\Delta\chi^2 = 7.7$, but the break energy lies at $E_\mathrm{break} = 3.6^{+2.4}_{-0.9}$ keV. Also the second photon index is different to their value ($\Gamma_\mathrm{2,Gallo} = 2.10^{+0.23}_{-0.19}$). This could be due to changes in the response matrices since 2006. Additional neutral absorption could not be required. Fig. 5.15 shows the EPIC pn, MOS1 and MOS2 spectra with the best fit of an absorbed broken power law and in comparison a single absorbed power law. In Table 5.5 the parameters for a single power law, an absorbed power law and the absorbed broken power law are listed.

In Table 5.5 one can see, that the 2–10 keV unabsorbed flux is lower than the absorbed flux. This is wrong. This phenomenon can be seen for all sources, but can not be explained.

The analysis of the optical data showed that the significance of the count rate in the UVW2 filter was too low and therefore no flux could be calculated (although Gallo et al. (2006) get a flux density of $12.6 \pm 0.5 \times 10^{-16}\,\mathrm{erg}^{-1}\,\mathrm{cm}^{-2}\,\mathrm{Å}^{-1}$ for the UVW2 filter). Therefore there is no corresponding data-point for this filter. The optical fluxes from the extracted OM data were derredened (Table 5.6) and plotted with the unabsorbed X-ray

---

[14] `http://www.astro.uni-bonn.de/~webaiub/english/tools_labsurvey.php`

Table 5.5: Best fit parameters for the EPIC spectra of PKS 2004−447 with three different models.

Parameter	`powerlaw`	`tbnew`×`powerlaw`	`tbnew`×`bknpower`
N_H $[10^{20}\,\mathrm{cm}^{-2}]$		1.8±1.0	$3.0^{+1.5}_{-1.6}$
A_Γ $[10^{-4}\,\mathrm{keV\,cm^2\,s^{-1}}]$	1.670±0.029	$1.75^{+0.07}_{-0.06}$	$1.81^{+0.08}_{-0.09}$
Γ	1.445±0.018	1.49±0.04	1.55±0.06
Γ_2			$1.31^{+0.07}_{-0.43}$
E_break [keV]			$3.6^{+2.4}_{-0.9}$
$F_{0.2-2\,\mathrm{keV}}$ $[10^{-13}\,\mathrm{erg\,cm^{-2}\,s^{-1}}]$	4.75±0.06	4.63±0.06	4.58±0.06
$F^\mathrm{unabs}_{0.2-2\,\mathrm{keV}}$ $[10^{-13}\,\mathrm{erg\,cm^{-2}\,s^{-1}}]$		4.89±0.07	5.09±0.07
$F_{2-10\,\mathrm{keV}}$ $[10^{-13}\,\mathrm{erg\,cm^{-2}\,s^{-1}}]$	10.38±0.13	10.15±0.13	10.48±0.13
$F^\mathrm{unabs}_{2-10\,\mathrm{keV}}$ $[10^{-13}\,\mathrm{erg\,cm^{-2}\,s^{-1}}]$		9.99±0.13	10.31±0.13
χ^2/dof	222.1/225.0	214.5/224.0	206.8/222.0
χ^2_red	0.99	0.96	0.93

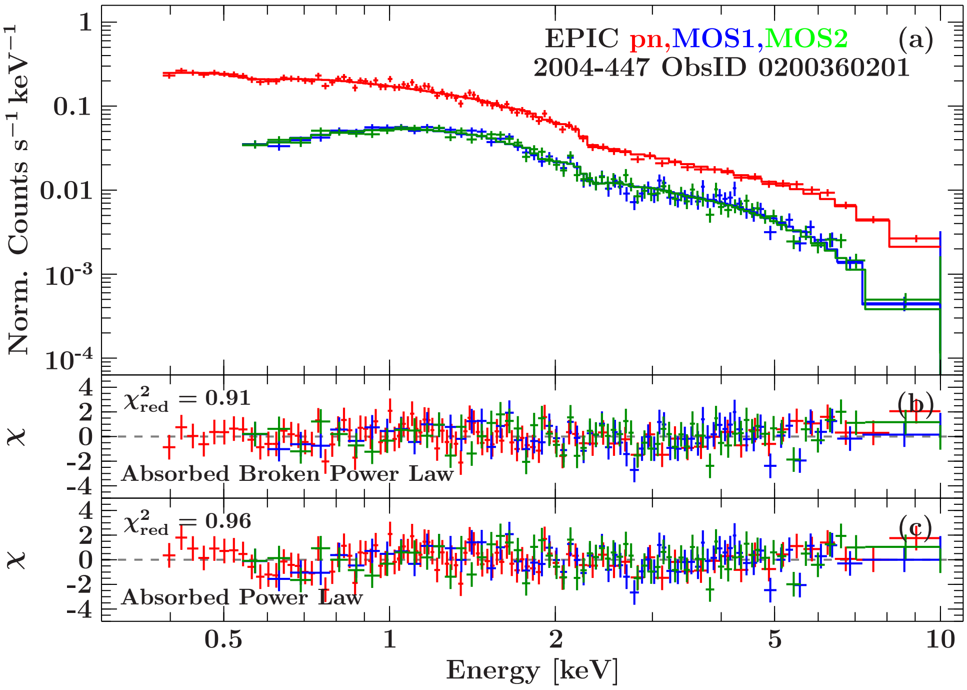

Figure 5.15: *(a)* EPIC pn, MOS1 and MOS2 spectra of 2004−447 and best fit model. *(b)* Best fit residuals for an absorbed broken power law. *(c)* Comparison with an absorbed power law. The pn data are shown in red, the MOS1 data in blue and the MOS2 data in green. The residuals are shown in the same colors.

fluxes to a SED (Fig. 5.16). This procedure was done for the following sources, too.

It is clearly seen, that there is a dip between the optical and the X-ray fluxes which indicates the double hump form that is often seen in radio-loud AGN and blazars. Gallo et al. (2006) explained the SED by synchrotron plus synchrotron self-Compton (SSC)

Table 5.6: Optical observed and dereddened fluxes for PKS 2004−447.

Filter	Flux density $[10^{-16}\,\mathrm{erg\,cm^{-2}\,s^{-1}\,\AA^{-1}}]$	Flux $[10^{-13}\,\mathrm{erg\,cm^{-2}\,s^{-1}}]$	Dereddened flux $[10^{-13}\,\mathrm{erg\,cm^{-2}\,s^{-1}}]$
UVW2	NULL	NULL	NULL
UVM2	1.1±0.3	2.5±0.6	3.9±0.9
UVW1	1.087±0.097	3.2±0.3	4.3±0.4
U	1.45±0.09	5.0±0.3	6.5±0.3
B	1.68±0.06	7.6±0.3	9.3±0.3

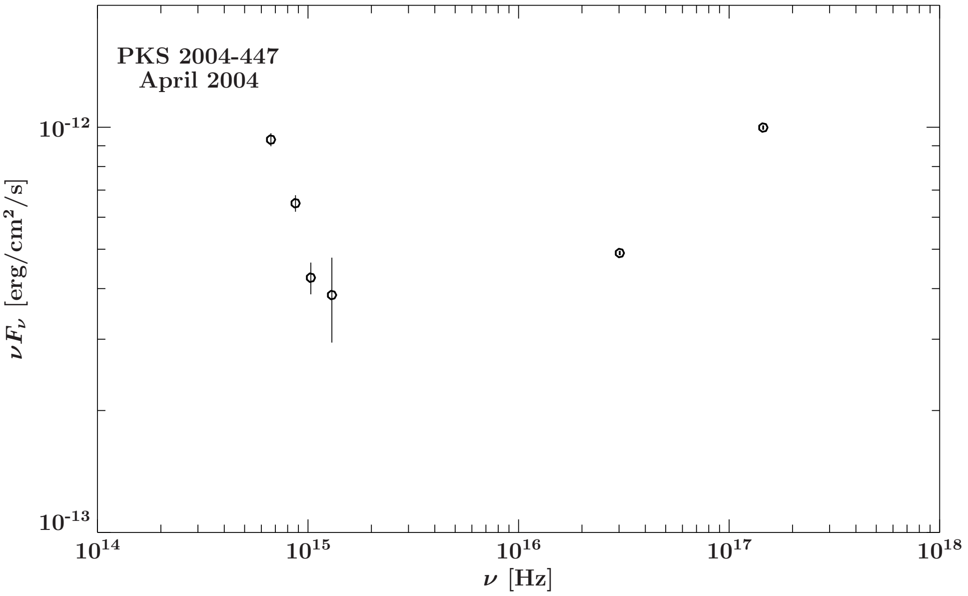

Figure 5.16: SED for 2004−447 from 2004.

processes. The errorbars for the optical and X-ray fluxes are sometimes really small and therefore difficult to see.

Table 5.7: Best fit parameters for PKS 2005−489 for an absorbed broken power law.

ObsID	0205920401	0304080301	0304080401
$N_{\rm H}$ [10^{20}cm^{-2}]	3.930	3.930	3.930
A_Γ [10^{-3} keV^{-1} cm^{-2} s^{-1}]	$3.22^{+0.14}_{-0.45}$	$22.7^{+0.04}_{-0.06}$	$4.45^{+0.16}_{-0.29}$
Γ	$3.17^{+0.25}_{-0.10}$	$2.49^{+0.06}_{-0.04}$	$2.60^{+0.12}_{-0.07}$
$E_{\rm break}$ [keV]	$0.84^{+0.36}_{-0.23}$	0.81 ± 0.07	0.75 ± 0.08
Γ_2	$2.99^{+0.05}_{-0.06}$	2.312 ± 0.009	$2.3238946598^{+0.0100248167}_{-0.0000000004}$
$F_{0.2-2\,{\rm keV}}$ [10^{-12} erg cm^{-2} s^{-1}]	7.63 ± 0.09	42.64 ± 0.14	15.10 ± 0.06
$F^{\rm unabs}_{0.2-2\,{\rm keV}}$ [10^{-12} erg cm^{-2} s^{-1}]	14.27 ± 0.16	79.29 ± 0.24	16.34 ± 0.06
$F_{2-10\,{\rm keV}}$ [10^{-12} erg cm^{-2} s^{-1}]	1.547 ± 0.018	26.42 ± 0.09	8.64 ± 0.04
$F^{\rm unabs}_{2-10\,{\rm keV}}$ [10^{-12} erg cm^{-2} s^{-1}]	2.159 ± 0.024	38.29 ± 0.12	7.694 ± 0.027
χ^2/dof	207.0/230.0	403.7/329.0	381.4/303.0
$\chi^2_{\rm red}$	0.90	1.23	1.26

5.2.2 PKS 2005-489

The optical variable BL Lac object PKS 2005−489 (position (equinox 2000.0): $20^{\rm h}09^{\rm m}25^{\rm s}.4$, -48°49′54″) is one of the brightest objects of this class in the Southern Hemisphere with a maximum visible magnitude of ~ 13 mag. It was discovered in the Parkes 2.7 GHz survey as a strong radio source (Wall, 1975) and some years later identified as a BL Lac (Wall et al., 1986). Its redshift was determined to $z = 0.071$ (Falomo et al., 1987). The galactic hydrogen absorption column from the LAB is 3.93×10^{20} cm^{-2}.

This source was three times observed by *XMM-Newton*. The first observation was on October 4, 2004 (revolution 0883, ObsID 0205920401, duration 14 ks). The EPIC pn data were taken in timing mode, the MOS1 data in timing uncompressed mode and in small window mode for the MOS2. For all three cameras the thin filter was used. The optical data were in OM science user defined mode for the V, U, B, UVW1 and UVM2 filters. The last two observations were on September 26 and 28, 2005 (revolutions 1062 and 1063, ObsIDs 0304080301 and 0304080401, durations 22.4 ks and 29 ks). The same modes were used for both observations: timing for the pn, small window for MOS1, large window for MOS2 (all with the thin filter) and OM science user defined for the V, U, B, UVW1 and UVM2 filters on September 26 and in addition to them also the UVW2 filter on September 28.

The same course for the analysis was done as before using a power law and a broken power law for each case but without fitting a simple power law. For the 2004 data the MOS1 spectrum was excluded, because data in timing mode were noisier than for the other modes. Consistently the MOS1 spectra were also excluded for the other observations. The pn spectra were binned to a single-to-noise of 4 and grouped by a factor of 3 up to 10 keV. For the MOS2 spectra the signal-to-noise was set to 3 and the grouping-factor to 2. The energy ranges were set to 0.5–10 keV for the pn and to 0.55–10 keV for the MOS2. Because of high background rates a period of ∼30 minutes at the end of ObsID 0304080401 was excluded (see Acero, 2009).

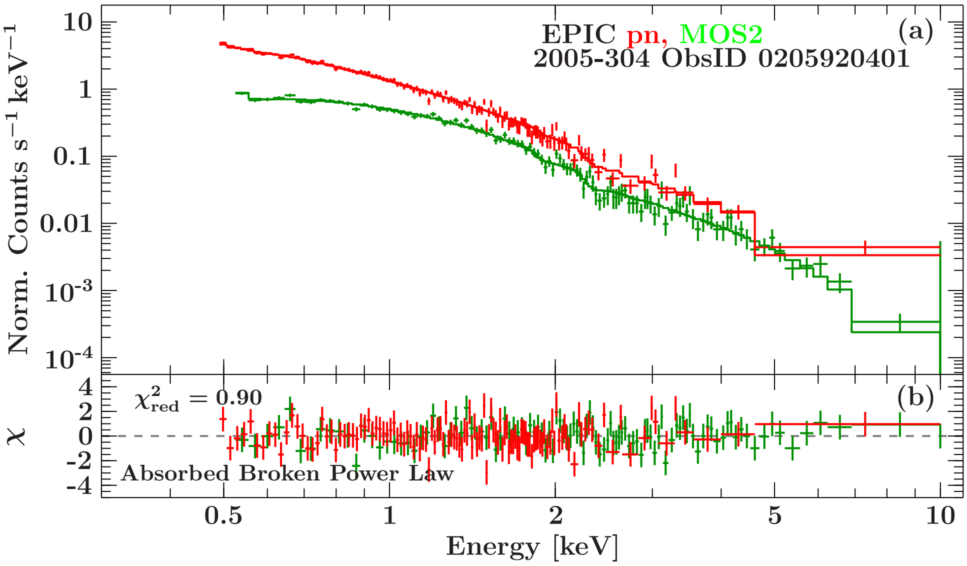

Figure 5.17: *(a)* EPIC pn and MOS2 spectra for PKS 2005−489, ObsID 0205920401. *(b)* Residuals for the best fit. The pn data are shown in red and the MOS2 data in green. The residuals are shown in the same colors.

For each observation a broken power law showed a better fit than a simple power law. Leaving the absorption as a free parameter gives good fits but lead to strange values for the second photon index ($\Gamma_2 = -1.96^{+10.97}_{-0.04}$ for ObsID 0205920401). Therefore an absorbed broken power law with frozen absorption gives the best fit (Fig. 5.17). The values obtained from this fit are shown in Table 5.7. For ObsID 0304080401 the lower limit for the second photon index is very small and because of that more valid digits had to be specified.

The values for the optical fluxes are listed in Table 5.8. One can see, that the source became brighter in 2005. The spectral energy distribution for the three observations are shown in Fig. 5.18. The source shows more variability in the X-rays than in the optical.

Table 5.8: Optical observed and dereddened fluxes for PKS 2005−489.

ObsID/ Filter	Flux density $[10^{-14}\,\mathrm{erg\,cm^{-2}\,s^{-1}\,\AA^{-1}}]$	Flux $[10^{-11}\,\mathrm{erg\,cm^{-2}\,s^{-1}}]$	Derredened flux $[10^{-11}\,\mathrm{erg\,cm^{-2}\,s^{-1}}]$
0205920401			
UVW2	—	—	—
UVM2	1.987±0.004	4.590±0.009	8.026±0.018
UVW1	1.6170±0.0015	4.705±0.004	6.844±0.007
U	1.4336±0.0012	4.932±0.004	6.815±0.006
B	1.1041±0.0012	4.968±0.005	6.436±0.007
V	1.0019±0.0020	5.440±0.011	6.654±0.014
0304080301			
UVW2	—	—	—
UVM2	2.726±0.004	6.297±0.009	10.013±0.015
UVW1	2.1472±0.0010	6.248±0.003	9.087±0.005
U	1.8708±0.0009	6.436±0.003	8.894±0.005
B	1.3754±0.0008	6.189±0.004	8.017±0.005
V	1.2254±0.0013	6.654±0.007	8.138±0.009
0304080401			
UVW2	2.79±0.03	5.91±0.06	10.93±0.13
UVM2	2.714±0.004	6.269±0.009	10.963±0.014
UVW1	2.1335±0.0010	6.209±0.003	9.029±0.004
U	1.8697±0.0008	6.432±0.003	8.888±0.004
B	1.3809±0.0007	6.214±0.003	8.050±0.004
V	1.2160±0.0012	6.603±0.007	8.076±0.008

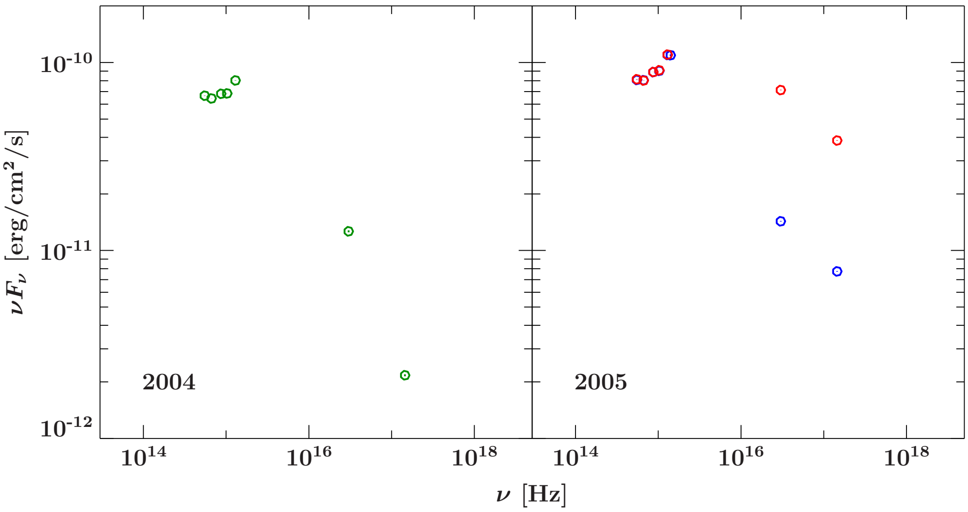

Figure 5.18: SED for 2005−489 from 2004 and 2005. ObsID 0205920401 is shown in green, 0304080301 in red and 0304080401 in blue.

5.2.3 Pictor A

The source Pictor A (ESO 252-GA018) is a FR-II type and LINER-galaxy (position (equinox 2000.0): $05^{\mathrm{h}}19^{\mathrm{m}}49^{\mathrm{s}}.7$, $-45°46'44''$). Its redshift was calculated to $z = 0.03498$ (Eracleous & Halpern, 2004). The galactic hydrogen absorption column is $3.12 \times 10^{20}\,\mathrm{cm}^{-2}$.

Pictor A was monitored four times by *XMM-Newton*. The first observation on January 19, 2001 (revolution 0204, ObsID 0090050201, scheduled duration 17.2 ks) could not be performed due to ERS-2[15] contingency. It was rescheduled on March 17, 2001. Thereby two observations were taken. The first one was for calibration of the EPIC cameras (revolution 0223, ObsID 0090050801, duration 8.8 ks). PN and MOS were in full frame mode with calibration closed filters therefore no spectra from the source could be extracted for this instruments. The OM was observing with the UVW1 filter in image mode. Immediately followed a 20.1 ks duration (revolution 0223, ObsID 090050701) where the MOS cameras were in small window free running mode and pn in full frame mode (all with the thin filter). The optical data were extended by the UVM2 and UVW2 filters. The last observation of Pictor A with *XMM-Newton* was on January 14, 2005 (revolution 0934, ObsID 0206390101, duration 54.8 ks). The EPIC data were filtered with the thin filter for the full frame (MOS1, pn) and large window (MOS2) modes. Optical data were taken in full low mode for U, B, UVW1, UVM2 and UVW2 filters.

The analysis procedure was the same as for PKS 2005−489. Again the absorbed broken power law with free absorption fits the data better than the equivalent model with a single power law ($\Delta\chi^2_{\mathrm{max}} = 26.3$ for ObsID 0206390101; see Fig. 5.19). The best fit parameters for this case are shown in Table 5.9. Burlon et al. (2011) analyzed the source with *Swift*-BAT. They used an absorbed power law and get a value for the photon index of $\Gamma = 1.90^{+0.17}_{-0.17}$.

The optical fluxes are shown in Table 5.10. The values from 2005 are much higher than for 2001. Fig. 5.20 shows the SED for this two cases. The dip between the synchrotron and the Compton hump can be guessed between the optical and the X-ray data points.

---

[15] ERS-2 (April 21, 2001 - July 5, 2011) was one of two European Remote Sensing Satellites of the ESA to observe the Earth.

Table 5.9: Best fit parameters for the EPIC pn spectra of Pictor A for an absorbed broken power law and an absorbed power law.

Broken Power law		
ObsID	0090050701	0206390101
$N_{\rm H}$ $[10^{20}{\rm cm}^{-2}]$	$3.8^{+0.7}_{-0.4}$	4.8 ± 0.5
A_Γ $[10^{-3}\,{\rm keV}^{-1}\,{\rm cm}^{-2}\,{\rm s}^{-1}]$	$1.743^{+0.034}_{-0.030}$	3.00 ± 0.04
Γ	$1.73^{+0.04}_{-1.87}$	$1.809^{+0.020}_{-0.019}$
$E_{\rm break}$ [keV]	$4.0^{+1.0}_{-1.9}$	$2.71^{+0.29}_{-0.32}$
Γ_2	$1.6062^{+0.0019}_{-0.0957}$	1.701 ± 0.025
$F_{0.2-2\,{\rm keV}}$ $[10^{-12}\,{\rm erg\,cm}^{-2}\,{\rm s}^{-1}]$	4.399 ± 0.026	6.796 ± 0.025
$F^{\rm unabs}_{0.2-2\,{\rm keV}}$ $[10^{-12}\,{\rm erg\,cm}^{-2}\,{\rm s}^{-1}]$	5.097 ± 0.030	8.69 ± 0.04
$F_{2-10\,{\rm keV}}$ $[10^{-12}\,{\rm erg\,cm}^{-2}\,{\rm s}^{-1}]$	7.21 ± 0.05	10.60 ± 0.04
$F^{\rm unabs}_{0.2-2\,{\rm keV}}$ $[10^{-12}\,{\rm erg\,cm}^{-2}\,{\rm s}^{-1}]$	7.01 ± 0.05	10.98 ± 0.04
χ^2/dof	435.9/423.0	647.8/561.0
$\chi^2_{\rm red}$	1.03	1.15
Power law		
ObsID	0090050701	0206390101
$N_{\rm H}$ $[10^{20}\,{\rm cm}^{-2}]$	3.4 ± 0.5	$3.95^{+0.31}_{-0.30}$
$A_{\rm pow}$ $[10^{-3}\,{\rm keV}^{-1}\,{\rm cm}^{-2}\,{\rm s}^{-1}]$	1.723 ± 0.027	2.94 ± 0.03
Γ	1.710 ± 0.016	1.763 ± 0.010
$F_{0.2-2\,{\rm keV}}$ $[10^{-12}\,{\rm erg\,cm}^{-2}\,{\rm s}^{-1}]$	4.414 ± 0.026	6.832 ± 0.025
$F^{\rm unabs}_{0.2-2\,{\rm keV}}$ $[10^{-12}\,{\rm erg\,cm}^{-2}\,{\rm s}^{-1}]$	5.018 ± 0.030	8.43 ± 0.04
$F_{2-10\,{\rm keV}}$ $[10^{-12}\,{\rm erg\,cm}^{-2}\,{\rm s}^{-1}]$	7.10 ± 0.05	10.45 ± 0.04
$F^{\rm unabs}_{0.2-2\,{\rm keV}}$ $[10^{-12}\,{\rm erg\,cm}^{-2}\,{\rm s}^{-1}]$	6.90 ± 0.04	10.82 ± 0.04
χ^2/dof	442.8/425.0	674.1/563.0
$\chi^2_{\rm red}$	1.04	1.20

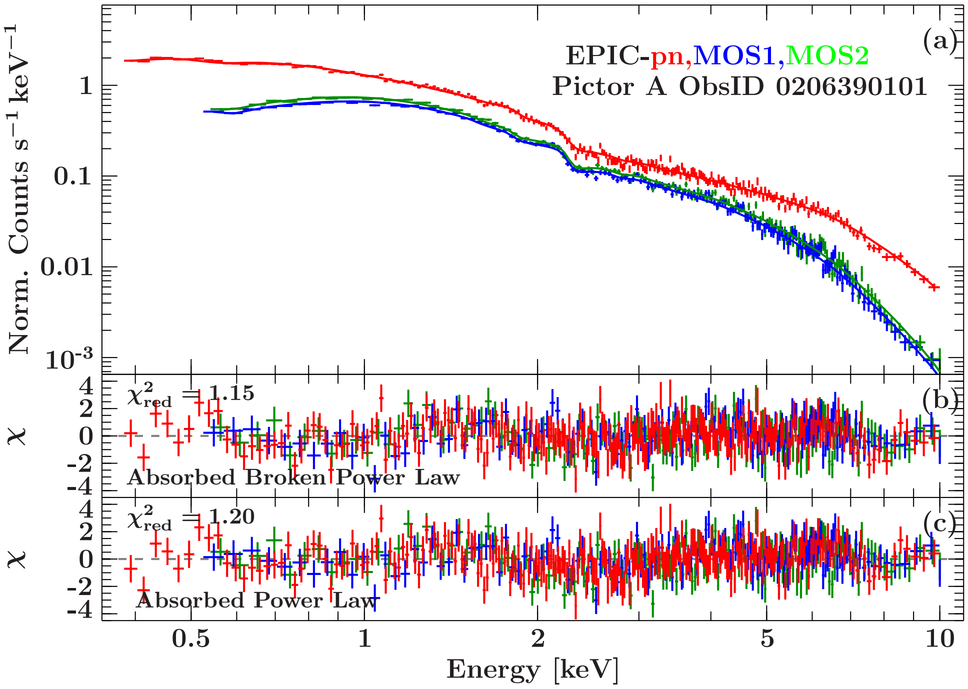

Figure 5.19: *(a)* EPIC pn, MOS1 and MOS2 spectra for Pictor A, ObsID 0206390101. *(b)* Residuals for the best fit model, an absorbed broken power law. *(c)* Residuals for an absorbed power law. The pn data are shown in red, the MOS1 data in blue and the MOS2 data in red. The residuals are shown in the same colors.

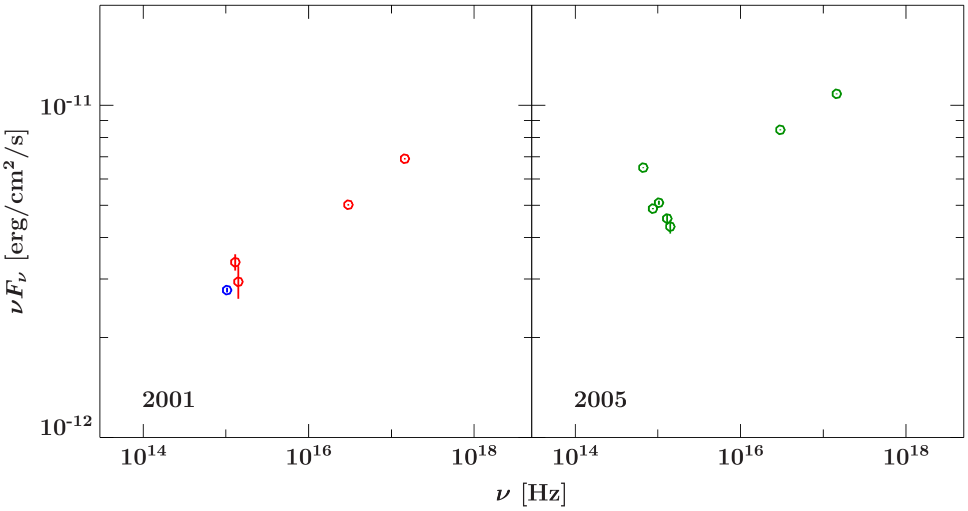

Figure 5.20: SED for Pictor A for 2001 and 2005. ObsID 0090050801 is shown in blue, 0090050701 in red and 0206390101 in green.

Table 5.10: Optical observed and dereddened fluxes for Pictor A.

Filter	Flux density $[10^{-16}\,\mathrm{erg\,cm^{-2}\,s^{-1}\,\AA^{-1}}]$	Flux $[10^{-13}\,\mathrm{erg\,cm^{-2}\,s^{-1}}]$	Dereddened flux $[10^{-13}\,\mathrm{erg\,cm^{-2}\,s^{-1}}]$
0090050701			
UVW2	8.51±0.95	18.0±2.0	29.4±3.
UVM2	9.3±0.5	21.5±1.2	33.7±1.93
UVW1	—	—	—
U	—	—	—
B	—	—	—
V	—	—	—
0090050801			
UVW2	—	—	—
UVM2	—	—	—
UVW1	7.09±0.11	20.6±0.3	27.8±0.4
U	—	—	—
B	—	—	—
V	—	—	—
0206390101			
UVW2	12.5±0.6	26.5±1.3	43.1±2.0
UVM2	12.7±0.4	29.3±0.9	45.6±1.6
UVW1	12.99±0.18	37.8±0.5	50.9±0.8
U	10.98±0.05	37.77±0.18	48.85±0.22
B	11.74±0.04	52.83±0.18	64.88±0.21
V	—	—	—

5.2.4 PKS 2155-304

The object PKS 2155−304 was discovered in 1978 as a X-ray source and identified with an optical object of $B_{\mathrm{mag}} \sim 14$ (Griffiths et al. 1978; position (equinox 2000.0): $21^{\mathrm{h}}58^{\mathrm{m}}52^{\mathrm{s}}.0$, $-30°13'32''$). It has strong variations in the optical and X-ray flux on timescales of a month (Griffiths et al., 1978). The 300 mJy radio source PKS 2155−304 was corresponded to the X-ray source (Shimmins & Bolton, 1974). On account of its physically behavior (optical properties, association with radio source) the source was classified as a high-energy peaked BL Lac object (HBL) with a flat radio spectrum, a steepening through the infrared-optical, and an elliptical galaxy (Griffiths et al., 1978). Its redshift was calculated to $z = 0.117$ (Brodie et al., 1983). The value for the galactic hydrogen absorption column is $1.48 \times 10^{20}\,\mathrm{cm}^{-2}$.

This source was the most observed of the TANAMI sample with *XMM-Newton*. There are 22 observations between 2000 and 2011. The OM was used in 2000 only with one filter per observation (UVW2: ObsID 0080940101, 0080940301, 0080940401, 0124930201; UVW1: 0124930101). Since 2001, all filters are typically used. For the spectral analysis it showed that using the pn spectra alone gives better fits than fitting the data of all EPIC instruments simultaneously. This behavior is due to different filter selections (thin, medium, thick filter) or modes (timing vs. image). Because of that, the analysis is limited to the EPIC pn spectra. For ObsID 0124930501 three different filter were used and analyzed here: medium filter (exposure ID 005), thin filter (008) and thick filter (009). Again, six different models were used.

For the case with frozen absorption the fits are not very good with a χ^2_{red} up to 8. This cases were therefore excluded. Fig. 5.21 shows the spectral parameters of all observations for the EPIC pn for the remaining four models. The `ISIS` notation for the models is: *(i)* `tbnew(`N_{H}`)`×`tbnew`×`bknpower`, *(ii)* `tbnew`×`bknpower`, *(iii)* `tbnew(`N_{H}`)`×`tbnew`×`powerlaw` and *(iv)* `tbnew`×`powerlaw`. The variability of the source can be seen in the changes of the unabsorbed 0.2–2 keV fluxes. At the end of 2001 there was a big outburst. One can see that with a broken power law one gets better χ^2_{red} than with a single power law. Between the two broken power law the χ^2_{red} shows no big differences. One exception is ObsID 0158960101 with the model of a broken power law with two absorptions. The value for the first photon index goes up 9. A reason for that could be, that the fit did not converge and therefore no correct values could be calculated, although the χ^2_{red} is 0.95. In Table 5.11 the values for the broken power law with a free absorption (case *ii*) are listed. Table 5.12 contains the absorbed and unabsorbed fluxes for the same model.

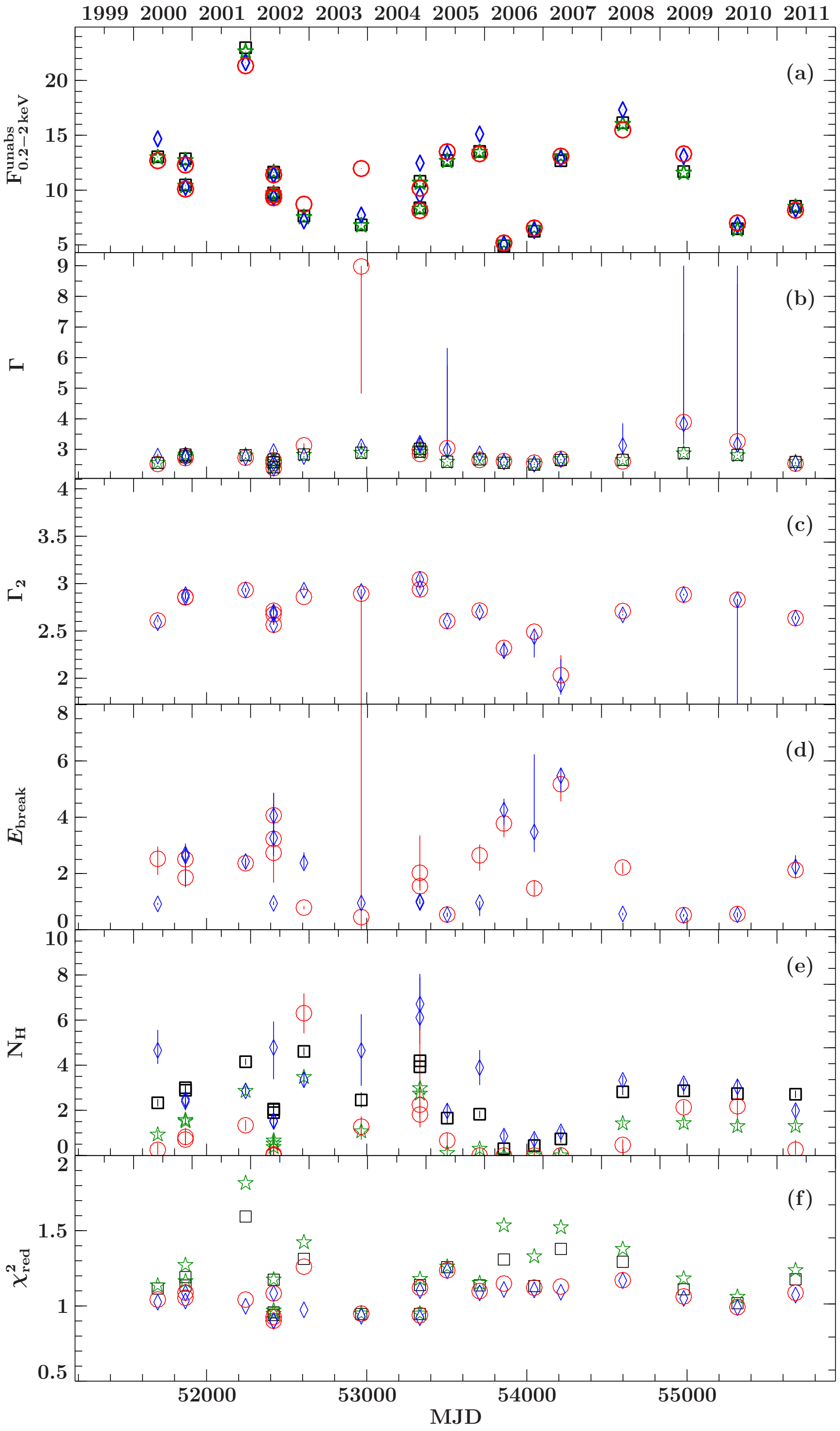

Figure 5.21: Spectral parameters for 2155−304. Showed are four different models: *red circle* broken power law with gal. N_{H} and additional intrinsic absorption; *blue diamond* broken power law with free absorption; *green star* power law with gal. N_{H} and additional intrinsic absorption; *black square* power law with free absorption. The following parameters are shown: *(a)* Unabsorbed 0.2–2 keV flux $F^{\mathrm{unabs}}_{0.2-2\,\mathrm{keV}}$, *(b)* photon index Γ, *(c)* second photon index Γ_2, *(d)* break energy E_{break}, *(e)* hydrogen column density N_{H}, *(f)* goodness of the fit χ^2_{red}. All units and the parameter values for an absorbed broken power law are listed in Table 5.11.

Table 5.11: Best fit parameters for the EPIC pn spectra of PKS 2155−304. The model in `ISIS` notation is: `tbnew` × `bknpower`.

ObsID	N_{H}^{a}	A_{Γ}^{b}	Γ	Γ_2	E_{break}^{c}	χ^2/dof	χ^2_{red}
0080940101	$2.39^{+0.17}_{-0.38}$	$3.324^{+0.015}_{-0.032}$	$2.737^{+0.008}_{-0.020}$	$2.857^{+0.032}_{-0.028}$	$2.70^{+0.29}_{-0.39}$	365.5/354.0	1.03
0080940301	$2.49^{+0.24}_{-0.49}$	$2.649^{+0.017}_{-0.028}$	$2.807^{+0.013}_{-0.033}$	$2.883^{+0.029}_{-0.040}$	$2.6^{+0.5}_{-1.0}$	367.1/338.0	0.95
0124930201	$4.7^{+1.0}_{-0.7}$	$3.94^{+0.05}_{-0.04}$	$2.78^{+0.08}_{-0.06}$	$2.5863910277^{+0.0000000009}_{-0.0000000006}$	0.92 ± 0.04	386.5/377.0	1.03
0124930301	$2.86^{+0.20}_{-0.22}$	5.85 ± 0.04	$2.742^{+0.010}_{-0.012}$	$2.934^{+0.019}_{-0.020}$	$2.43^{+0.12}_{-0.17}$	377.0/378.0	1.00
0124930501 (005)	$4.8^{+1.2}_{-1.5}$	$2.75^{+0.05}_{-0.06}$	$2.93^{+0.10}_{-0.13}$	$2.7003510584^{+0.0000000015}_{-0.0000000010}$	0.94 ± 0.07	271.1/302.0	0.90
0124930501 (008)	1.5 ± 0.4	$2.692^{+0.028}_{-0.024}$	$2.553^{+0.019}_{-0.016}$	$2.6751^{+0.1013}_{-0.0009}$	$3.3^{+1.2}_{-0.7}$	283.0/314.0	0.90
0124930501 (009)	1.5 ± 0.4	3.586 ± 0.030	2.389 ± 0.013	$2.56448^{+0.08814}_{-0.00008}$	$4.1^{+0.9}_{-0.8}$	387.9/358.0	1.08
0124930601	$3.35^{+0.35}_{-0.29}$	$1.946^{+0.017}_{-0.014}$	$2.766^{+0.019}_{-0.016}$	$2.929752^{+0.040543}_{-0.000011}$	$2.37^{+0.38}_{-0.21}$	351.5/361.0	0.97
0158960101	$4.6^{+1.7}_{-1.6}$	1.77 ± 0.04	$3.09^{+0.14}_{-0.10}$	$2.917^{+0.023}_{-0.022}$	$0.95^{+0.08}_{-0.09}$	238.3/256.0	0.93
0158960901	$6.1^{+2.0}_{-1.2}$	$2.07^{+0.06}_{-0.04}$	$3.20^{+0.16}_{-0.10}$	$3.0419293469^{+0.0000000016}_{-0.0113026761}$	$1.01^{+0.10}_{-0.08}$	234.9/255.0	0.92
0158961001	6.7 ± 1.2	2.77 ± 0.05	3.14 ± 0.10	$2.95005^{+0.00020}_{-0.00133}$	0.96 ± 0.06	334.9/304.0	1.10
0158961101	$1.97^{+0.31}_{-0.30}$	$2.9^{+0.6}_{-2.7}$	$2.99^{+3.33}_{-0.28}$	$2.6031536349^{+0.0099857965}_{-0.0000000012}$	0.54 ± 0.08	390.9/317.0	1.23
0158961301	3.9 ± 0.8	$3.80^{+0.05}_{-2.34}$	2.86 ± 0.07	$2.6960089469^{+0.0103501699}_{-0.0000000008}$	$0.96^{+0.06}_{-0.48}$	406.3/374.0	1.09
0158961401	$0.86^{+0.27}_{-0.25}$	1.451 ± 0.010	$2.593^{+0.013}_{-0.012}$	2.29 ± 0.09	$4.3^{+0.5}_{-0.6}$	384.8/347.0	1.11
0411780101	$0.72^{+0.26}_{-0.25}$	$1.883^{+0.014}_{-0.016}$	$2.516^{+0.013}_{-0.016}$	$2.44^{+0.04}_{-0.22}$	$3.5^{+2.8}_{-0.8}$	404.9/366.0	1.11
0411780201	$1.05^{+0.24}_{-0.22}$	$3.676^{+0.024}_{-0.023}$	2.672 ± 0.010	$1.93^{+0.27}_{-0.10}$	$5.47^{+0.27}_{-0.60}$	372.1/341.0	1.09
0411780301	$3.33^{+0.23}_{-0.22}$	$3.6^{+0.6}_{-1.5}$	$3.12^{+0.73}_{-0.22}$	2.670 ± 0.007	0.56 ± 0.05	460.2/394.0	1.17
0411780401	$3.18^{+0.24}_{-0.23}$	$1.6^{+1.0}_{-1.6}$	$3.8^{+5.2}_{-0.7}$	2.884 ± 0.009	0.51 ± 0.06	345.5/329.0	1.05
0411780501	3.0 ± 0.4	$1.35^{+0.25}_{-0.68}$	$3.16^{+5.84}_{-0.16}$	$2.826^{+0.011}_{-1.210}$	$0.53^{+0.09}_{-0.10}$	301.4/305.0	0.99
0411780601	$1.99^{+0.27}_{-0.26}$	$2.467^{+0.017}_{-0.016}$	2.551 ± 0.014	$2.636^{+0.020}_{-0.016}$	$2.24^{+0.42}_{-0.29}$	410.6/383.0	1.08

[a] In units of $10^{20}\mathrm{cm}^{-2}$. [b] In units of $10^{-2}\,\mathrm{keV}^{-1}\,\mathrm{cm}^{-2}\,\mathrm{s}^{-1}$. [c] In units of keV.

Table 5.12: Absorbed and unabsorbed X-ray fluxes for PKS 2155−304 for the model presented in Table 5.11.

ObsID	$F_{0.2-2\,\mathrm{keV}}$ $[10^{-12}\,\mathrm{erg\,cm^{-2}\,s^{-1}}]$	$F^{\mathrm{unabs}}_{0.2-2\,\mathrm{keV}}$ $[10^{-12}\,\mathrm{erg\,cm^{-2}\,s^{-1}}]$	$F_{2-10\,\mathrm{keV}}$ $[10^{-12}\,\mathrm{erg\,cm^{-2}\,s^{-1}}]$	$F^{\mathrm{unabs}}_{2-10\,\mathrm{keV}}$ $[10^{-12}\,\mathrm{erg\,cm^{-2}\,s^{-1}}]$
0080940101	106.75 ± 0.19	124.85 ± 0.22	28.58 ± 0.05	28.64 ± 0.05
0080940301	86.80 ± 0.15	102.61 ± 0.18	21.05 ± 0.04	21.10 ± 0.04
0124930201	112.68 ± 0.19	146.72 ± 0.25	44.15 ± 0.08	44.32 ± 0.08
0124930301	180.87 ± 0.26	216.3 ± 0.4	47.90 ± 0.07	48.04 ± 0.07
0124930501 (005)	83.76 ± 0.23	114.0 ± 0.4	26.37 ± 0.07	26.48 ± 0.07
0124930501 (008)	84.86 ± 0.23	93.25 ± 0.25	30.06 ± 0.08	30.10 ± 0.08
0124930501 (009)	105.13 ± 0.28	113.84 ± 0.30	50.43 ± 0.14	50.49 ± 0.14
0124930601	58.64 ± 0.10	72.03 ± 0.13	15.578 ± 0.028	15.628 ± 0.028
0158960101	56.53 ± 0.19	77.30 ± 0.26	12.60 ± 0.05	12.66 ± 0.05
0158960901	63.01 ± 0.20	94.88 ± 0.29	12.42 ± 0.04	12.49 ± 0.04
0158961001	80.33 ± 0.20	124.62 ± 0.30	18.86 ± 0.05	18.99 ± 0.05
0158961101	117.73 ± 0.27	133.9 ± 0.4	39.22 ± 0.09	39.28 ± 0.09
0158961301	117.65 ± 0.19	151.13 ± 0.24	36.29 ± 0.06	36.42 ± 0.06
0158961401	47.90 ± 0.10	50.52 ± 0.12	16.75 ± 0.04	16.77 ± 0.04
0411780101	60.69 ± 0.13	63.32 ± 0.14	23.44 ± 0.05	23.46 ± 0.05
0411780201	120.81 ± 0.20	128.65 ± 0.22	38.38 ± 0.07	38.41 ± 0.07
0411780301	141.59 ± 0.20	173.25 ± 0.26	46.12 ± 0.07	46.26 ± 0.07
0411780401	104.10 ± 0.19	130.77 ± 0.23	22.42 ± 0.04	22.49 ± 0.04
0411780501	55.17 ± 0.12	68.26 ± 0.14	13.361 ± 0.027	13.399 ± 0.027
0411780601	73.92 ± 0.13	82.61 ± 0.14	27.26 ± 0.05	27.30 ± 0.05

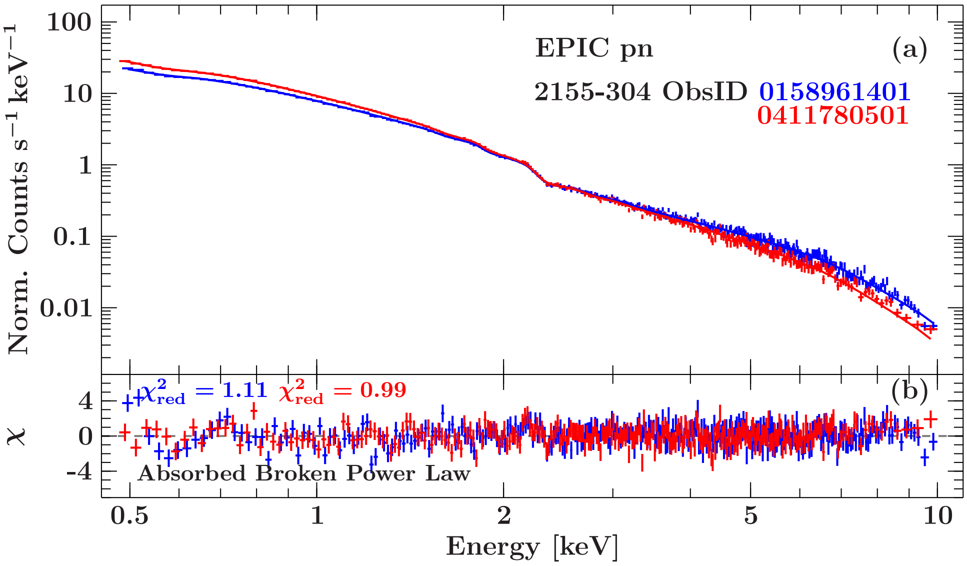

Figure 5.22: *(a)* EPIC pn spectra for PKS 2155−304 for two observations. The lower spectrum of ObsID 0158961401 is shown in red and the upper spectrum of ObsID 0411780501 is shown in blue. *(b)* Residuals for an absorbed broken power law with free absorption. The same colors as for the spectra were used.

Fig. 5.22 shows the spectra of two observations (0158961401, 0411780501) fitted by an absorbed broken power law with free absorption. It can be seen, that the source changes its behavior. For ObsID 0158961401 there are more high-energy counts and less soft-energy counts than for ObsID 0411780501. An analysis of ObsID 0158961401 can be found in Zhang (2008). They used a broken power law as the best model, too, but with fixed $N_{\rm H}$. Nevertheless, I got values similar to the values obtained by Zhang (2008) ($\Gamma = 2.60 \pm 0.01$, $E_{\rm break} = 4.49^{+0.37}_{-0.47}$, $\Gamma_2 = 2.27^{+0.08}_{-0.07}$). The spectra of PKS 2155−304 flattens in the most cases from the soft to hard X-rays with a break energy in the range 3–6 keV. For some observations (ObsID 0124930201, 0124930501 (005), 0158960101, 0158961001, 0158961101, 0158961301, 0411780301, 0411780401 and 0411780501) the break energy lies at ~1 keV and the errors for the second photon index could not be well constrained. Though the fits are good described by the model.

In Table 5.13 the optical fluxes are listed. Fig. 5.23 shows the spectral energy distribution from 2000 to 2011. Here only the synchrotron hump is seen because PKS 2155−304 peaks in the UV.

Table 5.13: Optical flux density, flux and derredend flux for PKS 2155−304. The flux density is obtained from the OM-software.

			Flux density $[10^{-14}\,\mathrm{erg\,cm^{-2}\,keV^{-1}\,\AA^{-1}}]$			
ObsID	V	B	U	UVW1	UVM2	UVW2
0080940101	—	—	—	—	—	7.468±0.003
0080940301	—	—	—	—	—	6.8618±0.0025
0080940401	—	—	—	—	—	7.898±0.008
0124930101	—	—	—	3.5925±0.0003	—	—
0124930201	—	—	—	—	—	5.1559±0.0022
0124930301	2.496±0.005	2.944±0.014	4.391±0.018	5.57±0.03	7.536±0.005	7.927±0.011
0124930501	1.1644±0.0016	1.397±0.008	2.078±0.011	—	—	3.630±0.007
0124930601	1.1778±0.0019	1.4243±0.0011	2.0385±0.0016	2.3474±0.0009	3.262±0.003	3.424±0.006
0158960101	—	—	2.760±0.012	3.3233±0.0011	4.481±0.003	—
0158960901	1.6361±0.0012	1.975±0.008	2.927±0.011	—	—	—
0158961001	—	1.958±0.009	—	3.4254±0.0010	4.525±0.003	4.894±0.005
0158961101	0.6563±0.0013	2.526±0.011	3.692±0.013	4.4177±0.0015	6.073±0.004	6.369±0.009
0158961301	3.251±0.003	3.76±0.03	5.42±0.03	6.685±0.019	9.037±0.005	9.404±0.011
0158961401	2.358±0.003	2.797±0.018	3.902±0.022	4.654±0.012	5.775±0.005	5.914±0.011
0411780101	3.187±0.003	3.62±0.03	5.11±0.03	6.015±0.012	8.112±0.005	8.592±0.011
0411780201	3.717±0.022	4.20±0.05	6.35±0.05	7.236±0.015	9.383±0.005	9.928±0.011
0411780301	2.372±0.003	2.825±0.019	4.13±0.03	5.1578±0.0096	7.125±0.005	7.399±0.011
0411780401	2.753±0.003	3.327±0.022	4.97±0.03	5.778±0.011	7.752±0.005	8.071±0.011
0411780501	1.421±0.003	1.6716±0.0017	2.4200	2.9959±0.0008	4.189±0.005	4.454±0.011
0411780601	1.6825±0.0019	1.971±0.013	2.848±0.017	3.3166±0.011	4.430±0.003	4.770±0.008

			Flux $[10^{-11}\,\mathrm{erg\,cm^{-2}\,keV^{-1}}]$			
ObsID	V	B	U	UVW1	UVM2	UVW2
0080940101	—	—	—	—	—	15.833±0.005
0080940301	—	—	—	—	—	14.547±0.005
0080940401	—	—	—	—	—	16.743±0.017

continued on the next page

Optical fluxes for PKS 2155−304 — continued

ObsID	V	B	U	UVW1	UVM2	UVW2
0124930101	—	—	—	10.4541±0.0009	—	—
0124930201	—	—	—	—	—	10.930±0.005
0124930301	13.554±0.003	13.25±0.06	15.11±0.06	16.21±0.09	17.409±0.011	16.804±0.023
0124930501	6.323±0.009	6.29±0.04	7.15±0.04	—	—	7.695±0.015
0124930601	6.395±0.010	6.409±0.005	7.013±0.005	6.831±0.003	7.535±0.007	7.259±0.012
0158960101	—	—	9.49±0.04	9.671±0.003	10.351±0.007	—
0158960901	8.884±0.006	8.87±0.04	10.07±0.04	—	—	—
0158961001	—	8.81±0.04	—	9.968±0.003	10.452±0.007	10.375±0.010
0158961101	3.564±0.007	11.37±0.05	12.70±0.05	12.856±0.004	14.029±0.009	13.503±0.020
0158961301	17.655±0.016	16.96±0.13	18.64±0.11	19.46±0.06	20.875±0.011	19.938±0.023
0158961401	12.806±0.015	12.59±0.08	13.42±0.08	13.54±0.03	13.341±0.011	12.537±0.023
0411780101	17.307±0.015	16.27±0.14	17.59±0.09	17.51±0.03	18.739±0.011	18.216±0.023
0411780201	20.186±0.012	18.89±0.20	21.85±0.17	21.07±0.04	21.675±0.011	21.047±0.026
0411780301	12.879±0.015	12.71±0.08	14.20±0.09	15.01±0.03	16.458±0.011	15.685±0.024
0411780401	14.950±0.015	14.974±0.099	17.09±0.12	16.82±0.03	17.907±0.011	17.111±0.024
0411780501	7.716±0.015	7.522±0.008	8.3300E+00	8.7179±0.0024	9.676±0.010	9.442±0.023
0411780601	9.136±0.010	8.86±0.06	9.80±0.06	9.651±0.003	10.233±0.008	10.113±0.017

Dereddend flux [$10^{-11}\,\mathrm{erg\,cm^{-2}\,keV^{-1}}$]

ObsID	V	B	U	UVW1	UVM2	UVW2
0080940101	—	—	—	—	—	19.964±0.007
0080940301	—	—	—	—	—	18.342±0.007
0080940401	—	—	—	—	—	21.111±0.022
0124930101	—	—	—	12.0379±0.0011	—	—
0124930201	—	—	—	—	—	13.782±0.006
0124930301	14.62±0.03	14.61±0.07	17.06±0.07	18.6698±0.0099	21.49±0.014	21.19±0.03
0124930501	6.8206±0.0096	6.93±0.04	8.07±0.04	—	—	9.703±0.019

continued on the next page

Optical fluxes for PKS 2155−304 — continued

ObsID	V	B	U	UVW1	UVM2	UVW2
0124930601	6.899±0.011	7.065±0.006	7.921±0.006	7.866±0.003	9.230±0.009	9.153±0.016
0158960101	—	—	10.72±0.05	11.136±0.004	12.776±0.009	—
0158960901	9.584±0.007	9.78±0.04	11.37±0.04	—	—	—
0158961001	—	9.71±0.04	—	11.478±0.003	12.901±0.009	13.082±0.013
0158961101	3.845±0.008	12.53±0.05	14.35±0.05	14.803±0.005	17.32±0.012	17.03±0.03
0158961301	19.045±0.017	18.69±0.14	21.05±0.13	22.40±0.06	25.77±0.014	25.14±0.03
0158961401	13.814±0.016	13.88±0.09	15.16±0.09	15.59±0.04	16.47±0.014	15.81±0.03
0411780101	18.671±0.016	17.93±0.15	19.87±0.10	20.16±0.04	23.13±0.014	22.97±0.03
0411780201	21.78±0.13	20.82±0.22	24.68±0.19	24.25±0.05	26.75±0.014	26.54±0.03
0411780301	13.894±0.016	14.01±0.09	16.04±0.10	17.28±0.03	20.31±0.014	19.78±0.03
0411780401	16.128±0.016	16.51±0.11	19.31±0.14	19.37±0.04	22.10±0.014	21.58±0.03
0411780501	8.323±0.017	8.292±0.008	9.42	10.038±0.003	11.94±0.013	11.91±0.03
0411780601	9.856±0.011	9.78±0.06	11.07±0.07	11.114±0.004	12.631±0.009	12.751±0.021

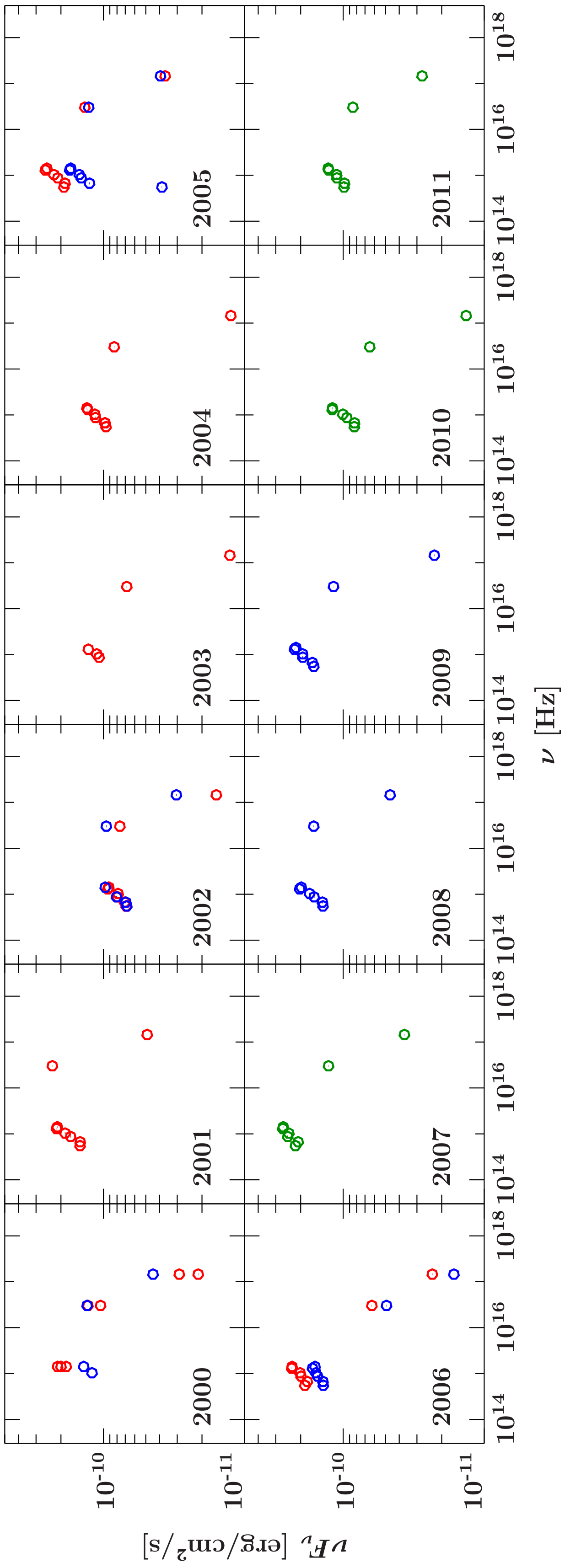

Figure 5.23: SED for 2155−304 from 2000-2011.

5.3 The Swift-satellite

The *Swift* mission is a multiwavelength observatory combining optical, X-ray and gamma-ray instruments (Gehrels et al., 2004). Its aim is to detect gamma-ray bursts (GRBs, Klebesadel et al., 1973), to determine their origin and to study the early universe out to $z > 10$. The NASA satellite was launched on November 20, 2004 into a low Earth orbit of 600 km and an inclination of 22°. Its lifetime was estimated to ∼8 yr due to orbital decay. On board it has three instruments (see Fig. 5.24):

- The *Burst Alert Telescope* (BAT, see Sec. 5.3.1)
- The *UV/Optical Telescope* (UVOT, see Sec. 5.3.2)
- The *X-Ray Telescope* (XRT, see Sec. 5.3.3)

Table 5.14: Overview of the properties of the instruments on board *Swift* (after Gehrels et al., 2004, Table 2, 3 and 4).

Instrument	Energy range/ Wavelength(UVOT)	FOV	Sensitivity
BAT	15–150 keV	1.4 sr (half-coded)	$\sim 10^{-8}$ erg cm^{-2} s^{-1}
XRT	0.2–10 keV	23.6×23.6 arcmin	2×10^{-14} erg cm^{-2} s^{-1} (1 mCrab) in 10^4 s
UVOT	170–600 nm	17×17 arcmin	$B = 24$ in white light in 1000 s

These instruments are explained in the following.

5.3.1 The Burst Alert Telescope (BAT)

The task of *Burst Alert Telescope* is to detect GRBs in an energy-range of 15–150 keV and to localize their positions with an accuracy of 1–4′ within 20 s after the event started. It was expected to detect > 100 GRBs/yr due to its large field of view (FOV, see Table 5.14). On April 13, 2010 the 500th GRB was detected[16]. After detecting a GRB the autonomous spacecraft slews and the other two instruments (XRT and UVOT) are pointing to the direction of the burst to take simultaneous multiwavelength observations. The BAT instrument consists of a coded-aperture composed of ∼ 52000 pieces of lead (5×5×1 mm) and a detector plane composed of 32768 pieces of CdZnTe (4×4×2 mm) (see Fig. 5.25). The details of BAT are described in Barthelmy et al. (2005) and Gehrels et al. (2004).

5.3.2 The UV/Optical Telescope (UVOT)

The design of the *UV/Optical Telescope* (UVOT) is based on the *Optical Monitor* (OM) on board *XMM-Newton* (see Sec. 5.1.4). It is co-aligned with the XRT. Similar to the OM it contains a filter wheel but with 11 positions (an unknown filter is added which occurs when the filter wheel has got lost; the OM contains 10 wheel positions). In Fig. 5.26 a schematic of UVOT can be seen. It consists of a modified Ritchey-Chrétien configuration with a 30 cm primary mirror. For details see Roming et al. (2005) and Gehrels et al. (2004).

---

[16] `http://www.nasa.gov/mission_pages/swift/bursts/500th.html`

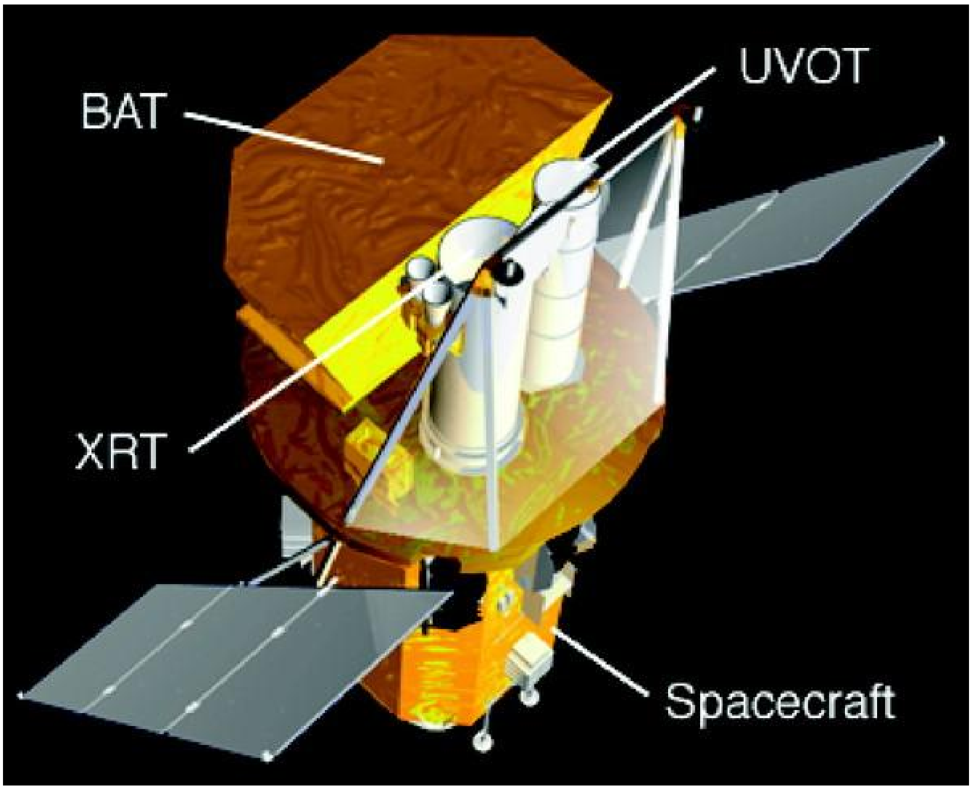

Figure 5.24: Overview of the *Swift* satellite. The three main instruments are seen.

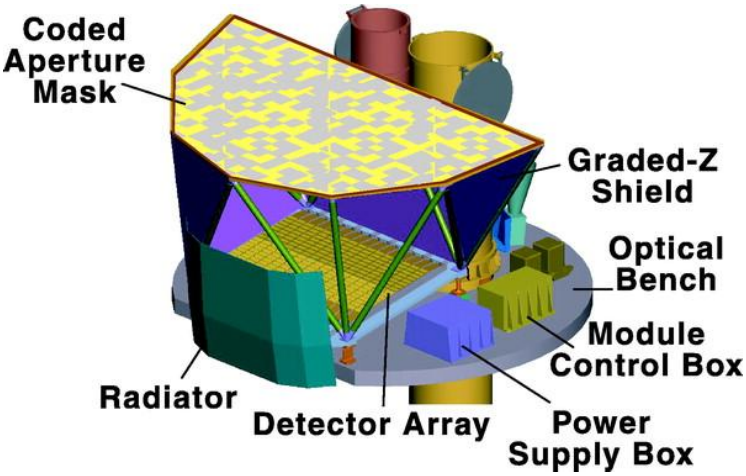

Figure 5.25: Schematic view of the BAT.

5.3.3 The X-Ray Telescope (XRT)

In an energy-range of 0.2–10 keV the *X-Ray Telescope* (XRT) is operating. It can measure fluxes, spectra and lightcurves of GRBs and afterglows over a wide range of more than 7 magnitudes in flux. It uses a grazing incidence Wolter I telescope. The infalling X-rays are focused on a thermoelectrically cooled CCD. A block diagram of the XRT shows the structure of the instrument in Fig. 5.27.

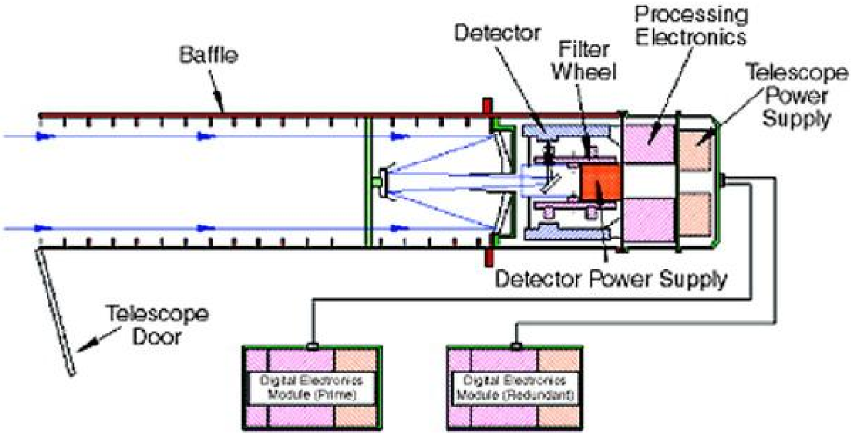

Figure 5.26: Schematic view of the UVOT. The light path is outlined.

The XRT operates in two states: Auto and Manual state. For calibration the Manual state is used and the science modes can be commanded. An automatically selection of the science mode due to the count rate of the source can be done in the Auto state. This state is also the normal operating mode. The different science modes in which the data can be taken are as following (Burrows et al. (2005); see Capalbi et al. (2005) for more details):

- **Image Long and Short** (IM): CCD is operating like an optical CCD; accurate position and good flux estimate for the source; for source fluxes between 25 mCrabs and at least 45 Crabs.
- **Low rate** (LR) and **Piled-up Photodiode** (PU): fast timing mode for extremely bright sources with a time resolution of about 0.14 ms; useful for incident fluxes up to 60 Crabs; pile-up for fluxes below 2 Crabs.
- **Windowed Timing** (WT): 200 column window covering the central 8 arcmin of the FOV; time resolution of 1.8 ms; for fluxes below 5000 mCrabs; minimal pile-up below 1000 mCrabs.
- **Photon Counting** (PC): full imaging and spectroscopic resolution is kept by a time resolution of 2.5 s; this mode is useful for sources with a flux below 1 mCrab.

Only data from the XRT in the PC mode were used for the analysis in this thesis.

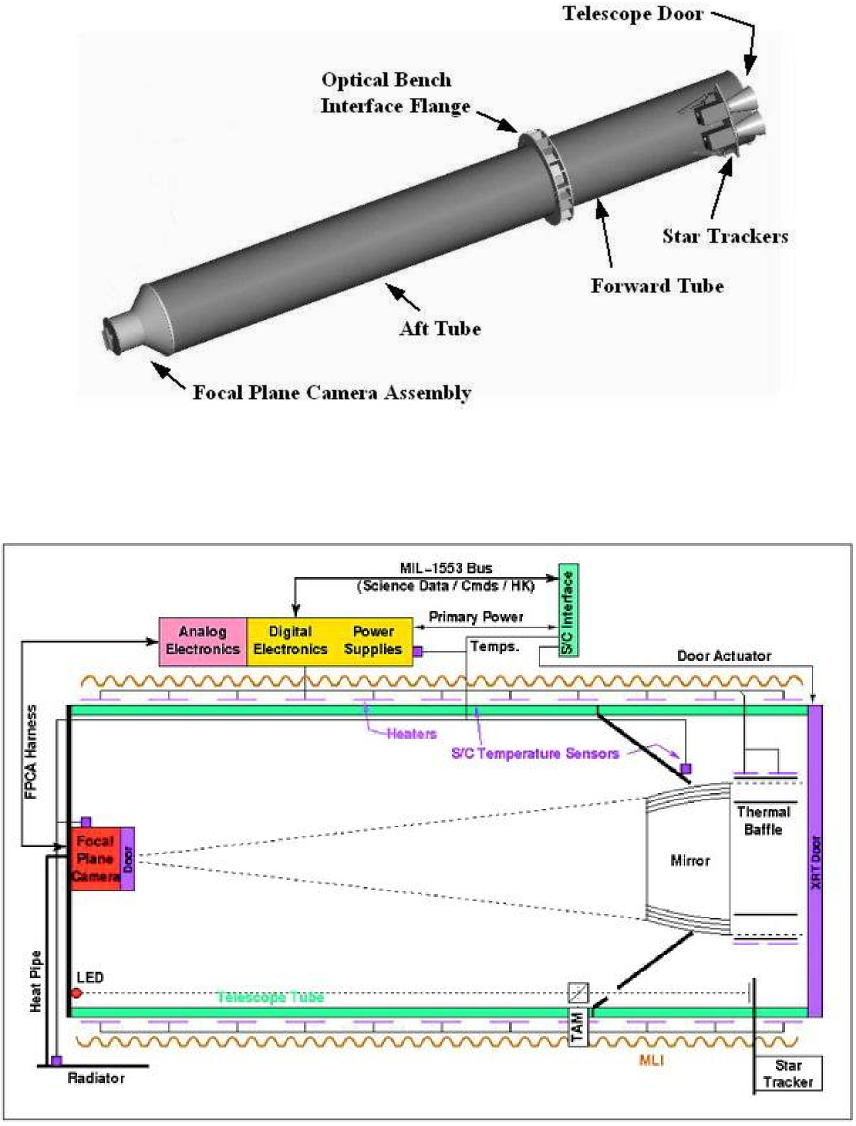

Figure 5.27: Schematic view of the XRT (upper figure). The lower figure shows the light path from the mirrors to the focal plane camera.

5.4 Data analysis

5.4.1 PKS 0208−512

PKS 0208−512 is a radio loud galaxy with a flat spectrum. Its redshift is calculated to $z = 1.003$ (Zhang et al., 2010). It has an optical magnitude in the B-filter of 18.3 mag (NED). The source is known to be a MeV-bright blazar with a variability of eight days (von Montigny et al., 1995).

For this source data taken from Swift/XRT were analyzed. It was observed several times in 2005 and since 2008 every year between September and December. The modes for the observations were window timing (wt) and photon counting (pc). Some of the observations had to be excluded from the analysis due to missing wt and pc data (00035002001, 00035002002, 00035002007 and 00035003008), not enough bins in the spectra (00035002050) and due to short exposure (00035002019). The data taken in wt-mode showed no useful spectra and were therefore excluded from the analysis, too. Only spectra in pc-mode were analyzed. Because of the bad single-to-noise for single observations their spectra were added up to a monthly averaged spectrum where more than one observation was available for the month. In Table A.4 the observations for the averaged spectra are listed with the start date and the XRT-exposure. The spectra were fitted with three different models: a single power law, an absorbed power law and an absorbed power law with the absorption column density N_H freezed to the value of the Leiden/Argentine/Bonn Galactic HI Survey of $1.84 \times 10^{20}\,\mathrm{cm}^{-2}$. The best fit parameters, including the absorbed fluxes, are shown in Table 5.15. The unabsorbed fluxes can be found in the appendix, Table A.5.

Table 5.15: Best fit parameters for PKS 0208−512 for three different models.

Data	N_H^a	A_Γ^b	Γ	$F^c_{0.2-2\,\mathrm{keV}}$	$F^c_{2-10\,\mathrm{keV}}$	χ^2/dof	χ^2_red
05_05							
power law		3.9 ± 0.4	1.60 ± 0.10	1.16 ± 0.09	1.79 ± 0.14	99.1/116.0	0.85
abs. power law (N_H)	1.84	4.2 ± 0.4	1.67 ± 0.10	1.17 ± 0.09	1.80 ± 0.14	97.9/116.0	0.84
abs. power law	$2.1^{+3.9}_{-2.1}$	$4.3^{+0.7}_{-0.6}$	$1.68^{+0.18}_{-0.16}$	1.16 ± 0.09	1.79 ± 0.14	97.9/115.0	0.85
09_08							
power law		3.2 ± 0.6	1.56 ± 0.22	0.95 ± 0.15	1.56 ± 0.24	24.3/30.0	0.81
abs. power law (N_H)	1.84	$3.4^{+0.6}_{-0.7}$	$1.63^{+0.24}_{-0.23}$	0.94 ± 0.15	1.55 ± 0.24	24.1/30.0	0.80
abs. power law	$1.8^{+9.4}_{-1.8}$	$3.4^{+1.3}_{-0.8}$	$1.63^{+0.39}_{-0.28}$	0.95 ± 0.15	1.56 ± 0.24	24.1/29.0	0.83
10_08							
power law		4.3 ± 0.4	1.63 ± 0.10	1.39 ± 0.10	1.99 ± 0.15	103.5/115.0	0.90
abs. power law (N_H)	1.84	4.6 ± 0.4	1.70 ± 0.12	1.30 ± 0.10	1.90 ± 0.14	104.2/115.0	0.91
abs. power law	$0.06^{+3.75}_{-0.06}$	$4.3^{+0.7}_{-0.4}$	$1.63^{+0.18}_{-0.10}$	1.39 ± 0.10	1.99 ± 0.15	103.5/114.0	0.91
11_08							
power law		3.10 ± 0.28	1.67 ± 0.13	1.01 ± 0.09	1.33 ± 0.10	97.2/104.0	0.93
abs. power law (N_H)	1.84	3.29 ± 0.30	1.74 ± 0.14	0.93 ± 0.08	1.27 ± 0.10	99.8/104.0	0.96
abs. power law	≤ 1.9	$3.10^{+0.31}_{-0.28}$	$1.67^{+0.14}_{-0.13}$	1.01 ± 0.09	1.33 ± 0.10	97.2/103.0	0.94
12_08							
power law		2.62 ± 0.14	1.65 ± 0.07	0.80 ± 0.04	1.13 ± 0.06	227.6/219.0	1.04
abs. power law (N_H)	1.84	2.79 ± 0.15	1.71 ± 0.07	0.79 ± 0.04	1.11 ± 0.06	227.0/219.0	1.04
abs. power law	$1.2^{+2.6}_{-1.2}$	$2.73^{+0.28}_{-0.23}$	1.69 ± 0.10	0.80 ± 0.04	1.13 ± 0.06	226.8/218.0	1.04
35002032							
power law		$1.9^{+0.5}_{-0.6}$	$1.55^{+0.31}_{-0.30}$	0.54 ± 0.12	0.88 ± 0.20	4.7/12.0	0.39
abs. power law (N_H)	1.84	2.1 ± 0.6	1.6 ± 0.4	0.57 ± 0.13	0.98 ± 0.22	4.4/12.0	0.37
abs. power law	8^{+22}_{-8}	$2.5^{+1.9}_{-1.0}$	$1.8^{+0.8}_{-0.6}$	0.54 ± 0.12	0.88 ± 0.20	3.9/11.0	0.35

continued on the next page

Best fit parameters for PKS 0208−512 — continued

Data	N_{H}	A_Γ	Γ	$F_{0.2-2\,\mathrm{keV}}$	$F_{2-10\,\mathrm{keV}}$	χ^2/dof	χ^2_{red}
09_09							
power law		2.0 ± 0.4	$1.76^{+0.22}_{-0.20}$	0.59 ± 0.10	0.68 ± 0.10	19.6/27.0	0.73
abs. power law (N_{H})	1.84	2.1 ± 0.4	$1.83^{+0.23}_{-0.22}$	0.62 ± 0.10	0.71 ± 0.12	19.1/27.0	0.71
abs. power law	4^{+14}_{-4}	$2.3^{+1.0}_{-0.7}$	$1.9^{+0.5}_{-0.4}$	0.59 ± 0.10	0.68 ± 0.10	18.8/26.0	0.72
10_09							
power law		2.4 ± 0.4	1.55 ± 0.19	0.74 ± 0.10	1.22 ± 0.15	26.4/44.0	0.60
abs. power law (N_{H})	1.84	2.5 ± 0.4	1.62 ± 0.20	0.69 ± 0.09	1.17 ± 0.15	27.4/44.0	0.62
abs. power law	≤ 5	$2.4^{+0.5}_{-0.4}$	$1.55^{+0.23}_{-0.19}$	0.74 ± 0.10	1.22 ± 0.15	26.4/43.0	0.61
11_09							
power law		2.06 ± 0.29	1.59 ± 0.17	0.62 ± 0.08	0.97 ± 0.13	45.1/47.0	0.96
abs. power law (N_{H})	1.84	2.2 ± 0.4	1.66 ± 0.18	0.61 ± 0.08	0.96 ± 0.13	44.9/47.0	0.96
abs. power law	$1.5^{+7.6}_{-1.5}$	$2.2^{+0.6}_{-0.4}$	$1.64^{+0.28}_{-0.20}$	0.62 ± 0.08	0.97 ± 0.13	44.9/46.0	0.98
12_09							
power law		2.0 ± 0.4	$1.67^{+0.26}_{-0.25}$	0.60 ± 0.09	0.84 ± 0.13	29.5/34.0	0.87
abs. power law (N_{H})	1.84	2.1 ± 0.4	1.73 ± 0.27	0.57 ± 0.09	0.81 ± 0.12	30.1/34.0	0.89
abs. power law	≤ 7	$2.0^{+0.5}_{-0.4}$	$1.67^{+0.31}_{-0.25}$	0.60 ± 0.09	0.84 ± 0.13	29.5/33.0	0.89
35002051							
power law		2.6 ± 0.4	1.62 ± 0.15	0.75 ± 0.09	0.97 ± 0.12	49.8/51.0	0.98
abs. power law (N_{H})	1.84	2.8 ± 0.4	1.69 ± 0.16	0.79 ± 0.10	1.16 ± 0.14	47.5/51.0	0.93
abs. power law	11^{+12}_{-9}	$3.8^{+1.5}_{-1.0}$	2.0 ± 0.4	0.75 ± 0.09	0.97 ± 0.12	43.6/50.0	0.87
09_10							
power law		$4.1^{+0.7}_{-0.8}$	1.48 ± 0.20	1.09 ± 0.16	2.2 ± 0.4	22.4/36.0	0.62
abs. power law (N_{H})	1.84	4.3 ± 0.8	$1.52^{+0.22}_{-0.20}$	1.11 ± 0.16	2.3 ± 0.4	22.2/36.0	0.63
abs. power law	4^{+16}_{-4}	$4.5^{+2.2}_{-1.2}$	$1.58^{+0.44}_{-0.29}$	1.09 ± 0.16	2.2 ± 0.4	22.1/35.0	0.63
10_10							
power law		4.1 ± 0.6	1.45 ± 0.17	1.24 ± 0.15	2.44 ± 0.30	33.5/47.0	0.71
abs. power law (N_{H})	1.84	4.3 ± 0.7	1.51 ± 0.18	1.17 ± 0.15	2.38 ± 0.29	34.1/47.0	0.73
abs. power law	≤ 6	$4.1^{+0.9}_{-0.6}$	$1.45^{+0.22}_{-0.17}$	1.24 ± 0.15	2.44 ± 0.30	33.5/46.0	0.73
11_10							
power law		3.9 ± 0.4	1.46 ± 0.10	1.11 ± 0.09	2.20 ± 0.18	82.1/104.0	0.79
abs. power law (N_{H})	1.84	4.1 ± 0.4	1.52 ± 0.12	1.13 ± 0.09	2.24 ± 0.18	80.9/104.0	0.78
abs. power law	$2.7^{+5.0}_{-2.7}$	$4.3^{+0.8}_{-0.7}$	$1.55^{+0.19}_{-0.17}$	1.11 ± 0.09	2.20 ± 0.18	80.8/103.0	0.78
12_10							
power law		3.7 ± 0.5	1.41 ± 0.14	1.03 ± 0.10	2.23 ± 0.23	44.9/66.0	0.68
abs. power law (N_{H})	1.84	4.0 ± 0.5	1.47 ± 0.15	1.07 ± 0.10	2.33 ± 0.24	44.0/66.0	0.67
abs. power law	4^{+9}_{-4}	$4.3^{+1.2}_{-0.9}$	$1.55^{+0.27}_{-0.24}$	1.03 ± 0.10	2.23 ± 0.23	43.5/65.0	0.67
07_11							
power law		$2.9^{+0.4}_{-0.5}$	$1.52^{+0.19}_{-0.18}$	0.87 ± 0.10	1.57 ± 0.19	47.9/50.0	0.96
abs. power law (N_{H})	1.84	3.0 ± 0.5	$1.56^{+0.19}_{-0.18}$	0.82 ± 0.10	1.54 ± 0.18	48.8/50.0	0.98
abs. power law	≤ 5	2.9 ± 0.5	$1.52^{+0.20}_{-0.18}$	0.87 ± 0.10	1.57 ± 0.19	47.9/49.0	0.98

[a] In units of 10^{20} cm^{-2}. [b] In units of 10^{-4} keV^{-1} cm^{2} s^{-1}. [c] In units of 10^{-12} erg cm^{-2} s^{-1}. Unabsorbed fluxes for the cases shown here can be found in the appendix Table A.5.

It showed, that a single power law describes the data very well. Including an absorption does not significantly change the χ^2. Although the flux of the source changes from 0.59 up to 1.39 10^{-12} erg cm^{-2} s^{-1} the photon index stays nearly constant over time with an averaged value of 1.57±0.17, i.e., comparable to the value of 1.60±0.05 found by Zhang et al. (2010) for the data of 2008.

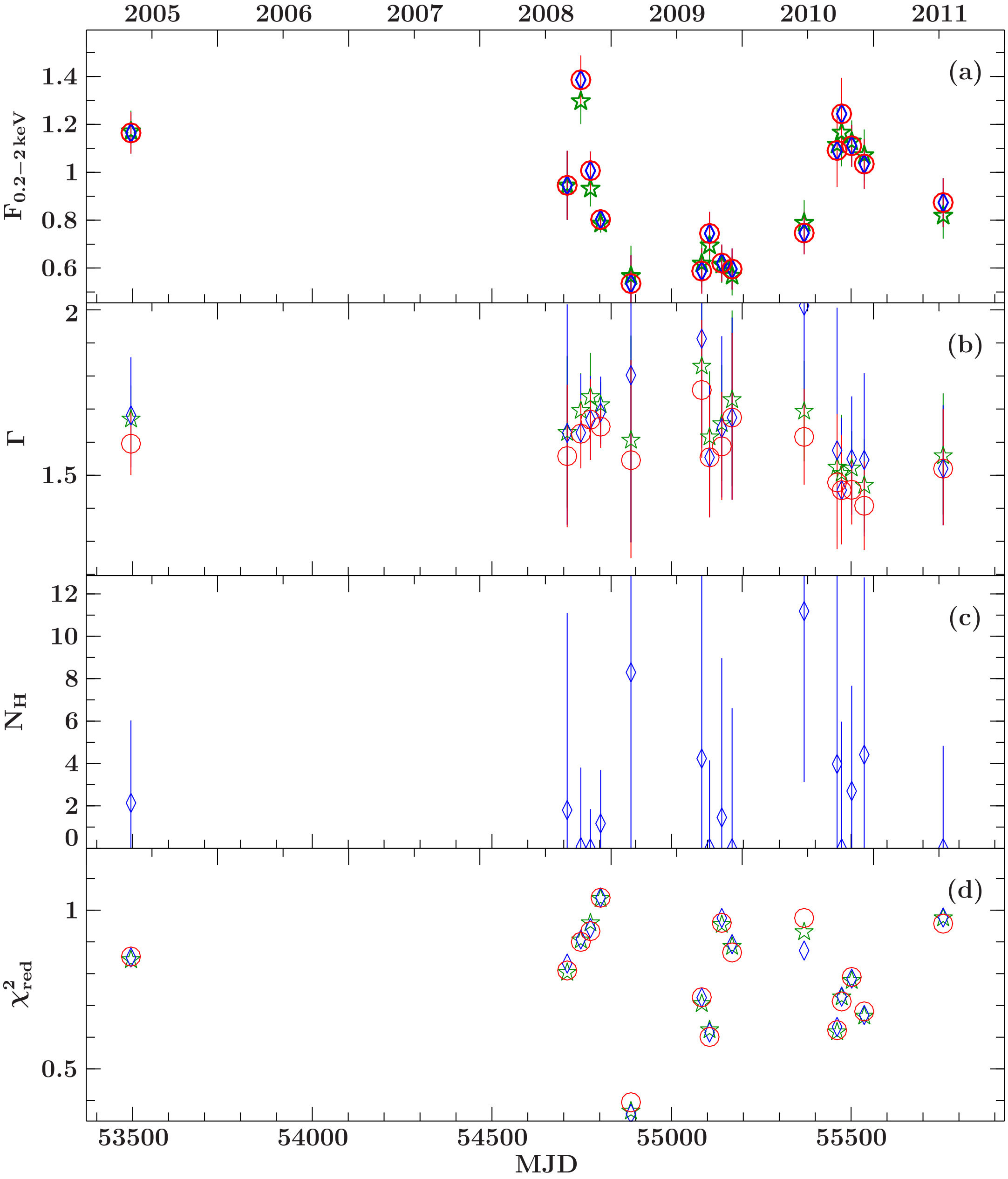

Figure 5.28: Spectral parameters for 0208−512. Showed are three different models: *red circle* single power law; *blue diamond* power law with free absorption; *green star* power law with gal. N_H. The following parameters are shown: *(a)* Absorbed 0.2–2 keV flux $F_{0.2-2\,\mathrm{keV}}$, *(b)* photon index Γ, *(c)* hydrogen column density N_H, *(d)* goodness of the fit χ^2_red. All units and the parameter values for the three models are listed in Table 5.15.

Now this is not the end. It is not even
the beginning of the end. But it is,
perhaps, the end of the beginning.

(Winston Churchill)

6 Conclusion and Outlook

Neutron stars and AGN are the most spectacular objects in the universe. An analysis of this objects showed their behavior and tried to understand the physics behind them.

B1509−58 is a very stable pulsar which shows no strong variations in its spectrum and pulse period. Therefore it is suitable to analyze the phase resolved spectrum. The pulsed emission gives insights into the physics of an isolated neutron star. In the unpulsed emission the high synchrotron radiation and the interactions with the interstellar medium can be seen. Due to its stability B1509−58 is qualified as a calibration source for further missions. This part of the Diploma Thesis will be published as a paper.

The analysis of AGNs is not that different to isolated neutron stars. The spectrum of an AGN can be described by an absorbed power law similar to the spectrum of B1509−58, but of course with different values. Five different AGN of the TANAMI sample were analyzed. From *XMM-Newton* simultaneous optical and X-ray data could be compared to spectral energy distributions, which shows the different radiation mechanisms over the energy range. The double hump form could be indicated for three sources, while for PKS 2155−304 the synchrotron peak lies in the UV and therefore the second peak is at higher energies than 10 keV. The variability for PKS 2155−304 in the optical and the X-ray can be described by changes of the acceleration of ejected particles and the cooling timescales of the relativistic electrons (Zhang et al., 2006). The spectra of PKS 2004−447, 2005−489, Pictor A and 2155−304 can all be well described by an absorbed broken power law. For PKS 0208−512 a single absorbed power law is sufficient.

To complete the SEDs for these sources, data from other satellites and telescopes must be added to be able to describe the radiation mechanism for the AGNs accurate.

A Appendix

A.1 B1509−58

The full results of the phase averaged monitoring observation spectra (see Sec. 3.3.2) are shown here. Table A.1 contains the observation identification (ObsID), the start and stop time of the observations in yyyy-mm-ddThh:mm:ss format and in Modified Julian Date (MJD), the exposure in seconds, the photon index Γ, the normalization of the photon index A_Γ, the hydrogen absorption column density N_H, the normalization of the frozen iron line at 6.4 keV A_Fe, the background-correction for the PCA A_Bkgcorr, the goodness of the fit χ^2, the degrees of freedom (dof) and the reduced goodness of the fir χ^2_red.

Table A.2 contains the 4–10 keV and 10–20 keV fluxes of the observations.

Table A.1: Best fit parameters for the phase averaged PCU2 spectra of all monitoring observations (Fig. 3.9).

ObsID	Start Time [MJD]	End Time [MJD]	Start Time^a	End Time^a	Exposure [s]	Γ	A_Γ^b	N_H $\left[10^{22}\,\mathrm{cm}^{-2}\right]$	A_Fe^c	A_Bkgcorr [%]	χ^2/dof	χ^2_{red}
					Epoch 1							
10208-01-09-00	50114.8	50114.9	1996-02-01T18:51:12	1996-02-01T20:35:44	3888.0	1.93 ± 0.07	$0.062^{+0.008}_{-0.007}$	$0.4^{+0.6}_{-0.4}$	1.4 ± 0.7	1.05 ± 0.07	33.9/48	0.71
10208-01-08-00	50148.1	50148.1	1996-03-06T01:52:00	1996-03-06T03:11:44	2976.0	$1.95^{+0.08}_{-0.07}$	$0.066^{+0.010}_{-0.009}$	0.9 ± 0.7	0.8 ± 0.8	1.02 ± 0.07	30.9/49	0.63
					Epoch 2							
10208-01-07-00	50186.6	50186.6	1996-04-13T13:37:36	1996-04-13T15:10:40	3328.0	2.12 ± 0.07	$0.084^{+0.012}_{-0.010}$	0.6 ± 0.6	1.5 ± 0.7	1.14 ± 0.06	42.3/46	0.92
					Epoch 3							
10208-01-06-00	50218.0	50218.1	1996-05-15T00:58:24	1996-05-15T03:56:48	3056.0	$1.95^{+0.07}_{-0.05}$	$0.066^{+0.010}_{-0.005}$	$0.13^{+0.58}_{-0.13}$	1.0 ± 0.8	0.93 ± 0.06	23.5/42	0.56
10208-01-05-00	50244.0	50244.0	1996-06-09T23:41:52	1996-06-10T00:34:40	2384.0	1.95 ± 0.08	$0.066^{+0.010}_{-0.009}$	$0.5^{+0.7}_{-0.5}$	1.0 ± 0.9	0.97 ± 0.07	47.4/42	1.13
10208-01-04-00	50277.0	50277.0	1996-07-12T23:20:48	1996-07-13T00:39:44	2496.0	2.06 ± 0.08	$0.077^{+0.013}_{-0.010}$	0.7 ± 0.7	1.5 ± 0.9	1.07 ± 0.07	29.2/42	0.70
10208-01-03-00	50311.3	50311.4	1996-08-16T07:24:00	1996-08-16T08:52:32	2928.0	$2.10^{+0.08}_{-0.07}$	$0.088^{+0.014}_{-0.012}$	$1.4^{+0.7}_{-0.6}$	$0.7^{+0.8}_{-0.7}$	1.04 ± 0.07	22.8/42	0.54
10208-01-02-00	50343.2	50343.2	1996-09-17T04:22:24	1996-09-17T05:25:52	3792.0	1.98 ± 0.07	$0.069^{+0.009}_{-0.008}$	$0.4^{+0.6}_{-0.4}$	1.5 ± 0.7	0.97 ± 0.06	24.2/42	0.58
10208-01-01-00	50372.7	50372.7	1996-10-16T16:01:36	1996-10-16T18:00:00	2720.0	2.01 ± 0.08	$0.072^{+0.012}_{-0.010}$	$0.6^{+0.7}_{-0.6}$	1.0 ± 0.8	1.06 ± 0.06	35.3/42	0.84
20802-01-01-00	50402.7	50402.7	1996-11-15T16:15:44	1996-11-15T17:05:04	1920.0	1.94 ± 0.05	0.063 ± 0.004	≤ 0.6	0.9 ± 0.9	0.96 ± 0.07	37.1/42	0.88
20802-01-02-00	50436.6	50436.6	1996-12-19T13:31:44	1996-12-19T14:58:40	2624.0	2.04 ± 0.08	$0.076^{+0.013}_{-0.010}$	0.9 ± 0.7	$1.6^{+0.8}_{-0.9}$	1.05 ± 0.07	21.1/42	0.50
20802-01-03-00	50460.1	50460.2	1997-01-12T03:13:36	1997-01-12T04:06:40	2816.0	2.11 ± 0.08	$0.086^{+0.014}_{-0.012}$	1.3 ± 0.7	1.1 ± 0.8	1.10 ± 0.07	28.3/42	0.67
20802-01-04-00	50494.1	50494.1	1997-02-15T01:58:24	1997-02-15T03:09:04	2320.0	2.06 ± 0.09	$0.081^{+0.015}_{-0.012}$	0.9 ± 0.7	1.1 ± 0.9	1.04 ± 0.07	25.6/42	0.61
20802-01-05-00	50526.6	50526.7	1997-03-19T14:55:12	1997-03-19T16:10:40	2896.0	2.05 ± 0.08	$0.077^{+0.012}_{-0.010}$	0.6 ± 0.6	1.8 ± 0.8	1.06 ± 0.07	28.7/42	0.68
20802-01-06-00	50549.5	50549.5	1997-04-11T12:13:20	1997-04-11T12:54:56	2144.0	2.11 ± 0.09	$0.091^{+0.016}_{-0.014}$	1.7 ± 0.7	≤ 0.9	1.01 ± 0.08	28.1/42	0.67
20802-01-07-00	50584.4	50584.4	1997-05-16T09:08:32	1997-05-16T10:42:40	2592.0	2.05 ± 0.08	$0.079^{+0.013}_{-0.010}$	0.8 ± 0.7	$0.8^{+0.8}_{-0.9}$	1.02 ± 0.07	27.0/42	0.64
20802-01-08-00	50606.8	50606.9	1997-06-07T20:01:04	1997-06-07T21:07:44	2688.0	$2.03^{+0.08}_{-0.07}$	$0.078^{+0.012}_{-0.010}$	$1.0^{+0.7}_{-0.6}$	1.0 ± 0.8	0.94 ± 0.07	31.1/42	0.74
20802-01-09-00	50635.4	50635.4	1997-07-06T08:26:56	1997-07-06T09:52:32	2768.0	2.06 ± 0.08	$0.078^{+0.013}_{-0.010}$	0.8 ± 0.7	1.6 ± 0.8	1.05 ± 0.07	34.5/42	0.82
20802-01-10-00	50661.1	50661.2	1997-08-01T03:20:32	1997-08-01T04:26:56	3952.0	2.09 ± 0.07	0.085 ± 0.010	1.3 ± 0.6	1.2 ± 0.7	1.05 ± 0.06	30.8/42	0.73
20802-01-11-00	50690.1	50690.1	1997-08-30T02:21:20	1997-08-30T03:06:40	2656.0	2.06 ± 0.08	$0.080^{+0.013}_{-0.010}$	1.2 ± 0.7	$0.4^{+0.8}_{-0.4}$	1.03 ± 0.07	22.1/42	0.53
20802-01-12-00	50717.8	50717.9	1997-09-26T20:02:08	1997-09-26T20:57:52	3328.0	2.04 ± 0.07	0.078 ± 0.010	0.8 ± 0.6	0.8 ± 0.8	0.98 ± 0.06	36.7/42	0.87
20802-01-13-00	50748.9	50748.9	1997-10-27T20:29:36	1997-10-27T21:48:32	2864.0	$2.02^{+0.08}_{-0.07}$	0.074 ± 0.010	0.7 ± 0.6	1.2 ± 0.8	0.96 ± 0.07	41.3/42	0.98
20802-01-14-00	50777.3	50777.4	1997-11-25T08:19:12	1997-11-25T09:09:36	2960.0	$2.03^{+0.08}_{-0.07}$	$0.076^{+0.012}_{-0.010}$	0.9 ± 0.6	1.0 ± 0.8	1.01 ± 0.07	22.3/42	0.53
20802-01-15-00	50804.0	50804.1	1997-12-21T23:24:00	1997-12-22T01:13:36	3296.0	2.01 ± 0.07	$0.074^{+0.010}_{-0.009}$	0.9 ± 0.6	1.5 ± 0.8	0.98 ± 0.07	26.9/42	0.64
30704-01-07-00	51009.3	51009.4	1998-07-15T07:56:00	1998-07-15T09:34:40	3456.0	2.06 ± 0.07	0.080 ± 0.010	1.1 ± 0.6	$1.1^{+0.7}_{-0.8}$	0.99 ± 0.06	41.2/42	0.98
30704-01-08-00	51030.3	51030.4	1998-08-05T08:18:40	1998-08-05T09:04:00	2704.0	2.01 ± 0.08	$0.074^{+0.012}_{-0.010}$	$0.6^{+0.7}_{-0.6}$	$1.7^{+0.8}_{-0.9}$	1.00 ± 0.07	20.1/42	0.48
30704-01-09-00	51058.1	51058.2	1998-09-02T03:16:16	1998-09-02T04:05:36	2864.0	2.08 ± 0.08	$0.081^{+0.013}_{-0.010}$	$1.0^{+0.7}_{-0.6}$	1.7 ± 0.8	1.04 ± 0.07	24.7/42	0.59
30704-01-10-00	51087.9	51088.0	1998-10-01T22:34:40	1998-10-02T00:01:04	2352.0	2.02 ± 0.08	$0.073^{+0.013}_{-0.010}$	0.8 ± 0.7	$0.6^{+0.9}_{-0.6}$	0.98 ± 0.08	28.3/42	0.67
30704-01-11-00	51117.9	51117.9	1998-10-31T20:47:12	1998-10-31T21:45:36	2688.0	2.04 ± 0.08	$0.076^{+0.012}_{-0.010}$	0.9 ± 0.7	$0.7^{+0.8}_{-0.7}$	0.99 ± 0.07	21.7/42	0.52
30704-01-12-00	51143.8	51143.9	1998-11-26T20:22:24	1998-11-26T22:22:40	2256.0	$2.02^{+0.09}_{-0.08}$	$0.074^{+0.013}_{-0.010}$	0.7 ± 0.7	1.3 ± 0.9	0.97 ± 0.08	39.3/42	0.94

continued on the next page

Best fit parameters for the phase averaged spectra — continued

ObsID	Start Time	End Time	Start Time[a]	End Time[a]	Exposure	Γ	A_{Γ}^{b}	$N_{\rm H}$	$A_{\rm Fe}^{d}$	$A_{\rm Bkgcorr}$	χ^2/dof	χ^2_{red}
30704-01-13-00	51191.7	51191.8	1999-01-13T16:52:32	1999-01-13T18:41:36	4032.0	2.02 ± 0.07	$0.073^{+0.010}_{-0.008}$	0.5 ± 0.5	1.3 ± 0.7	1.02 ± 0.06	33.1/42	0.79
40704-01-01-00	51219.9	51219.9	1999-02-10T21:48:32	1999-02-10T22:38:40	2832.0	2.03 ± 0.08	$0.073^{+0.012}_{-0.010}$	$0.6^{+0.7}_{-0.6}$	1.1 ± 0.8	1.04 ± 0.07	29.0/42	0.69
40704-01-02-00	51247.4	51247.4	1999-03-10T09:33:36	1999-03-10T10:23:44	1744.0	$1.95^{+0.10}_{-0.07}$	$0.064^{+18.628}_{-0.007}$	$0.19^{+0.77}_{-0.19}$	1.4 ± 1.0	0.97 ± 0.09	31.6/42	0.75
					Epoch 4							
40704-01-03-00	51277.3	51277.4	1999-04-09T08:01:04	1999-04-09T09:02:40	2352.0	$1.98^{+0.08}_{-0.06}$	$0.069^{+0.012}_{-0.007}$	$0.22^{+0.68}_{-0.22}$	1.4 ± 0.9	0.99 ± 0.08	24.4/36	0.68
40704-01-04-00	51303.2	51303.2	1999-05-05T03:45:52	1999-05-05T05:02:08	2608.0	2.08 ± 0.08	$0.085^{+0.015}_{-0.012}$	1.2 ± 0.7	$0.7^{+0.9}_{-0.7}$	0.98 ± 0.07	36.8/36	1.02
40704-01-05-00	51332.5	51332.5	1999-06-03T11:51:44	1999-06-03T12:50:40	3312.0	$2.08^{+0.08}_{-0.07}$	$0.084^{+0.013}_{-0.010}$	1.3 ± 0.6	0.8 ± 0.8	$1.03^{+0.06}_{-0.07}$	27.5/36	0.76
40704-01-06-00	51360.4	51360.5	1999-07-01T09:53:52	1999-07-01T11:26:40	2992.0	2.16 ± 0.08	$0.095^{+0.016}_{-0.013}$	1.7 ± 0.7	1.8 ± 0.8	$1.12^{+0.06}_{-0.07}$	23.4/36	0.65
40704-01-07-00	51392.2	51392.3	1999-08-02T05:34:24	1999-08-02T06:24:32	2976.0	2.03 ± 0.08	$0.074^{+0.012}_{-0.010}$	0.7 ± 0.7	1.3 ± 0.8	1.02 ± 0.07	20.4/36	0.57
40704-01-08-00	51417.2	51417.3	1999-08-27T05:14:24	1999-08-27T06:03:44	2832.0	2.01 ± 0.08	$0.074^{+0.012}_{-0.010}$	1.0 ± 0.7	$0.7^{+0.8}_{-0.7}$	0.98 ± 0.07	28.0/36	0.78
40704-01-10-00	51470.1	51470.1	1999-10-19T02:05:04	1999-10-19T02:54:56	2912.0	$2.00^{+0.08}_{-0.07}$	0.072 ± 0.010	0.7 ± 0.7	1.0 ± 0.8	0.99 ± 0.07	16.4/36	0.46
40704-01-11-00	51500.8	51500.9	1999-11-18T19:43:44	1999-11-18T20:32:32	2720.0	$2.00^{+0.08}_{-0.07}$	$0.070^{+0.012}_{-0.008}$	$0.3^{+0.7}_{-0.3}$	1.1 ± 0.8	1.01 ± 0.07	23.1/36	0.64
40704-01-12-00	51526.7	51526.7	1999-12-14T15:54:40	1999-12-14T16:20:48	1472.0	1.88 ± 0.05	$0.057^{+0.005}_{-0.004}$	≤ 0.7	2.2 ± 1.0	0.92 ± 0.09	21.2/36	0.59
40704-01-13-00	51556.8	51556.8	2000-01-13T19:10:24	2000-01-13T20:10:40	3584.0	2.05 ± 0.07	0.079 ± 0.010	1.0 ± 0.6	0.8 ± 0.7	1.01 ± 0.07	32.8/36	0.91
40704-01-14-00	51590.6	51590.6	2000-02-16T14:24:48	2000-02-16T15:45:36	2912.0	2.07 ± 0.08	$0.082^{+0.013}_{-0.010}$	1.0 ± 0.7	0.9 ± 0.8	1.01 ± 0.07	26.1/36	0.72
40704-01-15-00	51619.7	51619.8	2000-03-16T17:48:32	2000-03-16T19:26:40	3264.0	2.02 ± 0.07	0.074 ± 0.010	0.8 ± 0.6	1.3 ± 0.8	1.00 ± 0.07	32.3/36	0.90
50705-01-01-00	51654.5	51654.5	2000-04-20T12:21:20	2000-04-20T13:03:44	2384.0	1.98 ± 0.08	$0.069^{+0.012}_{-0.009}$	$0.5^{+0.7}_{-0.5}$	1.6 ± 0.9	1.00 ± 0.08	17.1/36	0.47
					Epoch 5							
50705-01-02-00	51684.7	51684.7	2000-05-20T16:57:20	2000-05-20T17:44:32	2592.0	2.06 ± 0.08	$0.081^{+0.014}_{-0.012}$	1.4 ± 0.7	$0.5^{+0.9}_{-0.5}$	$1.00^{+0.07}_{-0.08}$	22.0/36	0.61
50705-01-03-00	51715.3	51715.3	2000-06-20T06:03:44	2000-06-20T07:10:08	3952.0	2.03 ± 0.07	$0.076^{+0.010}_{-0.009}$	1.0 ± 0.6	0.9 ± 0.7	0.96 ± 0.06	26.9/36	0.75
50705-01-04-00	51744.4	51744.4	2000-07-19T09:00:48	2000-07-19T09:50:40	2768.0	2.03 ± 0.08	$0.074^{+0.012}_{-0.010}$	0.9 ± 0.7	0.9 ± 0.8	1.03 ± 0.07	24.8/36	0.69
50705-01-05-00	51764.9	51764.9	2000-08-08T21:56:16	2000-08-08T22:45:36	2416.0	1.99 ± 0.08	$0.070^{+0.012}_{-0.010}$	$0.6^{+0.7}_{-0.6}$	1.0 ± 0.9	0.96 ± 0.08	22.2/36	0.62
50705-01-07-00	51828.1	51828.1	2000-10-11T01:26:40	2000-10-11T02:48:32	2640.0	2.00 ± 0.08	$0.071^{+0.012}_{-0.010}$	0.8 ± 0.7	1.2 ± 0.9	0.99 ± 0.07	21.6/36	0.60
50705-01-08-00	51862.0	51862.0	2000-11-13T23:26:24	2000-11-14T00:40:00	3328.0	2.03 ± 0.07	0.075 ± 0.010	0.9 ± 0.6	1.5 ± 0.8	1.01 ± 0.07	20.6/36	0.57
50705-01-09-00	51885.2	51885.3	2000-12-07T05:08:48	2000-12-07T06:08:32	3472.0	2.02 ± 0.07	$0.074^{+0.010}_{-0.009}$	1.0 ± 0.6	$1.1^{+0.7}_{-0.8}$	1.00 ± 0.07	38.3/36	1.06
50705-01-10-00	51913.9	51914.0	2001-01-04T22:37:36	2001-01-04T23:41:04	2736.0	2.10 ± 0.08	$0.086^{+0.015}_{-0.012}$	1.7 ± 0.7	1.1 ± 0.8	$1.00^{+0.07}_{-0.08}$	29.8/36	0.83
50705-01-11-00	51941.8	51941.8	2001-02-01T19:21:04	2001-02-01T20:12:00	2976.0	2.03 ± 0.08	$0.076^{+0.012}_{-0.010}$	1.1 ± 0.7	1.4 ± 0.8	1.02 ± 0.07	26.9/36	0.75
50705-01-12-00	51969.4	51969.4	2001-03-01T09:04:32	2001-03-01T10:02:40	2944.0	2.03 ± 0.08	$0.074^{+0.012}_{-0.010}$	0.7 ± 0.7	0.9 ± 0.8	1.02 ± 0.07	28.7/36	0.80
50705-01-13-00	51997.6	51997.7	2001-03-29T15:31:28	2001-03-29T16:20:48	2944.0	2.07 ± 0.08	$0.082^{+0.013}_{-0.010}$	1.4 ± 0.7	0.9 ± 0.8	1.04 ± 0.07	21.1/36	0.59
60703-01-01-00	52027.5	52027.6	2001-04-28T12:52:16	2001-04-28T14:54:40	5056.0	2.06 ± 0.06	$0.081^{+0.010}_{-0.009}$	1.2 ± 0.5	0.7 ± 0.6	0.99 ± 0.06	28.1/36	0.78
60703-01-02-00	52054.6	52054.6	2001-05-25T13:55:12	2001-05-25T14:54:40	3376.0	$2.07^{+0.08}_{-0.07}$	$0.081^{+0.012}_{-0.010}$	1.3 ± 0.6	$0.5^{+0.8}_{-0.5}$	1.08 ± 0.07	28.8/36	0.80
60703-01-03-00	52082.7	52082.7	2001-06-22T16:20:32	2001-06-22T17:33:04	4288.0	$2.02^{+0.07}_{-0.06}$	$0.074^{+0.010}_{-0.008}$	0.8 ± 0.6	1.3 ± 0.7	1.00 ± 0.06	20.9/36	0.58
60703-01-04-01	52110.3	52110.3	2001-07-20T06:06:40	2001-07-20T06:38:40	1744.0	2.05 ± 0.10	$0.076^{+0.016}_{-0.013}$	$0.9^{+0.9}_{-0.8}$	$0.8^{+1.0}_{-0.8}$	1.04 ± 0.09	20.2/36	0.56
60703-01-04-00	52110.3	52110.3	2001-07-20T07:13:36	2001-07-20T08:31:44	3376.0	$2.08^{+0.08}_{-0.07}$	$0.080^{+0.012}_{-0.010}$	0.9 ± 0.6	$1.5^{+0.7}_{-0.8}$	1.08 ± 0.07	27.6/36	0.77
60703-01-05-00	52139.0	52139.1	2001-08-17T23:29:52	2001-08-18T01:26:40	2512.0	2.08 ± 0.09	$0.082^{+0.015}_{-0.012}$	1.1 ± 0.7	1.1 ± 0.9	1.02 ± 0.08	21.0/36	0.58

continued on the next page

Best fit parameters for the phase averaged spectra — continued

ObsID	Start Time	End Time	Start Time^a	End Time^a	Exposure	Γ	A_Γ^b	N_H	A_Fe^d	A_Bkgcorr	χ^2/dof	χ^2_{red}
60703-01-06-00	52166.2	52166.2	2001-09-14T05:12:48	2001-09-14T05:58:40	2544.0	2.06 ± 0.08	$0.081^{+0.014}_{-0.012}$	1.4 ± 0.7	$0.29^{+0.82}_{-0.29}$	0.99 ± 0.08	25.6/36	0.71
60703-01-06-01	52166.3	52166.3	2001-09-14T06:35:12	2001-09-14T07:08:32	1952.0	$2.01^{+0.10}_{-0.09}$	$0.069^{+0.014}_{-0.010}$	$0.5^{+0.8}_{-0.5}$	2.0 ± 1.0	1.04 ± 0.09	22.6/36	0.63
60703-01-07-00	52195.1	52195.1	2001-10-13T02:15:44	2001-10-13T02:48:48	1968.0	$2.04^{+0.10}_{-0.09}$	$0.076^{+0.015}_{-0.012}$	1.0 ± 0.8	$0.8^{+1.0}_{-0.8}$	1.03 ± 0.09	30.3/36	0.84
60703-01-07-01	52195.2	52195.2	2001-10-13T03:38:40	2001-10-13T05:12:32	2992.0	2.01 ± 0.08	$0.073^{+0.012}_{-0.010}$	0.9 ± 0.7	2.0 ± 0.8	1.00 ± 0.07	28.7/36	0.80
60703-01-08-00	52222.7	52222.7	2001-11-09T16:12:48	2001-11-09T16:38:56	1520.0	$1.97^{+0.10}_{-0.08}$	$0.066^{+0.015}_{-0.008}$	$0.28^{+0.86}_{-0.28}$	1.3 ± 1.0	1.00 ± 0.10	29.9/36	0.83
60703-01-08-01	52222.7	52222.8	2001-11-09T17:47:44	2001-11-09T18:25:36	2208.0	$1.96^{+0.09}_{-0.08}$	$0.068^{+0.012}_{-0.010}$	$0.8^{+0.8}_{-0.7}$	0.9 ± 0.9	$0.88^{+0.08}_{-0.09}$	30.5/36	0.85
60703-01-09-00	52250.9	52251.0	2001-12-07T20:48:48	2001-12-07T23:10:08	4880.0	2.06 ± 0.06	$0.076^{+0.010}_{-0.009}$	0.7 ± 0.5	1.6 ± 0.6	1.07 ± 0.06	38.8/36	1.08
60703-01-10-00	52278.8	52278.9	2002-01-04T18:49:36	2002-01-04T21:09:04	5248.0	2.06 ± 0.06	$0.078^{+0.009}_{-0.008}$	1.0 ± 0.5	0.8 ± 0.6	1.01 ± 0.06	22.6/36	0.63
60703-01-11-00	52307.0	52307.0	2002-02-01T23:56:16	2002-02-02T00:56:32	3392.0	2.12 ± 0.08	$0.087^{+0.013}_{-0.010}$	1.3 ± 0.6	1.4 ± 0.8	1.08 ± 0.07	19.1/36	0.53
60703-01-11-01	52307.1	52307.1	2002-02-02T01:31:12	2002-02-02T01:52:32	1216.0	2.12 ± 0.12	$0.091^{+0.023}_{-0.018}$	1.5 ± 1.0	$0.23^{+1.18}_{-0.23}$	$1.02^{+0.10}_{-0.12}$	15.9/36	0.44
60703-01-12-00	52333.4	52333.5	2002-02-28T09:54:56	2002-02-28T10:59:44	3520.0	2.01 ± 0.07	$0.073^{+0.010}_{-0.009}$	0.9 ± 0.6	0.7 ± 0.7	0.99 ± 0.07	23.8/36	0.66
60703-01-12-01	52333.5	52333.5	2002-02-28T12:09:52	2002-02-28T12:25:36	912.0	$1.97^{+0.14}_{-0.10}$	$0.064^{+0.020}_{-0.010}$	$0.4^{+1.2}_{-0.4}$	1.5 ± 1.4	0.91 ± 0.12	19.9/36	0.55
60703-01-13-00	52361.9	52361.9	2002-03-28T21:12:48	2002-03-28T21:59:44	2720.0	2.06 ± 0.08	$0.079^{+0.013}_{-0.010}$	1.0 ± 0.7	$0.6^{+0.8}_{-0.6}$	1.02 ± 0.08	28.6/36	0.79
60703-01-13-01	52361.9	52362.0	2002-03-28T22:47:44	2002-03-28T23:22:40	1984.0	$1.92^{+0.09}_{-0.05}$	$0.059^{+18.628}_{-0.004}$	$0.05^{+0.76}_{-0.05}$	$1.0^{+0.9}_{-1.0}$	0.99 ± 0.09	19.3/36	0.54
70701-01-01-00	52389.4	52389.4	2002-04-25T08:30:56	2002-04-25T08:55:44	1440.0	$2.13^{+0.12}_{-0.10}$	$0.090^{+0.020}_{-0.017}$	$1.7^{+0.8}_{-1.0}$	$0.9^{+1.0}_{-0.9}$	1.05 ± 0.10	24.5/36	0.68
70701-01-01-01	52389.6	52389.6	2002-04-25T13:25:36	2002-04-25T13:53:04	1616.0	2.11 ± 0.10	$0.089^{+0.019}_{-0.016}$	$1.8^{+0.7}_{-0.9}$	1.2 ± 1.0	1.03 ± 0.10	40.2/36	1.12
70701-01-01-02	52389.6	52389.6	2002-04-25T15:00:32	2002-04-25T15:30:08	1760.0	2.08 ± 0.10	$0.084^{+0.017}_{-0.014}$	1.2 ± 0.8	$0.3^{+1.0}_{-0.3}$	0.98 ± 0.10	39.7/36	1.10
70701-01-03-02	52445.2	52445.3	2002-06-20T05:43:44	2002-06-20T06:02:56	1120.0	2.09 ± 0.13	$0.082^{+0.023}_{-0.018}$	1.2 ± 1.0	$0.4^{+1.3}_{-0.4}$	1.03 ± 0.10	17.9/36	0.50
70701-01-03-01	52445.3	52445.3	2002-06-20T07:18:40	2002-06-20T07:40:48	1312.0	$2.05^{+0.12}_{-0.10}$	$0.075^{+0.019}_{-0.014}$	$0.6^{+1.0}_{-0.6}$	2.1 ± 1.2	1.05 ± 0.10	17.9/36	0.50
70701-01-03-00	52445.4	52445.4	2002-06-20T08:53:36	2002-06-20T09:18:08	1456.0	2.10 ± 0.10	$0.084^{+0.020}_{-0.016}$	1.2 ± 0.9	1.4 ± 1.0	0.98 ± 0.10	26.3/36	0.73
70701-01-04-00	52472.2	52472.2	2002-07-17T04:44:00	2002-07-17T05:20:00	2144.0	2.02 ± 0.09	$0.073^{+0.014}_{-0.012}$	0.8 ± 0.8	1.3 ± 0.9	1.04 ± 0.09	26.3/36	0.73
70701-01-04-01	52472.3	52472.3	2002-07-17T06:16:16	2002-07-17T07:28:32	3296.0	$2.06^{+0.08}_{-0.07}$	$0.081^{+0.012}_{-0.010}$	1.3 ± 0.6	$0.11^{+0.72}_{-0.11}$	1.02 ± 0.07	19.0/36	0.53
70701-01-05-00	52500.2	52500.3	2002-08-14T05:08:32	2002-08-14T07:13:36	3776.0	2.05 ± 0.07	0.080 ± 0.010	1.3 ± 0.6	0.7 ± 0.7	0.99 ± 0.07	42.0/36	1.17
70701-01-06-00	52527.2	52527.2	2002-09-10T04:45:04	2002-09-10T05:25:36	2192.0	2.10 ± 0.09	$0.085^{+0.016}_{-0.014}$	1.6 ± 0.8	1.1 ± 0.9	$1.05^{+0.08}_{-0.09}$	25.2/36	0.70
70701-01-06-01	52527.3	52527.3	2002-09-10T06:18:56	2002-09-10T06:59:44	2256.0	2.16 ± 0.09	$0.095^{+0.018}_{-0.015}$	1.7 ± 0.8	$0.8^{+0.9}_{-0.8}$	1.10 ± 0.08	30.0/36	0.83
70701-01-07-00	52552.0	52552.0	2002-10-04T22:57:20	2002-10-05T00:56:32	2512.0	2.05 ± 0.08	$0.079^{+0.014}_{-0.012}$	1.3 ± 0.7	1.1 ± 0.9	0.99 ± 0.08	25.5/36	0.71
70701-01-08-00	52583.5	52583.5	2002-11-05T11:37:20	2002-11-05T11:58:40	1056.0	$2.03^{+0.13}_{-0.12}$	$0.076^{+0.020}_{-0.016}$	1.0 ± 1.0	$0.9^{+1.3}_{-0.9}$	0.96 ± 0.10	26.7/37	0.72
70701-01-08-01	52583.6	52583.6	2002-11-05T13:14:40	2002-11-05T13:33:36	880.0	2.08 ± 0.14	$0.082^{+0.026}_{-0.019}$	1.3 ± 1.2	$1.4^{+1.4}_{-1.5}$	0.99 ± 0.12	31.1/37	0.84
70701-01-08-02	52583.6	52583.6	2002-11-05T14:52:32	2002-11-05T15:08:32	720.0	2.08 ± 0.15	$0.082^{+0.028}_{-0.020}$	$1.0^{+1.3}_{-1.0}$	1.6 ± 1.6	0.99 ± 0.14	31.9/37	0.86
70701-01-09-01	52616.6	52616.6	2002-12-08T13:27:12	2002-12-08T13:48:32	416.0	$2.09^{+0.20}_{-0.17}$	$0.081^{+0.041}_{-0.021}$	$0.8^{+1.7}_{-0.8}$	$1.3^{+2.0}_{-1.3}$	$1.00^{+0.17}_{-0.18}$	23.5/37	0.64
70701-01-10-00	52642.8	52642.8	2003-01-03T18:38:56	2003-01-03T19:58:56	3824.0	2.01 ± 0.07	$0.071^{+0.010}_{-0.009}$	0.5 ± 0.6	$0.6^{+0.7}_{-0.6}$	0.98 ± 0.06	34.0/37	0.92
70701-01-11-00	52670.0	52670.0	2003-01-30T23:26:56	2003-01-31T00:01:04	1920.0	2.12 ± 0.10	$0.086^{+0.018}_{-0.015}$	1.3 ± 0.8	$0.8^{+1.0}_{-0.8}$	1.08 ± 0.09	36.1/37	0.98
70701-01-11-01	52670.0	52670.0	2003-01-31T00:02:24	2003-01-31T00:27:44	1264.0	$2.06^{+0.12}_{-0.10}$	$0.079^{+0.020}_{-0.016}$	$0.8^{+1.0}_{-0.8}$	1.2 ± 1.2	0.99 ± 0.10	27.1/37	0.73
70701-01-11-02	52670.1	52670.1	2003-01-31T01:21:04	2003-01-31T02:24:32	2256.0	2.05 ± 0.09	$0.075^{+0.014}_{-0.012}$	0.8 ± 0.8	1.2 ± 0.9	1.02 ± 0.08	13.8/37	0.37
70701-01-12-00	52707.8	52707.9	2003-03-09T19:31:12	2003-03-09T21:24:32	4208.0	$2.02^{+0.07}_{-0.06}$	$0.072^{+0.010}_{-0.008}$	0.6 ± 0.6	1.4 ± 0.7	0.99 ± 0.06	24.4/37	0.66

continued on the next page

Best fit parameters for the phase averaged spectra — continued

ObsID	Start Time	End Time	Start Time[a]	End Time[a]	Exposure	Γ	A_{Γ}^{b}	$N_{\rm H}$	$A_{\rm Fe}^{d}$	$A_{\rm Bkgcorr}$	χ^2/dof	χ^2_{red}
70701-01-13-00	52733.0	52733.0	2003-04-04T00:43:28	2003-04-04T01:07:44	1248.0	$1.99^{+0.12}_{-0.10}$	$0.069^{+0.017}_{-0.013}$	$0.7^{+1.0}_{-0.7}$	$0.6^{+1.2}_{-0.6}$	0.95 ± 0.10	28.0/37	0.76
70701-01-13-01	52733.1	52733.1	2003-04-04T02:22:24	2003-04-04T02:42:40	992.0	$2.15^{+0.14}_{-0.13}$	$0.093^{+0.027}_{-0.020}$	$1.6^{+0.9}_{-1.0}$	$1.0^{+1.4}_{-1.0}$	1.05 ± 0.10	24.2/37	0.65
70701-01-13-02	52733.2	52733.2	2003-04-04T04:00:32	2003-04-04T04:16:32	784.0	2.12 ± 0.14	$0.092^{+0.026}_{-0.022}$	$1.7^{+0.8}_{-1.2}$	≤ 1.5	$0.99^{+0.12}_{-0.13}$	26.8/37	0.72
70701-01-13-03	52733.3	52733.3	2003-04-04T06:25:36	2003-04-04T06:47:44	1232.0	2.08 ± 0.12	$0.081^{+0.020}_{-0.017}$	1.1 ± 1.0	$0.4^{+1.2}_{-0.4}$	1.07 ± 0.10	29.6/37	0.80
70701-01-02-00	52757.3	52757.4	2003-04-28T06:32:32	2003-04-28T08:56:48	4384.0	$2.04^{+0.07}_{-0.06}$	$0.075^{+0.010}_{-0.009}$	0.7 ± 0.6	1.1 ± 0.7	0.97 ± 0.06	29.2/37	0.79
80803-01-01-00	52781.3	52781.4	2003-05-22T08:20:16	2003-05-22T09:19:44	3312.0	2.06 ± 0.07	$0.078^{+0.012}_{-0.010}$	1.2 ± 0.6	1.2 ± 0.8	1.03 ± 0.07	22.2/37	0.60
80803-01-02-00	52809.1	52809.2	2003-06-19T03:28:32	2003-06-19T05:31:44	2448.0	2.06 ± 0.09	$0.078^{+0.014}_{-0.012}$	$1.3^{+0.8}_{-0.7}$	1.0 ± 0.9	1.02 ± 0.08	32.2/37	0.87
80803-01-03-00	52835.1	52835.2	2003-07-15T03:25:36	2003-07-15T04:26:40	1520.0	$2.02^{+0.10}_{-0.09}$	$0.071^{+0.016}_{-0.010}$	$0.5^{+0.9}_{-0.5}$	$0.8^{+1.0}_{-0.8}$	1.03 ± 0.10	26.7/37	0.72
80803-01-03-01	52835.2	52835.2	2003-07-15T04:54:40	2003-07-15T06:11:44	2736.0	2.03 ± 0.08	$0.072^{+0.012}_{-0.010}$	$0.6^{+0.7}_{-0.6}$	1.8 ± 0.8	$1.04^{+0.07}_{-0.08}$	26.5/37	0.72
80803-01-04-00	52865.2	52865.2	2003-08-14T04:22:40	2003-08-14T05:00:48	2128.0	2.06 ± 0.09	$0.079^{+0.015}_{-0.013}$	1.1 ± 0.8	$1.1^{+0.9}_{-1.0}$	1.02 ± 0.08	35.8/37	0.97
80803-01-04-01	52865.2	52865.3	2003-08-14T05:57:04	2003-08-14T06:41:52	2512.0	2.04 ± 0.08	$0.078^{+0.013}_{-0.010}$	1.3 ± 0.7	$0.6^{+0.9}_{-0.6}$	0.97 ± 0.08	25.3/37	0.68
80803-01-05-00	52894.0	52894.0	2003-09-11T23:08:32	2003-09-12T00:01:04	3136.0	$1.99^{+0.08}_{-0.07}$	$0.067^{+0.010}_{-0.009}$	$0.5^{+0.7}_{-0.5}$	1.6 ± 0.8	0.97 ± 0.07	16.6/37	0.45
80803-01-05-01	52894.0	52894.0	2003-09-12T00:36:32	2003-09-12T01:03:44	1456.0	2.02 ± 0.10	$0.070^{+0.017}_{-0.013}$	$0.7^{+1.0}_{-0.7}$	1.7 ± 1.0	1.02 ± 0.10	31.2/37	0.84
80803-01-06-00	52921.2	52921.3	2003-10-09T05:55:28	2003-10-09T06:57:36	3392.0	2.05 ± 0.07	0.076 ± 0.010	0.9 ± 0.6	1.1 ± 0.7	1.02 ± 0.07	35.5/37	0.96
80803-01-06-01	52921.4	52921.4	2003-10-09T09:05:04	2003-10-09T09:31:44	1504.0	2.07 ± 0.10	$0.078^{+0.018}_{-0.015}$	1.1 ± 0.9	1.9 ± 1.0	1.08 ± 0.10	35.8/37	0.97
80803-01-07-02	52949.5	52949.5	2003-11-06T12:24:00	2003-11-06T12:43:44	1136.0	$2.11^{+0.13}_{-0.12}$	$0.087^{+0.023}_{-0.018}$	1.6 ± 1.0	1.3 ± 1.3	1.06 ± 0.12	23.7/37	0.64
80803-01-07-00	52950.0	52950.0	2003-11-06T23:24:48	2003-11-06T23:58:56	1408.0	2.02 ± 0.10	$0.072^{+0.017}_{-0.014}$	$0.8^{+1.0}_{-0.8}$	$0.8^{+1.0}_{-0.8}$	0.97 ± 0.10	25.8/37	0.70
80803-01-08-01	52978.0	52978.0	2003-12-05T00:31:28	2003-12-05T01:00:32	1728.0	2.08 ± 0.10	$0.081^{+0.018}_{-0.014}$	1.2 ± 0.9	$0.9^{+1.0}_{-0.9}$	1.07 ± 0.09	37.9/37	1.02
80803-01-08-00	52978.1	52978.1	2003-12-05T01:49:36	2003-12-05T02:56:32	3312.0	$2.07^{+0.08}_{-0.07}$	$0.080^{+0.012}_{-0.010}$	1.2 ± 0.6	0.9 ± 0.8	1.03 ± 0.07	34.5/37	0.93
80803-01-09-00	53005.9	53006.0	2004-01-01T22:09:04	2004-01-02T00:01:04	4384.0	$2.06^{+0.07}_{-0.06}$	$0.079^{+0.010}_{-0.009}$	$1.1^{+0.6}_{-0.5}$	1.2 ± 0.7	0.99 ± 0.06	26.2/37	0.71
80803-01-10-00	53035.9	53036.0	2004-01-31T22:24:32	2004-01-31T23:24:32	3296.0	2.11 ± 0.08	$0.086^{+0.013}_{-0.012}$	$1.3^{+0.7}_{-0.6}$	0.9 ± 0.8	1.07 ± 0.07	30.4/37	0.82
80803-01-11-00	53061.6	53061.7	2004-02-26T14:46:40	2004-02-26T17:52:32	6560.0	$2.09^{+0.06}_{-0.05}$	$0.082^{+0.009}_{-0.008}$	1.1 ± 0.5	1.1 ± 0.6	1.03 ± 0.05	29.3/37	0.79
90803-01-01-00	53089.7	53089.7	2004-03-25T17:10:24	2004-03-25T17:58:40	2704.0	1.98 ± 0.08	0.067 ± 0.010	$0.6^{+0.7}_{-0.6}$	1.8 ± 0.8	$0.95^{+0.07}_{-0.08}$	22.7/37	0.61
90803-01-01-01	53089.8	53089.8	2004-03-25T18:48:00	2004-03-25T19:22:40	2048.0	2.16 ± 0.10	$0.094^{+0.018}_{-0.016}$	$1.9^{+0.7}_{-0.8}$	1.4 ± 1.0	1.06 ± 0.08	24.4/37	0.66
90803-01-02-00	53115.7	53115.7	2004-04-20T15:47:12	2004-04-20T16:21:52	2064.0	$1.95^{+0.09}_{-0.07}$	$0.064^{+0.012}_{-0.007}$	$0.29^{+0.73}_{-0.29}$	1.2 ± 0.9	0.93 ± 0.09	22.2/37	0.60
90803-01-02-01	53115.7	53115.8	2004-04-20T17:21:20	2004-04-20T18:02:40	2416.0	$2.09^{+0.09}_{-0.08}$	$0.084^{+0.015}_{-0.013}$	1.2 ± 0.7	$0.16^{+0.84}_{-0.16}$	1.03 ± 0.08	9.9/37	0.27
90803-01-03-00	53140.8	53140.8	2004-05-15T19:09:36	2004-05-15T19:39:44	1616.0	2.14 ± 0.10	$0.091^{+0.020}_{-0.017}$	$1.8^{+0.7}_{-0.9}$	1.1 ± 1.0	1.08 ± 0.10	37.9/37	1.02
90803-01-03-01	53140.9	53140.9	2004-05-15T20:48:32	2004-05-15T21:14:40	1360.0	2.06 ± 0.10	$0.080^{+0.019}_{-0.015}$	$1.4^{+1.0}_{-0.9}$	$0.7^{+1.2}_{-0.7}$	0.97 ± 0.10	18.6/37	0.50
90803-01-03-02	53140.9	53141.0	2004-05-15T22:26:24	2004-05-15T22:48:32	1152.0	$2.10^{+0.13}_{-0.12}$	$0.085^{+0.023}_{-0.018}$	1.1 ± 1.0	1.8 ± 1.3	1.03 ± 0.10	24.6/37	0.66
90803-01-04-00	53167.1	53167.1	2004-06-11T01:20:16	2004-06-11T02:58:08	3808.0	2.04 ± 0.07	$0.073^{+0.010}_{-0.009}$	0.8 ± 0.6	1.3 ± 0.7	1.01 ± 0.06	35.1/37	0.95
90803-01-05-00	53202.1	53202.2	2004-07-16T03:15:28	2004-07-16T05:02:40	4192.0	2.04 ± 0.07	$0.074^{+0.010}_{-0.009}$	0.9 ± 0.6	1.1 ± 0.7	1.02 ± 0.06	20.2/37	0.55
90803-01-06-00	53225.2	53225.2	2004-08-08T04:24:32	2004-08-08T05:01:52	2080.0	2.04 ± 0.09	$0.075^{+0.015}_{-0.012}$	0.9 ± 0.8	$1.1^{+0.9}_{-1.0}$	1.00 ± 0.08	29.5/37	0.80
90803-01-06-01	53225.2	53225.3	2004-08-08T05:59:28	2004-08-08T06:42:56	2480.0	$2.12^{+0.09}_{-0.08}$	$0.088^{+0.016}_{-0.013}$	1.7 ± 0.7	≤ 0.8	1.02 ± 0.08	35.6/37	0.96
90803-01-07-00	53257.7	53257.8	2004-09-09T16:39:44	2004-09-09T18:02:40	3488.0	2.10 ± 0.07	$0.083^{+0.012}_{-0.010}$	1.4 ± 0.6	0.9 ± 0.7	1.04 ± 0.07	29.3/37	0.79
90803-01-08-00	53288.8	53288.8	2004-10-10T19:48:32	2004-10-10T20:14:08	1424.0	2.05 ± 0.10	$0.077^{+0.018}_{-0.015}$	$1.3^{+1.0}_{-0.9}$	1.2 ± 1.0	1.02 ± 0.10	25.3/37	0.68

continued on the next page

Best fit parameters for the phase averaged spectra — continued

ObsID	Start Time	End Time	Start Time^a	End Time^a	Exposure	Γ	A_Γ^b	N_H	A_{Fe}^d	$A_{Bkgcorr}$	χ^2/dof	χ^2_{red}
90803-01-08-01	53288.9	53288.9	2004-10-10T21:22:40	2004-10-10T21:54:56	1824.0	$2.00^{+0.10}_{-0.09}$	$0.073^{+0.015}_{-0.012}$	1.1 ± 0.8	$0.20^{+0.96}_{-0.20}$	0.93 ± 0.09	16.1/37	0.44
90803-01-08-02	53289.0	53289.0	2004-10-10T22:57:20	2004-10-10T23:36:00	2208.0	1.99 ± 0.09	$0.070^{+0.013}_{-0.010}$	0.8 ± 0.8	$0.6^{+0.9}_{-0.6}$	0.99 ± 0.09	29.5/37	0.80
90803-01-09-00	53312.5	53312.5	2004-11-03T12:40:32	2004-11-03T12:58:40	1040.0	$2.21^{+0.10}_{-0.13}$	$0.104^{+0.018}_{-0.023}$	$2.20^{+0.30}_{-1.08}$	$0.6^{+1.3}_{-0.6}$	1.13 ± 0.12	20.2/37	0.55
90803-01-09-01	53312.6	53312.6	2004-11-03T14:01:20	2004-11-03T14:29:36	1664.0	2.07 ± 0.10	$0.078^{+0.017}_{-0.014}$	1.0 ± 0.9	1.8 ± 1.0	1.03 ± 0.10	25.6/37	0.69
90803-01-10-00	53340.8	53340.9	2004-12-01T20:14:56	2004-12-01T21:15:44	3296.0	2.06 ± 0.07	$0.078^{+0.012}_{-0.010}$	1.1 ± 0.6	$0.6^{+0.8}_{-0.6}$	1.02 ± 0.07	17.3/37	0.47
90803-01-10-01	53340.9	53341.0	2004-12-01T22:25:04	2004-12-01T22:56:32	1312.0	$2.09^{+0.12}_{-0.10}$	$0.082^{+0.020}_{-0.016}$	1.2 ± 1.0	1.6 ± 1.2	0.97 ± 0.10	30.5/37	0.82
90803-01-11-00	53366.7	53366.8	2004-12-27T16:05:36	2004-12-27T18:04:32	5024.0	2.06 ± 0.06	$0.075^{+0.009}_{-0.008}$	0.6 ± 0.5	1.6 ± 0.6	1.02 ± 0.06	37.9/37	1.02
90803-01-13-00	53419.8	53419.9	2005-02-18T19:28:48	2005-02-18T21:20:32	4272.0	2.08 ± 0.07	0.081 ± 0.010	1.1 ± 0.6	1.3 ± 0.7	1.04 ± 0.06	13.0/37	0.35
91803-01-01-02	53450.0	53450.0	2005-03-20T23:33:36	2005-03-21T00:03:44	1536.0	2.02 ± 0.10	$0.072^{+0.016}_{-0.012}$	$0.6^{+0.9}_{-0.6}$	≤ 0.9	1.00 ± 0.10	26.2/37	0.71
91803-01-01-00	53450.1	53450.1	2005-03-21T01:12:32	2005-03-21T01:37:36	1264.0	$1.98^{+0.12}_{-0.10}$	$0.068^{+0.017}_{-0.010}$	$0.5^{+1.0}_{-0.5}$	$0.26^{+1.15}_{-0.26}$	0.99 ± 0.10	19.8/37	0.54
91803-01-01-01	53450.1	53450.1	2005-03-21T02:50:24	2005-03-21T03:12:32	1056.0	$1.98^{+0.07}_{-0.06}$	0.066 ± 0.006	≤ 1.1	$0.6^{+1.2}_{-0.6}$	0.97 ± 0.10	26.2/37	0.71
91803-01-02-00	53480.7	53480.7	2005-04-20T15:37:36	2005-04-20T17:25:36	3712.0	2.07 ± 0.07	0.078 ± 0.010	1.0 ± 0.6	1.3 ± 0.7	1.04 ± 0.07	36.4/37	0.98
91803-01-03-00	53506.6	53506.6	2005-05-16T14:41:36	2005-05-16T15:26:40	2400.0	$2.08^{+0.09}_{-0.08}$	$0.084^{+0.015}_{-0.013}$	$1.6^{+0.8}_{-0.7}$	$0.4^{+0.9}_{-0.4}$	1.00 ± 0.08	31.2/37	0.84
91803-01-03-01	53506.7	53506.8	2005-05-16T17:58:24	2005-05-16T18:35:44	1920.0	$2.06^{+0.10}_{-0.09}$	$0.080^{+0.016}_{-0.013}$	1.2 ± 0.8	$0.8^{+1.0}_{-0.8}$	1.00 ± 0.09	28.0/37	0.76
91803-01-04-00	53534.2	53534.2	2005-06-13T04:57:36	2005-06-13T05:24:00	1472.0	2.08 ± 0.10	$0.083^{+0.019}_{-0.015}$	1.4 ± 0.9	≤ 1.1	1.01 ± 0.10	16.4/37	0.44
91803-01-05-00	53562.5	53562.5	2005-07-11T11:25:20	2005-07-11T13:02:40	2736.0	2.09 ± 0.08	$0.085^{+0.014}_{-0.012}$	1.5 ± 0.7	$0.9^{+0.8}_{-0.9}$	0.99 ± 0.07	31.1/37	0.84
91803-01-05-01	53562.7	53562.7	2005-07-11T15:52:32	2005-07-11T16:22:40	1760.0	2.01 ± 0.10	$0.071^{+0.015}_{-0.012}$	$0.7^{+0.9}_{-0.7}$	$0.4^{+1.0}_{-0.4}$	0.99 ± 0.09	30.0/37	0.81
91803-01-06-00	53590.2	53590.3	2005-08-08T05:52:00	2005-08-08T07:48:32	4528.0	2.03 ± 0.06	$0.074^{+0.009}_{-0.008}$	0.7 ± 0.5	$0.7^{+0.6}_{-0.7}$	1.01 ± 0.06	28.2/37	0.76
91803-01-07-00	53618.9	53619.0	2005-09-05T22:17:20	2005-09-05T23:30:56	4384.0	2.08 ± 0.07	$0.081^{+0.010}_{-0.009}$	1.2 ± 0.6	1.1 ± 0.7	1.02 ± 0.06	24.7/37	0.67
91803-01-08-01	53647.8	53647.9	2005-10-04T20:18:24	2005-10-04T20:45:52	1568.0	2.07 ± 0.10	$0.081^{+0.018}_{-0.015}$	1.3 ± 0.9	$0.7^{+1.0}_{-0.7}$	1.00 ± 0.10	22.8/37	0.62
91803-01-08-00	53647.9	53647.9	2005-10-04T21:53:20	2005-10-04T22:26:56	1984.0	2.06 ± 0.09	$0.080^{+0.016}_{-0.013}$	1.2 ± 0.8	$0.6^{+1.0}_{-0.6}$	0.99 ± 0.09	25.8/37	0.70
91803-01-09-00	53674.4	53674.4	2005-10-31T08:46:08	2005-10-31T10:18:40	3904.0	2.03 ± 0.07	$0.074^{+0.010}_{-0.009}$	0.9 ± 0.6	$0.4^{+0.7}_{-0.4}$	0.99 ± 0.07	26.1/37	0.70
91803-01-10-00	53701.9	53701.9	2005-11-27T20:40:16	2005-11-27T21:05:36	1088.0	$2.16^{+0.12}_{-0.13}$	$0.094^{+0.023}_{-0.020}$	$1.8^{+0.7}_{-1.0}$	$0.16^{+1.26}_{-0.16}$	$1.10^{+0.10}_{-0.12}$	34.2/37	0.92
91803-01-10-01	53701.9	53701.9	2005-11-27T21:38:40	2005-11-27T22:56:32	3344.0	$2.05^{+0.08}_{-0.07}$	$0.076^{+0.012}_{-0.010}$	0.9 ± 0.6	1.2 ± 0.8	1.03 ± 0.07	27.9/37	0.75
91803-01-11-00	53733.1	53733.1	2005-12-29T02:20:32	2005-12-29T03:23:44	3392.0	2.06 ± 0.07	$0.079^{+0.012}_{-0.010}$	1.1 ± 0.6	1.4 ± 0.8	1.00 ± 0.07	26.2/37	0.71
91803-01-12-00	53758.8	53758.8	2006-01-23T18:22:40	2006-01-23T19:15:44	2976.0	2.10 ± 0.08	$0.082^{+0.014}_{-0.012}$	0.9 ± 0.7	1.2 ± 0.8	1.05 ± 0.07	20.9/37	0.57
91803-01-12-01	53758.8	53758.9	2006-01-23T20:08:32	2006-01-23T20:33:36	1440.0	1.95 ± 0.06	0.061 ± 0.005	≤ 0.9	1.6 ± 1.0	1.02 ± 0.09	24.3/37	0.66
91803-01-13-00	53789.0	53789.0	2006-02-22T23:28:32	2006-02-23T00:28:32	3312.0	$2.07^{+0.08}_{-0.07}$	$0.079^{+0.012}_{-0.010}$	1.0 ± 0.6	0.9 ± 0.8	1.02 ± 0.07	24.3/37	0.66
91803-01-13-01	53789.1	53789.1	2006-02-23T02:36:32	2006-02-23T03:00:32	1280.0	$2.21^{+0.08}_{-0.12}$	$0.104^{+0.013}_{-0.022}$	$2.38^{+0.13}_{-0.98}$	$1.1^{+1.2}_{-1.1}$	1.14 ± 0.10	23.7/37	0.64
92803-01-01-00	53816.7	53816.8	2006-03-22T17:06:08	2006-03-22T19:03:44	3808.0	2.09 ± 0.07	$0.080^{+0.012}_{-0.010}$	1.0 ± 0.6	$0.6^{+0.7}_{-0.6}$	1.04 ± 0.06	39.2/37	1.06
92803-01-02-00	53844.5	53844.6	2006-04-19T12:37:04	2006-04-19T13:21:52	2624.0	2.04 ± 0.08	$0.073^{+0.013}_{-0.010}$	0.7 ± 0.7	1.1 ± 0.8	1.00 ± 0.08	23.5/37	0.64
92803-01-02-01	53844.6	53844.6	2006-04-19T14:11:12	2006-04-19T14:49:36	2224.0	$1.96^{+0.09}_{-0.08}$	$0.065^{+0.012}_{-0.009}$	$0.5^{+0.8}_{-0.5}$	0.9 ± 0.9	0.92 ± 0.08	32.8/37	0.89
92803-01-03-00	53872.2	53872.3	2006-05-17T05:38:08	2006-05-17T06:18:08	2384.0	2.06 ± 0.09	$0.075^{+0.014}_{-0.012}$	$0.8^{+0.8}_{-0.7}$	1.1 ± 0.9	1.04 ± 0.08	46.0/37	1.24
92803-01-04-00	53901.3	53901.4	2006-06-15T07:54:40	2006-06-15T08:25:36	1648.0	1.98 ± 0.05	0.066 ± 0.005	≤ 0.6	1.3 ± 1.0	0.97 ± 0.09	33.7/37	0.91
92803-01-04-01	53901.4	53901.4	2006-06-15T09:33:04	2006-06-15T10:17:36	1376.0	$1.98^{+0.10}_{-0.08}$	$0.066^{+0.016}_{-0.009}$	$0.3^{+1.0}_{-0.3}$	$0.7^{+1.0}_{-0.7}$	0.97 ± 0.10	30.2/37	0.82

continued on the next page

Best fit parameters for the phase averaged spectra — continued

ObsID	Start Time	End Time	Start Time^a	End Time^a	Exposure	Γ	A_Γ^b	N_H	A_Fe^d	A_Bkgcorr	χ^2/dof	χ^2_{red}
92803-01-04-02	53901.5	53901.5	2006-06-15T11:02:40	2006-06-15T11:33:36	1680.0	2.06 ± 0.10	$0.078^{+0.017}_{-0.014}$	$0.9^{+0.9}_{-0.8}$	1.0 ± 1.0	$0.98^{+0.09}_{-0.10}$	19.5/37	0.53
92803-01-05-02	53926.0	53926.0	2006-07-10T00:20:16	2006-07-10T00:33:36	784.0	$2.03^{+0.16}_{-0.10}$	$0.070^{+0.025}_{-0.012}$	$0.4^{+1.3}_{-0.4}$	$0.10^{+1.45}_{-0.10}$	1.00 ± 0.12	27.0/37	0.73
92803-01-05-00	53926.1	53926.1	2006-07-10T01:54:08	2006-07-10T02:18:08	1424.0	$2.02^{+0.12}_{-0.10}$	$0.069^{+0.017}_{-0.010}$	$0.4^{+1.0}_{-0.4}$	1.0 ± 1.0	1.00 ± 0.10	24.6/37	0.66
92803-01-05-01	53926.5	53926.5	2006-07-10T11:01:36	2006-07-10T11:41:36	2016.0	2.12 ± 0.10	$0.084^{+0.017}_{-0.014}$	1.1 ± 0.8	1.8 ± 1.0	1.09 ± 0.08	36.2/37	0.98
92803-01-06-00	53951.6	53951.6	2006-08-04T13:29:36	2006-08-04T14:01:36	1728.0	2.11 ± 0.10	$0.086^{+0.019}_{-0.015}$	1.4 ± 0.9	1.2 ± 1.0	1.04 ± 0.09	31.3/37	0.85
92803-01-06-01	53951.6	53951.7	2006-08-04T15:10:24	2006-08-04T15:36:32	1360.0	$2.11^{+0.12}_{-0.10}$	$0.086^{+0.020}_{-0.017}$	$1.3^{+1.0}_{-0.9}$	1.3 ± 1.2	1.04 ± 0.10	28.4/37	0.77
92803-01-06-02	53951.7	53951.7	2006-08-04T16:48:16	2006-08-04T17:10:40	1136.0	2.15 ± 0.13	$0.094^{+0.024}_{-0.020}$	$1.8^{+0.8}_{-1.0}$	$0.8^{+1.3}_{-0.8}$	1.08 ± 0.10	21.6/37	0.58
92803-01-07-00	53981.2	53981.2	2006-09-03T05:22:08	2006-09-03T05:59:44	2240.0	$1.98^{+0.09}_{-0.08}$	$0.067^{+0.012}_{-0.009}$	$0.5^{+0.8}_{-0.5}$	1.2 ± 0.9	0.97 ± 0.08	33.8/37	0.91
92803-01-07-01	53981.3	53981.3	2006-09-03T06:54:56	2006-09-03T07:39:44	2672.0	2.06 ± 0.08	$0.081^{+0.013}_{-0.010}$	1.4 ± 0.7	$0.8^{+0.9}_{-0.8}$	$0.98^{+0.07}_{-0.08}$	21.9/37	0.59
92803-01-03-01	54008.9	54008.9	2006-09-30T21:47:44	2006-09-30T22:08:32	1152.0	2.07 ± 0.12	$0.080^{+0.020}_{-0.016}$	$0.9^{+1.0}_{-0.9}$	1.3 ± 1.3	0.98 ± 0.10	27.7/37	0.75
92803-01-08-00	54009.0	54009.0	2006-09-30T23:21:52	2006-10-01T00:23:44	3392.0	$2.08^{+0.08}_{-0.07}$	$0.080^{+0.012}_{-0.010}$	1.1 ± 0.6	1.1 ± 0.8	1.03 ± 0.07	27.5/37	0.74
92803-01-09-00	54035.0	54035.1	2006-10-27T01:08:16	2006-10-27T01:51:44	2480.0	2.04 ± 0.08	$0.077^{+0.013}_{-0.010}$	1.3 ± 0.7	$0.3^{+0.9}_{-0.3}$	1.00 ± 0.08	39.1/37	1.06
92803-01-09-01	54035.1	54035.1	2006-10-27T02:47:44	2006-10-27T03:32:48	2688.0	2.00 ± 0.08	$0.071^{+0.012}_{-0.010}$	0.8 ± 0.7	$0.6^{+0.8}_{-0.6}$	0.96 ± 0.08	16.3/37	0.44
92803-01-10-00	54067.0	54067.1	2006-11-27T23:56:32	2006-11-28T02:04:32	4560.0	2.03 ± 0.06	$0.073^{+0.009}_{-0.008}$	0.7 ± 0.5	0.9 ± 0.7	1.00 ± 0.06	24.6/37	0.67
92803-01-11-01	54092.2	54092.2	2006-12-23T05:16:16	2006-12-23T05:52:32	1904.0	2.04 ± 0.10	$0.072^{+0.015}_{-0.012}$	$0.6^{+0.8}_{-0.6}$	1.1 ± 1.0	$1.03^{+0.08}_{-0.09}$	20.5/37	0.55
92803-01-11-00	54092.3	54092.3	2006-12-23T06:45:20	2006-12-23T07:35:44	2480.0	2.09 ± 0.09	$0.083^{+0.015}_{-0.013}$	$1.3^{+0.8}_{-0.7}$	$0.3^{+0.9}_{-0.3}$	1.06 ± 0.08	27.7/37	0.75
92803-01-12-00	54120.3	54120.4	2007-01-20T07:24:32	2007-01-20T08:47:44	3520.0	2.13 ± 0.07	$0.088^{+0.013}_{-0.010}$	1.5 ± 0.6	$0.5^{+0.7}_{-0.5}$	1.07 ± 0.07	27.4/37	0.74
92803-01-13-00	54150.8	54150.8	2007-02-19T19:16:16	2007-02-19T19:51:44	2000.0	$2.06^{+0.10}_{-0.09}$	$0.078^{+0.016}_{-0.013}$	1.1 ± 0.8	$0.5^{+1.0}_{-0.5}$	$1.00^{+0.08}_{-0.09}$	23.8/37	0.64
92803-01-13-01	54150.9	54150.9	2007-02-19T20:50:40	2007-02-19T21:15:44	1392.0	$2.01^{+0.10}_{-0.08}$	$0.070^{+18.628}_{-0.009}$	$0.24^{+0.89}_{-0.24}$	1.3 ± 1.0	0.94 ± 0.10	21.7/37	0.59
92803-01-13-02	54150.9	54151.0	2007-02-19T22:24:32	2007-02-19T22:49:36	1376.0	$2.05^{+0.12}_{-0.10}$	$0.076^{+0.019}_{-0.015}$	1.1 ± 1.0	$1.1^{+1.2}_{-1.1}$	0.97 ± 0.10	26.7/37	0.72
92803-01-14-00	54171.4	54171.4	2007-03-12T08:25:04	2007-03-12T08:41:36	944.0	$2.03^{+0.14}_{-0.13}$	$0.072^{+0.022}_{-0.016}$	$0.8^{+1.2}_{-0.8}$	$1.3^{+1.4}_{-1.3}$	0.92 ± 0.12	25.3/37	0.69
92803-01-14-01	54171.4	54171.4	2007-03-12T09:59:12	2007-03-12T10:15:44	960.0	1.99 ± 0.07	$0.066^{+0.007}_{-0.006}$	≤ 0.8	≤ 1.1	0.96 ± 0.10	24.5/37	0.66
92803-01-14-02	54171.5	54171.5	2007-03-12T11:34:08	2007-03-12T12:20:32	2768.0	2.10 ± 0.08	$0.083^{+0.014}_{-0.012}$	1.1 ± 0.7	$0.6^{+0.8}_{-0.6}$	0.99 ± 0.07	30.5/37	0.82
92803-01-15-00	54190.7	54190.8	2007-03-31T17:51:12	2007-03-31T19:47:44	4656.0	2.08 ± 0.06	$0.080^{+0.010}_{-0.009}$	1.0 ± 0.5	$0.9^{+0.6}_{-0.7}$	1.02 ± 0.06	25.0/37	0.68
92803-01-16-00	54222.3	54222.4	2007-05-02T07:42:24	2007-05-02T09:05:36	3808.0	2.04 ± 0.07	$0.074^{+0.010}_{-0.009}$	0.8 ± 0.6	0.7 ± 0.7	0.98 ± 0.06	31.2/37	0.84
92803-01-17-01	54273.0	54273.1	2007-06-22T01:03:44	2007-06-22T01:25:36	1280.0	2.15 ± 0.12	$0.094^{+0.022}_{-0.019}$	$1.8^{+0.8}_{-1.0}$	$0.6^{+1.2}_{-0.6}$	1.01 ± 0.10	19.9/37	0.54
92803-01-17-00	54273.1	54273.2	2007-06-22T02:38:40	2007-06-22T03:40:32	2608.0	$2.04^{+0.09}_{-0.08}$	$0.074^{+0.013}_{-0.010}$	0.7 ± 0.7	1.1 ± 0.9	$0.99^{+0.07}_{-0.08}$	24.0/37	0.65
93803-01-01-00	54293.7	54293.8	2007-07-12T17:36:16	2007-07-12T18:05:36	1504.0	$2.12^{+0.12}_{-0.10}$	$0.083^{+0.020}_{-0.016}$	$0.8^{+1.0}_{-0.8}$	1.7 ± 1.0	1.04 ± 0.09	18.3/37	0.50
93803-01-01-01	54293.8	54293.8	2007-07-12T19:11:28	2007-07-12T19:39:28	1472.0	$2.07^{+0.12}_{-0.10}$	$0.074^{+0.019}_{-0.013}$	$0.6^{+1.0}_{-0.6}$	1.0 ± 1.0	$1.03^{+0.09}_{-0.10}$	25.7/37	0.69
93803-01-01-02	54293.8	54293.9	2007-07-12T20:12:00	2007-07-12T21:13:36	1360.0	$2.08^{+0.12}_{-0.10}$	$0.080^{+0.020}_{-0.016}$	1.2 ± 1.0	1.6 ± 1.2	1.00 ± 0.10	21.8/37	0.59
93803-01-02-00	54321.9	54322.0	2007-08-09T21:43:28	2007-08-09T23:06:40	4032.0	2.03 ± 0.07	$0.072^{+0.010}_{-0.009}$	0.6 ± 0.6	0.8 ± 0.7	1.00 ± 0.06	31.8/37	0.86
93803-01-03-00	54347.1	54347.1	2007-09-04T02:56:16	2007-09-04T03:35:44	2272.0	2.08 ± 0.09	$0.080^{+0.015}_{-0.013}$	1.3 ± 0.8	1.3 ± 0.9	1.07 ± 0.08	29.0/37	0.78
93803-01-03-01	54347.2	54347.2	2007-09-04T04:30:40	2007-09-04T05:17:04	2704.0	$2.10^{+0.09}_{-0.08}$	$0.082^{+0.014}_{-0.012}$	1.1 ± 0.7	1.0 ± 0.8	1.04 ± 0.07	21.1/37	0.57
93803-01-04-00	54375.0	54375.0	2007-10-01T23:07:28	2007-10-02T00:57:04	4960.0	2.09 ± 0.06	$0.083^{+0.010}_{-0.009}$	1.3 ± 0.5	$0.5^{+0.6}_{-0.5}$	1.01 ± 0.06	25.1/37	0.68
93803-01-05-00	54401.2	54401.3	2007-10-28T04:42:40	2007-10-28T06:14:40	3120.0	2.04 ± 0.08	$0.073^{+0.012}_{-0.010}$	$0.7^{+0.7}_{-0.6}$	2.1 ± 0.8	0.98 ± 0.07	24.4/37	0.66

continued on the next page

Best fit parameters for the phase averaged spectra — continued

ObsID	Start Time	End Time	Start Time[a]	End Time[a]	Exposure	Γ	A_{Γ}^{b}	N_{H}	A_{Fe}^{d}	A_{Bkgcorr}	χ^2/dof	χ^2_{red}
93803-01-05-01	54401.3	54401.3	2007-10-28T07:30:24	2007-10-28T08:00:32	1504.0	2.09 ± 0.10	$0.082^{+0.019}_{-0.015}$	$1.4^{+1.0}_{-0.9}$	1.6 ± 1.0	1.02 ± 0.10	39.5/37	1.07
93803-01-06-00	54429.2	54429.2	2007-11-25T04:00:16	2007-11-25T05:56:00	4896.0	2.05 ± 0.06	$0.075^{+0.009}_{-0.008}$	0.8 ± 0.5	1.1 ± 0.6	1.02 ± 0.06	23.3/37	0.63
93803-01-07-00	54456.8	54456.9	2007-12-22T19:37:04	2007-12-22T20:27:44	2944.0	2.07 ± 0.08	$0.077^{+0.013}_{-0.010}$	0.8 ± 0.7	1.0 ± 0.8	1.02 ± 0.07	26.3/37	0.71
93803-01-07-01	54456.9	54456.9	2007-12-22T21:28:00	2007-12-22T21:52:32	1440.0	2.08 ± 0.10	$0.082^{+0.020}_{-0.016}$	$1.4^{+1.0}_{-0.9}$	1.2 ± 1.2	1.00 ± 0.10	29.9/37	0.81
93803-01-08-00	54484.1	54484.2	2008-01-19T02:34:24	2008-01-19T03:50:56	4144.0	2.04 ± 0.07	$0.073^{+0.010}_{-0.009}$	0.6 ± 0.6	0.8 ± 0.7	1.05 ± 0.06	23.1/37	0.62
93803-01-09-00	54516.8	54516.9	2008-02-20T19:56:48	2008-02-20T20:42:40	2464.0	2.10 ± 0.09	$0.080^{+0.015}_{-0.012}$	0.9 ± 0.7	1.8 ± 0.9	1.06 ± 0.08	25.5/37	0.69
93803-01-10-00	54542.8	54542.8	2008-03-17T18:13:04	2008-03-17T18:45:52	1952.0	$2.02^{+0.10}_{-0.08}$	$0.068^{+0.014}_{-0.008}$	$0.29^{+0.76}_{-0.29}$	1.0 ± 1.0	1.02 ± 0.09	32.0/37	0.86
93803-01-10-01	54542.8	54542.9	2008-03-17T19:27:28	2008-03-17T20:26:56	3424.0	2.05 ± 0.07	0.074 ± 0.010	0.6 ± 0.6	$1.1^{+0.7}_{-0.8}$	1.00 ± 0.07	30.4/37	0.82
93803-01-11-00	54570.3	54570.3	2008-04-14T06:44:00	2008-04-14T07:01:36	880.0	$2.01^{+0.15}_{-0.14}$	$0.070^{+0.022}_{-0.016}$	$0.8^{+1.2}_{-0.8}$	$0.7^{+1.4}_{-0.7}$	0.91 ± 0.12	27.6/37	0.75
93803-01-11-01	54570.4	54570.5	2008-04-14T09:51:44	2008-04-14T11:13:36	3536.0	$2.08^{+0.08}_{-0.07}$	$0.079^{+0.012}_{-0.010}$	1.1 ± 0.6	$0.6^{+0.7}_{-0.6}$	1.00 ± 0.06	26.3/37	0.71
93803-01-12-01	54595.7	54595.7	2008-05-09T16:55:28	2008-05-09T17:44:32	1520.0	$2.13^{+0.12}_{-0.10}$	$0.086^{+0.020}_{-0.017}$	$1.2^{+1.0}_{-0.9}$	1.8 ± 1.0	1.06 ± 0.10	31.1/37	0.84
93803-01-13-00	54626.5	54626.6	2008-06-09T12:37:36	2008-06-09T14:37:52	3648.0	2.11 ± 0.07	$0.084^{+0.013}_{-0.010}$	1.3 ± 0.6	1.3 ± 0.7	1.03 ± 0.06	20.4/37	0.55
93803-01-14-00	54652.1	54652.1	2008-07-05T02:02:24	2008-07-05T02:22:40	1200.0	$2.26^{+0.12}_{-0.13}$	$0.112^{+0.025}_{-0.024}$	$1.9^{+0.6}_{-1.0}$	$0.24^{+1.23}_{-0.24}$	1.07 ± 0.10	31.7/37	0.86
93803-01-14-01	54652.1	54652.2	2008-07-05T03:35:12	2008-07-05T04:02:56	1584.0	2.07 ± 0.10	$0.082^{+0.018}_{-0.015}$	1.5 ± 0.9	$0.09^{+1.07}_{-0.09}$	0.99 ± 0.09	25.0/37	0.67
93803-01-14-02	54652.2	54652.2	2008-07-05T05:09:36	2008-07-05T05:43:44	1984.0	2.15 ± 0.10	$0.091^{+0.019}_{-0.016}$	$1.5^{+0.9}_{-0.8}$	1.3 ± 1.0	1.06 ± 0.08	36.2/37	0.98
93803-01-15-00	54680.2	54680.2	2008-08-02T05:04:16	2008-08-02T05:42:40	2272.0	2.07 ± 0.09	$0.077^{+0.014}_{-0.012}$	$0.6^{+0.8}_{-0.6}$	2.3 ± 0.9	1.05 ± 0.08	31.7/37	0.86
93803-01-15-01	54680.3	54680.3	2008-08-02T06:43:28	2008-08-02T07:02:40	1120.0	$2.01^{+0.13}_{-0.09}$	$0.070^{+18.629}_{-0.009}$	$0.27^{+0.99}_{-0.27}$	$0.7^{+1.3}_{-0.7}$	0.92 ± 0.10	27.8/37	0.75
93803-01-15-02	54680.3	54680.4	2008-08-02T08:20:32	2008-08-02T08:43:44	1344.0	$2.00^{+0.12}_{-0.10}$	$0.067^{+0.017}_{-0.012}$	$0.6^{+1.0}_{-0.6}$	1.5 ± 1.2	1.01 ± 0.10	48.5/37	1.31
93803-01-16-02	54708.9	54708.9	2008-08-30T21:01:52	2008-08-30T21:21:04	1120.0	$1.97^{+0.13}_{-0.07}$	$0.064^{+18.629}_{-0.006}$	$0.06^{+1.02}_{-0.06}$	$0.9^{+1.2}_{-0.9}$	0.93 ± 0.10	37.2/37	1.01
93803-01-16-01	54708.9	54709.0	2008-08-30T22:36:00	2008-08-30T23:00:48	1472.0	$2.10^{+0.12}_{-0.10}$	$0.079^{+0.019}_{-0.015}$	$0.8^{+1.0}_{-0.8}$	1.1 ± 1.0	1.06 ± 0.10	19.8/37	0.54
93803-01-16-00	54709.0	54709.0	2008-08-31T00:09:52	2008-08-31T00:40:48	1840.0	$2.06^{+0.10}_{-0.09}$	$0.074^{+0.016}_{-0.010}$	$0.5^{+0.8}_{-0.5}$	1.7 ± 1.0	1.02 ± 0.09	26.8/37	0.72
93803-01-17-00	54736.1	54736.2	2008-09-27T02:38:24	2008-09-27T04:05:36	2240.0	2.11 ± 0.09	$0.084^{+0.016}_{-0.013}$	1.0 ± 0.8	2.1 ± 0.9	1.01 ± 0.08	22.8/37	0.62
93803-01-17-01	54736.3	54736.3	2008-09-27T06:59:12	2008-09-27T07:31:44	1696.0	2.05 ± 0.10	$0.076^{+0.017}_{-0.013}$	$0.7^{+0.9}_{-0.7}$	1.9 ± 1.0	0.97 ± 0.09	18.9/37	0.51
93803-01-18-00	54764.0	54764.0	2008-10-24T23:06:24	2008-10-24T23:49:36	2432.0	2.06 ± 0.09	$0.076^{+0.014}_{-0.012}$	0.9 ± 0.7	1.3 ± 0.9	1.00 ± 0.08	29.3/37	0.79
93803-01-18-01	54764.0	54764.1	2008-10-25T00:39:28	2008-10-25T01:20:32	2256.0	$2.14^{+0.10}_{-0.09}$	$0.089^{+0.018}_{-0.015}$	1.7 ± 0.8	$0.7^{+0.9}_{-0.7}$	1.05 ± 0.08	27.4/37	0.74
93803-01-19-00	54791.8	54791.9	2008-11-21T20:12:16	2008-11-21T20:45:04	1728.0	2.16 ± 0.10	$0.092^{+0.020}_{-0.017}$	1.3 ± 0.9	$0.8^{+1.0}_{-0.8}$	1.07 ± 0.09	26.9/37	0.73
93803-01-19-01	54792.0	54792.0	2008-11-21T23:21:36	2008-11-22T00:05:52	2480.0	2.14 ± 0.09	$0.086^{+0.016}_{-0.013}$	$1.1^{+0.8}_{-0.7}$	0.9 ± 0.9	1.05 ± 0.07	22.2/37	0.60
93803-01-20-00	54819.8	54819.9	2008-12-19T20:06:08	2008-12-19T21:59:44	4528.0	2.11 ± 0.07	0.083 ± 0.010	1.2 ± 0.6	1.1 ± 0.7	1.03 ± 0.06	43.1/37	1.17
94803-01-01-00	54851.5	54851.5	2009-01-20T12:09:20	2009-01-20T12:26:08	928.0	$2.06^{+0.14}_{-0.13}$	$0.078^{+0.024}_{-0.017}$	$0.9^{+1.2}_{-0.9}$	$1.2^{+1.4}_{-1.2}$	0.95 ± 0.12	33.5/37	0.90
94803-01-01-01	54851.6	54851.6	2009-01-20T13:43:12	2009-01-20T14:06:40	1312.0	$2.05^{+0.12}_{-0.08}$	$0.070^{+18.629}_{-0.009}$	$0.21^{+0.95}_{-0.21}$	1.1 ± 1.2	1.03 ± 0.10	25.2/37	0.68
94803-01-01-02	54851.6	54851.7	2009-01-20T15:18:08	2009-01-20T15:46:40	1664.0	2.09 ± 0.10	$0.082^{+0.018}_{-0.015}$	1.2 ± 0.9	$0.6^{+1.0}_{-0.6}$	0.99 ± 0.09	18.7/37	0.51
94803-01-02-00	54876.3	54876.4	2009-02-14T08:20:32	2009-02-14T09:37:36	3744.0	2.05 ± 0.07	$0.075^{+0.010}_{-0.009}$	0.6 ± 0.6	0.9 ± 0.7	0.98 ± 0.06	24.7/37	0.67
94803-01-02-01	54876.4	54876.4	2009-02-14T10:03:44	2009-02-14T10:15:44	672.0	2.04 ± 0.09	$0.069^{+0.009}_{-0.008}$	≤ 1.1	2.6 ± 1.6	0.96 ± 0.12	17.6/37	0.48
94803-01-03-00	54909.7	54909.7	2009-03-19T15:52:00	2009-03-19T16:35:44	2544.0	2.08 ± 0.09	$0.080^{+0.014}_{-0.012}$	1.1 ± 0.7	$0.5^{+0.9}_{-0.5}$	0.99 ± 0.08	25.3/37	0.68
94803-01-03-01	54909.7	54909.7	2009-03-19T17:26:08	2009-03-19T17:43:44	976.0	$2.06^{+0.14}_{-0.10}$	$0.075^{+0.022}_{-0.013}$	$0.5^{+1.2}_{-0.5}$	1.8 ± 1.4	$1.02^{+0.12}_{-0.13}$	30.1/37	0.81

continued on the next page

Best fit parameters for the phase averaged spectra — continued

ObsID	Start Time	End Time	Start Time[a]	End Time[a]	Exposure	Γ	A_Γ^b	N_H	A_Fe^d	A_Bkgcorr	χ^2/dof	χ^2_{red}
94803-01-04-00	54934.4	54934.4	2009-04-13T08:52:32	2009-04-13T10:06:08	4400.0	2.08 ± 0.07	$0.078^{+0.010}_{-0.009}$	1.0 ± 0.6	1.2 ± 0.7	1.01 ± 0.06	27.3/37	0.74
94803-01-05-00	54961.4	54961.5	2009-05-10T10:18:24	2009-05-10T12:14:40	4448.0	2.07 ± 0.07	$0.079^{+0.010}_{-0.009}$	$0.9^{+0.6}_{-0.5}$	0.8 ± 0.7	1.00 ± 0.06	23.9/37	0.64
94803-01-06-00	54987.4	54987.5	2009-06-05T10:24:32	2009-06-05T12:24:48	4816.0	$2.06^{+0.07}_{-0.06}$	$0.078^{+0.010}_{-0.009}$	$1.1^{+0.6}_{-0.5}$	0.9 ± 0.7	0.99 ± 0.06	26.0/37	0.70
94803-01-07-00	55018.2	55018.3	2009-07-06T04:20:48	2009-07-06T06:13:36	4432.0	2.06 ± 0.07	$0.074^{+0.010}_{-0.009}$	0.9 ± 0.6	1.4 ± 0.7	1.00 ± 0.06	25.5/37	0.69
94803-01-08-00	55045.6	55045.6	2009-08-02T14:19:44	2009-08-02T15:08:48	2880.0	2.14 ± 0.08	$0.091^{+0.016}_{-0.013}$	1.6 ± 0.7	0.9 ± 0.8	1.04 ± 0.07	12.5/37	0.34
94803-01-08-01	55045.7	55045.7	2009-08-02T15:49:04	2009-08-02T16:25:36	1856.0	$2.06^{+0.10}_{-0.09}$	$0.074^{+0.016}_{-0.012}$	$0.5^{+0.8}_{-0.5}$	1.3 ± 1.0	1.01 ± 0.09	19.9/37	0.54
94803-01-09-00	55075.1	55075.2	2009-09-01T01:58:08	2009-09-01T03:44:48	4096.0	2.08 ± 0.07	0.077 ± 0.010	0.8 ± 0.6	1.2 ± 0.7	1.04 ± 0.06	37.0/37	1.00
94803-01-11-01	55128.3	55128.5	2009-10-24T08:14:24	2009-10-24T12:01:36	4912.0	2.05 ± 0.06	$0.077^{+0.010}_{-0.009}$	$1.1^{+0.6}_{-0.5}$	$0.6^{+0.7}_{-0.6}$	0.96 ± 0.05	44.7/37	1.21
94803-01-11-02	55128.8	55129.0	2009-10-24T20:01:20	2009-10-25T00:36:32	9552.0	2.08 ± 0.05	0.078 ± 0.007	0.9 ± 0.4	1.1 ± 0.5	1.02 ± 0.04	25.4/37	0.69
94803-01-11-03	55129.3	55129.5	2009-10-25T07:54:56	2009-10-25T12:10:56	6000.0	2.07 ± 0.06	$0.076^{+0.009}_{-0.008}$	0.7 ± 0.5	1.0 ± 0.6	1.02 ± 0.05	28.2/37	0.76
94803-01-11-04	55129.8	55130.0	2009-10-25T20:11:12	2009-10-26T00:10:56	10304.0	2.09 ± 0.05	0.080 ± 0.007	1.0 ± 0.4	1.0 ± 0.5	1.01 ± 0.04	32.3/37	0.87
94803-01-11-05	55130.0	55130.3	2009-10-26T00:42:24	2009-10-26T08:03:44	13376.0	2.11 ± 0.04	$0.083^{+0.007}_{-0.006}$	$1.18^{+0.31}_{-0.30}$	1.1 ± 0.4	1.03 ± 0.04	26.3/37	0.71
94803-01-11-06	55130.3	55130.6	2009-10-26T08:03:28	2009-10-26T14:54:40	10096.0	2.04 ± 0.05	$0.074^{+0.007}_{-0.006}$	0.8 ± 0.4	1.1 ± 0.5	1.00 ± 0.04	33.3/37	0.90
94803-01-12-00	55155.9	55155.9	2009-11-20T20:56:16	2009-11-20T21:29:52	1984.0	2.18 ± 0.10	$0.095^{+0.020}_{-0.017}$	1.7 ± 0.9	$0.7^{+1.0}_{-0.7}$	1.11 ± 0.08	35.6/37	0.96
94803-01-12-01	55155.9	55156.0	2009-11-20T22:30:08	2009-11-20T23:09:52	2352.0	2.10 ± 0.09	$0.079^{+0.015}_{-0.013}$	0.9 ± 0.8	1.0 ± 0.9	1.06 ± 0.08	24.7/37	0.67
94803-01-13-00	55185.1	55185.2	2009-12-20T02:34:24	2009-12-20T04:32:48	5136.0	$2.10^{+0.07}_{-0.06}$	$0.081^{+0.010}_{-0.009}$	0.9 ± 0.5	1.3 ± 0.6	1.05 ± 0.05	29.6/37	0.80
95803-01-01-00	55214.9	55215.0	2010-01-18T22:36:32	2010-01-19T00:36:48	4784.0	2.16 ± 0.07	$0.090^{+0.012}_{-0.010}$	1.7 ± 0.6	1.2 ± 0.7	1.08 ± 0.06	42.9/37	1.16
95803-01-02-00	55242.8	55242.9	2010-02-15T20:18:24	2010-02-15T22:13:36	3824.0	2.06 ± 0.07	$0.075^{+0.010}_{-0.009}$	0.8 ± 0.6	1.8 ± 0.7	1.02 ± 0.06	20.3/37	0.55
95803-01-03-00	55270.4	55270.5	2010-03-15T10:35:12	2010-03-15T11:22:40	2720.0	$2.06^{+0.09}_{-0.08}$	$0.073^{+0.013}_{-0.010}$	$0.6^{+0.7}_{-0.6}$	1.3 ± 0.8	1.03 ± 0.07	39.0/37	1.05
95803-01-03-01	55270.5	55270.5	2010-03-15T12:05:04	2010-03-15T12:37:36	1600.0	2.12 ± 0.10	$0.084^{+0.020}_{-0.016}$	0.9 ± 0.9	1.7 ± 1.0	1.01 ± 0.09	25.3/37	0.68
95803-01-04-00	55295.9	55295.9	2010-04-09T21:14:40	2010-04-09T22:42:40	3648.0	2.10 ± 0.07	$0.081^{+0.012}_{-0.010}$	1.0 ± 0.6	1.0 ± 0.7	$1.01^{+0.06}_{-0.07}$	19.6/37	0.53

[a] In yyyy-mm-ddThh:mm:ss format. [b] In units of $\mathrm{keV}^{-1}\,\mathrm{cm}^{-2}\,\mathrm{s}^{-1}$. [c] In units of $10^{-4}\,\mathrm{cm}^{-2}\,\mathrm{s}^{-1}$.

Table A.2: Fluxes for the best fit parameters for the phase averaged PCU2 spectra of all monitoring observations (Fig.3.9).

ObsID	$F_{4-10\,\mathrm{keV}}$ $[10^{-10}\,\mathrm{erg\,cm^{-2}\,s^{-1}}]$	$F_{10-20\,\mathrm{keV}}$ $[10^{-10}\,\mathrm{erg\,cm^{-2}\,s^{-1}}]$
Epoch 1		
10208-01-09-00	1.010 ± 0.009	0.792 ± 0.007
10208-01-08-00	1.018 ± 0.010	0.798 ± 0.008
Epoch 2		
10208-01-07-00	0.962 ± 0.009	0.650 ± 0.006
Epoch 3		
10208-01-06-00	1.046 ± 0.010	0.804 ± 0.008
10208-01-05-00	1.032 ± 0.010	0.800 ± 0.009
10208-01-04-00	0.998 ± 0.010	0.711 ± 0.008
10208-01-03-00	1.017 ± 0.010	0.718 ± 0.007
10208-01-02-00	1.027 ± 0.009	0.772 ± 0.007
10208-01-01-00	1.008 ± 0.010	0.747 ± 0.008
20802-01-01-00	1.035 ± 0.012	0.805 ± 0.009
20802-01-02-00	1.013 ± 0.010	0.735 ± 0.008
20802-01-03-00	0.994 ± 0.010	0.693 ± 0.007
20802-01-04-00	1.017 ± 0.010	0.728 ± 0.008
20802-01-05-00	1.015 ± 0.010	0.725 ± 0.007
20802-01-06-00	1.022 ± 0.010	0.726 ± 0.008
20802-01-07-00	1.015 ± 0.010	0.734 ± 0.008
20802-01-08-00	1.046 ± 0.010	0.774 ± 0.008
20802-01-09-00	1.005 ± 0.010	0.717 ± 0.007
20802-01-10-00	1.005 ± 0.009	0.708 ± 0.006
20802-01-11-00	1.013 ± 0.010	0.738 ± 0.008
20802-01-12-00	1.027 ± 0.009	0.750 ± 0.007
20802-01-13-00	1.026 ± 0.010	0.758 ± 0.008
20802-01-14-00	1.021 ± 0.010	0.752 ± 0.007
20802-01-15-00	1.028 ± 0.009	0.763 ± 0.007
30704-01-07-00	1.016 ± 0.009	0.736 ± 0.007
30704-01-08-00	1.047 ± 0.010	0.772 ± 0.008
30704-01-09-00	1.000 ± 0.010	0.702 ± 0.007
30704-01-10-00	1.015 ± 0.010	0.756 ± 0.008
30704-01-11-00	1.005 ± 0.010	0.736 ± 0.008
30704-01-12-00	1.035 ± 0.010	0.765 ± 0.008
30704-01-13-00	1.004 ± 0.008	0.736 ± 0.006
40704-01-01-00	0.989 ± 0.010	0.724 ± 0.007
40704-01-02-00	1.016 ± 0.013	0.779 ± 0.010
Epoch 4		
40704-01-03-00	1.029 ± 0.010	0.771 ± 0.008
40704-01-04-00	1.021 ± 0.010	0.727 ± 0.008
40704-01-05-00	1.010 ± 0.009	0.722 ± 0.007

continued on the next page

Fluxes — continued

ObsID	$F_{4-10\,\mathrm{keV}}$	$F_{10-20\,\mathrm{keV}}$
40704-01-06-00	0.990 ± 0.010	0.665 ± 0.007
40704-01-07-00	1.004 ± 0.010	0.735 ± 0.007
40704-01-08-00	1.026 ± 0.010	0.769 ± 0.008
40704-01-10-00	1.022 ± 0.010	0.768 ± 0.008
40704-01-11-00	1.006 ± 0.010	0.749 ± 0.008
40704-01-12-00	1.052 ± 0.014	0.844 ± 0.010
40704-01-13-00	1.023 ± 0.009	0.748 ± 0.007
40704-01-14-00	1.011 ± 0.010	0.723 ± 0.007
40704-01-15-00	1.019 ± 0.010	0.753 ± 0.007
50705-01-01-00	1.027 ± 0.010	0.773 ± 0.008
	Epoch 5	
50705-01-02-00	1.011 ± 0.010	0.740 ± 0.008
50705-01-03-00	1.017 ± 0.009	0.753 ± 0.006
50705-01-04-00	0.990 ± 0.010	0.728 ± 0.008
50705-01-05-00	1.016 ± 0.010	0.767 ± 0.008
50705-01-07-00	1.009 ± 0.010	0.755 ± 0.008
50705-01-08-00	1.016 ± 0.009	0.747 ± 0.007
50705-01-09-00	1.016 ± 0.009	0.756 ± 0.007
50705-01-10-00	1.001 ± 0.010	0.710 ± 0.007
50705-01-11-00	1.022 ± 0.010	0.755 ± 0.007
50705-01-12-00	0.991 ± 0.010	0.725 ± 0.007
50705-01-13-00	1.011 ± 0.010	0.733 ± 0.007
60703-01-01-00	1.022 ± 0.008	0.742 ± 0.006
60703-01-02-00	0.983 ± 0.009	0.708 ± 0.007
60703-01-03-00	1.019 ± 0.008	0.755 ± 0.006
60703-01-04-01	0.997 ± 0.013	0.726 ± 0.009
60703-01-04-00	0.981 ± 0.009	0.689 ± 0.007
60703-01-05-00	0.992 ± 0.010	0.704 ± 0.008
60703-01-06-00	1.012 ± 0.010	0.741 ± 0.008
60703-01-06-01	0.986 ± 0.012	0.725 ± 0.009
60703-01-07-00	1.000 ± 0.012	0.735 ± 0.009
60703-01-07-01	1.020 ± 0.010	0.755 ± 0.007
60703-01-08-00	1.002 ± 0.013	0.758 ± 0.010
60703-01-08-01	1.046 ± 0.010	0.814 ± 0.009
60703-01-09-00	0.987 ± 0.008	0.705 ± 0.006
60703-01-10-00	0.997 ± 0.007	0.722 ± 0.006
60703-01-11-00	0.986 ± 0.009	0.680 ± 0.006
60703-01-11-01	1.007 ± 0.015	0.706 ± 0.010
60703-01-12-00	1.006 ± 0.009	0.755 ± 0.007
60703-01-12-01	0.992 ± 0.017	0.757 ± 0.013
60703-01-13-00	0.999 ± 0.010	0.724 ± 0.008
60703-01-13-01	0.999 ± 0.012	0.790 ± 0.009
70701-01-01-00	0.980 ± 0.014	0.681 ± 0.010

continued on the next page

Fluxes — continued

ObsID	$F_{4-10\,\mathrm{keV}}$	$F_{10-20\,\mathrm{keV}}$
70701-01-01-01	1.010 ± 0.013	0.714 ± 0.009
70701-01-01-02	1.008 ± 0.012	0.723 ± 0.009
70701-01-03-02	0.973 ± 0.016	0.691 ± 0.010
70701-01-03-01	0.986 ± 0.014	0.699 ± 0.010
70701-01-03-00	0.991 ± 0.014	0.694 ± 0.010
70701-01-04-00	1.000 ± 0.010	0.738 ± 0.009
70701-01-04-01	1.004 ± 0.009	0.735 ± 0.007
70701-01-05-00	1.012 ± 0.009	0.740 ± 0.007
70701-01-06-00	0.998 ± 0.010	0.707 ± 0.008
70701-01-06-01	0.974 ± 0.010	0.658 ± 0.008
70701-01-07-00	1.003 ± 0.010	0.731 ± 0.008
70701-01-08-00	1.015 ± 0.016	0.748 ± 0.012
70701-01-08-01	0.995 ± 0.018	0.705 ± 0.013
70701-01-08-02	1.009 ± 0.019	0.711 ± 0.014
70701-01-09-01	0.980 ± 0.025	0.684 ± 0.018
70701-01-10-00	0.991 ± 0.009	0.736 ± 0.007
70701-01-11-00	0.968 ± 0.012	0.669 ± 0.008
70701-01-11-01	1.015 ± 0.015	0.728 ± 0.010
70701-01-11-02	0.982 ± 0.010	0.710 ± 0.008
70701-01-12-00	0.990 ± 0.008	0.724 ± 0.006
70701-01-13-00	1.004 ± 0.015	0.763 ± 0.010
70701-01-13-01	0.987 ± 0.017	0.674 ± 0.012
70701-01-13-02	1.019 ± 0.019	0.721 ± 0.014
70701-01-13-03	0.973 ± 0.015	0.695 ± 0.010
70701-01-02-00	0.983 ± 0.008	0.711 ± 0.006
80803-01-01-00	0.994 ± 0.009	0.721 ± 0.007
80803-01-02-00	0.980 ± 0.010	0.712 ± 0.008
80803-01-03-00	0.980 ± 0.013	0.723 ± 0.010
80803-01-03-01	0.982 ± 0.010	0.713 ± 0.007
80803-01-04-00	1.003 ± 0.012	0.727 ± 0.009
80803-01-04-01	1.012 ± 0.010	0.749 ± 0.008
80803-01-05-00	0.993 ± 0.010	0.745 ± 0.007
80803-01-05-01	0.968 ± 0.014	0.708 ± 0.010
80803-01-06-00	0.986 ± 0.009	0.715 ± 0.007
80803-01-06-01	0.981 ± 0.013	0.697 ± 0.010
80803-01-07-02	0.987 ± 0.015	0.689 ± 0.010
80803-01-07-00	0.995 ± 0.014	0.740 ± 0.010
80803-01-08-01	0.976 ± 0.013	0.696 ± 0.009
80803-01-08-00	0.983 ± 0.009	0.704 ± 0.007
80803-01-09-00	1.008 ± 0.008	0.728 ± 0.006
80803-01-10-00	0.977 ± 0.009	0.680 ± 0.007
80803-01-11-00	0.981 ± 0.007	0.690 ± 0.005
90803-01-01-00	1.006 ± 0.010	0.756 ± 0.008

continued on the next page

Fluxes — continued

ObsID	$F_{4-10\,\mathrm{keV}}$	$F_{10-20\,\mathrm{keV}}$
90803-01-01-01	0.971 ± 0.012	0.656 ± 0.008
90803-01-02-00	1.020 ± 0.012	0.786 ± 0.009
90803-01-02-01	0.993 ± 0.010	0.706 ± 0.008
90803-01-03-00	0.975 ± 0.013	0.670 ± 0.009
90803-01-03-01	1.001 ± 0.014	0.729 ± 0.010
90803-01-03-02	1.005 ± 0.016	0.697 ± 0.010
90803-01-04-00	0.984 ± 0.009	0.717 ± 0.006
90803-01-05-00	0.980 ± 0.008	0.713 ± 0.006
90803-01-06-00	0.989 ± 0.012	0.723 ± 0.009
90803-01-06-01	0.975 ± 0.010	0.687 ± 0.008
90803-01-07-00	0.980 ± 0.009	0.693 ± 0.007
90803-01-08-00	0.984 ± 0.014	0.718 ± 0.010
90803-01-08-01	1.015 ± 0.012	0.773 ± 0.010
90803-01-08-02	1.003 ± 0.010	0.762 ± 0.009
90803-01-09-00	0.956 ± 0.016	0.628 ± 0.010
90803-01-09-01	0.983 ± 0.013	0.699 ± 0.009
90803-01-10-00	0.990 ± 0.009	0.719 ± 0.007
90803-01-10-01	0.984 ± 0.014	0.691 ± 0.010
90803-01-11-00	0.967 ± 0.008	0.687 ± 0.006
90803-01-13-00	0.981 ± 0.008	0.695 ± 0.006
91803-01-01-02	0.980 ± 0.013	0.728 ± 0.010
91803-01-01-00	1.002 ± 0.015	0.766 ± 0.012
91803-01-01-01	0.990 ± 0.016	0.745 ± 0.012
91803-01-02-00	0.967 ± 0.009	0.688 ± 0.006
91803-01-03-00	0.997 ± 0.010	0.719 ± 0.008
91803-01-03-01	1.000 ± 0.012	0.725 ± 0.009
91803-01-04-00	1.004 ± 0.014	0.729 ± 0.010
91803-01-05-00	0.991 ± 0.010	0.704 ± 0.007
91803-01-05-01	0.995 ± 0.013	0.745 ± 0.010
91803-01-06-00	0.984 ± 0.008	0.720 ± 0.006
91803-01-07-00	0.981 ± 0.008	0.697 ± 0.006
91803-01-08-01	0.995 ± 0.013	0.718 ± 0.010
91803-01-08-00	1.005 ± 0.012	0.730 ± 0.009
91803-01-09-00	0.997 ± 0.009	0.739 ± 0.007
91803-01-10-00	0.965 ± 0.016	0.661 ± 0.010
91803-01-10-01	0.983 ± 0.009	0.710 ± 0.007
91803-01-11-00	1.005 ± 0.009	0.724 ± 0.007
91803-01-12-00	0.960 ± 0.010	0.665 ± 0.007
91803-01-12-01	0.965 ± 0.014	0.735 ± 0.010
91803-01-13-00	0.977 ± 0.009	0.697 ± 0.007
91803-01-13-01	0.962 ± 0.015	0.633 ± 0.010
92803-01-01-00	0.965 ± 0.009	0.682 ± 0.006
92803-01-02-00	0.982 ± 0.010	0.715 ± 0.008

continued on the next page

Fluxes — continued

ObsID	$F_{4-10\,\mathrm{keV}}$	$F_{10-20\,\mathrm{keV}}$
92803-01-02-01	1.006 ± 0.010	0.777 ± 0.009
92803-01-03-00	0.964 ± 0.010	0.691 ± 0.008
92803-01-04-00	0.987 ± 0.013	0.736 ± 0.010
92803-01-04-01	0.988 ± 0.014	0.751 ± 0.010
92803-01-04-02	0.996 ± 0.013	0.718 ± 0.009
92803-01-05-02	0.939 ± 0.019	0.689 ± 0.014
92803-01-05-00	0.961 ± 0.014	0.707 ± 0.010
92803-01-05-01	0.967 ± 0.012	0.662 ± 0.008
92803-01-06-00	0.990 ± 0.013	0.692 ± 0.009
92803-01-06-01	0.982 ± 0.014	0.680 ± 0.010
92803-01-06-02	0.984 ± 0.016	0.673 ± 0.010
92803-01-07-00	1.000 ± 0.010	0.755 ± 0.009
92803-01-07-01	1.012 ± 0.010	0.739 ± 0.008
92803-01-03-01	0.995 ± 0.016	0.706 ± 0.010
92803-01-08-00	0.971 ± 0.009	0.689 ± 0.007
92803-01-09-00	0.999 ± 0.010	0.741 ± 0.008
92803-01-09-01	1.002 ± 0.010	0.757 ± 0.008
92803-01-10-00	0.988 ± 0.008	0.725 ± 0.006
92803-01-11-01	0.957 ± 0.012	0.694 ± 0.009
92803-01-11-00	0.968 ± 0.010	0.687 ± 0.008
92803-01-12-00	0.965 ± 0.009	0.669 ± 0.006
92803-01-13-00	0.980 ± 0.012	0.712 ± 0.009
92803-01-13-01	0.991 ± 0.014	0.728 ± 0.010
92803-01-13-02	0.975 ± 0.014	0.708 ± 0.010
92803-01-14-00	0.976 ± 0.017	0.714 ± 0.013
92803-01-14-01	0.964 ± 0.017	0.725 ± 0.013
92803-01-14-02	0.971 ± 0.010	0.682 ± 0.007
92803-01-15-00	0.968 ± 0.008	0.686 ± 0.006
92803-01-16-00	0.975 ± 0.009	0.713 ± 0.007
92803-01-17-01	0.978 ± 0.015	0.670 ± 0.010
92803-01-17-00	0.977 ± 0.010	0.710 ± 0.008
93803-01-01-00	0.949 ± 0.014	0.642 ± 0.009
93803-01-01-01	0.938 ± 0.014	0.663 ± 0.010
93803-01-01-02	0.979 ± 0.014	0.695 ± 0.010
93803-01-02-00	0.981 ± 0.009	0.719 ± 0.006
93803-01-03-00	0.968 ± 0.010	0.686 ± 0.008
93803-01-03-01	0.962 ± 0.010	0.671 ± 0.007
93803-01-04-00	0.975 ± 0.008	0.694 ± 0.006
93803-01-05-00	0.984 ± 0.010	0.710 ± 0.007
93803-01-05-01	0.980 ± 0.014	0.693 ± 0.010
93803-01-06-00	0.974 ± 0.008	0.703 ± 0.006
93803-01-07-00	0.963 ± 0.010	0.686 ± 0.007
93803-01-07-01	0.988 ± 0.014	0.707 ± 0.010

continued on the next page

Fluxes — continued

ObsID	$F_{4-10\,\mathrm{keV}}$	$F_{10-20\,\mathrm{keV}}$
93803-01-08-00	0.967 ± 0.008	0.701 ± 0.006
93803-01-09-00	0.962 ± 0.010	0.665 ± 0.008
93803-01-10-00	0.960 ± 0.012	0.705 ± 0.009
93803-01-10-01	0.981 ± 0.009	0.707 ± 0.007
93803-01-11-00	0.976 ± 0.018	0.732 ± 0.013
93803-01-11-01	0.963 ± 0.009	0.687 ± 0.007
93803-01-12-01	0.955 ± 0.014	0.649 ± 0.009
93803-01-13-00	0.971 ± 0.009	0.676 ± 0.006
93803-01-14-00	0.947 ± 0.015	0.599 ± 0.010
93803-01-14-01	0.991 ± 0.014	0.722 ± 0.010
93803-01-14-02	0.957 ± 0.012	0.646 ± 0.008
93803-01-15-00	0.971 ± 0.010	0.677 ± 0.008
93803-01-15-01	0.989 ± 0.016	0.730 ± 0.012
93803-01-15-02	0.974 ± 0.015	0.728 ± 0.010
93803-01-16-02	0.991 ± 0.016	0.753 ± 0.012
93803-01-16-01	0.938 ± 0.014	0.651 ± 0.010
93803-01-16-00	0.960 ± 0.012	0.680 ± 0.009
93803-01-17-00	0.975 ± 0.010	0.666 ± 0.008
93803-01-17-01	0.984 ± 0.013	0.702 ± 0.009
93803-01-18-00	0.984 ± 0.010	0.707 ± 0.008
93803-01-18-01	0.953 ± 0.010	0.655 ± 0.008
93803-01-19-00	0.961 ± 0.013	0.648 ± 0.009
93803-01-19-01	0.948 ± 0.010	0.645 ± 0.008
93803-01-20-00	0.951 ± 0.008	0.661 ± 0.006
94803-01-01-00	0.989 ± 0.017	0.708 ± 0.013
94803-01-01-01	0.940 ± 0.015	0.672 ± 0.010
94803-01-01-02	0.979 ± 0.013	0.695 ± 0.010
94803-01-02-00	0.978 ± 0.009	0.706 ± 0.007
94803-01-02-01	0.948 ± 0.020	0.663 ± 0.014
94803-01-03-00	0.966 ± 0.010	0.689 ± 0.008
94803-01-03-01	0.968 ± 0.017	0.684 ± 0.012
94803-01-04-00	0.960 ± 0.008	0.681 ± 0.006
94803-01-05-00	0.975 ± 0.008	0.693 ± 0.006
94803-01-06-00	0.973 ± 0.008	0.702 ± 0.006
94803-01-07-00	0.959 ± 0.008	0.688 ± 0.006
94803-01-08-00	0.966 ± 0.010	0.660 ± 0.007
94803-01-08-01	0.963 ± 0.012	0.687 ± 0.009
94803-01-09-00	0.954 ± 0.009	0.671 ± 0.006
94803-01-11-01	0.982 ± 0.008	0.718 ± 0.006
94803-01-11-02	0.966 ± 0.006	0.685 ± 0.004
94803-01-11-03	0.960 ± 0.007	0.683 ± 0.005
94803-01-11-04	0.961 ± 0.006	0.677 ± 0.004
94803-01-11-05	0.963 ± 0.005	0.670 ± 0.004

continued on the next page

Fluxes — continued

ObsID	$F_{4-10\,\mathrm{keV}}$	$F_{10-20\,\mathrm{keV}}$
94803-01-11-06	0.973 ± 0.006	0.706 ± 0.004
94803-01-12-00	0.939 ± 0.012	0.625 ± 0.008
94803-01-12-01	0.940 ± 0.010	0.654 ± 0.008
94803-01-13-00	0.950 ± 0.008	0.659 ± 0.006
95803-01-01-00	0.941 ± 0.008	0.636 ± 0.006
95803-01-02-00	0.963 ± 0.009	0.685 ± 0.007
95803-01-03-00	0.936 ± 0.010	0.664 ± 0.007
95803-01-03-01	0.968 ± 0.013	0.661 ± 0.009
95803-01-04-00	0.957 ± 0.009	0.669 ± 0.006

A.2 Epoch folding

Epfold

With the `ISIS` command `epfold` a pulse period can be calculated for a given lightcurve.The command is used as follows: `epfold(barytime,rate,pstart,pstop)`.The epoch folding is performed between the periods pstart and pstop.

Epferror

With the `ISIS` command `epferror` errors for the pulse period determined with `epfold` can be calculated. The command is executed with:
`epferror(barytime,rate,period;ntrial)`
The expiration of this simulations follows the following basic points (after the `ISIS` help for `epferror`):

1. Calculate a mean profile with given period.
2. Compute the intensity for all times applying the period multiplied profile.
3. Simulate an error for all times (assuming normal distribution with sigma = error, or, if not gives sqrt(rate)).
4. Perform epoch folding for that simulated lightcurve.
5. Go to step 2. Ntrial times, sum up the maximum of epoch folding found.
6. Compute the standard deviation of the Ntrial maxima obtained and take these as the error.

A.3 *XMM-Newton*

Table A.3: Start and stop dates for the *XMM-Newton* observations of PKS 2155−304.

ObsID	Start time yyyy-mm-ddThh:mm:ss	End time yyyy-mm-ddThh:mm:ss
0124930201	2000-05-31T00:52:59	2000-05-31T17:21:38
0080940101	2000-11-19T19:00:40	2000-11-20T10:55:39
0080940301	2000-11-20T13:15:19	2000-11-21T05:25:19
0124930301	2001-11-30T15:54:06	2001-12-01T04:17:30
0124930501	2002-05-24T11:18:09	2002-05-24T20:08:10
0124930501	2002-05-24T20:31:33	2002-05-25T05:19:52
0124930501	2002-05-25T05:43:16	2002-05-25T14:01:35
0124930601	2002-11-29T23:32:52	2002-11-30T15:20:17
0158960101	2003-11-23T00:52:28	2003-11-23T08:16:59
0158960901	2004-11-22T21:41:36	2004-11-23T05:36:06
0158961001	2004-11-23T19:52:01	2004-11-24T06:58:11
0158961101	2005-05-12T12:57:05	2005-05-12T20:51:35
0158961301	2005-11-30T20:40:02	2005-12-01T13:19:33
0158961401	2006-05-01T12:31:58	2006-05-02T06:24:50
0411780101	2006-11-07T00:31:25	2006-11-07T08:50:03
0411780201	2007-04-22T04:13:21	2007-04-22T22:57:52
0411780301	2008-05-12T15:08:36	2008-05-13T08:01:29
0411780401	2009-05-28T08:14:46	2009-05-29T02:07:37
0411780501	2010-04-28T23:53:46	2010-04-29T19:32:18
0411780601	2011-04-26T13:56:43	2011-04-27T07:32:54

A.4 *Swift*

Table A.4: Swift observations for PKS 0208−512.

Observation ID	Start Time yyyy-mm-ddThh:mm:ss	XRT exposure [s]	Added Spectrum mm_yy
00035002001	2005-04-23T00:06:35	12377.629	—
00035002002	2005-04-01T10:17:01	395.28	—
00035002003	2005-05-04T23:59:02	2102.838	05_05
00035002004	2005-05-12T00:32:02	2120.71	05_05
00035002005	2005-05-10T00:15:02	4159.417	05_05
00035002006	2008-08-31T13:15:00	1475.349	09_08
00035002007	2008-09-09T12:37:01	1287.327	—
00035002008	2008-09-23T09:20:01	1094.821	—
00035002009	2008-09-30T19:57:01	1083.286	09_08
00035002010	2008-10-08T10:44:01	997.468	10_08

continued on the next page

Swift observations — continued

Observation ID	Start Time	XRT exposure	Added Spectrum
00035002012	2008-10-17T23:04:01	1229.774	10_08
00035002013	2008-10-21T11:59:13	444.449	10_08
00035002014	2008-10-23T13:32:01	3688.442	10_08
00035002015	2008-10-28T01:07:01	1655.394	10_08
00035002016	2008-11-04T08:18:01	1071.467	11_08
00035002017	2008-11-10T15:31:45	3758.078	11_08
00035002018	2008-11-18T12:54:01	1161.029	11_08
00035002019	2008-11-22T21:39:24	0.906	—
00035002020	2008-11-23T11:43:01	1396.71	11_08
00035002021	2008-11-25T10:17:01	2172.342	11_08
00035002022	2008-12-02T14:07:00	1194.519	12_08
00035002023	2008-12-09T11:32:01	1027.089	12_08
00035002024	2008-12-14T15:21:00	1001.118	12_08
00035002025	2008-12-16T00:55:01	1454.958	12_08
00035002026	2008-12-17T07:27:01	4237.692	12_08
00035002027	2008-12-20T01:38:00	4188.762	12_08
00035002028	2008-12-20T17:36:01	4378.898	12_08
00035002029	2008-12-23T01:40:01	4387.057	12_08
00035002030	2008-12-24T19:29:01	4175.554	12_08
00035002031	2008-12-26T02:23:01	4595.873	12_08
00035002032	2009-02-24T23:59:00	1899.019	—
00035002033	2009-09-10T02:38:01	1203.088	09_09
00035002034	2009-09-17T03:21:01	1448.232	09_09
00035002035	2009-09-24T22:03:00	1406.226	09_09
00035002036	2009-10-01T22:36:01	1007.929	10_09
00035002037	2009-10-09T23:16:00	1762.61	10_09
00035002038	2009-10-15T17:23:17	818.097	10_09
00035002039	2009-10-29T13:09:01	1093.229	10_09
00035002040	2009-10-29T02:13:01	779.757	10_09
00035002041	2009-11-04T23:59:01	1273.666	11_09
00035002042	2009-11-12T02:11:00	1707.472	11_09
00035002043	2009-11-19T07:41:01	1183.134	11_09
00035002044	2009-11-26T01:46:01	1491.841	11_09
00035002045	2009-12-03T13:36:01	1060.59	12_09
00035002046	2009-12-10T01:21:01	875.046	12_09
00035002047	2009-12-16T03:58:01	1074.963	12_09
00035002048	2009-12-24T03:03:01	1133.291	12_09
00035002049	2009-12-30T22:42:01	1351.439	12_09
00035002050	2010-01-07T07:24:01	1143.321	—
00035002051	2010-06-22T01:47:01	4987.807	—
00041512002	2010-09-21T23:00:01	1248.066	09_10
00041512003	2010-09-27T04:42:02	1200.074	09_10
00041512004	2010-10-04T17:39:01	1343.91	10_10

continued on the next page

Swift observations — continued

Observation ID	Start Time	XRT exposure	Added Spectrum
00041512006	2010-10-18T07:54:24	634.342	10_10
00041512007	2010-10-25T21:15:00	1190.966	10_10
00041512008	2010-11-01T13:49:01	1173.224	11_10
00041512009	2010-11-08T04:53:00	1000.409	11_10
00041512010	2010-11-14T00:32:01	2274.125	11_10
00041512011	2010-11-22T12:26:01	1108.22	11_10
00041512012	2010-11-29T14:36:01	1602.172	11_10
00041512013	2010-12-06T13:38:01	1377.902	12_10
00041512014	2010-12-13T01:17:00	1777.783	12_10
00041512015	2010-12-19T13:04:01	1291.256	12_10
00041512017	2010-12-28T20:22:01	898.405	12_10
00035002052	2011-07-14T05:34:00	1385.598	07_11
00035002053	2011-07-15T19:52:00	3196.301	07_11

Table A.5: Absorbed and unabsorbed for PKS 0208−512 for three different models. The differences between the 2–10 keV fluxes are listed in the last column.

Data	$F_{0.2-2\,\mathrm{keV}}$	$F^{\mathrm{unabs}}_{0.2-2\,\mathrm{keV}}$	$F_{2-10\,\mathrm{keV}}$	$F^{\mathrm{unabs}}_{2-10\,\mathrm{keV}}$	$F^{\mathrm{unabs}}_{2-10\,\mathrm{keV}} - F_{2-10\,\mathrm{keV}}$ [erg cm^{-2} s^{-1}]
05_05					
power law	1.16 ± 0.09		1.79 ± 0.14		
abs. power law (N_{H})	1.17 ± 0.09	1.34 ± 0.10	1.80 ± 0.14	1.81 ± 0.14	1.93×10^{-15}
abs. power law	1.16 ± 0.09	1.36 ± 0.10	1.79 ± 0.14	1.79 ± 0.14	2.24×10^{-15}
09_08					
power law	0.95 ± 0.15		1.56 ± 0.24		
abs. power law (N_{H})	0.94 ± 0.15	1.09 ± 0.17	1.55 ± 0.24	1.56 ± 0.24	1.63×10^{-15}
abs. power law	0.95 ± 0.15	1.09 ± 0.17	1.56 ± 0.24	1.56 ± 0.24	1.60×10^{-15}
10_08					
power law	1.39 ± 0.10		1.99 ± 0.15		
abs. power law (N_{H})	1.30 ± 0.10	1.51 ± 0.12	1.90 ± 0.14	1.90 ± 0.14	2.05×10^{-15}
abs. power law	1.39 ± 0.10	1.39 ± 0.10	1.99 ± 0.15	1.99 ± 0.15	6.66×10^{-17}
11_08					
power law	1.01 ± 0.09		1.33 ± 0.10		
abs. power law (N_{H})	0.93 ± 0.08	1.09 ± 0.09	1.27 ± 0.10	1.27 ± 0.10	1.40×10^{-15}
abs. power law	1.01 ± 0.09	1.01 ± 0.09	1.33 ± 0.10	1.33 ± 0.10	0.0
12_08					
power law	0.80 ± 0.04		1.13 ± 0.06		
abs. power law (N_{H})	0.79 ± 0.04	0.92 ± 0.05	1.11 ± 0.06	1.12 ± 0.06	1.22×10^{-15}
abs. power law	0.80 ± 0.04	0.89 ± 0.05	1.13 ± 0.06	1.13 ± 0.06	7.76×10^{-16}
35002032					
power law	0.54 ± 0.12		0.88 ± 0.20		
abs. power law (N_{H})	0.57 ± 0.13	0.64 ± 0.15	0.98 ± 0.22	0.98 ± 0.22	1.02×10^{-15}
abs. power law	0.54 ± 0.12	0.82 ± 0.19	0.88 ± 0.20	0.88 ± 0.20	4.49×10^{-15}
09_09					
power law	0.59 ± 0.10		0.68 ± 0.10		
abs. power law (N_{H})	0.62 ± 0.10	0.74 ± 0.12	0.71 ± 0.12	0.71 ± 0.12	8.22×10^{-16}

continued on the next page

Absorbed and unabsorbed fluxes for PKS 0208−512 — continued

Data	$F^{a}_{0.2-2\,\mathrm{keV}}$	$F^{\mathrm{unabs},a}_{0.2-2\,\mathrm{keV}}$	$F^{a}_{2-10\,\mathrm{keV}}$	$F^{\mathrm{unabs},a}_{2-10\,\mathrm{keV}}$	$F^{\mathrm{unabs}}_{2-10\,\mathrm{keV}}-F_{2-10\,\mathrm{keV}}$
abs. power law	0.59 ± 0.10	0.82 ± 0.14	0.68 ± 0.10	0.68 ± 0.10	1.87×10^{-15}
10_09					
power law	0.74 ± 0.10		1.22 ± 0.15		
abs. power law (N_H)	0.69 ± 0.09	0.80 ± 0.10	1.17 ± 0.15	1.17 ± 0.15	1.22×10^{-15}
abs. power law	0.74 ± 0.10	0.74 ± 0.10	1.22 ± 0.15	1.22 ± 0.15	0.0
11_09					
power law	0.62 ± 0.08		0.97 ± 0.13		
abs. power law (N_H)	0.61 ± 0.08	0.71 ± 0.09	0.96 ± 0.13	0.97 ± 0.13	1.02×10^{-15}
abs. power law	0.62 ± 0.08	0.70 ± 0.09	0.97 ± 0.13	0.97 ± 0.13	8.12×10^{-16}
12_09					
power law	0.60 ± 0.09		0.84 ± 0.13		
abs. power law (N_H)	0.57 ± 0.09	0.63 ± 0.10	0.81 ± 0.12	0.81 ± 0.12	8.89×10^{-16}
abs. power law	0.60 ± 0.09	0.60 ± 0.09	0.84 ± 0.13	0.84 ± 0.13	0.0
35002051					
power law	0.75 ± 0.09		0.97 ± 0.12		
abs. power law (N_H)	0.79 ± 0.10	0.92 ± 0.12	1.16 ± 0.14	1.16 ± 0.14	1.25×10^{-15}
abs. power law	0.75 ± 0.09	1.43 ± 0.17	0.97 ± 0.12	0.97 ± 0.12	7.33×10^{-15}
09_10					
power law	1.09 ± 0.16		2.2 ± 0.4		
abs. power law (N_H)	1.11 ± 0.16	1.21 ± 0.17	2.3 ± 0.4	2.3 ± 0.4	2.30×10^{-15}
abs. power law	1.09 ± 0.16	1.28 ± 0.18	2.2 ± 0.4	2.2 ± 0.4	4.95×10^{-15}
10_10					
power law	1.24 ± 0.15		2.44 ± 0.30		
abs. power law (N_H)	1.17 ± 0.15	1.33 ± 0.17	2.38 ± 0.29	2.38 ± 0.29	2.35×10^{-15}
abs. power law	1.24 ± 0.15	1.24 ± 0.15	2.44 ± 0.30	2.44 ± 0.30	0.0
11_10					
power law	1.11 ± 0.09		2.20 ± 0.18		
abs. power law (N_H)	1.13 ± 0.09	1.29 ± 0.10	2.24 ± 0.18	2.24 ± 0.18	2.23×10^{-15}
abs. power law	1.11 ± 0.09	1.34 ± 0.10	2.20 ± 0.18	2.20 ± 0.18	3.26×10^{-15}
12_10					
power law	1.03 ± 0.10		2.23 ± 0.23		
abs. power law (N_H)	1.07 ± 0.10	1.22 ± 0.13	2.33 ± 0.24	2.33 ± 0.24	2.26×10^{-15}
abs. power law	1.03 ± 0.10	1.34 ± 0.14	2.23 ± 0.23	2.23 ± 0.23	5.39×10^{-15}
07_11					
power law	0.87 ± 0.10		1.57 ± 0.19		
abs. power law (N_H)	0.82 ± 0.10	0.92 ± 0.10	1.54 ± 0.18	1.54 ± 0.18	1.56×10^{-15}
abs. power law	0.87 ± 0.10	0.87 ± 0.10	1.57 ± 0.19	1.57 ± 0.19	0.0

[a] In units of 10^{-12} erg cm^{-2} s^{-1}.

List of Figures

List of Tables

Bibliography

Acero F., 2009, A&A 2, 2

Aharonian F., Akhperjanian A.G., Aye K.M., et al., 2005, A&A 435, L17

Anders E., Grevesse N., 1989, Geochim. Cosmochim. Acta 53, 197

Aschenbach B., Citterio O., Ellwood J.M., et al., 1987, The high throughput X-ray Spectroscopy Mission. Report of the Telescope Working Group, European Space Agency

Baade W., Zwickey F., 1934, Proceedings of the National Academy of Science 20, 254

Barthelmy S.D., Barbier L.M., Cummings J.R., et al., 2005, Space Sci. Rev. 120, 143

Brazier K.T.S., Becker W., 1997, MNRAS 284, 335

Brodie J.P., Bowyer S., Clarke J.T., Henry P., 1983, In: Bulletin of the American Astronomical Society, Vol. 15. Bulletin of the American Astronomical Society, p. 956

Burlon D., Ajello M., Greiner J., et al., 2011, ApJ 728, 58

Burrows D.N., Hill J.E., Nousek J.A., et al., 2005, Space Sci. Rev. 120, 165

Capalbi M., Perri M., Saija B., et al., 2005, The SWIFT XRT Data Reduction Guide, Version 1.2

Caraveo P.A., Mereghetti S., Bignami G.F., 1994, Astrophys. J., Lett. 423, L125

Cardelli J.A., Clayton G.C., Mathis J.S., 1989, ApJ 345, 245

Caswell J.L., Milne D.K., Wellington K.J., 1981, MNRAS 195, 89

Chandrasekhar S., 1931, ApJ 74, 81

Cusumano G., Mineo T., Massaro E., et al., 2001, A&A 375, 397

DeLaney T., Gaensler B.M., Arons J., Pivovaroff M.J., 2006, ApJ 640, 929

den Herder J.W., Brinkman A.C., Kahn S.M., et al., 2001 365, L7

Drinkwater M.J., Webster R.L., Francis P.J., et al., 1997, MNRAS 284, 85

Eracleous M., Halpern J.P., 2004, ApJS 150, 181

ESA: XMM-Newton SOC 2011, XMM-Newton User Handbook, Issue 2.9

Falomo R., Maraschi L., Treves A., Tanzi E.G., 1987, Astrophys. J., Lett. 318, L39

Fanaroff B.L., Riley J.M., 1974, MNRAS 167, 31P

Fath E.A., 1909, Lick Observatory Bulletin 5, 71

Fitzpatrick E.L., 1999, PASP 111, 63

Forot M., Hermsen W., Renaud M., et al., 2006, Astrophys. J., Lett. 651, L45

Fürst F., 2008, *Master's thesis*, Friedrich-Alexander Universität Erlangen-Nürnberg

Gaensler B.M., Arons J., Kaspi V.M., et al., 2002, ApJ 569, 878

Gaensler B.M., Brazier K.T.S., Manchester R.N., et al., 1999, MNRAS 305, 724

Gallo L.C., Edwards P.G., Ferrero E., et al., 2006, MNRAS 370, 245

Gehrels N., Chincarini G., Giommi P., et al., 2004, ApJ 611, 1005

Griffiths R.E., Briel U., Wade R.A., et al., 1978 3279, 2

Gunji S., Hirayama M., Kamae T., et al., 1994, ApJ 428, 284

Haensel P., Potekhin A.Y., Yakovlev D.G., 2007, Neutron Stars 1 : Equation of State and Structure, Vol. 326 of *Astrophysics and Space Science Library*, Astrophysics and Space Science Library, Springer Verlag

Hertz H., 1887, Ueber sehr schnelle electrische Schwingungen, 267(7), Annalen der Physik

Hoffmeister C., 1929, Astronomische Nachrichten 236, 233

Hubble E.P., 1926, ApJ 64, 321

Jahoda K., Markwardt C.B., Radeva Y., et al., 2006, ApJS 163, 401

Jahoda K., Swank J.H., Giles A.B., et al., 1996, In: Siegmund O.H., Gummin M.A. (eds.) Proc. EUV, X-Ray, and Gamma-Ray Instrumentation for Astronomy VII, Vol. 2808. SPIE, p.59

Jansen F., Lumb D., Altieri B., et al., 2001 365, L1

Jansky K.G., 1933, Nat 132, 66

Kawai N., Okayasu R., Brinkmann W., et al., 1991, Astrophys. J., Lett. 383, L65

Kawai N., Okayasu R., Sekimoto Y., 1993, In: Friedlander M., Gehrels N., Macomb D. (eds.) Compton Gamma-Ray Observatory, Vol. 280. American Institute of Physics Conference Series, p. 213

Kellermann K.I., Sramek R., Schmidt M., et al., 1989, AJ 98, 1195

Kippenhahn R., Weigert A., 1990, Stellar Structure and Evolution, Springer Verlag

Klebesadel R.W., Strong I.B., Olson R.A., 1973, Astrophys. J., Lett. 182, L85

Kreykenbohm I., Coburn W., Wilms J., et al., 2002, A&A 395, 129

Krolik J., 1998, Active Galactic Nuclei, Princeton University Press

Kühnel M., 2011, *Master's thesis*, Friedrich-Alexander Universität Erlangen-Nürnberg

Kuiper L., Hermsen W., Krijger J.M., et al., 1999, A&A 351, 119

Laurent P., Paul J., Claret A., et al., 1994, A&A 286, 838

Levine A.M., Bradt H., Cui W., et al., 1996, Astrophys. J., Lett. 469, L33

Litzinger E., Pottschmidt K., Wilms J., et al., in prep., Monitoring PSR B1509-58 with RXTE

Livingstone M.A., Kaspi V.M., 2011, ApJ 742, 31

Livingstone M.A., Kaspi V.M., Gavriil F.P., Manchester R.N., 2005, ApJ 619, 1046

Livingstone M.A., Kaspi V.M., Gavriil F.P., et al., 2007, Ap&SS 308, 317

Lorimer D.R., 2008, Living Reviews in Relativity 11, 8

Lyne A.G., Graham-Smith F., 1998, Pulsar astronomy, Cambridge University Press, second edition edition

Manchester R.N., Tuohy I.R., D'Amico N., 1982, Astrophys. J., Lett. 262, L31

Marsden D., Blanco P.R., Gruber D.E., et al., 1997, Astrophys. J., Lett. 491, L39

Mason K.O., Breeveld A., Much R., et al., 2001 365, L36

Matz S., Ulmer M.P., Grabelsky D.A., et al., 1994, ApJ 434, 288

Maxwell J.C., 1865, Philosophical Transactions of the Royal Society of London 155, 459

Mineo T., Cusumano G., Maccarone M.C., et al., 2001, A&A 380, 695

Oppenheimer J.R., Volkoff G.M., 1939, Physical Review 55, 374

Osterbrock D.E., 1989, Astrophysics of Gaseous Nebulae and Active Galactic Nuclei, University Science Books

Osterbrock D.E., Pogge R.W., 1985, ApJ 297, 166

Padmanabhan T., 2001, Theoretical Astrophysics, Volume 2: Stars and Stellar Systems, Cambridge

University Press

Peterson B.M., 1997, An Introduction to Active Galactic Nuclei, Cambridge, New York Cambridge University Press

Predehl P., Schmitt J.H.M.M., 1995 293, 889

Prialnik D., 2000, An Introduction to the Theory of Stellar Structure and Evolution, Cambridge University Press

Ridpath I., 1989, Star Tales (Faith & Fame S.), Lutterworth Press

Rodgers A.W., Campbell C.T., Whiteoak J.B., 1960, MNRAS 121, 103

Roming P.W.A., Kennedy T.E., Mason K.O., et al., 2005, Space Sci. Rev. 120, 95

Röntgen K., 1895, Über eine neue Art von Strahlen, Technical report, Würzburger Physikalisch-medizinische Gesellschaft

Rothschild R.E., Blanco P.R., Gruber D.E., et al., 1998, ApJ 496, 538

Rothschild R.E., Wilms J., Tomsick J., et al., 2006, ApJ 641, 801

Rots A.H., Jahoda K., Macomb D.J., et al., 1998, ApJ 501, 749

Rybicki G.B., Lightman A.P., 2004, Radiative Processes in Astrophysics, Wiley-VCH

Saito Y., Kawai N., Kamae T., Shibata S., 1997, In: Dermer C.D., Strickman M.S., Kurfess J.D. (eds.) Proceedings of the Fourth Compton Symposium, Vol. 410. American Institute of Physics Conference Series, p. 628

Seward F.D., Harnden, Jr. F.R., 1982, Astrophys. J., Lett. 256, L45

Seward F.D., Harnden, Jr. F.R., Murdin P., Clark D.H., 1983, ApJ 267, 698

Seward F.D., Harnden, Jr. F.R., Szymkowiak A., Swank J., 1984, ApJ 281, 650

Seyfert C.K., 1943, ApJ 97, 28

Shimmins A.J., Bolton J.G., 1974, Australian Journal of Physics Astrophysical Supplement 32, 1

Short A.D., Keay A., Turner M.J., 1998, In: O. H. Siegmund & M. A. Gummin (ed.) Society of Photo-Optical Instrumentation Engineers (SPIE) Conference Series, Vol. 3445. Society of Photo-Optical Instrumentation Engineers (SPIE) Conference Series, p.13

Shu F.H., 1991, Physics of Astrophysics, Vol. I, University Science Books

Strüder L., Briel U., Dennerl K., et al., 2001 365, L18

Swank J., Rothschild R., Bradt H., et al., 1995a, The RXTE technical appendix F, NASA/GSFC

Swank J., Rothschild R.E., Bradt H., et al., 1995b, The RXTE technical appendix F, NASA/GFSC

Takáts K., Vinkó J., 2006, MNRAS 372, 1735

Talavera A., OMCal Team 2011, XMM-Newton Optical and UV Monitor (OM) Calibration Status, XMM-SOC-CAL-TN-0019 Issue 6.0

Tamura K., Kawai N., Yoshida A., Brinkmann W., 1996, PASJ 48, L33

Thielemann F.K., Hirschi R., Liebendörfer M., Diehl R., 2011, In: R. Diehl, D. H. Hartmann, & N. Prantzos (ed.) Lecture Notes in Physics, Berlin Springer Verlag, Vol. 812. Lecture Notes in Physics, Berlin Springer Verlag, p.153

Trussoni E., Brinkmann W., Ogelman H., et al., 1990, A&A 234, 403

Trussoni E., Massaglia S., Caucino S., et al., 1996, A&A 306, 581

Turner M.J.L., Abbey A., Arnaud M., et al., 2001 365, L27

Ulmer M.P., 1994, ApJS 90, 789

Ulmer M.P., Matz S.M., Wilson R.B., et al., 1993, ApJ 417, 738

Unsöld A., Baschek B., 1988, Der neue Kosmos, Springer Verlag

Urry C.M., Padovani P., 1995, PASP 107, 803

von Montigny C., Bertsch D.L., Chiang J., et al., 1995, ApJ 440, 525

Wall J.V., 1975, The Observatory 95, 196

Wall J.V., Pettini M., Danziger I.J., et al., 1986, MNRAS 219, 23P

Walt Disney 1994, The Lion King, Walt Disney Pictures

Wilms J., 2007, Introduction to Astronomy II, Lecture Notes at the FAU Erlangen-Nürnberg

Wilms J., 2008, Astrophysical Radiatio Processes, Lecture Notes at the FAU Erlangen-Nürnberg

Wilms J., Allen A., McCray R., 2000, ApJ 542, 914

Wilms J., Kadler M., 2008/2009, X-Ray Astronomy II, Lecture Notes at the FAU Erlangen-Nürnberg

Wilms J., Kadler M., 2010, Active Galactic Nuclei, Lecture Notes at the FAU Erlangen-Nürnberg

Yatsu Y., Kawai N., Kataoka J., et al., 2005, ApJ 631, 312

Zhang L., Cheng K.S., 2000, A&A 363, 575

Zhang S., Collmar W., Torres D.F., et al., 2010 514, A69

Zhang W., Giles A.B., Jahoda K., et al., 1993, In: O. H. Siegmund (ed.) Society of Photo-Optical Instrumentation Engineers (SPIE) Conference Series, Vol. 2006., p.324

Zhang Y.H., 2008, ApJ 682, 789

Zhang Y.H., Bai J.M., Zhang S.N., et al., 2006, ApJ 651, 782

Danksagung

Ich möchte mich bei allen bedanken, die mir geholfen habe diese Arbeit zu erstellen und die mir zu dieser Zeit zur Seite standen.

Meinem Betreuer Jörn Wilms, den man auch immer wieder die gleichen Fragen stellen konnte ohne dass es ihn ermüdete einem eine ausreichende Erklärung zu geben. Der einem auch die Möglichkeit geboten hat internationale Konferenzen zu besuchen und dort die Arbeit anderer Astronomen kennen zu lernen.

Meinem zweiten Betreuer Matthias Kadler, der mich in die Welt der Radioastronomie führen wollte, aber doch die Röntgenastronomie für diese Arbeit hat gewähren lassen. Dafür werde ich mich in meiner weiteren Arbeit der Radioastronomie zuwenden.

Katja Pottschmidt und Rick Rothschild für ihre Hilfe bei der Analyse von B1509−58.

Meinen Kollegen Matthias Kühnel, Thomas Dauser, Refiz Duro und Felix Fürst die ich bei Problemen beim programmieren und mit ISIS öfters aufsuchen musste.

Dem Knigge-Zimmer, das immer für Unterhaltung sorgte, wenn einem die Arbeit über den Kopf zu wachsen schien.

Allen anderen Kollegen der Sternwarte für die wunderbare Zeit und die lustigen und wissenswerte Gespräche beim Mittagessen und den zahlreichen Feiern.

Ganz besonderer Dank gilt natürlich meiner Familie, die mich immer unterstützt hat, auch wenn ich während des Studiums manchmal ins Zweifeln gekommen bin. Meinem Freund, der das gleiche Schicksal teilte wie ich und sich tapfer durch die Diplomarbeit gekämpft hat und dennoch Zeit für mich hatte.

Hiermit erkläre ich, dass ich die Arbeit selbstständig angefertigt und keine anderen als die angegebenen Hilfsmittel verwendet habe.

Bamberg, 16. Dezember 2011

Eugenia Litzinger